HIGH TEMPERATURE PACKED BED THERMAL STORAGE FOR SOLAR GAS TURBINES

Peter Klein

A thesis submitted to the Faculty of Engineering and the Built Environment, University of the Witwatersrand, Johannesburg, in fulfilment of the requirements for the degree of Doctor of Philosophy.

Johannesburg, 2016

Declaration

I declare that this thesis is my own, unaided work. It is being submitted for the degree of Doctor of Philosophy to the University of the Witwatersrand, Johannesburg. It has not been submitted before for any degree or examination to any other University.

_____

Peter Klein
26th day of May 2016

Abstract

Solar powered gas micro-turbines present opportunities for off-grid power generation. Due to the intermittent nature of the solar energy supply, existing Solar Gas Turbine (SGT) plants employ hybridisation with fossil fuels to generate dispatchable power. In this work sensible heat and latent heat storage solutions are investigated as a means of increasing the solar share of a SGT cycle, thus reducing the consumption of diesel fuel.

The sensible heat storage concept was based on a pressurised packed bed of spherical ceramic particles, using air as the heat transfer fluid. An axisymmetric, two-phase heat transfer model of the system was developed, based on the continuous solid phase approach. The model was successfully validated against experimental data from a packed bed of alumino-silicate particles over the temperature ranges of gas turbine cycles (350-900 °C and 600-900 °C). The validated numerical model was utilised to conduct a parametric design study of a six hour (1.55 MWh_{th}) storage system for a gas micro-turbine. The results show that a high storage efficiency and high utilisation factor can be achieved when combining sensible heat storage in alumina with fossil fuel hybridisation, with somewhat lower values without hybridisation. An analysis of different inventory geometries showed that a packed bed of spherical particles is best suited to pressurised sensible heat storage.

The latent heat storage concept was based on a pressurised packed bed of Encapsulated Phase Change Material (EPCM) particles. Sodium sulphate was identified as a suitable phase change material for the gas turbine cycle. The sensible heat storage model was extended to account for intra-particle temperature gradients and phase change within the particles. The intra-particle phase change model was validated against published experimental data for a single EPCM sphere heated and cooled by convection. The full EPCM storage model was further successfully validated against experimental data from a packed bed of macro-encapsulated sodium sulphate particles with alumina shells, up to a temperature of 950 °C.

A comparison of the two storage concepts for a 7 m^3 bed shows that a packed bed of encapsulated sodium sulphate particles would have a 36% lower energy storage capacity than a bed of solid alumina particles. This is due to the limited melt fraction in the EPCM bed when a temperature limit is placed on the base. Increasing the packed bed volume to 10.5 m^3 would provide a comparable thermal performance to the 7 m^3 solid alumina bed, at a 12% lower storage mass. A hybrid three-layer packed bed is proposed to increase the volumetric energy storage density. Modelling shows that this concept could provide a small increase of 5.3% in the amount of energy discharged above 850 °C, compared to the solid alumina particles only.

In loving memory of David Klein. A proud Witsie.

Acknowledgements

I would like to acknowledge the Council for Scientific and Industrial Research (CSIR) and the South African National Energy Development Institute (SANEDI) for their financial support which has made this research possible. I wish to sincerely thank my supervisor Professor John Sheer for his patience, guidance and the time that he has invested into this research project. I have enjoyed our many thought provoking discussions. I would also like to express my gratitude to the following people:

Thomas Roos from the CSIR for introducing me to the field of concentrating solar power and giving me the opportunity to conduct research in this area, and for his assistance during experiments;

Martin Beyers and cerAdvance for their expert input regarding ceramic materials, and for manufacturing the hollow alumina shells and porous alumina particles used in this research;

Dr Dawie Van Vuuren and the CSIR MSM group for allowing me to conduct experiments in their high temperature laboratory;

My parents, David and Margie Klein, for the unwavering support of my studies and for all the opportunities they have afforded me in life;

Richard Klein for his recommendations and assistance regarding numerical programming techniques;

My partner Genevieve Vieira for sacrificing time with me and for supporting me throughout my studies;

The Allen family, Kenneth, Sandy and Philip for helping me to get over the finish line;

My colleague Maurice Maliage for his assistance during experiments;

Graeme Utton for helping to fill the encapsulated sodium sulphate particles for testing;

Professor Anne Love for her input regarding analytical modelling techniques.

Dr Igle Gledhill for her advice and encouragement.

Contents

List of Figures

List of Tables

Nomenclature

Roman Symbols

a_{ij}	unknown series coefficient for fluid phase
a_p	particle surface area per unit volume [m^{-1}]
a_v	parameter in velocity flow profile in Eq.(2.26)
A	Area [m^2]
b_{ij}	unknown series coefficient for solid phase
b_v	non dimensional bed radius according to Vortmeyer and Schuster (1983)
B	deformation factor
c	specific heat capacity at constant pressure [J/kgK]
Δc_s	normalised change in solid phase heat capacity [J/kgK]
c_d	form drag coefficient of a sphere
C	equipment capital cost [ZAR]
C_v	constant in Eq.(2.25)
C_A	viscous pressure loss coefficient in Eq.(2.71)
C_B	inertial pressure loss coefficient in Eq.(2.71)
C_d	discharge coefficient for differential pressure flow measurement device
C_D	thermal fluid dispersion coefficient
d_p	particle diameter [m]
d_c	conical inlet diameter [m]
d_o	orifice plate diameter [m]
D	packed bed diameter [m]
D_o	orifice plate pipe diameter [m]

e_{ij}	unknown series coefficient for wall phase
E	Young's modulus [Pa]
f_p	duct friction factor
f_1	viscous pressure loss coefficient in Eq.(2.32)
f_2	inertial pressure loss coefficient in Eq.(2.32)
F_s	form factor accounting for particle deformation in Eq.(2.43)
g_{ij}	unknown series coefficient for particle phase
G_z	fluid mass flux (superficial) [kg/sm^2]
h_c	natural convection heat transfer coefficient for vertical cylinder [W/m^{2}K]
h_f	fluid specific enthalpy [J/kg]
h_s	solid specific enthalpy [J/kg]
h_p	inter-phase heat transfer coefficient [W/m^{2}K]
h_p^*	modified inter-phase heat transfer coefficient [W/m^{2}K]
h_r	radiation heat transfer coefficient [W/m^{2}K^4]
$\overline{h}_r$	linearised radiation heat transfer coefficient [W/m^{2}K]
Δh_{pt}	enthalpy change for solid-solid phase transition [kJ/kg]
Δh_{fus}	enthalpy of fusion for phase change material [kJ/kg]
k	thermal conductivity [W/mK]
$k_{\mathrm{eff,f}}$	effective fluid phase thermal conductivity [W/mK]
$k_{\mathrm{eff,s}}$	effective solid phase thermal conductivity [W/mK]
$k_{\mathrm{eff}}^{\mathrm{sr}}$	void radiation and solid conduction component of $k_{\mathrm{eff,s}}$ [W/mK]
$k_{\mathrm{eff}}^{\mathrm{sf}}$	fluid and solid conduction component of $k_{\mathrm{eff,s}}$ [W/mK]
$k_{\mathrm{eff}}^{\mathrm{sc}}$	contact area and solid conduction component of $k_{\mathrm{eff,s}}$ [W/mK]
K_B	Blake constant
K_D	Darcy permeability [m^2]
K_K	Kozeny constant
L_c	tortuous flow length through packed bed [m]
L_z	packed bed length [m]

$\dot{m}$	mass flow rate [kg/s]
MF	melt fraction
n_v	parameter in velocity flow profile in Eq.(2.26)
N_A	number of particles per unit area [m^{-2}]
N_{helio}	number of heliostats
N_L	number of particles per unit length [m^{-1}]
N_p	number of particle elements
N_r	number of radial elements
N_v	constant in void fraction correlation, given by Eq.(2.25)
N_w	number of wall elements
N_z	number of axial elements
p_s	external pressure on particles due to packed bed mass [Pa]
p_0	solid PCM heat capacity at reference temperature [J/kgK]
p_1	linear gradient in solid PCM heat capacity with temperature [J/kgK^2]
P	pressure [Pa]
P_u	upstream pressure from orifice plate [Pa]
ΔP	pressure drop across the packed bed [Pa]
ΔP_c	pressure difference between ambient and throat of conical inlet [Pa]
ΔP_o	pressure difference across orifice plate [Pa]
Q	thermal energy [J]
Q_c	thermal energy supplied during charging cycle [J]
Q_d	thermal energy extracted during discharging cycle [J]
Q_m	thermal energy stored per unit mass [J/kg]
Q_v	thermal energy stored per unit volume [J/m^3]
$Q_{\Delta P}$	thermal energy used by the packed bed blower during charging [J]
$\dot{q}_c$	heat flux at outer packed bed wall [W/m^2]
$\dot{q}_f$	fluid heat flux at inner packed bed wall [W/m^2]
$\dot{q}_p$	heat flux at particle surface [W/m^2]

$\dot{q}_s$	solid heat flux at inner packed bed wall [W/m^2]
r	radial bed coordinate [m]
R	packed bed radius [m]
R_o	outer packed bed wall radius [m]
Δr	radial element size [m]
S	packing parameter related to volumetric arrangement of particles
S_F	packing parameter related to volumetric arrangement of particles
t	time [s]
Δt	time step size [s]
T	temperature [K]
$T_{\text{in,c}}$	inlet air temperature to storage during charging [K]
$T_{\text{in,d}}$	inlet air temperature to storage during discharging [K]
T_b	base temperature of storage at $z = L_z$ [K]
T_d	discharge temperature from storage [K]
ΔT_{rec}	temperature change across the solar receiver [K]
ΔT_m	melting temperature range for phase change material [K]
ΔT_{fs}	temperature difference between fluid and particle surface [K]
T_m	melting temperature of phase change material [K]
T_{m1}	start of melting temperature range for phase change material [K]
T_{m2}	end of melting temperature range for phase change material [K]
u_p	particle specific internal energy [J/kg]
u_s	solid specific internal energy [J/kg]
U^*	axial fluid superficial plug flow velocity [m/s]
U_z	axial fluid superficial flow velocity [m/s]
U_{therm}	thermocline velocity [m/s]
UF	utilisation factor
V	packed bed volume [m^3]
v	local radial element coordinate

w	local axial element coordinate
w_{sh}	encapsulated PCM shell thickness [m]
$\mathbf{X}$	percentage excess air
x	local particle element coordinate
Y	expansibility factor
Y_K	non-dimensional temporal variable in Schumann model analytical solution
z	axial bed coordinate [m]
Z_K	non-dimensional spatial variable in Schumann model analytical solution
Δz	axial element size [m]

Greek Symbols

α	thermal diffusivity [m^2/s]
β_{PCM}	volumetric thermal expansion coefficient for the liquid PCM [K^{-1}]
β_f	isobaric volumetric thermal expansion coefficient for the fluid phase [K^{-1}]
β_o	diameter ratio of orifice plate
β_v	parameter that relates the flow profiles in finite and semi-infinite packed beds
δ_{PCM}	position of phase change front [m]
ε	void fraction
ε_∞	void fraction at the centre of the packed bed
η_{blower}	electrical efficiency of blower
η_{helio}	annual heliostat efficiency
η_{rec}	receiver efficiency
η_{turb}	thermal to electric conversion efficiency of gas turbine
γ	emissivity
Λ	component of Damköhler equivalent thermal conductivity
λ	fluid to solid thermal conductivity ratio
μ	dynamic viscosity [Pa s]
μ_{eff}	effective fluid viscosity [Pa s]
ν_{PCM}	kinematic viscosity of liquid PCM [m^2/s]

ν_s	Poisson ratio
ϕ	Hermite polynomial
ψ	pressure loss coefficient (friction factor)
Ψ_p	shape factor for non spherical particles
Ψ_v	void fraction distribution function
ρ	density [kg/m^3]
σ	Stefan-Boltzmann constant (5.67×10^{-8}) [W/m^{2}K^4]
θ_c	angular cylindrical bed coordinate [rad]
Θ_{PCM}	normalised phase change material temperature
Θ_f	normalised fluid phase temperature
Θ_s	normalised solid phase temperature
ζ	intra-particle radial coordinate [m]
ξ	storage efficiency
$\Delta\zeta$	particle element size [m]

Superscripts

avg	average value
k	radial element number
l	axial element number
m	particle element number
max	maximum value
min	minimum value
n	time step number

Subscripts

a	ambient
c	charging cycle
conv	convection
d	discharging cycle
f	fluid phase

fuel	LP gas fuel
PCM	phase change material
p	particle
rad	radiation
rec	receiver
ref	reference
rs	radiation shield
s	solid phase
sb	solid phase half a particle diameter from the wall
solar	solar energy
SOLGATE	receiver from SOLGATE project
st	storage
stoich	stoichiometric
turb	turbine
tc	thermocouple
w	wall phase
$w1$	inner wall region
$w2$	outer wall region

Non-Dimensional Variables

j_H	Colburn j factor
Bi_p	particle Biot number
Nu_p	particle Nusselt number
Pr	Prandtl number
Ra_p	intra-particle Rayleigh number for liquid PCM
Re_Ψ	particle Reynolds number defined by Yoshida et al. (1962)
Re_c	conical inlet Reynolds number
Re_m	modified particle Reynolds number
Re_o	orifice Reynolds number

Re_p	particle Reynolds number

Acronyms

C-S	Continuous-Solid heat transfer model
CFD	Computational Fluid Dynamics
CSIR	Council for Scientific and Industrial Research
CSP	Concentrating Solar Power
D-C	Dispersion-Concentric heat transfer model
DME	Department of Minerals and Energy
DNI	Direct Normal Irradiance
EPCM	Encapsulated Phase Change Material
FOB	Free On Board shipping
KTA	German Nuclear Safety Standards Commission
LCOE	Levelised Cost of Electricity
MLPB	Multi Layered Packed Bed
NRMSD	Normalised Root Mean Square Deviation
PCM	Phase Change Material
PV	Photovoltaic
RMS	Root Mean Square
SGT	Solar Gas Turbine
TES	Thermal Energy Storage
TMY	Typical Meteorological Year
ZBS	Zehner-Bauer-Schlünder model for solid effective thermal conductivity

List of Publications

This work resulted in the following peer-reviewed publications:

Journal Papers

Klein, P., Roos, T. and Sheer, T. 2015, Parametric analysis of a high temperature packed bed thermal storage design for a solar gas turbine, *Solar Energy* **118**, 59–73.

Conference Papers

Klein, P., Roos, T.H. and Sheer, T.J. 2014, Experimental investigation into a packed bed thermal storage solution for solar gas turbine systems, *Energy Procedia* **4**9, 840–849.

Klein, P., Roos, T.H. and Sheer, T.J. 2014, Analysis of regenerative thermal storage geometries for solar gas turbines, *in Proceedings of the 15th International Heat Transfer Conference, IHTC-15*, Kyoto Japan, IHTC15-9580.

Klein, P., Roos, T.H. and Sheer, T.J. 2014, High temperature thermal storage using encapsulated phase change materials for solar gas turbines, *in Proceedings of the 2nd Southern African Solar Energy Conference*, Port Elizabeth.

Chapter 1

Introduction

1.1 Concentrating solar power in South Africa

Currently 93% of South Africa's electricity is generated from coal fired power stations (Eberhard, 2011). Hartnady (2010) predicts that coal production in the country will reach its peak in the year 2020. In the future the decreasing supply of coal will lead to increasing electricity prices, thus affecting the potential for economic growth. The development and implementation of effective renewable energy technologies will allow South Africa to reduce its fossil fuel dependence, while simultaneously addressing environmental concerns related to the emission of greenhouse gases.

Due to the geographic location of South Africa on the sun belt, it receives high levels of solar radiation. The potential power generation capacity from solar energy is extensive. The South African Department of Minerals and Energy (DME) estimate that 194 000 km^2 of South African land receives Direct Normal Irradiance (DNI) levels suitable for the deployment of Concentrating Solar Power (CSP) plants (DME, 2003) . Fluri (2009) calculated that South Africa has a potential installed CSP capacity of 547.6 GW_e. Therefore solar radiation is an abundant renewable energy resource for power generation in the country.

CSP plants concentrate solar radiation and convert it into thermal energy that is used to drive a conventional heat engine, such as a Rankine, Brayton or Stirling cycle. Although insolation is a clean and abundant energy source its supply is intermittent and somewhat unpredictable in nature. This is a core technical challenge in the design of solar power stations that are required to generate predictable power delivery to the grid. The primary advantage of CSP technology over Photovoltaic (PV) systems is the ability to provide dispatchable power

through hybridisation with fossil fuels and Thermal Energy Storage (TES). The implementation of thermal storage allows for the decoupling of energy supply and demand. This is particularly important in the South African context, which experiences a high evening peak demand for electricity. The value of thermal storage was recognised during the third bidding window of the Renewable Energy Independent Power Producer Procurement Programme (REIPPP). A premium of 270% on the base bid price (1.65 ZAR/kWh) was allowed by the National Energy Regulator (NERSA), for electricity produced between 16:30 and 21:30.

In addition to electricity generation tied to the national grid, CSP plants offer new opportunities for off-grid power supply. This is due to the ability to deliver electricity when insolation is not available. Despite South Africa's extensive electrification programme undertaken over the past two decades, 55% of the rural population and 15% of the total population do not have access to electricity (Longe et al., 2014). These rural areas are generally sparsely populated and costly to connect to the national grid. The average cost of connecting a rural household to the grid is 42% higher than an urban household (Bongwe, 2013). In order to provide electricity to remote rural areas DME (2003) propose the development of mini-grids that consist of a centralised power generation unit at a local level. These systems are not linked to the national grid but instead provide power to a rural community at loads below 500 kW_e (IEA, 2011). One of the key approaches of the (DME, 2003) is the co-generation of electricity and thermal energy in rural areas, which is suited to CSP applications.

CSP technology also has the potential to provide electricity to remote industrial and mining operations that currently operate on diesel generators. The case study of the South African mine CRONIMET provides insight into the savings that can be achieved by offsetting diesel costs with solar power. A 24% reduction in diesel usage was achieved by installing a 1 MW_e PV plant that provides 60% of the mine's peak electricity needs. At an average diesel cost of 0.41 USD/kWh the payback period of the plant was only three years (Boyse et al., 2014). A CSP plant with TES would further offset diesel costs during night-time operation.

1.2 Description of solar gas turbine cycle

Central receiver (or power tower) CSP plants utilise a field of individually tracking mirrors (heliostats) that concentrate solar radiation onto a tower based receiver. Traditionally these systems utilised a steam turbine as the heat engine to generate electricity. However, recent developments in high temperature, pressurised air receivers, allow central receiver systems to provide a high grade heat source to drive a gas turbine cycle. The SOLGATE project was

first to demonstrate the technical feasibility of Solar Gas Turbine (SGT) cycles by successfully operating a modified 250 kW_e helicopter gas turbine off solar thermal energy (Heller et al., 2006). Subsequent projects such as SOLUGAS in Spain (4.6 MW_e gas turbine) and PEGASE in France (1.4 MW_e gas turbine) are focused on the scale up demonstration of SGTs for combined cycles (Grange et al., 2014; Quero et al., 2014). Solarised combined cycles employ a non-recuperated gas turbine powered by solar thermal energy. The waste heat generated by the gas turbine is used to drive a secondary steam cycle.

The use of a standalone recuperated gas turbine offers many advantages over a steam turbine for off-grid power generation. Brayton cycles do not require the economies of scale of Rankine cycles and can be implemented in micro-turbine capacity (100-350 kW_e) at efficiency levels up to 30%. They also do not require cooling water and are readily hybridisable with fossil fuels. The waste heat exhausted from the micro-turbine can be used as the energy input into a secondary cycle such as a hot water heat exchanger, absorption chiller or multi-effect desalination unit. This approach provides an integrated energy solution for rural communities and industries, while significantly increasing the overall system efficiency.

The current study is based on a gas micro-turbine cycle. The plant that is analysed is the Turbec T100 gas turbine, but the results are generalizable to other types of gas micro-turbines. The T100 is a commercially available micro-turbine that produces 100 kW_e and 170 kW_{th} at standard ISO conditions. The turbine inlet temperature is 950 °C and the compressor pressure ratio is 4.5. The T100 was successfully operated off solar energy, using a tubular receiver, during the EU FP7 SOLHYCO project (Amsbeck et al., 2010). The Israeli-Spanish company AORA Solar has commercialised a modular SGT system based on the T100 gas turbine. According to Aora (2012) each power module (single SGT unit) can sustain a 60-80 home community, with a plant footprint of 2000 m^2 per module. Currently the company operates two plants based on this technology.

A diagram of the T100 SGT cycle with the proposed thermal storage system is presented in Figure 1.1. The standard recuperated Brayton cycle is modified to accept thermal energy from a pressurised solar receiver. In the SGT cycle air is drawn into the compressor where it is pressurised. The pressurised air is preheated in the recuperator, before passing through the solar receiver (either tubular or volumetric), where it absorbs the required thermal energy for power generation. In the hybridised SGT cycle the solar receiver and the combustor of the gas turbine are connected in a series arrangement, allowing boosting of the turbine inlet temperature with fossil fuels. The hot pressurised air is then expanded through the turbine, and exhausted through the recuperator to atmosphere. The shaft of the turbine is coupled to an electric generator.

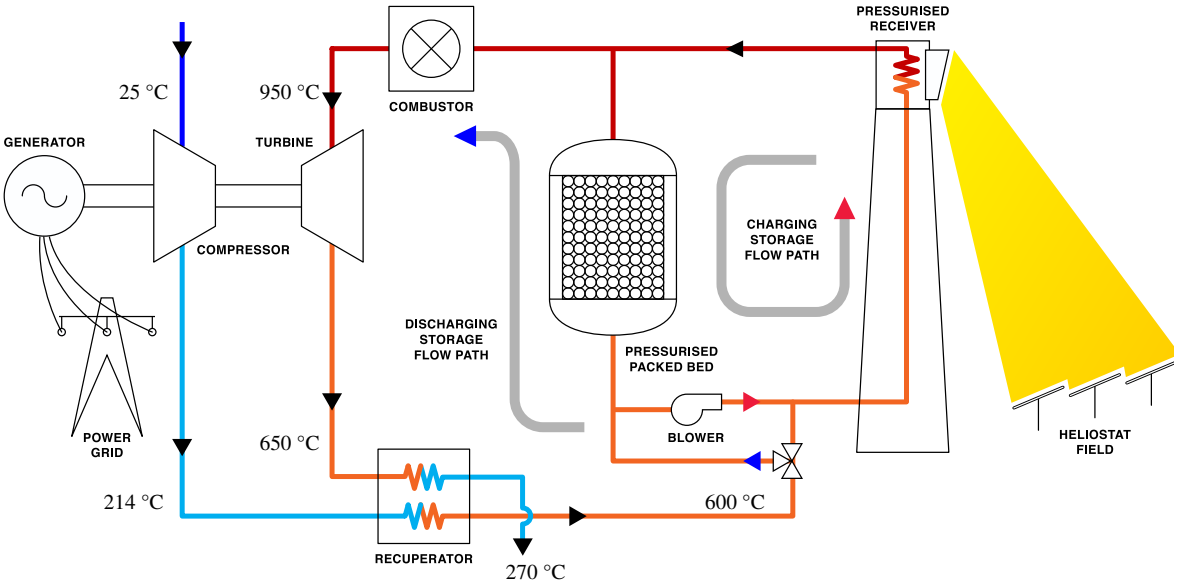

Figure 1.1: Schematic of gas micro-turbine cycle with thermal storage (Klein et al., 2015)

The pressurised packed bed thermal storage is connected in a parallel configuration with the solar receiver. During periods of excess solar energy supply, the packed bed is charged (heated) by re-circulating a portion of the air flow between the bed and solar receiver, using a blower. When solar energy is not available, energy is withdrawn from the thermal storage by closing a valve and diverting air through the packed bed instead of the receiver.

1.3 Sensible heat thermal storage in a packed bed

The heat transfer and pressure drop in a packed bed are influenced by the particle packing structure, which can be either random or a structured arrangement. The difficulties and cost in creating a large structured packed bed exclude this packing structure as a contender for the thermal storage system under consideration. Therefore only randomly packed beds are analysed in this study.

Sensible heat storage systems are based on the temperature change of a solid or liquid storage medium. The stored thermal energy is a function of the storage mass, heat capacity and temperature change between the charging and discharging cycles. Sensible heat TES systems include thermal oil reservoirs, single and dual tank molten salt storage, mixed media thermocline storage using rock/oil or rock/molten salt, high temperature heat regenerators and pressurised fluids (Stine and Geyer, 2001). At present sensible heat energy storage is the only technology to be commercialised on large scale CSP plants.

High temperature sensible heat storage in ceramic media is referred to as heat regenerator technology. These systems are employed in the metallurgical, chemical process and glass industries. In regenerators the gaseous heat transfer fluid is in direct contact with the storage material, thus allowing for the efficient transfer of thermal energy. As described by Zunft et al. (2009), thermal storage in heat regenerators is a "self-evident" choice for CSP plants using air cooled receivers. Regenerators exist in a variety of different design configurations. In general, high temperature applications are limited to fixed bed regenerators, consisting of either a randomly packed bed of particles or a structured bed.

A typical packed bed regenerator comprises an internally insulated tank that is randomly packed with ceramic particles. The heat transfer fluid flows through the voids between the particles and thermal energy is transferred via convection. Regenerators based on randomly packed media are used in regenerative thermal oxidisers and waste heat recovery systems. Too et al. (2012) conducted a review of a number of direct and indirect thermal storage systems for SGT applications, proposing a packed bed regenerator as a near term storage solution. Amsbeck et al. (2010) presented a nine hour storage design using a pressurised packed bed for the T100 gas turbine. Zunft et al. (2014) state that packed bed regenerators have the potential to provide a cost effective thermal storage design, despite the "open questions" regarding thermal cycling stresses. Tamme et al. (1990) recommend packed beds for thermal storage applications up to 1 MW_{th} power levels.

Thermal storage in ceramic packed beds for CSP applications was first demonstrated by the TSA (Technology programme Solar Air receiver) project in Spain. This research programme involved the testing of a 2.5 MW_{th} air cooled receiver, which provided heated air at 700 °C to drive a steam generator. The thermal storage consisted of a cylindrical packed bed that incorporated 18 tonnes of alumina (Al_2O_3) spheres, with a storage capacity of 1 MWh_{th}. Subsequent to the TSA project, Abengoa Solar proposed an air receiver concept with a 20 MWh_{th} ceramic thermal storage system for the PS10 CSP plant. Ultimately this concept was not implemented but a detailed storage design was developed, based on a 630 m^3 packed bed with 390 tonnes of $3/4''$ ceramic saddles (Pitz-Paal et al., 2005).

1.4 Latent heat thermal storage in a packed bed

Due to the difficulties in transporting hot pressurised air, the storage subsystem should be located in close proximity to the gas turbine in the receiver tower. The proposed packed bed concept must also be placed within a pressure vessel. Therefore there are strong economic

drivers to reduce the mass and volume of the storage. The disadvantage of sensible heat thermal storage is the low energy storage density of the material. Ceramic regenerators require a large mass that is energy intensive and costly to manufacture. The primary cost of the storage system is related to the specific cost of the storage material (per kilogram), as well as the total storage mass required. Therefore cost savings can be achieved by utilising low cost storage materials and also by decreasing the storage mass. Reductions in the volume of the storage system will also decrease the cost of the pressure vessel required.

One method of improving the energy storage density of the packed bed is to make use of Encapsulated Phase Change Materials (EPCM) (Yagi and Akiyama, 1995). These latent heat storage systems utilise the melting and solidification of a Phase Change Material (PCM) to increase the energy storage density. Tamme et al. (1991) studied a 250 MWh_{th} hybrid latent heat storage system. The results of this study showed that the storage mass (and volume) could be reduced by 20% in comparison to sensible heat storage in ceramics. The storage mass could be reduced by a total of 36% if three cascaded PCMs were utilised, with different melting points.

Inorganic PCMs are suited to SGT thermal storage applications as they have low material costs (less than 1 USD/kg) and the ability to operate at high temperatures. Suitable materials include alkali-metal and alkaline-earth-metal fluoride, chloride, carbonate and sulphate salts. The encapsulation process involves the retention of the PCM within an inert shell or matrix material. The high surface area of the packed bed increases the rate of heat transfer in the latent heat storage system, negating the effects of poor thermal conductivity of inorganic salts. The EPCM particles provide a self supporting structure to retain the molten salt, thus eliminating potential corrosion issues. EPCM particles are not limited to inorganic salts. Metallic PCMs can also be considered, although at a higher cost than the salts (greater than 2 USD/kg).

In order for the EPCM packed bed concept to be effective low cost encapsulation techniques need to be developed. Research into EPCMs is currently being conducted by Florida State University (Goswami, 2012) and by the company Terreflore (Mathur et al., 2014). Terreflore have developed a EPCM based on $NaNO_3$ at a cost of below 5 USD/kWh_{th} for the storage material (Mathur et al., 2014). The manufacturing process utilises a sacrificial polymer as the intermediate layer between the PCM and shell material. Mathur et al. (2014) estimated a processing cost of 0.25 USD/kg for the encapsulation and 0.75 USD/kg for the raw PCM. For comparison, sensible heat storage in alumina would cost approximately 11 USD/kWh_{th}, assuming a raw material cost of 1.3 USD/kg and temperature change of 350 °C.

1.5 Motivation

Section 1.5.1 introduces the rationale for developing a thermal storage system for off-grid SGT applications. The limitations of current thermal storage systems for high temperature applications are outlined in Section 1.5.2. The need for further research into sensible heat and latent heat storage systems is discussed in Sections 1.5.3 and 1.5.4 respectively.

1.5.1 Increasing solar share

Although hybridised SGTs can produce power when insolation is not available, the solar share (fraction of power produced using solar energy) is significantly reduced. Schwarzbözl et al. (2006) calculated that for a 1.4 MW_e gas turbine operating 24 hours a day, the solar share is reduced to 15% (annual DNI of 2015 $kWh/m^2/yr$). Amsbeck et al. (2010) conducted a study on the benefits of incorporating a nine hour thermal storage into a SGT based on the T100. The results showed that inclusion of thermal storage has the potential to increase the solar share from below 25% to 82% for the conditions analysed.

In rural locations in South Africa it is likely that diesel would be used as the fossil fuel in the hybrid gas turbine. Bischof-Niemz (2015) states that the cost for diesel power generation in utility scale open cycle gas turbines is 3.11 ZAR/kWh_e. This cost will increase for smaller generators in remote areas. Boyse et al. (2014) claim a cost of 0.41 USD/kWh_e for electricity generated from diesel in off-grid mining applications in South Africa. Assuming an average 2014 exchange rate of 10.85 ZAR/USD (SARB, n.d.) this equates to 4.45 ZAR/kWh_e. Cost effective pressurised thermal storage could be competitive with diesel hybridisation while increasing the solar share of the plant and decreasing greenhouse gas emissions.

1.5.2 Limitations of current thermal storage technologies

The two-tank molten salt thermal storage system represents the current state of the art for solar steam turbine cycles. In this design the storage medium and the heat transfer fluid in the receiver consist of a molten salt. Nitrate based molten salts are limited to a maximum operating temperature of below 560 °C. Forsberg et al. (2007) and Too et al. (2012) discuss the potential of developing a molten salt thermal storage system for a gas turbine, based on eutectic mixtures of high temperature fluoride, chloride and fluoroborate salts. Fluoride salts have also been proposed as liquid coolants for high temperature nuclear reactors (Williams, 2006). Although these molten salts are chemically stable at high temperature (greater than

800 °C), they exhibit severe corrosion issues when in contact with existing high temperature steels for storage tanks, receiver tubes, piping and pumps. Until the corrosion of these salts can be addressed, a two-tank molten salt system is not suitable for a SGT. Molten salt thermal storage is also inefficient for an air based cycle, as an added heat exchanger is required.

1.5.3 Need for additional research into sensible heat storage in a packed bed

Due to the complexity of integrating a high temperature, pressurised thermal storage system into a gas turbine cycle, this work proposes sensible heat storage for the first generation storage design. The effective design of this system requires detailed modelling that is able to predict the transient thermal characteristics of the packed bed. From the literature reviewed, available SGT thermal storage designs are limited to a preliminary analysis conducted by Amsbeck et al. (2010). Therefore further detailed parametric design studies are required, based on validated numerical modelling. Despite the use of packed beds in various industrial applications, Zunft et al. (2009) recommend further research with respect to CSP applications.

Although the heat transfer in packed beds has been previously studied in the chemical engineering field, this research is generally limited to applications below 300 °C. From the literature reviewed, no detailed thermocline temperature measurements from within a packed bed could be sourced over the temperature ranges of recuperated (600-1000 °C) and non-recuperated gas turbine cycles (350-1000 °C). In cases where high temperature data is available, such as Nsofor (2005), the packed bed was heated from an initial ambient temperature and discharged by cooling with ambient air. As described by Klein et al. (2014) this introduces a large variation in the heat capacity of the ceramic particles that is not present across the operating temperature range of a gas turbine cycle. Thus experimental data over the actual operating temperature ranges of SGTs is still required.

There are also open research questions regarding the heat transfer in the near wall region of small scale packed beds. Due to the limited size of the pressurised packed bed system, it is possible that for certain particle sizes the particle-to-tank diameter ratio is less than 40. This has the potential to introduce a bypass flow effect in the near wall region. The effect of wall channelling is generally not included in thermal storage models and its influence needs to be analysed.

At high temperature radiation, heat exchange in the packed bed also needs to be carefully considered. The models presented in the literature frequently do not include particle-to-particle, and particle-to-wall radiation heat exchange. The effect of radiation needs to be further investigated.

1.5.4 Need for additional research into latent heat storage in a packed bed

In order to improve the energy storage density of the packed bed this study proposes that a second generation storage design could make use of advanced storage materials such as EPCMs. By utilising more complex storage materials, a packed bed of EPCMs offers the potential for reductions in the storage mass and cost. Due to these potential advantages, further research should be conducted into EPCMs. Suitable high temperature PCMs and encapsulation methods need to be identified and analysed with respect to a SGT cycle. Once a suitable PCM and encapsulation technique is selected the heat transfer in the packed bed of EPCMs needs to be analysed.

Previous experimental and numerical studies into EPCMs are predominantly focused on low temperature systems below 100 °C. There are a limited number of investigations at high temperature. In particular there are no studies that could be sourced that discuss the use of EPCMs to provide thermal storage for a gas turbine. The development of a detailed heat transfer model will allow for an optimal packed bed storage design to be generated, which has not been previously considered for a gas turbine cycle.

Due to the difficulties involved in testing high temperature PCMs there is a limited amount of experimental data available for temperatures exceeding 900 °C. Heat transfer data from a packed bed of EPCMs is required to validate the numerical modelling and ensure accurate design predictions. Different types of PCM and encapsulation methods need to be investigated to further develop this storage technology. This study aims to conduct an initial investigation into the different types of PCM available for the high temperature thermal storage system. The development of a final low cost encapsulation technique is beyond the scope of this thesis.

Design studies should be conducted before any detailed development of the EPCM material is conducted. An analysis of potential encapsulation techniques is conducted in this work with the aim of generating temperature measurements from a packed bed of EPCM particles. If the heat transfer results from the EPCM packed bed are promising, further research into

effective scalable encapsulation methods should be pursued. However, due to the added complexity of using the EPCM particles there should be a clear increase in the thermal performance of the storage system or a decrease in the storage costs. If the design studies do not highlight an increase in thermal performance or cost reduction then it is recommended that the solid ceramic particles are used or alternative EPCMs are developed.

1.6 Research objectives and contributions

The overall objective of this thesis is to investigate high temperature, packed bed thermal storage systems for a SGT, based on sensible heat or latent heat TES technology. The specific project objectives are summarised below:

1. **The study of sensible heat storage using a packed bed of ceramic particles:**
    - to develop a comprehensive numerical model of the forced convection heat transfer within a packed bed of ceramic particles;
    - to design, manufacture and test, a high temperature laboratory-scale packed bed facility;
    - to validate the sensible heat storage model against experimental temperature measurements over the temperature ranges of potential SGT cycles;
    - to utilise the validated storage model to conduct a parametric design study of a nominal six hour packed bed thermal storage for a SGT cycle.
2. **The study of latent heat storage using a packed bed of EPCM particles:**
    - to develop a numerical model of the melting and solidification of a PCM;
    - to develop a numerical model of the forced convection heat transfer within a packed bed of EPCM particles;
    - to identify potential PCMs and encapsulation methods that are suitable for a SGT cycle;
    - to design, manufacture and test, a laboratory-scale packed bed of EPCMs;
    - to validate the latent heat storage model against experimental temperature measurements from a packed bed of EPCM particles;
    - to compare the thermal storage performance of a packed bed of EPCM particles to that of solid ceramic particles.

1.7 Thesis Outline

The objectives of this study are divided between sensible heat storage in ceramic particles and latent heat storage in EPCM particles. The convective and inter-particle (i.e. between particles) heat transfer mechanisms are common to both types of packed beds. In general, only the intra-particle (i.e within the particle) heat transfer differs between the two storage materials. The study of EPCM particles is thus an extension of the research conducted on the solid ceramic particles. Therefore this thesis is structured so that common aspects of the ceramic and EPCM packed beds are first addressed in each chapter. This information is then followed by specific details regarding the sensible heat or latent storage systems. This methodology is applied throughout the thesis to both the experimental and numerical work that was completed. Due to the broad nature of this study the relevant literature is surveyed in the separate chapters where applicable, instead of in one central chapter. The structure of the thesis is presented in Figures 1.2 and 1.3. The sections are color coded to show if they are: (1) applicable to both sensible and latent heat storage; (2) applicable to sensible heat storage only or (3) applicable to latent heat storage only.

Chapter 2 presents the development of the heat transfer and pressure drop models that were used to analyse the different packed bed concepts. The heat transfer models account for variable thermophysical properties and are applicable to packed beds of ceramic and EPCM particles. Due to the complexity of the governing partial differential equations a numerical solution is required. Chapter 3 describes the numerical technique of Orthogonal Collocation on Finite Elements (OCFE). This numerical method is used to solve the governing heat transfer and fluid flow equations. The effective heat capacity method is introduced for the solution of the phase change process within each EPCM particle.

Chapter 4 describes the laboratory scale packed bed test facility that was used in this study. The test apparatus, instrumentation and testing methods are introduced. The test facility was packed with 19 mm alumino-silicate particles to analyse the sensible heat storage and 45 mm encapsulated sodium sulphate particles to analyse the latent heat storage. The identification of suitable PCMs and encapsulation methods are also discussed in this chapter.

The experimental data collected from the test facility was used to validate the numerical modelling. The validation of the sensible heat transfer model is presented in Chapter 5 and the validation of the latent heat model is presented in Chapter 6. The heat transfer modelling of a single EPCM sphere is also compared to experimental data from Yagi and Akiyama (1995) in Chapter 6.

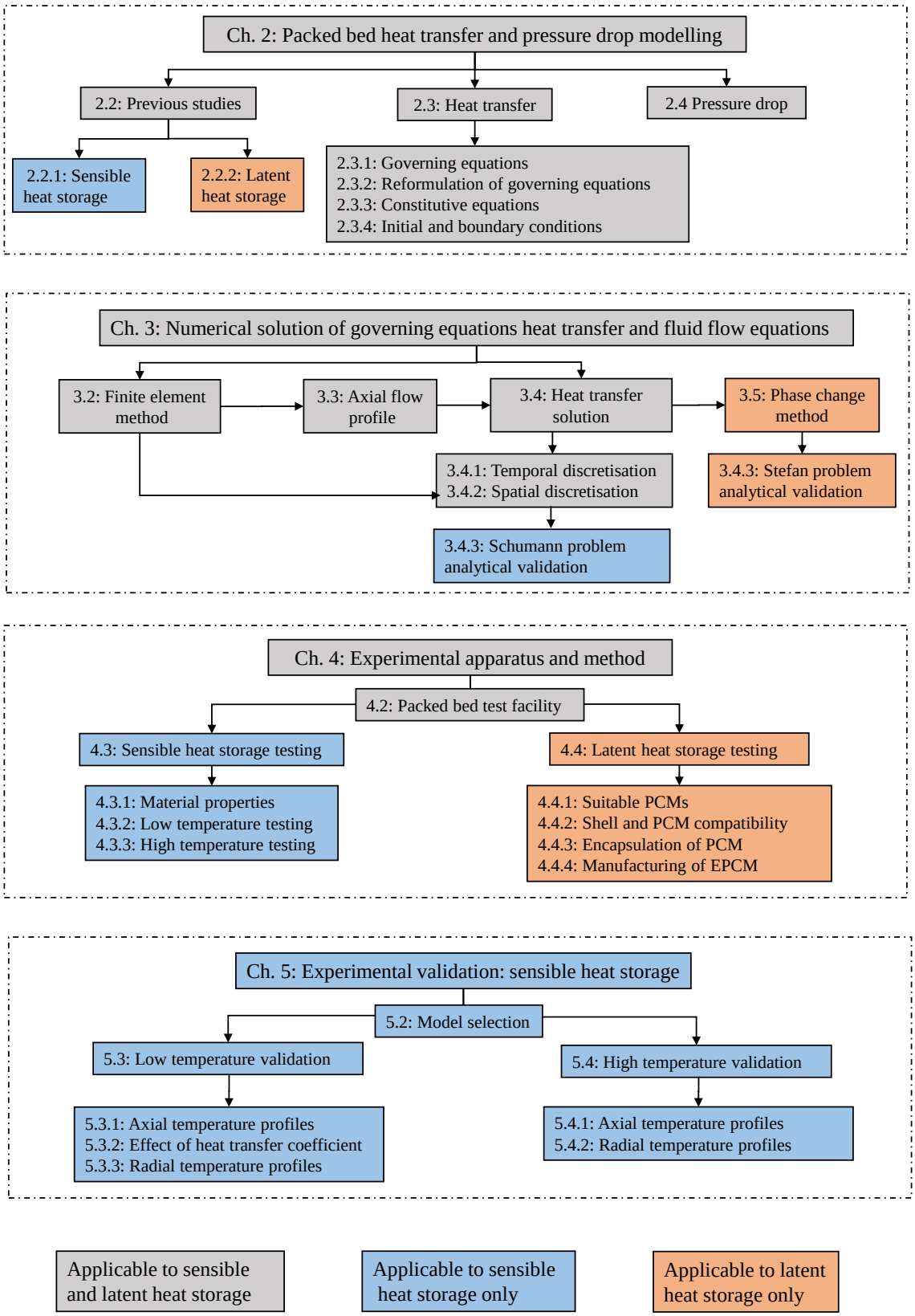

Figure 1.2: Structure of thesis (Chapters 2-5)

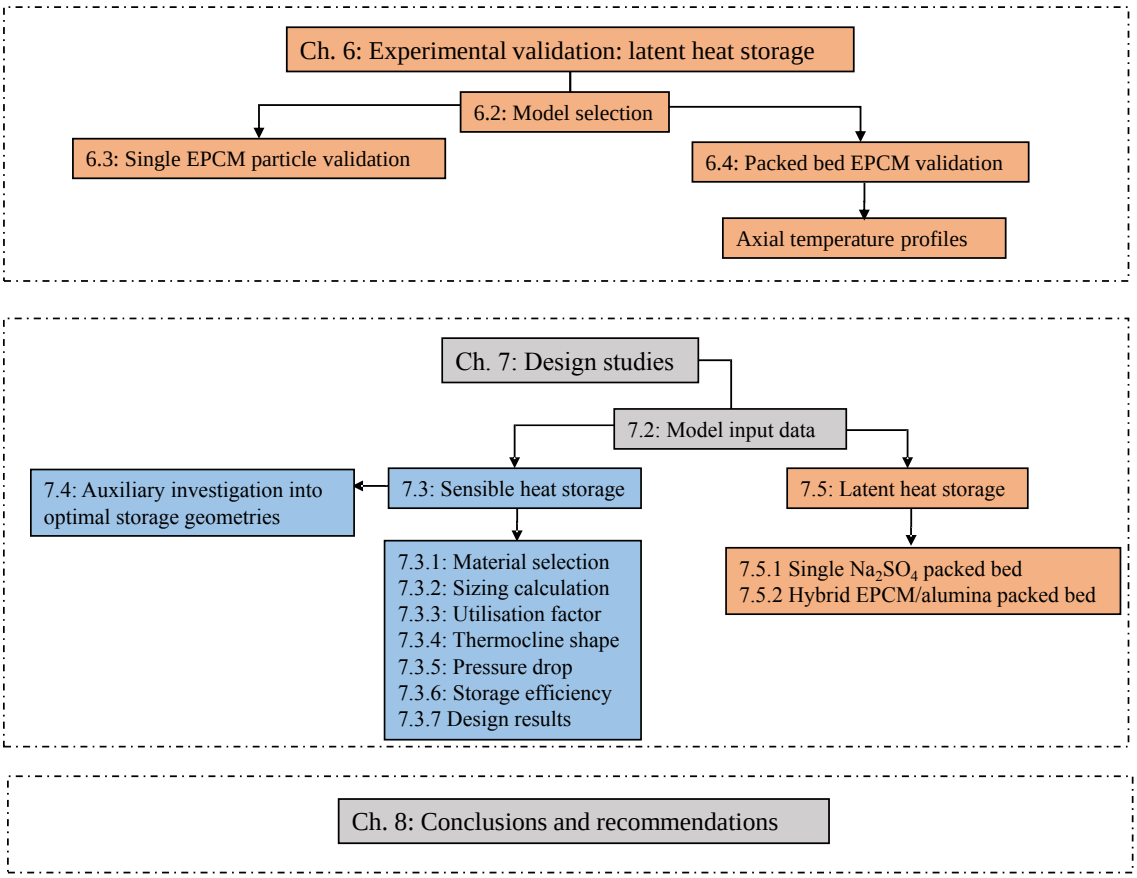

Figure 1.3: Structure of thesis (Chapters 6-8)

The validated sensible heat storage model was utilised to conduct a parametric design study for a nominal six hour (1.55 MWh_{th}, 7 m^3) packed bed TES for the T100 gas turbine. Details of this study are provided in Chapter 7. The study involved varying the aspect ratio (L_z/D) of the packed bed and the size of the particles. The results are analysed with respect to the storage efficiency and utilisation factor, which are two metrics introduced to determine the optimal storage design. An auxiliary design study is also presented that compares the thermal performance of a packed bed a spheres to alternative core geometries.

Chapter 7 also presents a comparison of the thermal performance of EPCM particles to solid ceramic particles. The discharge temperature profile from a packed bed of Na_2SO_4 particles is compared to that from an Al_2O_3 packed bed. The concept of a multi-layer packed bed is introduced in this chapter that consists of Na_2SO_4, Al_2O_3 and NaCl-KCl particles. The results and conclusions of this thesis are summarised in Chapter 8 and recommendations for further research are provided.

Chapter 2

Packed bed heat transfer and pressure drop modelling

2.1 Introduction

This chapter presents the development of the heat transfer and pressure drop models utilised to analyse the packed bed thermal storage unit. The thermal performance of the packed bed is determined through a detailed analysis of the forced convection heat transfer between the air and packed particles. A literature review of previous modelling of packed bed thermal storage systems is presented in Section 2.2. As described by Wakao and Kaguei (1982), packed bed heat transfer models can be broadly classified into two categories, namely: the Continuous-Solid (C-S) and Dispersion-Concentric (D-C) models. These models are presented and discussed in Section 2.3.1. In Section 2.3.2 the governing equations are reformulated from specific fluid enthalpy and specific solid internal energy into fluid and solid temperatures. The constitutive heat transfer equations, which are predominantly of a semi-empirical nature are described in Section 2.3.3. The boundary conditions required to solve the heat transfer models are presented in Section 2.3.4.

Parasitic energy losses due to the pressure drop over the packed bed need to be calculated in order to analyse the storage efficiency. The classical equation for pressure drop through porous media is the Ergun equation (Ergun, 1952), which is described in Section 2.4.1. A second pressure drop model, based on research conducted by the German Nuclear Safety Standards Commission (KTA) is presented in Section 2.4.2.

2.2 Previous numerical studies

2.2.1 Sensible heat thermal storage

Forced convection heat transfer in randomly packed beds has received significant research attention over the past decades. Early studies were based on the analytical solutions to the Schumann model (Schumann, 1929; Klinkenberg, 1948). Due to the limited applicability of the analytical solutions, further investigations relied on numerical modelling (Beasley and Clark, 1984; Ismail and Stuginsky, 1999). Wakao and Kaguei (1982) provide an overview of convective heat transfer models and constitutive correlations for randomly packed beds. Previous research papers are primarily focused on low temperature systems with a maximum temperature below 200 °C. Fewer studies are available on the heat transfer in a packed bed where the charging temperature exceeds 600 °C.

Meier et al. (1991) analysed thermal storage in rock beds using air as the working fluid. This analysis was based on a one-dimensional, one-phase dynamic model that was solved analytically and compared to experimental data from a packed bed of magnesium silicate particles. The model results were in reasonable agreement with the experimental data, although the effects of wall channelling led to an uncertainty in the core mass flow rate in the experiment. The temperature range was 25-550 °C and constant thermophysical properties were assumed for the solid phase. The air specific heat capacity was also modelled as constant, while the density, kinematic viscosity and thermal conductivity were varied with temperature. Hänchen et al. (2011) also studied the heat transfer in a packed bed of crushed steatite rock over the 20-550 °C temperature range. A parametric study on the system was conducted using a model based on constant solid phase thermophysical properties. The heat transfer model was validated against the experimental data of Meier et al. (1991).

Jalalzadeh-Azar et al. (1996), Adebiyi et al. (1998) and Nsofor (2005) studied a packed bed of zirconia pellets for high temperature industrial heat recovery. Jalalzadeh-Azar et al. (1996) utilised a one-dimensional, two-phase heat transfer model which was validated against experimental data at temperatures between ambient and 900 °C. The effects of gas radiation and intra-particle conduction were studied, while the convective heat transfer correlations of Bradshaw et al. (1970) and Wakao and Kaguei (1982) were found to be suitable up to a temperature of 960 °C. Adebiyi et al. (1998) state that due to the large temperature range, significant temperature dependent variations in the fluid and solid properties must be taken into account. This work utilised a fully implicit time stepping model, while updating the thermo-physical properties at the last known temperature (time lagging procedure). The

variable property model was also compared to the constant property Schumann model for a packed bed of copper particles. The results showed that there was not a large difference in the temperature profile predictions. The predictions from the Nsofor (2005) model showed good agreement with experimental measurements up to a maximum temperature of 1000 °C.

The heat transfer in a high temperature packed bed was analysed by Du Toit et al. (2006) for nuclear applications. The governing energy equations for the fluid and solid phases were derived in terms of enthalpy and internal energy respectively in two-dimensions. These equations were solved using a systems-based CFD approach. The model was validated against experimental data from the SANA experiments, conducted by Niessen and Stöcker (1997). Both nitrogen and helium were used as heat transfer fluids for the case of natural convection heat transfer in the packed bed.

Varone et al. (2010) presented a parametric study of a 1 MWh_{th} packed bed heat storage system. In this work CO_2 was used as the heat transfer fluid while the core material was based on fire brick. The temperature range of the system was 150-550 °C and constant thermophysical properties were used in the modelling. Mongibello et al. (2013) also conducted a parametric analysis on a high temperature regenerative energy storage system with CO_2 as the working fluid. Packed beds of both alumina and zirconia particles were analysed over the temperature range 670-850 °C. The two dimensional, two-phase modelling was derived in terms of fluid and solid temperatures, but it was not stated whether constant or variable thermophysical properties were implemented. Experimental data over the temperature range 100-350 °C was used to validate the model.

Zanganeh et al. (2012) developed a one-dimensional, two-phase heat transfer model for a high temperature rock bed thermal storage using air as the heat transfer fluid. An enthalpy formulation of the governing energy equations was used and validated against experimental data from a pilot-scale test facility. The model accounted for temperature dependent changes in the thermophysical properties of the air and rock. A design study was presented for an array of two 7.2 GWh_{th} packed bed storage units.

Allen (2014) studied a rock bed thermal storage system for a CSP plant based on a modified combined cycle CSP plant, using air as the heat transfer medium in the receiver and storage. A one-dimensional heat transfer model was used to analyse the storage system, based on an E-NTU method. This model was validated against experimental measurements up to 530 °C. Extensive pressure drop measurements across rock beds were also conducted, and a method was presented to optimise the particle size and bed length for a commercial scale system.

Avila-Marin et al. (2014) utilised a one-dimensional, two-phase heat transfer model to study a high temperature regenerative thermal storage system for CSP plants using air cooled receivers. The numerical model was compared to experimental data up to a maximum temperature of 640 °C. One of the potential causes of deviations between the numerical predictions and the experimental results was attributed to the use of temperature averaged thermophysical properties in the heat transfer model.

A survey of the relevant literature shows that the choice of adopting constant or temperature dependent thermophysical properties is varied when modelling the heat transfer in high temperature packed beds. Many authors utilise constant thermophysical properties across wide operating temperature ranges without justifying this assumption. Therefore it is important to derive a clear criterion for when the constant property assumption is accurate for high temperature regenerators. This is achieved in the current work by rigorously deriving the governing heat transfer equations for use with temperature dependent properties and comparing the results to the constant property models.

Previous studies that include the effects of the local void fraction increase at the packed bed wall are generally limited to low temperature (below 200 °C) and do not include radiation effects. The modelling presented in this study is comprehensive and addresses all relevant heat transfer mechanisms in the high temperature packed bed. Three key areas exist where there is a potential improvement over existing models: (1) the inclusion of the local porosity increase at the bed wall and the associated wall channelling flow effect; (2) the in-depth treatment of radiation in the packed bed, via the modified Zehner-Bauer-Schlünder (ZBS) effective conductivity correlation and a radiation boundary condition between solid particles and the bed wall; (3) the inclusion of temperature dependent thermophysical properties.

2.2.2 Latent heat thermal storage

A number of modelling studies have been conducted on packed beds of EPCM particles at temperatures below 100 °C. Beasley et al. (1989) developed a one-dimensional model to analyse a packed bed of encapsulated paraffin wax particles, using air as the heat transfer fluid. Both isothermal and non-isothermal phase change was studied. The EPCM modelling was validated against experimental data and utilised to conduct a design analysis.

Benmansour et al. (2006) presented a two-dimensional, two-phase model to study the heat transfer in a packed bed of encapsulated paraffin wax spheres. The governing equations were discretised using the finite difference approach and solved using the alternating direction

implicit method. The model compared favourably with experimental measurements. Regin et al. (2009) also studied a packed bed of paraffin wax spheres using a modified form of the Schumann model. The effects of capsule size, inlet fluid temperature and flow rate were analysed up to a maximum temperature of 70 °C.

Fewer studies have been conducted on high temperature EPCMs. Adebiyi (1991) numerically investigated a packed bed of EPCMs. The governing equations consisted of a modified form of the Schumann model that accounted for intra-particle heat transfer. A second law analysis showed that a single PCM does not always produce better thermal performance than sensible heat storage. Adebiyi et al. (1996) extended this work by modelling a packed bed containing five EPCMs with different melting points. Simulations were conducted using high temperature cylindrical EPCMs at temperatures up to 1500 K. The results showed that the use of multiple PCMs can improve thermal performance of the storage unit.

Jalalzadeh-Azar et al. (1997) modelled the heat transfer in a bed of composite Na_2SO_4/SiO_2 particles. The PCM melting was studied using the effective heat capacity method in which a pseudo-specific heat capacity was defined. The model was validated using high temperature experimental test data. A numerical analysis showed that thermal performance of the Na_2SO_4/SiO_2 particles was inferior to solid zirconia particles on an equal volume basis for the conditions analysed.

Yagi and Akiyama (1995) analysed the phase change process within a single spherical EPCM for both inorganic salt and metallic PCMs. The model was based on the enthalpy method for the phase change process and validated against heat transfer experiments for a single sphere. The numerical analysis of the heat transfer within a packed bed of EPCMs was also presented. This study concluded that metallic PCMs are best suited to packed bed TES applications due to their ability to store and release energy isothermally.

Goswami (2012) studied the heat transfer and natural convection flow within a single sphere of encapsulated $NaNO_3$. The model was based on the conservation of mass, momentum and energy. The solution was generated using the finite volume method with an enthalpy-porosity method to track the phase change front.

Nithyanandam et al. (2014) analysed the heat transfer in a single tank molten salt thermocline system. The filler material for the packed bed was an EPCM consisting of a carbonate eutectic of Li_2CO_3-Na_2CO_3. The heat transfer fluid in the system was Solar Salt. The results showed that it is important for the PCM melting temperature to be above the minimum allowable exit fluid temperature. Smaller capsule sizes were shown to be most efficient, offering the largest reductions in the volume of the storage tank.

Previous studies of EPCM packed beds either model the intra-particle temperature profiles or they assume a lumped capacitance approach for the PCM. In cases where the heat transfer within the particles is included, a simplified packed bed model is often utilised that does not include inter-particle heat transfer. The model presented in this study provides the following improvements over previous models: (1) the inclusion of the local porosity increase at the bed wall and the associated wall channelling flow effect; (2) intra-particle heat transfer and natural convection within the liquid PCM are taken into account; (3) inter-particle heat transfer via conduction and radiation is included; (4) heat transfer in the packed bed analysed in two dimensions (5) a radiation boundary condition between the EPCM particles and the bed wall is implemented.

2.3 Packed bed heat transfer

The simulated storage, shown in Figure 2.1, system consists of a cylindrical packed bed with an insulated wall. The model domain is divided into the bed and wall regions. For comparison with the packed bed test facility the modelled wall consists of an inner metal wall (Nimonic 75) and an outer insulation layer of ceramic fibre blanket, up to 150 mm thickness.

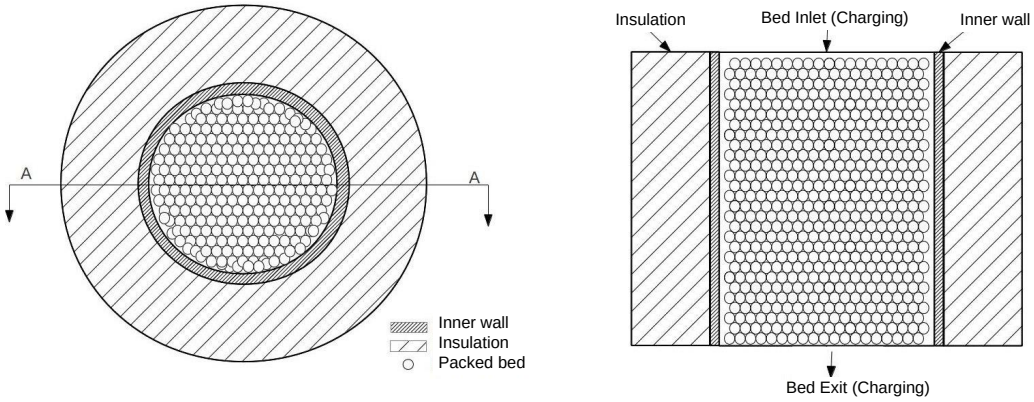

(a) Top view (b) A-A Sectioned view

Figure 2.1: Diagram of the test section from the packed bed test facility

The heat transfer models are formulated in an axisymmetric coordinate system. Due to the complexities involved, the individual particles are not modelled explicitly. Instead a global bed model is introduced, described by volume-averaged heat transport parameters. The technique of local volume-averaging methods in porous media is described in detail by Kaviany (1995). Both the Continuous-Solid (C-S) and the Dispersion-Concentric (D-C)

models are dynamic, two-phase models that account for discrete fluid and solid phases. The overall heat transfer in a packed bed is a complex phenomenon and consists of the following heat transfer mechanisms:

- conduction through the solid particles;
- conduction through the fluid;
- radiation between solid particles;
- radiation between the solid particles and the bed wall;
- convection between the fluid and the solid particles;
- convection between the fluid and the wall;
- thermal dispersion in the fluid.

For the EPCM particles two extra intra-particle (within) heat transfer phenomena exist:

- melting/solidification of the PCM;
- natural convection currents within the liquid PCM.

2.3.1 Governing equations

The governing energy equations for the packed bed are derived to be used with temperature dependent thermophysical properties. This requires the formulation of the energy equations on the basis of specific fluid enthalpy and specific solid internal energy (Zanganeh et al., 2012), where:

$$h_f = \int_{T_{\text{ref}}}^{T_f} c_f(T)\,\mathrm{d}T \tag{2.1}$$

and

$$u_s = \int_{T_{\text{ref}}}^{T_s} c_s(T)\,\mathrm{d}T \tag{2.2}$$

The fluid energy equation, given by Eq.(2.3), is common to both the C-S and D-C models. This form of the energy equation does not take into account the temporal pressure gradient, viscous dissipation or the potential energy change across the packed bed. These terms are

negligible for the convective heat transfer in a packed bed. Due to the large axial pressure gradient from the packed bed blower only axial flow is modelled.

$$\varepsilon \frac{\partial \left(\rho_f h_f\right)}{\partial t} + \frac{\partial \left(G_z h_f\right)}{\partial z} = h_p a_p (T_s - T_f) + \nabla \cdot \left(k_{\text{eff,f}} \nabla T_f\right) \tag{2.3}$$

The term a_p represents the available surface area for heat exchange between the packed spherical particles and the fluid. The particle surface area per unit volume for spherical particles is calculated by:

$$a_p = \frac{6(1-\varepsilon)}{d_p} \tag{2.4}$$

The difference between the C-S and D-C models lies in the treatment of intra-particle conductive heat transfer. The C-S model assumes that the discrete solid particles are isothermal and behave as a single continuous solid phase. Thus no intra-particle temperature gradients are taken into account and the solid energy equation is:

$$(1-\varepsilon)\,\rho_s \frac{\partial u_s}{\partial t} = h_p a_p (T_f - T_s) + \nabla \cdot (k_{\text{eff,s}} \nabla T_s) \tag{2.5}$$

The D-C model consists of two energy equations for the solid phase. The intra-particle heat transfer is modelled by assuming a concentric temperature profile within a series of representative spherical particles. The energy equation for the spherical particles is:

$$\rho_p \frac{\partial u_p}{\partial t} = \frac{1}{\zeta^2} \frac{\partial}{\partial \zeta} \left(\zeta^2 k_p \frac{\partial T_p}{\partial \zeta} \right) \tag{2.6}$$

At the particle surface ($\zeta = d_p/2$), energy is exchanged with the fluid phase by convection and with surrounding particles by conduction and radiation. An energy balance conducted on the particle surface (Laguerre et al., 2008) yields:

$$\dot{q}_p + h_p \left(T_f - T_s\right) + \frac{\nabla \cdot (k_{\text{eff,s}} \nabla T_s)}{a_p} = 0 \tag{2.7}$$

where:

$$\dot{q}_p = -k_p \left. \frac{\partial T_p}{\partial \zeta} \right|_{\zeta = d_p/2} \tag{2.8}$$

The first term in Eq.(2.7) models the energy transferred from the particle surface to the centre (energy stored). The second term represents convective heat exchange at the particle surface, while the third term models inter-particle heat transfer.

In Eq.(2.7) the term T_s represents the temperature field of the particle surfaces:

$$T_s = T_p\big|_{\zeta=d_p/2} \tag{2.9}$$

Beasley and Clark (1984) state that under transient conditions the thermal capacity of the packed bed wall can influence the heat transfer in the near-wall region of the packed bed. As it is an objective of the current research to model the near-wall region accurately, an energy equation for the packed bed wall is included for both the C-S and D-C models. This equation assumes constant thermophysical properties and is given by:

$$\rho_w c_w \frac{\partial T_w}{\partial t} = \nabla \cdot (k_w \nabla T_w) \tag{2.10}$$

2.3.2 Reformulation of governing equations in terms of fluid and solid temperatures

Zanganeh et al. (2012) utilised a similar formulation of Eqs.(2.3) and (2.5) to solve directly for h_f and u_s using an explicit finite difference scheme. The values of T_f and T_s at each time step were then calculated from h_f and u_s using a non-linear Newton-Raphson method. This approach requires the solution of a large number of non-linear equations, as well as a small time step to ensure stability. This results in an increase in the computation time. Due to the length of time that must be simulated in a thermal storage system (multiple hours) it is preferable to formulate the governing equations in terms of the fluid and solid temperatures. The governing energy equations presented by Jalalzadeh-Azar et al. (1996) and Adebiyi et al. (1998) were expressed in terms of temperature. However, no mathematical justification of these equations was provided for use with temperature dependent thermophysical properties. Therefore in this research the governing energy equations are reformulated in terms of the fluid and solid temperatures, without making the assumption of constant thermophysical properties. This ensures the correct energy balance is maintained in the packed bed.

The continuity equation for one-dimensional fluid flow in the packed bed, accounts for temporal changes in the fluid density due to rapid heating or cooling of the air, where:

$$\varepsilon \frac{\partial \rho_f}{\partial t} + \frac{\partial G_z}{\partial z} = 0 \tag{2.11}$$

Using the product rule of differentiation, the L.H.S. of the fluid energy equation can be expressed as:

$$\varepsilon\frac{\partial\left(\rho_f h_f\right)}{\partial t}+\frac{\partial\left(G_z h_f\right)}{\partial z}=\left(\varepsilon\frac{\partial\rho_f}{\partial t}+\frac{\partial G_z}{\partial z}\right)h_f+\varepsilon\rho_f\frac{\partial h_f}{\partial t}+G_z\frac{\partial h_f}{\partial z} \tag{2.12}$$

When combined with the continuity equation, Eq.(2.12) can be simplified without assuming that ρ_f or G_z are constant:

$$\varepsilon\frac{\partial\left(\rho_f h_f\right)}{\partial t}+\frac{\partial\left(G_z h_f\right)}{\partial z}=\varepsilon\rho_f\frac{\partial h_f}{\partial t}+G_z\frac{\partial h_f}{\partial z} \tag{2.13}$$

The equation of state for fluid specific enthalpy is:

$$h_f=h_f(T_f,P_f) \tag{2.14}$$

Rohsenow et al. (1998) use the chain rule of differentiation to show:

$$\frac{Dh_f}{Dt}=\left.\frac{\partial h_f}{\partial P_f}\right|_{T_f}\frac{DP_f}{Dt}+\left.\frac{\partial h_f}{\partial T_f}\right|_{P_f}\frac{DT_f}{Dt} \tag{2.15}$$

$$=\frac{1}{\rho_f}(1-\beta_f T_f)\frac{DP_f}{Dt}+c_f\frac{DT_f}{Dt} \tag{2.16}$$

where D/Dt represents the substantive derivative and $\beta_f=1/T_f$ for an ideal gas. Rohsenow et al. (1998) state explicitly that c_f need not be constant:

$$\frac{Dh_f}{Dt}=c_f\frac{DT_f}{Dt} \tag{2.17}$$

$$=c_f\frac{\partial T_f}{\partial t}+c_f U_z\frac{\partial T_f}{\partial z} \tag{2.18}$$

Therefore Eq.(2.3) is reformulated in terms of the fluid temperature as:

$$\varepsilon\rho_f c_f\frac{\partial T_f}{\partial t}+c_f G_z\frac{\partial T_f}{\partial z}=h_p a_p(T_s-T_f)+\nabla\cdot\left(k_{\text{eff,f}}\nabla T_f\right) \tag{2.19}$$

For the solid phase the internal energy can be expressed in terms of the solid temperature (Faris, 2004):

$$\frac{\partial u_s}{\partial t}=\frac{\partial u_s}{\partial\rho_s}\underbrace{\frac{\partial\rho_s}{\partial t}}_{0}+\frac{\partial u_s}{\partial T_s}\frac{\partial T_s}{\partial t}=\frac{\partial h_s}{\partial T_s}\frac{\partial T_s}{\partial t} \tag{2.20}$$

$$=c_s\frac{\partial T_s}{\partial t} \tag{2.21}$$

Equation (2.21) is derived by assuming the solid phase density is constant. The solid energy equation for the C-S model is:

$$(1-\varepsilon)\,\rho_s c_s \frac{\partial T_s}{\partial t} = h_p a_p (T_f - T_s) + \nabla \cdot (k_{\text{eff,s}} \nabla T_s) \tag{2.22}$$

while the energy equation for the D-C model becomes:

$$\rho_p c_p \frac{\partial T_p}{\partial t} = \frac{1}{\zeta^2} \frac{\partial}{\partial \zeta} \left(\zeta^2 k_p \frac{\partial T_p}{\partial \zeta} \right) \tag{2.23}$$

Appendix A provides the correlations for the temperature dependent thermophysical properties that are utilised in this work for the ceramic and PCM storage materials. The temperature dependent properties of the sensible heat storage material tested in this study are also discussed in Section 4.3.1. The heat capacity variations of the PCM are outlined in Section 4.4.

2.3.3 Constitutive equations

As described by Visser (2007) the heat transfer mechanisms in the packed bed can be modelled using constitutive equations that are "typically obtained from experimental measurements." The heat transfer parameters modelled include the void fraction profile (ε), the axial velocity profile ($U_z(r)$), the inter-phase heat transfer coefficient (h_p) and the effective thermal conductivities of the fluid and solid phases ($k_{\text{eff,f}}, k_{\text{eff,s}}$). The required constitutive equations are presented in this section for randomly packed beds with spherical particle shapes.

Void fraction

The void fraction refers to the ratio of the volume of voids between the solid particles to the total volume of the packed bed. Using the technique of volume-averaging, the local void fraction is given by Kaviany (1995) as:

$$\varepsilon(r,z,\theta_c) = \frac{1}{V} \int_V \Psi_v(r,z,\theta_c)\,\mathrm{d}V \tag{2.24}$$

where $\Psi_v(r,z,\theta_c)$ is a function defined as 1 if the local point (r,z,θ_c) is located in a void region and 0 if the point is located in a solid region.

Due to the confining effect of the wall on randomly packed spheres, non-uniform radial variations in void fraction occur in packed beds. For spherical particles experimental data indicates the presence of damped oscillations in void fraction from unity at the wall to an asymptotic value of approximately 0.4, within five particle diameters in the radial direction (Benenati and Brosilow, 1962). Vafai (1984) states that the oscillations present in the void fraction distribution are secondary effects and the focus should be placed on the decay of the average void fraction from the bed wall. Hunt and Tien (1990) present the following model:

$$\varepsilon(r) = \varepsilon_{\infty}\left(1 + C_v \exp\left(-N_v \frac{(R-r)}{d_p}\right)\right) \tag{2.25}$$

where C_v and N_v are empirical constants listed in Table 2.1. Figure 2.2 presents a comparison of the exponential void fraction models with the oscillatory void fraction model of Martin (1978). The coefficients proposed by Hunt and Tien (1990) and Amiri and Vafai (1994) accurately capture the average decay in void fraction of the Martin model. Therefore as suggested by Du Toit (2008), the model of Hunt and Tien (1990) is utilised.

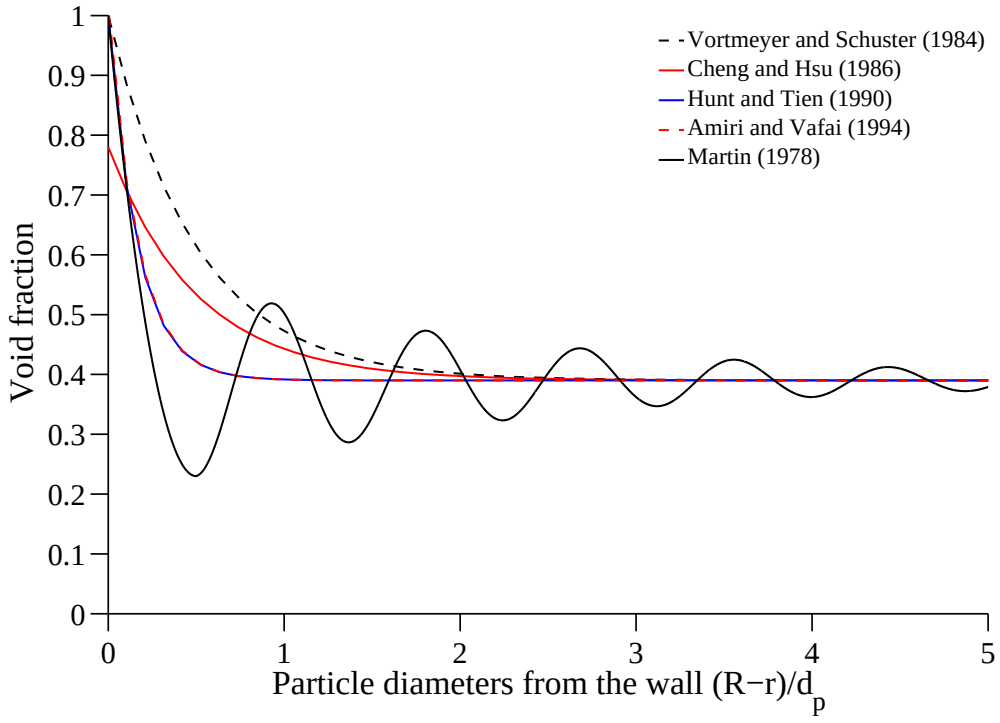

Figure 2.2: Comparison of void fraction correlations

Table 2.1: Exponential void fraction correlation coefficients

Author	N_V Value	C_V Value
Vortmeyer and Schuster (1983)	2	$\frac{1}{\varepsilon_\infty} - 1$
Cheng and Hsu (1986)	2	1
Hunt and Tien (1990)	6	$\frac{1}{\varepsilon_\infty} - 1$
Amiri and Vafai (1994)	6	1.6

Velocity channelling profile

The radial variation in void fraction causes a maldistibution of flow in the packed bed. The higher void fraction near the wall leads to increased permeability and a reduction in resistance to fluid flow. This introduces a velocity channelling effect into the bed, whereby the velocity in the near-wall region is higher than in the centre of the bed. The combined effects of the increased near wall permeability and the boundary layer effect lead to a maximum velocity peak offset from the wall by $d_p/4$ to $d_p/2$ for spheres (Vortmeyer and Schuster, 1983).

Based upon the experimental data collected by Schwartz and Smith (1953), Fahien and Stankovic (1979) developed an empirical equation to account for the velocity variation in the bed. Martin (1978) and Botterill and Denloye (1978) proposed bypass flow models that consist of two distinct regions of void fraction and flow velocity. The introduction of two zones of flow was also advocated by McGreavy et al. (1986) who proposed a wall zone and a core zone of fluid flow. Vortmeyer and Schuster (1983) presented a semi-analytical model for the radial velocity distribution in a packed bed. This model is based on the general analytical expression for a semi-infinite packed bed, with fitted empirical coefficients. As described by Skaare (1993) the equation allows for the radial velocity profile to be generated for different flow conditions and bed to particle diameter ratios. Despite only being validated for flow at 293 K, it is commonly used to analyse other flow conditions due to a lack of available information. Tsotsas and Schlünder (1988) state that the original paper contained typographical errors and that the correct Vortmeyer and Schuster model is given by:

$$\frac{U_z}{U^*} = \beta_v \left(1 - \exp\left(a_v \frac{R-r}{d_p}\right)\right)\left(1 - n_v \left(\frac{R-r}{d_p}\right)\right) \tag{2.26}$$

for $1 \leq \mathrm{Re}_p \leq 1000$, n_v is given by:

$$n_v = -1803 + 201.62(\ln(\mathrm{Re}_p) + 4) - 3737(\ln(\mathrm{Re}_p) + 4)^{\frac{1}{2}} + 5399(\ln(\mathrm{Re}_p) + 4)^{\frac{1}{3}} \tag{2.27}$$

and

$$a_v = \frac{4n_v}{4 - n_v} \tag{2.28}$$

$$b_v = \frac{R}{d_p} \tag{2.29}$$

$$\beta_v = \frac{b_v^2}{2}\left(\frac{b_v^2}{2} - \frac{(a_v b_v + 1)(n_v b_v - 1)}{a_v^2} + n_v\left(\frac{b_v^2}{a_v} + \frac{2b_v}{a_v^2} + \frac{2}{a_v^3}\right) - \frac{\exp(a_v b_v)}{a_v^2}\left(1 - n_v b_v + \frac{2n_v}{a_v}\right)\right)^{-1} \tag{2.30}$$

The particle Reynolds for the packed bed is defined by:

$$\mathrm{Re}_p = \frac{\rho_f U_z d_p}{\mu_f} = \frac{G_z d_p}{\mu_f} \tag{2.31}$$

As discussed by Benyahia (2004) the disadvantage of the empirical approaches is that the models are based on exit velocity profiles, which do not adequately represent the actual velocity within the packed bed. The difficulties in attempting to measure the velocity from within a packed bed are noted by Vortmeyer and Schuster (1983). It is for this reason that they suggest that the most accurate means of predicting the true velocity channelling profile is through the solution of the Brinkman momentum equation. This approach is advocated by multiple authors, including Cheng and Hsu (1986), Skaare (1993), Winterberg and Tsotsas (2000).

Brinkman (1949) studied the work of Darcy and proposed that a macroscopic viscous shear term should be added to Darcy's equation to account for the viscous effects at the boundary wall. The extended Brinkman momentum equation, combines the Ergun pressure loss equation, given by Eq.(2.71), with the Brinkman correction factor, where:

$$\frac{dP}{dz} = -f_1(r)U_z(r) - f_2(r)U_z^2(r) + \mu_{\mathrm{eff}}\left(\frac{\partial^2 U_z(r)}{\partial r^2} + \frac{1}{r}\frac{\partial U_z(r)}{\partial r}\right) \tag{2.32}$$

where the coefficients f_1 and f_2 are dependent on the local void fraction:

$$f_1(r) = 150\frac{(1-\varepsilon(r))^2}{\varepsilon(r)^3}\frac{\mu_f}{d_p^2} \tag{2.33}$$

$$f_2(r) = 1.75\frac{(1-\varepsilon(r))}{\varepsilon(r)^3}\frac{\rho_f}{d_p} \tag{2.34}$$

subject to the boundary conditions:

$$\frac{\partial U_z}{\partial r}(0) = 0 \tag{2.35}$$

$$U_z(R) = 0 \tag{2.36}$$

The original form of the extended Brinkman equation presented by Vortmeyer and Schuster (1983) made use of the molecular fluid viscosity in the near wall region. However, this was found to overestimate the peak in velocity profile when compared to experimental data. For this reason (Giese et al., 1998) introduced the concept of effective viscosity to match the model to experimental data for spheres at $\mathrm{Re}_p < 500$, where:

$$\frac{\mu_{\mathrm{eff}}}{\mu_f} = 2\exp\left(3.5\times10^{-3}\mathrm{Re}_p\right) \tag{2.37}$$

It must be noted that the use of the Brinkman momentum equation provides an approximate solution of the axial flow profile. It is based on average fluid properties and assumes no radial flow. Daszkowski and Eigenberger (1992) solved the full Navier-Stokes equations to study channelling flow in a packed bed. Their work showed that there is a large radial flow in the first particle layer. The radial flow then tends to zero and the axial flow profile stays constant along the bed. This research also showed that the axial flow profile is not strongly affected by radial fluid temperature gradients. Therefore, the use of the Brinkman model is considered acceptable for resolving the axial flow profile in the packed bed TES. This flow profile is imposed on the heat transfer model, thus decoupling the heat transfer and flow equations. This approach provides a solution that will account for wall channelling in the bed while reducing the simulation times compared to a full coupled Navier Stokes model.

Effective solid thermal conductivity

The effective solid thermal conductivity accounts for heat transfer in the solid phase under stagnant conditions where convective mechanisms are not present. The correlation that is

commonly used to model the effective solid conductivity in packed beds is based upon the unit cell theory of Zehner and Schlünder (1970), Bauer and Schlünder (1978) (as cited in IAEA, 2001) and Tsotsas and Schlünder (1990), collectively referred to as the Zehner, Bauer, Schlünder (ZBS) model. This model is based upon the theory of a cylindrical unit cell containing two deformable half particles surrounded by a stagnant fluid.

As noted by the IAEA (2001) the standard ZBS model must be modified to account for radiation heat exchange at high temperatures. The modified model consists of three simultaneous modes of heat transfer for a packed bed of spheres:

- Void radiation and solid conduction - $k_{\text{eff}}^{\text{sr}}$;
- Fluid conduction and solid conduction - $k_{\text{eff}}^{\text{sf}}$;
- Contact conduction and solid conduction - $k_{\text{eff}}^{\text{sc}}$.

The modified version of the ZBS effective solid thermal conductivity as described by IAEA (2001) and Visser (2007) is:

$$k_{\text{eff}}^{\text{sr}} = \left(\left[1 - \sqrt{1-\varepsilon} \right] \varepsilon + \frac{\sqrt{1-\varepsilon}}{2/\gamma_s - 1} \frac{B+1}{B} \frac{1}{1 + \frac{1}{(2/\gamma_s - 1)\Lambda}} \right) 4\sigma T_s^3 d_p \tag{2.38}$$

where:

$$B = 1.25 \left(\frac{1-\varepsilon}{\varepsilon} \right)^{\frac{10}{9}} \tag{2.39}$$

$$\Lambda = \frac{k_s}{4\sigma T^3 d_p} \tag{2.40}$$

$$\frac{k_{\text{eff}}^{\text{sf}}}{k_f} = 1 - \sqrt{1-\varepsilon} + \frac{2\sqrt{1-\varepsilon}}{1-\lambda B} \left[\frac{(1-\lambda)B}{(1-\lambda B)^2} \ln\left(\frac{1}{\lambda B} \right) - \frac{B+1}{2} - \frac{B-1}{1-\lambda B} \right] \tag{2.41}$$

where:

$$\lambda = \frac{k_f}{k_s} \tag{2.42}$$

$$\frac{k_{\text{eff}}^{\text{sc}}}{k_s} = \left(\frac{(3(1-\nu_s^2)}{4E} \frac{F_s d_p}{2} \right)^{\frac{1}{3}} \frac{1}{0.531S} \frac{N_A}{N_L} \tag{2.43}$$

where:

$$F_s = p_s \frac{S_F}{N_A} \tag{2.44}$$

N_A and N_L are the number of particles per area and per length respectively. For a cubic arrangement these are given the values of $N_A = d_p^{-2}$ and $N_L = d_p^{-1}$, while S_F and S are equal to unity. The external pressure p is determined by the weight of the packed particles. The total effective conductivity in the packed bed is calculated through the summation of these individual conductivity components:

$$k_{\text{eff,s}} = k_{\text{eff}}^{\text{sr}} + k_{\text{eff}}^{\text{sf}} + k_{\text{eff}}^{\text{sc}} \tag{2.45}$$

As noted by Visser (2007), the ZBS correlation breaks down in the near-wall region as the void fraction tends to unity. This is due to the radiation component of the model (Eq.(2.38)) which tends to infinity. Tsotsas (2002) presented an alternative radiative component for the ZBS model in the near wall region. However, as described by Van Antwerpen (2009), this modified form is not continuous with the parent ZBS correlation in the core region of the packed bed. This introduces added numerical difficulties. Therefore in the current study the approach of IAEA (2001) is used. The effective solid thermal conductivity in the near wall region is calculated using an average near wall void fraction value. This value is calculated by averaging the exponential void fraction profile over a distance of half a particle diameter away from the wall. This approach was also used in the model of Yagi and Kunii (1961, cited in Van Antwerpen (2009)) for the calculation of the effective solid thermal conductivity in the near wall region.

Effective fluid thermal conductivity

The effective fluid conductivity term represents the heat transport through axial and radial dispersion (braiding effect). The parameter can be correlated as a linear function of Reynolds number (Wakao and Kaguei, 1982), where:

$$\frac{k_{\text{eff,f}}}{k_f} = C_D \text{Re}_p \text{Pr} \tag{2.46}$$

As described by Beasley and Clark (1984), the value of C_D is 0.1 in the radial direction and between 0.2 and 1 in the axial direction. Wakao and Kaguei (1982) recommend a value of 0.5 in the axial direction ($\text{Re}_p > 0.8$) and 0.1 in the radial direction. Values of 0.3 and 0.1 were implemented in the current study for the axial and radial dispersion coefficients respectively,

as these parameters best represented the experimental temperature profiles. The models of Jalalzadeh-Azar et al. (1996) and Zanganeh et al. (2012) neglected axial fluid dispersion in the modelling of a high temperature packed bed.

It has been noted by researchers that there is a sharp decrease in the fluid mixing in the near wall region (Winterberg et al., 2000; Koning, 2002). This has the effect of reducing the degree of thermal dispersion and increasing the resistance to heat transfer. In the current model, the effective fluid conductivity in the near-wall region is decreased linearly to k_f within one particle diameter of the wall to account for the reduction in thermal mixing in the packed bed.

Inter-phase heat transfer coefficient

The inter-phase heat transfer coefficient describes the heat transfer between the solid particles and the fluid, thus coupling the fluid and solid energy equations. A large number of empirical correlations have been proposed to calculate this coefficient. Wakao et al. (1979) provide a detailed overview of the experimental results of a large number of authors, including Gunn and De Souza (1974) and Kunii and Smith (1960). They have proposed the following empirical relationship:

$$\mathrm{Nu}_p = 2 + 1.1\mathrm{Pr}^{1/3}\mathrm{Re}_p^{0.6} \tag{2.47}$$

where Nu_p is the particle Nusselt number defined as:

$$\mathrm{Nu}_p = \frac{h_p d_p}{k_f} \tag{2.48}$$

This correlation is valid over the range $15 < \mathrm{Re}_p < 8500$. However, there is no clear indication given on the limit of void fraction values. It is assumed that this equation is only valid for the bulk of the packed bed where $\varepsilon \approx 0.4$. The German Nuclear Safety Standards Commission (KTA) proposed a correlation for spherical particles under the conditions $100 < \mathrm{Re}_p < 10^5$, $20 < D/d_p$ and $0.36 < \varepsilon < 0.42$. It is given by:

$$\mathrm{Nu}_p = \frac{1.27\mathrm{Pr}^{1/3}\mathrm{Re}_p^{0.36}}{\varepsilon^{1.18}} + \frac{0.033\mathrm{Pr}^{1/2}\mathrm{Re}_p^{0.86}}{\varepsilon^{1.07}} \tag{2.49}$$

Yoshida et al. (1962) presented a correlation that takes into account the geometry of the packing material, through a shape factor Ψ_p. Table 2.2 provides a list of the particle shape factors.

The correlation is presented in terms of the Colburn j factor where:

$$j_H = \begin{cases} 0.91 Re_{\Psi}^{-0.51} \Psi_p & \text{if } \mathrm{Re}_{\Psi} \leq 50 \\ 0.61 Re_{\Psi}^{-0.41} \Psi_p & \text{if } \mathrm{Re}_{\Psi} > 50 \end{cases} \tag{2.50}$$

where

$$j_H = \frac{h_p}{c_f G_z} Pr^{2/3} \tag{2.51}$$

$$Re_{\Psi} = \frac{G_z}{a_p \Psi_p \mu_f} \tag{2.52}$$

Table 2.2: Particle shape factors (Rahman, 2009)

Particle shape	ψ_p	Particle shape	ψ_p
Sphere	1	Raschig ring	0.79
Cylinder	0.91	Partition ring	0.67
Flake	0.86	Berl saddle	0.8

The correlation presented by Gunn (1978) is valid for $\mathrm{Re}_p < 10^5$ and clearly outlines the void fraction bounds of $0.35 < \varepsilon < 1$. Therefore this correlation was utilised to calculated the inter-phase heat transfer coefficient for the C-S and D-C models. The particle Nusselt number is calculated by:

$$\mathrm{Nu}_p = (7 - 10\varepsilon + 5\varepsilon^2)(1 + 0.7\mathrm{Pr}^{1/3}\mathrm{Re}_p^{0.2}) + (1.33 - 2.4\varepsilon + 1.2\varepsilon^2)\mathrm{Pr}^{1/3}\mathrm{Re}_p^{0.7} \tag{2.53}$$

Figure 2.3 shows a comparison of the predicted particle Nusselt numbers from the correlations presented in this section. Each correlation predicts a similar trend in Nusselt number as a function of particle Reynolds number. However there is a spread of approximately 35% in values between the Gunn and Yoshida et al. correlations. The Gunn correlation predicts the highest of values of particle Nusselt number of four correlations.

The C-S model utilises a lumped capacitance approach to model how the solid particles absorb and release energy. In order to correct for the effects of finite particle thermal conductivity the heat transfer coefficient can be modified. This method entails reducing h_p such that the energy absorbed by the isothermal particle is equal to that absorbed by a non-isothermal particle.

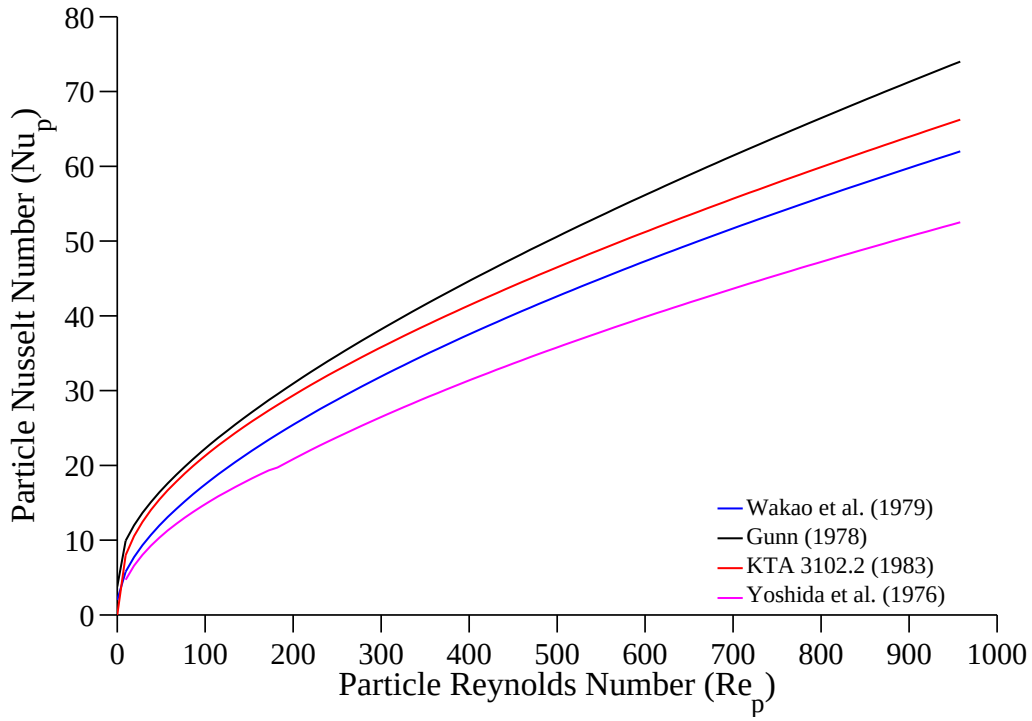

Figure 2.3: Comparison of Nusselt number correlations for spheres with $\varepsilon = 0.4$

Jeffreson (1972) proposed the following correction factor:

$$h_p^* = \frac{h_p}{1 + 0.2\mathrm{Bi}_p} \tag{2.54}$$

where the particle Biot number is defined as:

$$\mathrm{Bi}_p = \frac{h_p d_p}{2k_s} \tag{2.55}$$

Numerical tests, presented in Section 5.2 show that Eq.(2.54) is accurate for Biot numbers as high as five for sensible heat storage modelling, using ceramic heat storage materials.

2.3.4 Initial and boundary conditions

The model domain is divided into two regions, namely the packed bed and container wall. For comparison with the packed bed test facility the modelled wall consists of an inner metal container (Nimonic 75) and an outer insulation layer of ceramic fibre blanket (150 mm).

The charging and discharging of the packed bed is controlled by varying inlet fluid temperature, flow rate and flow direction. In order to suppress natural convection effects the flow would enter from the top of the packed bed during charging and from the base during discharging (reverse direction). This is termed counter-current heat recovery. Due to the design of the test facility, experimental data was only available in co-current heat recovery mode where the flow direction was not reversed during cooling. Figure 2.4 shows the boundary conditions for the C-S heat transfer model domain (representing Figure 2.1). Symmetry boundary conditions are imposed on the fluid and solid phases along the bed centreline. The charging and discharging of the packed bed model is governed by varying the inlet fluid temperature.

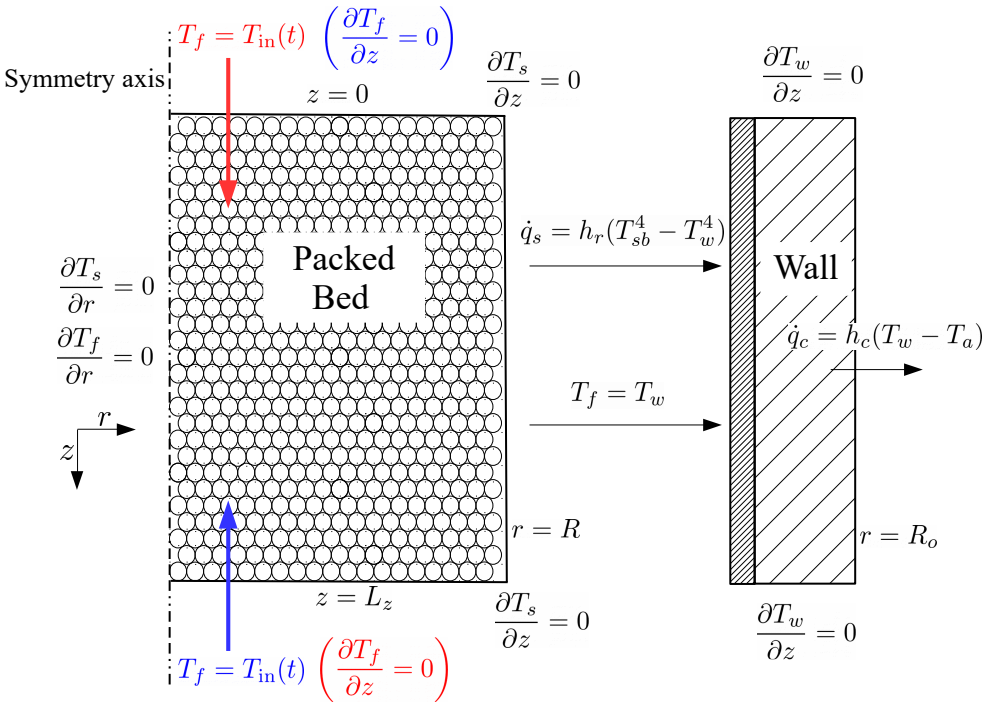

Figure 2.4: Boundary conditions for the C-S heat transfer model (charging shown in red, discharging in blue)

For the initial preheating test the fluid, solid and wall are all assumed to be at uniform ambient temperature T_a. For subsequent heating and cooling tests an initial temperature distribution is specified based on the final temperature distribution of the previous heating or cooling simulation. This is due to axial and radial temperature gradients that develop during the heating and cooling of the packed bed.

The boundary conditions for the fluid temperature and solid surface temperature are the same for the D-C and C-S heat transfer models. However, as shown in Figure 2.5 there are an extra two boundary conditions for each of the representative spherical particles. A symmetry boundary condition is applied to each particle centre, while Eq.(2.7) is applied to the surface of each particle.

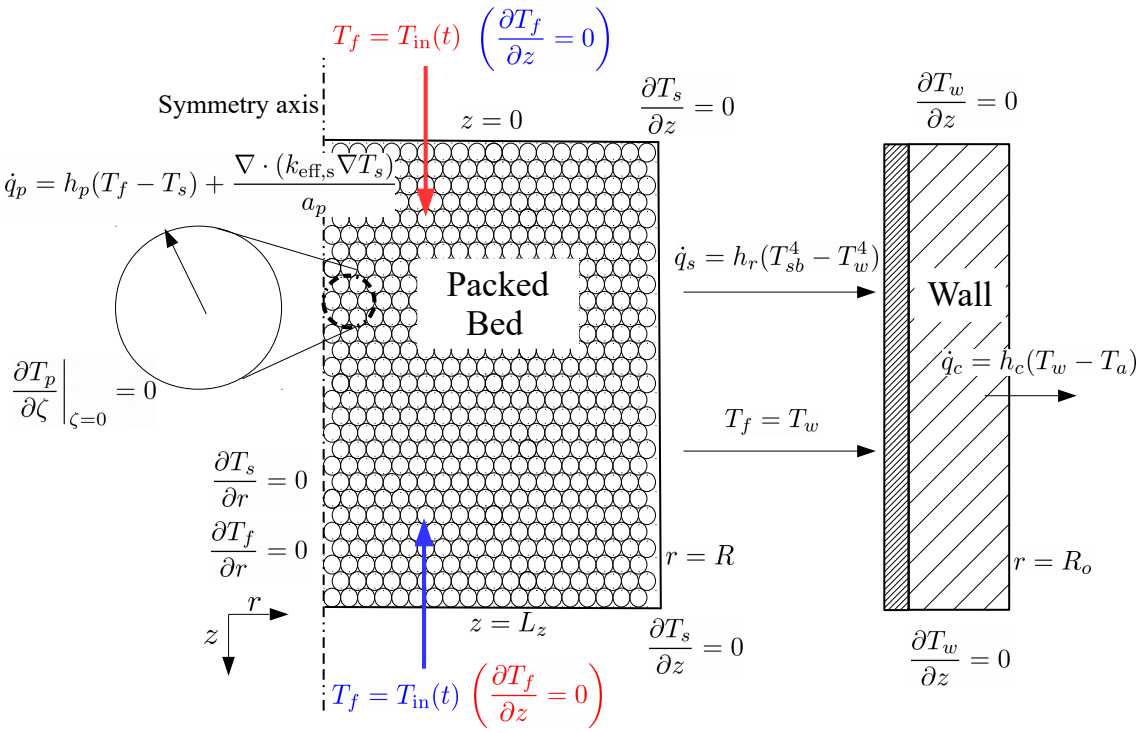

Figure 2.5: Boundary conditions for the D-C heat transfer model (charging shown in red, discharging shown in blue)

In the C-S and D-C models both the fluid and solid phases exchange energy with the inner wall. Measurements of heat transfer in packed beds have shown that there is an increased resistance to radial heat flow at the bed wall. Previous packed bed models utilised a wall heat transfer coefficient for the fluid phase (Vortmeyer and Haidegger, 1991). This is essentially a lumped parameter that includes all of the near wall effects. In the current work, wall channelling and the decrease in thermal dispersion at the wall are taken into account. Therefore, as described by Winterberg et al. (2000) and Visser (2007) the fluid boundary condition is:

$$T_f = T_w \tag{2.56}$$

$$\dot{q}_f = -k_{\text{eff,f}}(R)\frac{\partial T_f}{\partial r} = -k_f \frac{\partial T_f}{\partial r} \tag{2.57}$$

The solid particles exchange energy with the wall through radiation. Visser (2007) presented the development of a solid radiation boundary condition for high temperature packed beds. This radiation boundary condition is utilised in the current work to model the radiation heat exchange between the solid and the inner wall. The subscript '*sb*' represents the temperature of the solid at a distance of one particle radius from the wall. Along the bed wall at $r = R$:

$$\dot{q}_s = -k_{\text{eff,s}} \frac{\partial T_s}{\partial r} = h_r (T_{sb}^4 - T_w^4) \tag{2.58}$$

where:

$$h_r = \sigma \left(\frac{1}{\gamma_s} + \frac{1}{\gamma_w} - 1 \right) \tag{2.59}$$

At the fluid-wall and solid-wall interface the heat flow must be conserved. Therefore the heat leaving the fluid and solid phases must enter the wall. Along the inner bed wall at $r = R$ the boundary condition is calculated using an energy balance, where:

$$-k_w \frac{\partial T_w}{\partial r} = \dot{q}_f + \dot{q}_s \tag{2.60}$$

The natural convection heat exchange between the outer vessel wall and the ambient environment was modelled as natural convection heat transfer over a vertical cylinder. Along the outer vessel wall at $r = R_o$ the correlation used is:

$$\dot{q}_c = -k_w \frac{\partial T_w}{\partial r} = h_c (T_w - T_{\text{a}}) \tag{2.61}$$

where, according to Nag (2007):

$$h_c = 1.42 \left(\frac{T_w - T_a}{L_z} \right)^{0.25} \tag{2.62}$$

The constant 1.42 in this equation carries units of $\text{W/K}^{\frac{5}{4}}\text{m}^{\frac{7}{4}}$, and is derived using the properties of atmospheric air and ambient temperature.

At the interface between the metal wall and the insulation, continuity of temperature and heat flux was enforced such that:

$$T_{w1} = T_{w2} \tag{2.63}$$

$$k_{w1} \frac{\partial T_{w1}}{\partial r} = k_{w2} \frac{\partial T_{w2}}{\partial r} \tag{2.64}$$

2.4 Pressure drop in packed beds

The efficient thermodynamic design of a packed bed thermal storage system must carefully consider both the heat transfer and pressure drop characteristics. High interstitial flow velocities increase the rate of heat transfer in the bed, while also increasing the pressure drop. In charging mode a blower is used to circulate air through the packed bed and receiver. If the pressure drop across the bed is excessively high, the blower will require a high power input. In discharge mode, the compressor of the gas turbine will move air through the packed bed directly. In this case, if the pressure drop across the bed is too high the efficiency and power output of the system will be reduced. This section presents the relevant literature regarding pressure drop for flow through randomly packed beds. The Ergun equation (Ergun, 1952) is presented in this section and its development discussed in detail. The KTA (1981) equation is also considered and compared with the Ergun equation.

2.4.1 Development of the Ergun equation

Darcy model

The Darcy model consists of a semi-empirical equation that governs the macroscopic pressure drop for a fluid moving through an infinitely extended porous medium, under creeping flow conditions ($\mathrm{Re}_p \to 0$). As described by Kaviany (1995), the bulk resistance to flow is a function of the fluid viscosity and Darcy permeability (a measure of flow conductance) of the solid such that:

$$\frac{dP}{dz} = -\frac{\mu_f}{K_D} U_z \tag{2.65}$$

Blake-Kozeny model

The Blake-Kozeny model is based on the assumption that the flow through a packed bed can be modelled as flow through a bundle of tortuous irregularly shaped capillaries with a uniform average cross sectional area.

The Blake-Kozeny equation for macroscopic pressure drop in a packed bed under laminar flow conditions is given by Du Plessis and Woudberg (2008) as:

$$\Delta P = -36K_B \frac{(1-\varepsilon)^2}{\varepsilon^3} \frac{\mu_f L_c U_z}{d_p^2} \tag{2.66}$$

Extensive empirical data has shown that the constant $K_B = 2$ and that a correction factor of 25/12 should be used to account for the tortuous flow path in the packed bed, yielding:

$$\frac{dP}{dz} = -150 \frac{(1-\varepsilon)^2}{\varepsilon^3} \frac{\mu_f U_z}{d_p^2} \tag{2.67}$$

Carman (1937) advocated for the modification of Eq.(2.66) with the introduction of the Kozeny constant (K_K). The modified Blake-Kozeny equation is referred to as the Carman-Kozeny-Blake equation and it is given by:

$$\frac{dP}{dz} = -36K_K \frac{(1-\varepsilon)^2}{\varepsilon^3} \frac{\mu_f U_z}{d_p^2} \tag{2.68}$$

According to Kaviany (1995), research has shown that the Kozeny constant should be given the value of five for a packed bed. Therefore the Eq.(2.68) is equivalent to:

$$\frac{dP}{dz} = -180 \frac{(1-\varepsilon)^2}{\varepsilon^3} \frac{\mu_f U_z}{d_p^2} \tag{2.69}$$

According to Bird et al. (2002) the Blake-Kozeny model is valid in the region of $\varepsilon < 0.5$ and $\mathrm{Re}_p/(1-\varepsilon) < 10$.

Burke-Plummer model

At higher Reynolds numbers the Forchheimer flow regime ($\mathrm{Re}_p > 100$) is encountered and the relationship between pressure drop and superficial velocity becomes non-linear. This is due to the inertial effects in the packed bed. A detailed study of the inertial effects of flow through packed beds at higher Reynolds numbers was completed by Burke and Plummer (1928) and the following empirical relationship was defined:

$$\frac{dP}{dz} = -1.75 \frac{(1-\varepsilon)}{\varepsilon^3} \frac{\rho_f U_z^2}{d_p} \tag{2.70}$$

Ergun model

Ergun (1952) studied the Blake-Kozeny and Burke-Plummer equations and experimental data. He proposed that the total pressure drop for flow through a packed bed was due to the viscous friction forces as well as kinetic energy losses. In order to develop a comprehensive model to cover both turbulent and laminar flow regimes, Ergun added Eqs.(2.67) and (2.70) to give:

$$\frac{dP}{dz} = -C_A \frac{(1-\varepsilon)^2}{\varepsilon^3} \frac{\mu_f U_z}{d_p^2} - C_B \frac{(1-\varepsilon)}{\varepsilon^3} \frac{\rho_f U_z^2}{d_p} \tag{2.71}$$

The coefficients C_A and C_B were given the values of 150 and 1.75 by Ergun. Thus for very low flow velocities the equation reduces to the Blake-Kozeny equation and for very high velocities the Burke-Plummer equation. As described by Bird et al. (2002) the "empirical superposition of asymptotes often leads to satisfactory results." Allen (2014), determined that despite the Ergun equation being based on experimental data over the range $1 < \mathrm{Re}_m < 2400$, it over-predicts the pressure drop across packed spheres for $\mathrm{Re}_m > 700$. Various authors have presented alternative values for C_A and C_B, based on their own experimental data. These constants are shown in Table 2.3.

Table 2.3: Various empirical Ergun coefficients (Vorayos et al., 2008)

Author	C_A	C_B
Ergun (1952)	150	1.75
Macdonald et al. (1979)	180	1.8
Fand et al. (1987)	225	1.61
Yu et al. (2002)	203	1.95

Analytical derivation of Ergun constants

Du Plessis and Woudberg (2008) note that the use of empirically derived constants for the Ergun equation leads to limited applicability of the model. In their paper they produce a pore scale derivation of these constants. This analytical approach holds for the entire range of porosity values and can be generalised based on the packed bed geometry. The development of the model is based on the concept of a granular representative unit cell (RUC). This is defined as the smallest rectangular control volume element into which the average geometric properties of the packed bed are embedded. The resulting equations of the granular RUC model to determine the constants C_A and C_B are given below in Eqs.(2.72) and (2.73). Figure

2.6 shows the variation in the Ergun coefficients. At a bulk bed void fraction of 0.4 the predicted values of C_A and C_B are 175 and 1.8 respectively. These coefficients are in good agreement with the empirical coefficients presented in Table 2.3.

$$C_A = \frac{25.4\varepsilon^3}{(1-\varepsilon)^{\frac{2}{3}}(1-(1-\varepsilon)^{\frac{1}{3}})(1-(1-\varepsilon)^{\frac{2}{3}})^2} \tag{2.72}$$

$$C_B = \frac{\varepsilon^2 c_d}{2\left(1-(1-\varepsilon)^{\frac{2}{3}}\right)^2} \tag{2.73}$$

The parameter c_d represents the form drag coefficient of a single sphere or particle placed in an infinite velocity stream and is taken as 1.9 by Du Plessis and Woudberg (2008).

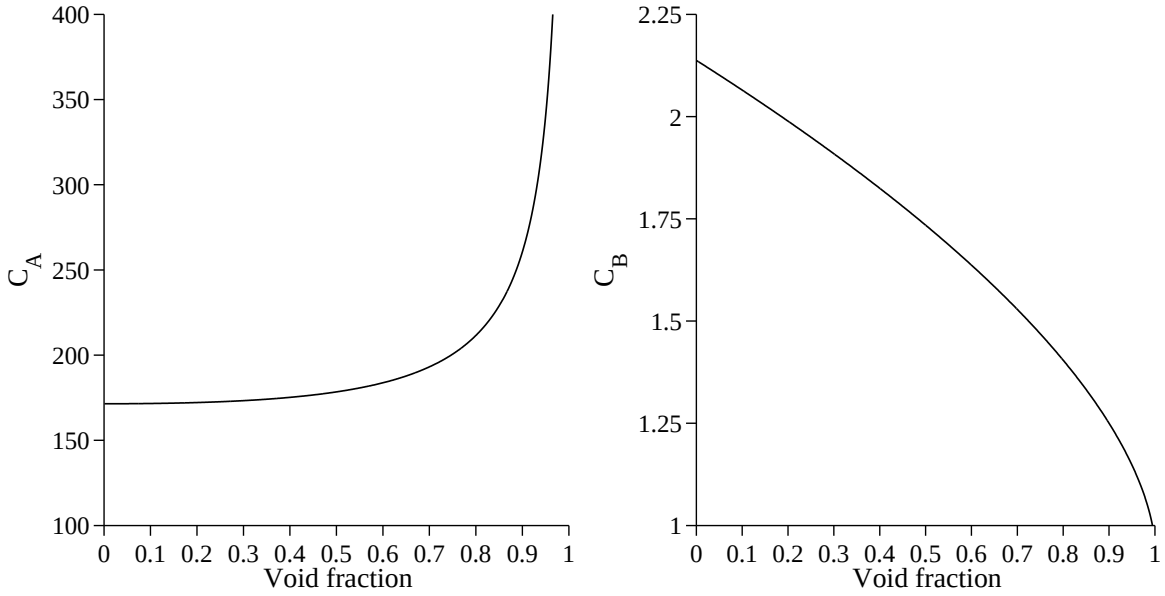

(a) Viscous coefficient

(b) Inertial coefficient

Figure 2.6: Calculated Ergun equation coefficients according to the RUC model of Du Plessis and Woudberg (2008)

2.4.2 KTA model

The German Nuclear Safety Standards Commission (KTA) conducted a detailed analysis of the literature regarding pressure drop across packed beds of uniform spherical particles. Achenbach (1995) found that there was a large scatter in the experimental data for pressure drop through different packed beds. This was thought to be due to the strong influence that void fraction has on pressure drop. In a large number of the papers examined in this study the

void fraction was not determined accurately enough or not at all. KTA (1981) noted that the relevant papers that did include an accurate calculation of void fraction could be modelled by Eqs.(2.74) and (2.75) . The pressure loss across the packed bed is calculated by:

$$\frac{\Delta P}{L} = -\psi \left(\frac{1-\varepsilon}{\varepsilon^3} \right) \left(\frac{\rho_f}{d_p} \right) U_z^2 \tag{2.74}$$

where ψ is the coefficient of loss of pressure through friction, defined by:

$$\psi = \frac{160}{\mathrm{Re}_m} + \frac{3}{\mathrm{Re}_m^{0.1}} \tag{2.75}$$

where Re_m is the modified Ergun Reynolds number given by:

$$\mathrm{Re}_m = \frac{\mathrm{Re}_p}{1-\varepsilon} \tag{2.76}$$

The limits for the KTA model are $1 < \mathrm{Re}_m < 10^5$, $0.36 < \varepsilon < 0.42$ and $L > 5d_p$. The first term in Eq.(2.75) represents the asymptotic solution of the pressure loss coefficient for laminar flow and the second term is for the turbulent flow. Achenbach (1995) measured the pressure drop in a packed bed experiment at various particle Reynolds numbers and compared it to the KTA model. The results of Achenbach show a good correlation between the measured and predicted pressure loss coefficient.

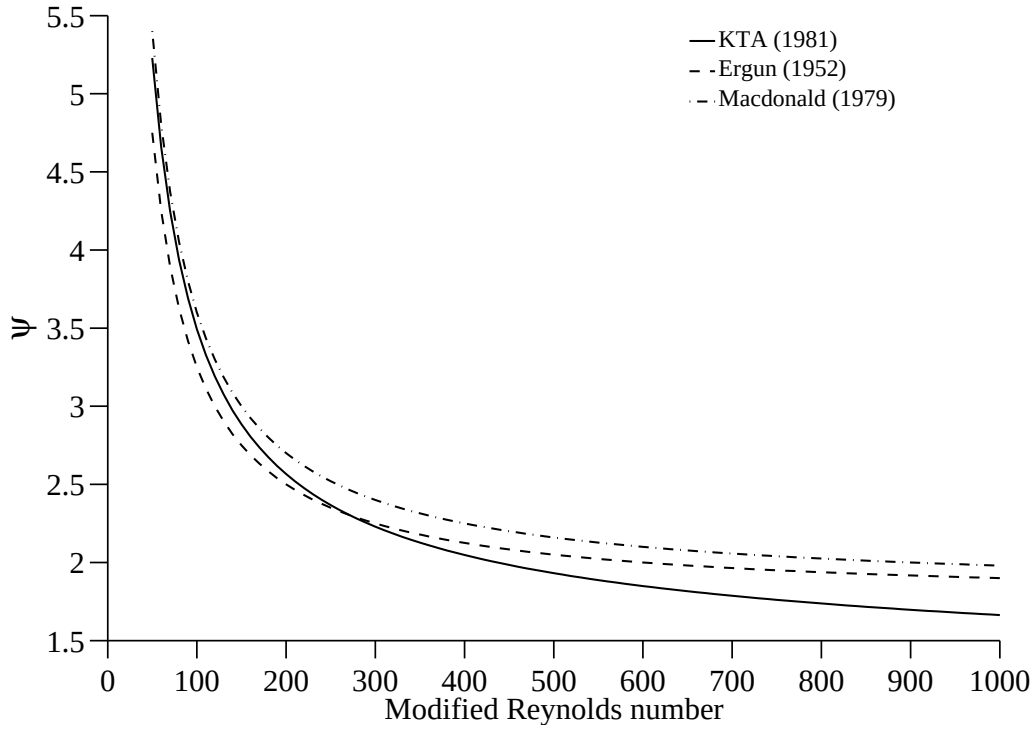

Figure 2.7: Comparison of pressure loss coefficient for the Ergun and KTA equations

Figure 2.7 shows a comparison of the pressure loss coefficient between the Ergun and KTA equations. At low modified Reynolds numbers (below 200) all three equations predict a similar pressure loss coefficient. However, at modified Reynolds numbers greater than 500 the KTA equation predicts a lower pressure drop coefficient. For comparison with the KTA model the pressure loss coefficient for the Ergun equation is calculated by:

$$\psi = \frac{C_A}{\mathrm{Re}_m} + C_B \tag{2.77}$$

2.5 Conclusions

This chapter presented the mathematical development of the heat transfer, fluid flow and pressure drop models that are implemented in this thesis. Previous numerical studies related to sensible heat and latent heat storage were discussed. The governing energy equations for the Continuous-Solid and Dispersion-Concentric heat transfer models were developed on the basis of specific fluid enthalpy and solid internal energy. These equations were reformulated in terms of fluid and solid phase temperatures, in order to facilitate an efficient numerical solution. Near wall flow effects were modelled through the extended Brinkman momentum equation and the Ergun and KTA models were presented to calculate the pressure drop across the packed bed.

The constitutive equations required for the solution of the C-S and D-C models were presented, which involved re-contextualising a number of semi-empirical heat transfer correlations that were developed primarily for the chemical engineering and nuclear engineering fields. The particle Reynolds numbers of the sensible heat and latent heat experiments conducted in this work are below 300 and are within range of the presented correlations for packed beds. For reference, a larger 7 m^3 storage unit design with $L_z/D = 3$ and $\dot{m}_d = 0.64$ kg/s has a particle Reynolds number between 92 and 461 depending on the choice particle diameter ($d_p = 10$ mm to 50 mm). The two dimensional boundary conditions for both the C-S and D-C models were introduced. The inclusion of a radiation boundary condition between the solid particles and the wall is an improvement on previous two dimensional models for high temperature TES.

Chapter 3

Numerical solution of governing heat transfer and fluid flow equations

3.1 Introduction

In Chapter 2 the C-S and D-C heat transfer models were introduced for the packed bed thermal storage system. Due to the complexity of the governing equations, an analytical solution is not possible. Therefore a numerical solution needs to be developed. This chapter describes the numerical technique of Orthogonal Collocation on Finite Elements (OCFE) that was used to study the thermal performance of the packed bed. Orthogonal collocation and the OCFE method are introduced in Section 3.2. The solutions of the fluid flow and heat transfer equations are presented in Sections 3.3 and 3.4 respectively. The phase change within the EPCM particles is modelled using the effective heat capacity method, outlined in Section 3.5. This method involves increasing the heat capacity of the solid particles during the melting or solidification of the PCM, in order to account for the latent heat of fusion.

3.2 Orthogonal collocation on finite elements

3.2.1 Orthogonal collocation

Collocation forms part of the method of weighted residuals, of which the well known Galerkin and Least Squares methods are an example. An unknown solution is represented by a series

expansion of smooth basis functions consisting of orthogonal polynomials. The Galerkin and collocation methods employ different weighting functions. The collocation weighting function is the Dirac delta function, such that the residual at a set of collocation points is forced to zero, i.e. the differential equation is solved exactly at these collocation points.

Global collocation methods offer a high level of accuracy if the problem solution is smooth and continuous. As the number of collocation points is increased, rapid convergence is achieved. However, the numerical approximation deteriorates in accuracy when steep gradients, such as boundary layers or interior fronts, are present. This is due to difficulties that are encountered in utilising a global (high order) polynomial to represent a non-smooth solution. In general, spurious oscillations will develop, known as the Gibbs phenomenon, and a large number of nodes will be required to generate an acceptable solution. It is for this reason that the technique of OCFE has been developed.

In the OCFE method, global collocation is modified to utilise lower order polynomials on finite element sub domains, creating a piecewise continuous solution. OCFE is advocated as an efficient numerical method for the solution of partial differential equations involving steep gradients in localised sections of a problem domain (Finlayson, 1980). This technique combines the high accuracy of orthogonal collocation, with the flexibility of the finite element method. Therefore it is suitable for modelling the thermal performance of a packed bed thermal storage system as it allows for efficient numerical solutions while maintaining high accuracy.

3.2.2 Cubic Hermite polynomials

In this work the cubic Hermite polynomials were implemented as the basis function for the collocation procedure. Hermite polynomials are used extensively in the spline interpolation of data. The piecewise solution is **C1** continuous. Therefore the point value and first derivatives are continuous at the element boundaries. This makes cubic Hermite polynomials a highly efficient basis function for OCFE (Chang and Finlayson, 1978). Figure 3.1 shows the four basis functions plotted on a unit interval. The polynomials are only valid on the domain [0,1] and therefore require a transformation between the global and local element coordinate systems. For the kl^{th} element of radial width Δr^k and axial width Δz^l the coordinate

transformation is given by:

$$v = \frac{r - r^k}{r^{k+1} - r^k} = \frac{r - r^k}{\Delta r^k} \tag{3.1}$$

$$w = \frac{z - z^l}{z^{l+1} - z^l} = \frac{z - z^l}{\Delta z^l} \tag{3.2}$$

For the D-C model the extra dimension for the intra-particle temperature profiles yields a coordinate transformation for the m$^{\text{th}}$ internal element of:

$$x = \frac{\zeta - \zeta^m}{\zeta^{m+1} - \zeta^m} = \frac{\zeta - \zeta^m}{\Delta \zeta^m} \tag{3.3}$$

As described by Finlayson (1980), the Hermite polynomials are defined as:

$$\phi_1(v) = (1+2v)(1-v)^2 \tag{3.4}$$

$$\phi_2(v) = v(1-v)^2 \Delta r^k \tag{3.5}$$

$$\phi_3(v) = (3-2v)v^2 \tag{3.6}$$

$$\phi_4(v) = (v-1)v^2 \Delta r^k \tag{3.7}$$

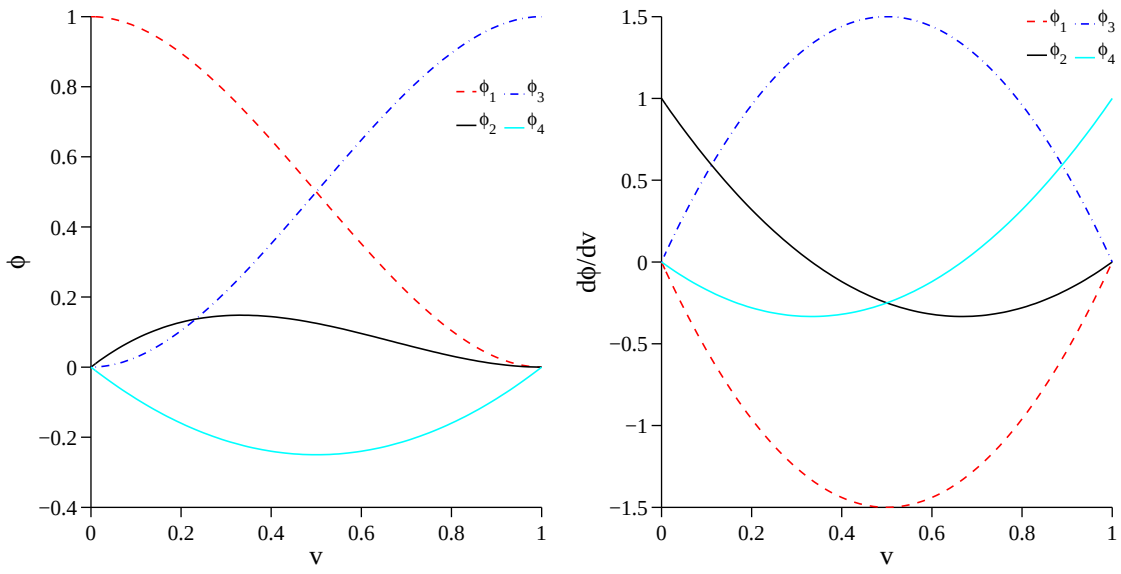

Figure 3.1: Hermite basis functions on a unit interval for $\Delta r^k = 1$

3.2.3 OCFE in one spatial dimension

The OCFE procedure, based on cubic Hermite polynomials, is outlined in this section for solving a one-dimensional partial differential equation. First the domain is divided into finite

elements. The solution variable within the k^{th} element is approximated by the following series expansion:

$$T^k(r) = \sum_{i=1}^{4} a_i^k \phi_i(v) \tag{3.8}$$

The spatial derivatives are defined as:

$$\frac{\partial T^k}{\partial r} = \frac{1}{\Delta r^k} \sum_{i=1}^{4} a_i^k \frac{\mathrm{d}\phi_i(v)}{\mathrm{d}v} \tag{3.9}$$

$$\frac{\partial^2 T^k}{\partial r^2} = \frac{1}{\left(\Delta r^k\right)^2} \sum_{i=1}^{4} a_i^k \frac{\mathrm{d}^2\phi_i(v)}{\mathrm{d}v^2} \tag{3.10}$$

The Hermite polynomials are arranged such that the unknown series coefficients represent either the value of T or $\partial T/\partial r$ at the points $v = 0$ or $v = 1$. As the nodes between elements are shared, the solution is piecewise continuous. In order to generate a solution, a total of $2(N_r + 1)$ equations are required to solve for the series coefficients. The differential equation is satisfied exactly at two collocation points within each element, yielding a total of $2N_r$ algebraic equations. The remaining two equations are generated by collocating the two boundary conditions. Figure 3.2 shows the node locations for three elements. The interior collocation points are chosen to be the Gauss quadrature points:

$$v_{1,2} = \frac{1}{2}\left(1 \pm \frac{1}{\sqrt{3}}\right) \tag{3.11}$$

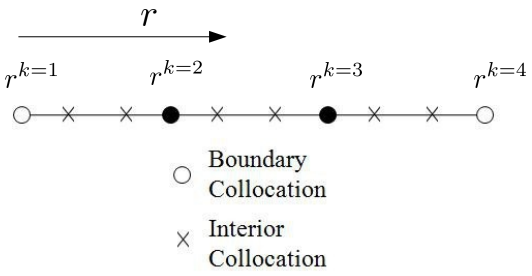

Figure 3.2: Location of collocation points in one-dimension (3 elements)

3.2.4 OCFE in two spatial dimensions

In two-dimensions the solution within each element is approximated by the tensor product of two one-dimensional polynomials. Assuming a domain of *r*-*z*, the solution variable in the

kl^{th} element is approximated by:

$$T^{kl}(r,z) = \sum_{i=1}^{4}\sum_{j=1}^{4} a_{ij}^{kl}\phi_i(v)\phi_j(w) \tag{3.12}$$

The partial derivatives of the solution variable with respect to r and z are:

$$\frac{\partial T^{kl}}{\partial r} = \frac{1}{\Delta r^k}\sum_{i=1}^{4}\sum_{j=1}^{4} a_{ij}^{kl}\frac{\mathrm{d}\phi_i}{\mathrm{d}v}\phi_j \tag{3.13}$$

$$\frac{\partial^2 T^{kl}}{\partial r^2} = \frac{1}{\left(\Delta r^k\right)^2}\sum_{i=1}^{4}\sum_{j=1}^{4} a_{ij}^{kl}\frac{\mathrm{d}^2\phi_i}{\mathrm{d}v^2}\phi_j \tag{3.14}$$

$$\frac{\partial T^{kl}}{\partial z} = \frac{1}{\Delta z^l}\sum_{i=1}^{4}\sum_{j=1}^{4} a_{ij}^{kl}\phi_i\frac{\mathrm{d}\phi_j}{\mathrm{d}w} \tag{3.15}$$

$$\frac{\partial^2 T^{kl}}{\partial z^2} = \frac{1}{\left(\Delta z^l\right)^2}\sum_{i=1}^{4}\sum_{j=1}^{4} a_{ij}^{kl}\phi_i\frac{\mathrm{d}^2\phi_j}{\mathrm{d}w^2} \tag{3.16}$$

Each finite element has four interior collocation points at which the differential equation is satisfied. The solution requires a total of $4(N_r+1)(N_z+1)$ algebraic equations. The interior collocation procedure yields a total of $4N_rN_z$ equations. The remaining equations are derived by collocating the boundary conditions on the nodes shown in Figure 3.3.

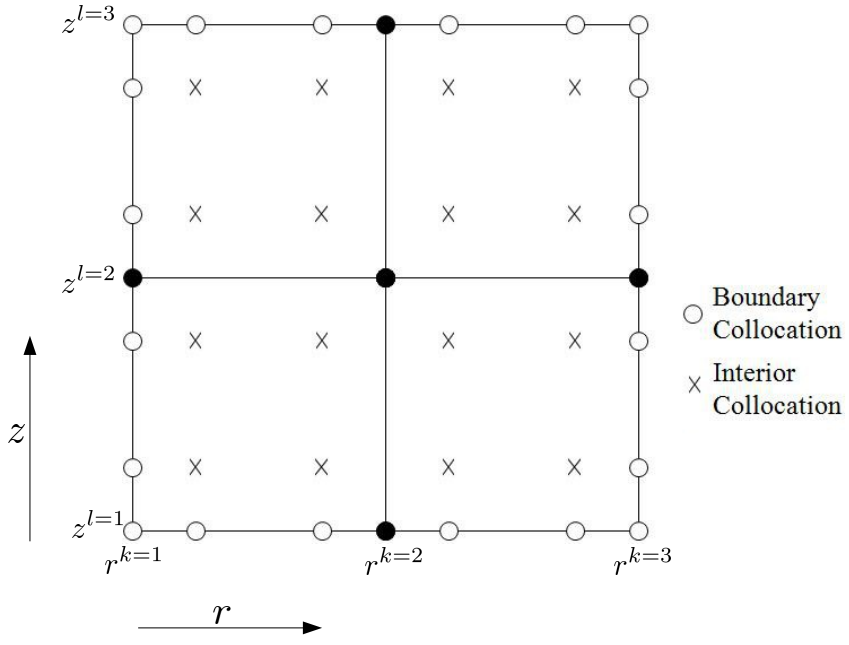

Figure 3.3: Location of collocation points in two-dimensions (4 elements depicted)

In two-dimensions the coefficients of the cubic Hermite polynomials represent T, $\partial T/\partial r$, $\partial T/\partial z$, $\partial^2 T/\partial r\partial z$ at the four corner nodes of the element. As a corner node is shared by adjacent elements, the solution is piecewise continuous. If the local element's corner nodes are labelled according to Figure 3.4, the interpretation unknown series coefficients are described by Eqs.(3.17)-(3.20).

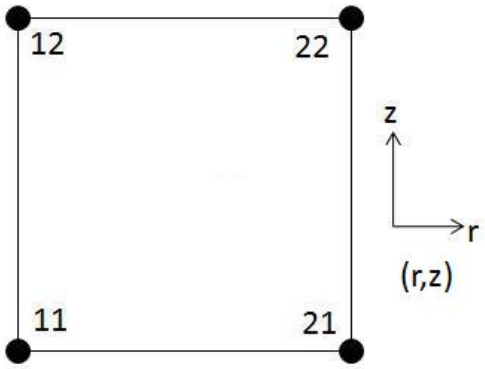

Figure 3.4: Local node numbering for element corners

Node (1,1):

$$\begin{bmatrix} a_{11}^{kl} & a_{12}^{kl} \\ a_{21}^{kl} & a_{22}^{kl} \end{bmatrix} = \begin{bmatrix} T_{11}^{kl} & \dfrac{\partial T_{11}^{kl}}{\partial z} \\ \dfrac{\partial T_{11}^{kl}}{\partial r} & \dfrac{\partial^2 T_{11}^{kl}}{\partial r \partial z} \end{bmatrix} \tag{3.17}$$

Node (2,1):

$$\begin{bmatrix} a_{31}^{kl} & a_{32}^{kl} \\ a_{41}^{kl} & a_{42}^{kl} \end{bmatrix} = \begin{bmatrix} T_{21}^{kl} & \dfrac{\partial T_{21}^{kl}}{\partial z} \\ \dfrac{\partial T_{21}^{kl}}{\partial r} & \dfrac{\partial^2 T_{21}^{kl}}{\partial r \partial z} \end{bmatrix} \tag{3.18}$$

Node (1,2):

$$\begin{bmatrix} a_{13}^{kl} & a_{14}^{kl} \\ a_{23}^{kl} & a_{24}^{kl} \end{bmatrix} = \begin{bmatrix} T_{12}^{kl} & \dfrac{\partial T_{12}^{kl}}{\partial z} \\ \dfrac{\partial T_{12}^{kl}}{\partial r} & \dfrac{\partial^2 T_{12}^{kl}}{\partial r \partial z} \end{bmatrix} \tag{3.19}$$

Node (2,2):

$$\begin{bmatrix} a_{33}^{kl} & a_{34}^{kl} \\ a_{43}^{kl} & a_{44}^{kl} \end{bmatrix} = \begin{bmatrix} T_{22}^{kl} & \dfrac{\partial T_{22}^{kl}}{\partial z} \\ \dfrac{\partial T_{22}^{kl}}{\partial r} & \dfrac{\partial^2 T_{22}^{kl}}{\partial r \partial z} \end{bmatrix} \tag{3.20}$$

Therefore Eq.(3.12), expands to:

$$\begin{aligned} T^{kl}(r,z) = {} & T_{11}\phi_1\phi_1 + \frac{\partial T_{11}}{\partial z}\phi_1\phi_2 + \frac{\partial T_{11}}{\partial r}\phi_2\phi_1 + \frac{\partial^2 T_{11}}{\partial z \partial r}\phi_2\phi_2 \\ & + T_{12}\phi_1\phi_3 + \frac{\partial T_{12}}{\partial z}\phi_1\phi_4 + \frac{\partial T_{12}}{\partial r}\phi_2\phi_3 + \frac{\partial^2 T_{12}}{\partial z \partial r}\phi_2\phi_4 \\ & + T_{21}\phi_3\phi_1 + \frac{\partial T_{21}}{\partial z}\phi_3\phi_2 + \frac{\partial T_{21}}{\partial r}\phi_4\phi_1 + \frac{\partial^2 T_{21}}{\partial z \partial r}\phi_4\phi_2 \\ & + T_{22}\phi_3\phi_3 + \frac{\partial T_{22}}{\partial z}\phi_3\phi_4 + \frac{\partial T_{22}}{\partial r}\phi_4\phi_3 + \frac{\partial^2 T_{22}}{\partial z \partial r}\phi_4\phi_4 \end{aligned} \tag{3.21}$$

3.3 Solution of the axial flow profile

As described in Section 2.3.3, wall channelling can influence the heat transfer in a small scale packed bed used for TES. Meier et al. (1991) state that these effects are most prominent in packed beds with D/d_p ratios below 40. Experimental heat transfer data collected from laboratory scale packed beds is often at low D/d_p ratios due to practical constraints. One of the aims of the current research is to analyse the flow channelling profile to determine what effect it has on the heat transfer within a packed bed. The numerical solution of the axial flow profile is presented in this section.

The extended Brinkman equation, given by Eq.(2.32), is solved using a one-dimensional OCFE analysis, as described in Section 3.2.3. The superficial velocity profile and its associated radial derivatives within each finite element are approximated by:

$$U_z^k = \sum_{i=1}^{4} a_i^k \phi_i \tag{3.22}$$

The non-linear differential equation is satisfied exactly at the interior points, generating $2N_r$ non-linear algebraic equations.

$$\frac{\partial P}{\partial z} = -f_1 \sum_{i=1}^{4} a_i^k \phi_i - f_2 \left(\sum_{i=1}^{4} a_i^k \phi_i \right)^2 + \mu_{\text{eff}} \left(\frac{1}{\left(\Delta r^k\right)^2} \sum_{i=1}^{4} a_i^k \frac{\mathrm{d}^2 \phi_i}{\mathrm{d}v^2} + \frac{1}{r \Delta r^k} \sum_{i=1}^{4} a_i^k \frac{\mathrm{d}\phi_i}{\mathrm{d}v} \right) \tag{3.23}$$

The final two equations that are required for a solution are produced by collocating the two boundary points

$$\frac{\partial U_z(0)}{\partial r} = \frac{1}{\Delta r^k} \sum_{i=1}^{4} a_i^1 \frac{\mathrm{d}\phi_i(0)}{\mathrm{d}v} = a_2^1 \phi_2 = 0 \tag{3.24}$$

$$U_z(R) = \sum_{i=1}^{4} a_i^{N_r} \phi_i(1) = a_3^{N_r} \phi_3 = 0 \tag{3.25}$$

Thus there are $2N_r + 2$ simultaneous, non-linear algebraic equations that can be evaluated to determine the unknown series coefficients a_i^k. These non-linear algebraic equations are solved using an iterative technique. Once the superficial velocity profile is calculated, Eq.(3.26) is used to calculate the fluid mass flow rate. The axial pressure gradient is then adjusted and the velocity profile is solved again. This process continues until convergence of the specified and calculated mass flow rates is achieved.

$$\dot{m}_f = 2\pi \int_0^R \rho_f U_z r \, \mathrm{d}r \tag{3.26}$$

Figure 3.5 presents the superficial velocity profiles, normalised by the plug flow velocity U_z^*. The peak in velocity is located approximately half a particle diameter from the wall. Figure 3.5(a) shows the effect of μ_{eff} on the velocity profiles. Increasing the effective viscosity decreases the maximum velocity peak in the near wall region. The effective viscosity correlation of Giese et al. (1998), given by Eq.(2.37), increases as an exponential function of Reynolds number. Therefore as the Reynolds number increases the peak in the velocity profile decreases. Figure 3.5(b) shows the effect of Reynolds number of the velocity profile when using the Giese et al. (1998) correlation.

As the peak velocity in the near wall increases, the velocity in the core region of the packed bed decreases. This core velocity is important for accurately determining the speed that the axial thermocline moves through the packed bed. Figure 3.5(b) shows the calculated superficial velocity at the centre of the packed bed relative to the plug flow velocity. The D/d_p ratio is seen to play a dominant role in the reduction in core velocity. At low D/d_p ratios the near wall region extends further into the packed bed and therefore there is larger

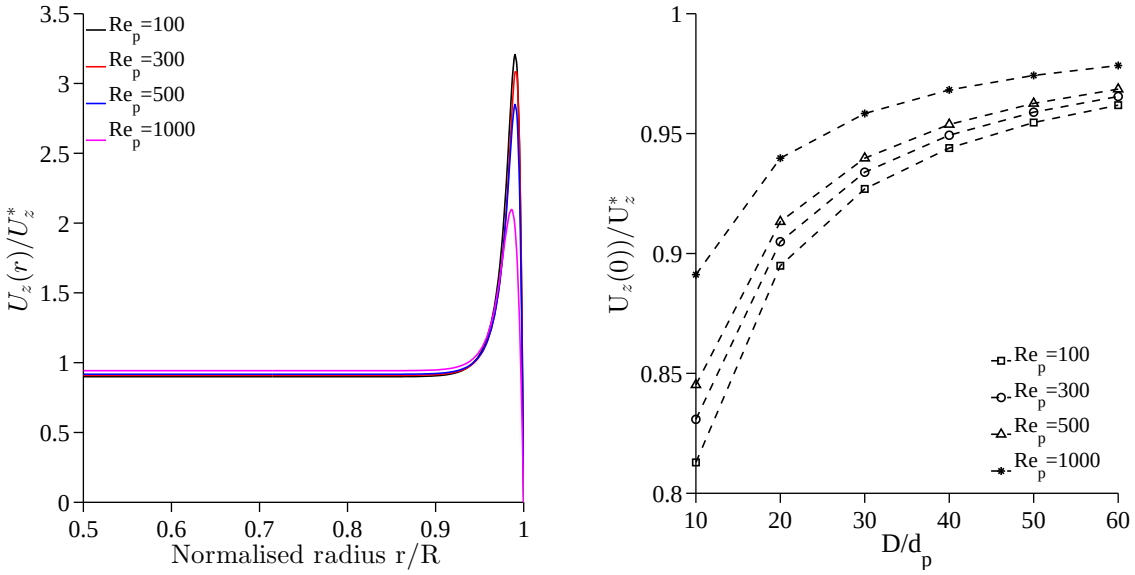

(a) Flow profile for D/d_p=21,

(b) Core superficial velocity

Figure 3.5: Wall channelling flow profile for $T_f = 775$ °C and $P = 87$ kPa

decrease in the core velocity. As the D/d_p ratio increases to large values the core velocity tends towards the plug flow velocity. It is of interest that even at D/d_p ratios above 40, which is the limit recommend by Meier et al. (1991), there remains a small decrease in core velocity (3-5%).

3.4 Solution of the governing heat transfer equations

3.4.1 Temporal discretisation

Due to the transient nature of the heat transfer analysis the governing equations must be discretised with respect to time. Temporal discretisation is achieved using an implicit finite difference method. A backward difference operator is implemented with a truncation error of $\mathbf{O}(\Delta t)$. In the transient analysis series coefficients are a function of time. A new set of series coefficients are calculated at each time step $n+1$ as a function of the previous solution field at time step n. The temporal terms are discretised as follows:

$$\frac{\partial T}{\partial t} = \frac{T^{n+1} - T^n}{\Delta t} + \mathbf{O}(\Delta t) \tag{3.27}$$

After discretisation the fluid energy equation, Eq.(2.19) is:

$$\frac{\varepsilon\rho_f^{n+1}c_f^{n+1}}{\Delta t}\left(T_f^{n+1}-T_f^n\right)+c_f^{n+1}G_z^{n+1}\frac{\partial T_f}{\partial z}^{n+1}=h_p^{n+1}a_p(T_s^{n+1}-T_f^{n+1})+\nabla\cdot\left(k_{\text{eff,f}}^{n+1}\nabla T_f^{n+1}\right) \tag{3.28}$$

and the discretised wall energy equation, Eq.(2.10) is:

$$\frac{\rho_w c_w^{n+1}}{\Delta t}\left(T_w^{n+1}-T_w^n\right)=\nabla\cdot\left(k_w\nabla T_w^{n+1}\right) \tag{3.29}$$

The discretised C-S solid phase energy equation Eq.(2.22) is:

$$\frac{(1-\varepsilon)\rho_s c_s^{n+1}}{\Delta t}\left(T_s^{n+1}-T_s^n\right)=h_p^{n+1}a_p(T_f^{n+1}-T_s^{n+1})+\nabla\cdot\left(k_{\text{eff,s}}^{n+1}\nabla T_s^{n+1}\right) \tag{3.30}$$

and the discretised D-C solid phase energy equation Eq.(2.23) is:

$$\frac{\rho_p c_p^{n+1}}{\Delta t}\left(T_p^{n+1}-T_p^n\right)=\frac{1}{r^2}\frac{\partial}{\partial r}\left(r^2k_p^{n+1}\frac{\partial T_p}{\partial r}^{n+1}\right) \tag{3.31}$$

The discretised continuity equation Eq.(2.11) is:

$$\varepsilon\frac{\rho_f^{n+1}-\rho_f^n}{\Delta t}+\frac{\partial G_z}{\partial z}^{n+1}=0 \tag{3.32}$$

The implicit time stepping requires an iterative approach to solve for the temperature dependent thermophysical properties of the fluid and solid materials, and their associated spatial derivatives. Appendix A provides the correlations used in the calculation of these properties. At each time step the solution is iterated until the required convergence is achieved. The temperature field at iteration $i+1$ is generated by solving the governing equations using the properties evaluated at iteration i. The physical properties are then updated using the new temperature field and the process is repeated until convergence. The spatial derivatives in physical properties such as $k_{\text{eff,s}}$, are evaluated by numerically differentiating the property field using cubic Hermite splines at iteration step i. The use of the Hermite basis functions ensures consistency with the numerical method used to solve the governing equations. This is important in maintaining the conservation of energy.

3.4.2 Spatial discretisation

Subsequent to the temporal discretisation, the OCFE method as outlined above in Section 3.2 is then applied to solve the coupled fluid, solid and wall temperature fields. As an example the fluid phase solution is described in this section. Appendix B provides further details of the discretised equations for all of the phases. Equation (3.28) is rewritten as:

$$A_f T_f^{n+1} + B_f \frac{\partial T_f}{\partial z}^{n+1} + C_f \frac{\partial^2 T_f}{\partial z^2}^{n+1} + D_f \frac{\partial^2 T_f}{\partial r^2}^{n+1} + E_f \frac{\partial T_f}{\partial r}^{n+1} + F_f T_s^{n+1} = T_f^n \quad (3.33)$$

where:

$$A_f = 1 + \frac{h_p^{n+1} a_p \Delta t}{\varepsilon \rho_f^{n+1} c_f^{n+1}} \quad (3.34)$$

$$B_f = \frac{\Delta t}{\varepsilon \rho_f^{n+1} c_f^{n+1}} \left(c_f^{n+1} G_z^{n+1} - \frac{\partial k_{\text{eff,fz}}^{n+1}}{\partial z} \right) \quad (3.35)$$

$$C_f = -\frac{k_{\text{eff,fz}}^{n+1} \Delta t}{\varepsilon \rho_f^{n+1} c_f^{n+1}} \quad (3.36)$$

$$D_f = -\frac{k_{\text{eff,fr}}^{n+1} \Delta t}{\varepsilon \rho_f^{n+1} c_f^{n+1}} \quad (3.37)$$

$$E_f = -\frac{\Delta t}{\varepsilon \rho_f^{n+1} c_f^{n+1}} \left(\frac{k_{\text{eff,fr}}^{n+1}}{r} + \frac{\partial k_{\text{eff,fr}}^{n+1}}{\partial r} \right) \quad (3.38)$$

$$F_f = -\frac{h_p^{n+1} a_p \Delta t}{\varepsilon \rho_f^{n+1} c_f^{n+1}} \quad (3.39)$$

The two-dimensional collocation procedure is then carried out at the four interior nodes of each finite element. These equations are given by:

$$\begin{aligned} &A_f \sum_{i=1}^{4}\sum_{j=1}^{4} a_{ij}^{kl} \phi_i \phi_j + \frac{B_f}{\Delta z^l} \sum_{i=1}^{4}\sum_{j=1}^{4} a_{ij}^{kl} \phi_i \frac{d\phi_j}{dw} + \frac{C_f}{\left(\Delta z^l\right)^2} \sum_{i=1}^{4}\sum_{j=1}^{4} a_{ij}^{kl} \phi_i \frac{d^2\phi_j}{dw^2} \\ &+ \frac{D_f}{\left(\Delta r^k\right)^2} \sum_{i=1}^{4}\sum_{j=1}^{4} a_{ij}^{kl} \frac{d^2\phi_i}{dv^2} \phi_j + \frac{E_f}{\Delta r^k} \sum_{i=1}^{4}\sum_{j=1}^{4} a_{ij}^{kl} \frac{d\phi_i}{dv} \phi_j + F_f T_s^{n+1} = T_f^n \end{aligned} \quad (3.40)$$

The boundary conditions are then collocated on the boundary nodes. For example the symmetry boundary condition at the bed centre is:

$$\frac{\partial T_f}{\partial r}^{n+1} = 0 \tag{3.41}$$

which in collocated form yields:

$$\frac{1}{\Delta r^1} \sum_{i=1}^{4} \sum_{j=1}^{4} a_{ij}^{1l} \frac{d\phi_i}{dv} \phi_j = \sum_{j=1}^{4} a_{2j}^{1l} \phi_j = 0 \tag{3.42}$$

All of the unknown coefficients are then solved in a coupled manner with the other phases, and the solution procedure is repeated.

Details of the finite element mesh used for each simulation are presented in Appendix C, including mesh dependency studies. Due to the fourth order accuracy of the finite elements, OCFE is an efficient method that yields accurate solutions even on relatively coarse meshes. This allows rapid approximate solutions that can be used in a future real time predictive capability for an operational TES.

3.4.3 Analytical validation for sensible heat storage

The numerical solutions to the C-S and D-C heat transfer models were compared to the Klinkenberg (1948) analytical solution to the Schumann equations for a simplified packed bed analysis. This one-dimensional analytical equation is accurate to the exact Schumann solution to within 0.6%, with an error that further decreases as the simulation progresses in time. The assumptions of the Schumann model are: (1) plug flow, (2), constant void fraction (3) no radial heat transfer, (4) constant thermophysical properties and (5) no dispersion in the fluid or solid phases. These assumptions were imposed on the C-S and D-C models to allow for a direct comparison of the results with the analytical solution. For the D-C model a very high value of thermal conductivity (1000 W/mK) was used for the particles, to ensure a uniform particle temperature. Details of the analytical model and validation are provided in Appendix D. As shown in Figure 3.6 the C-S and D-C models are in excellent agreement with the analytical solution.

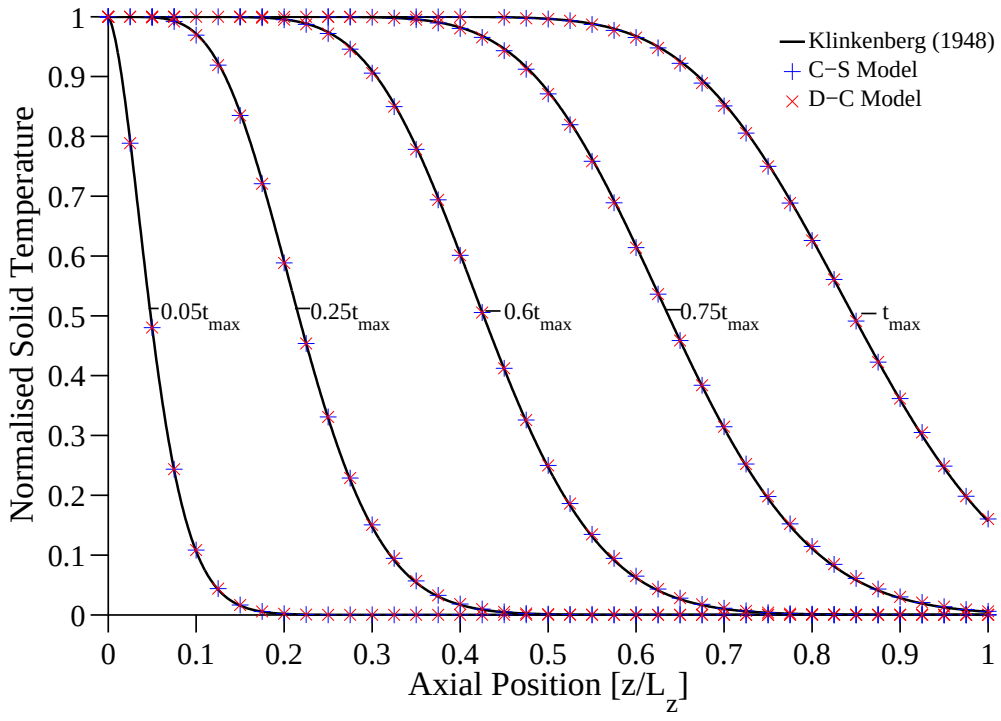

Figure 3.6: Comparison of the analytical and numerical solutions to the Schumann model; $\mathrm{Re}_p = 200$, $L_z = 2$, $d_p = 20$ mm

3.5 Solution of the phase change heat transfer

This section describes the numerical method utilised to solve the heat transfer within the EPCMs while undergoing a phase a change. Two numerical techniques exist for the solution of phase change problems, namely: variable grid and fixed grid methods. Variable grids involve tracking the phase change front as it moves through the PCM. Fixed grid methods handle the phase change process implicitly, which is suited to packed bed modelling. Therefore a fixed grid method is implemented in this work. Gong (1996) provides an extensive overview of fixed grid modelling methods, which may be classified according as: the effective heat capacity method, the enthalpy method and the source based method..

The effective heat capacity technique is utilised to solve the phase change problem. In this approach the latent heat of the PCM is approximated by an increase in the particle heat capacity over a small melting temperature range of ΔT_m. For PCMs that undergo an isothermal phase change, this method requires the assumption of a small artificial melting temperature

range. In its simplest form the effective heat of the PCM is given by:

$$c_{\text{PCM}} = \begin{cases} c_{s,\text{PCM}}, & \text{if } T_{\text{PCM}} \leq T_{m1} \\ \dfrac{\Delta h_{\text{fus}}}{\Delta T_m}, & \text{if } T_{m1} < T_{\text{PCM}} \leq T_{m2} \\ c_{l,\text{PCM}}, & \text{if } T_{m2} < T_{\text{PCM}} \end{cases} \tag{3.43}$$

where the temperature bounds of the PCM melting region are given by:

$$T_{m1} = T_m - 0.5\Delta T_m \tag{3.44}$$

$$T_{m2} = T_m + 0.5\Delta T_m \tag{3.45}$$

Convergence challenges are encountered in the effective heat capacity method due to temperature oscillations. Various authors such as Pham (1986); Lemmon (1981); Comini et al. (1974) have proposed alternative formulations for the effective heat capacity. However, as described by Gong (1996), some of these methods still lead to non-convergence when implemented with implicit, iterative time stepping schemes. Gong's analysis showed that non-convergence is caused by heat capacity formulations that are non-conservative. Therefore, in the current work the conservative effective heat capacity method, proposed by Gong (1996), is utilised. This method is explained in detail below for the case of the EPCM particle melting. As shown in Figure 3.7 there exist six possible conditions for the melting of the PCM. In order to maintain a conservative scheme, the energy absorbed by the PCM is calculated by evaluating area under the heat capacity-temperature curve.

The Gong method assumes that the solid and liquid heat capacities of the PCM are constant. This is a good approximation for the liquid heat capacity of the PCMs considered in this work. In the solid phase the PCM particles undergo large temperature changes and therefore exhibit variations in heat capacity. Therefore the conservative heat capacity method was extended to include linear variations in the PCM solid heat capacity. The solid heat capacity at time steps n and $n+1$ is evaluated by:

$$c_{s,\text{PCM}}^{n+1} = p_1 T_{\text{PCM}}^{n+1} + p_0 \tag{3.46}$$

$$c_{s,\text{PCM}}^{n} = p_1 T_{\text{PCM}}^{n} + p_0 \tag{3.47}$$

where $p_{0,1}$ are coefficients based on a linear fit with experimental data. The heat capacity of the solid at the start of the melting region is denoted by $c_{s,\text{PCM}}^{*}$ and is calculated by:

$$c_{s,\text{PCM}}^{*} = p_1 T_{m1} + p_0 \tag{3.48}$$

In Figure 3.7 the energy absorbed is calculated from the area under the heat capacity-temperature curve. The width of the phase change region in this figure is exaggerated to demonstrate the numerical method. The following equations are used to calculate the energy absorbed by the PCM:

Figure 3.7(a) describes remaining in the solid region where $T_{\mathrm{PCM}}^{n} \leq T_{m1}$ and $T_{\mathrm{PCM}}^{n+1} \leq T_{m1}$. The energy absorbed by the PCM is:

$$\frac{\partial h_{\mathrm{PCM}}}{\partial t} = \frac{1}{\Delta t} \frac{c_{s,\mathrm{PCM}}^{n+1} + c_{s,\mathrm{PCM}}^{n}}{2} \left(T_{\mathrm{PCM}}^{n+1} - T_{\mathrm{PCM}}^{n} \right) \tag{3.49}$$

Figure 3.7(b) describes stepping into the phase change region where $T_{\mathrm{PCM}}^{n} \leq T_{m1}$ and $T_{m1} < T_{\mathrm{PCM}}^{n+1} \leq T_{m2}$. The energy absorbed by the PCM is calculated by:

$$\frac{\partial h_{\mathrm{PCM}}}{\partial t} = \frac{1}{\Delta t} \left(\frac{c_{s,\mathrm{PCM}}^{*} + c_{s,\mathrm{PCM}}^{n}}{2} \left(T_{m1} - T_{\mathrm{PCM}}^{n} \right) + \frac{\Delta h_{\mathrm{fus}}}{\Delta T_{m}} \left(T_{\mathrm{PCM}}^{n+1} - T_{m1} \right) \right) \tag{3.50}$$

Figure 3.7(c) describes skipping over the phase change region where $T_{\mathrm{PCM}}^{n} \leq T_{m1}$ and $T_{m2} < T_{\mathrm{PCM}}^{n+1}$. The energy absorbed by the PCM is calculated by:

$$\frac{\partial h_{\mathrm{PCM}}}{\partial t} = \frac{1}{\Delta t} \left(\frac{c_{s,\mathrm{PCM}}^{*} + c_{s,\mathrm{PCM}}^{n}}{2} \left(T_{m1} - T_{\mathrm{PCM}}^{n} \right) + \Delta h_{\mathrm{fus}} + c_{l,\mathrm{PCM}} \left(T_{\mathrm{PCM}}^{n+1} - T_{m2} \right) \right) \tag{3.51}$$

Figure 3.7(d) describes remaining in the phase change region where $T_{m1} < T_{\mathrm{PCM}}^{n} \leq T_{m2}$ and $T_{m1} \leq T_{\mathrm{PCM}}^{n+1} < T_{\mathrm{PCM}}^{n+1}$. The energy absorbed by the PCM is calculated by

$$\frac{\partial h_{\mathrm{PCM}}}{\partial t} = \frac{1}{\Delta t} \frac{\Delta h_{\mathrm{fus}}}{\Delta T_{m}} \left(T_{\mathrm{PCM}}^{n+1} - T_{\mathrm{PCM}}^{n} \right) \tag{3.52}$$

Figure 3.7(e) describes stepping out of the phase change region where $T_{m1} < T_{\mathrm{PCM}}^{n} \leq T_{m2}$ and $T_{m2} < T_{\mathrm{PCM}}^{n+1}$. The energy absorbed by the PCM is calculated by

$$\frac{\partial h_{\mathrm{PCM}}}{\partial t} = \frac{1}{\Delta t} \left(\frac{\Delta h_{\mathrm{fus}}}{\Delta T_{m}} \left(T_{m2} - T_{\mathrm{PCM}}^{n} \right) + c_{l,\mathrm{PCM}} \left(T_{\mathrm{PCM}}^{n+1} - T_{m2} \right) \right) \tag{3.53}$$

Figure 3.7(f) describes remaining in the liquid region where $T_{m2} < T_{\mathrm{PCM}}^{n}$ and $T_{m2} < T_{\mathrm{PCM}}^{n+1}$. The energy absorbed by the PCM is calculated by

$$\frac{\partial h_{\mathrm{PCM}}}{\partial t} = \frac{c_{l,\mathrm{PCM}}}{\Delta t} \left(T_{\mathrm{PCM}}^{n+1} - T_{\mathrm{PCM}}^{n} \right) \tag{3.54}$$

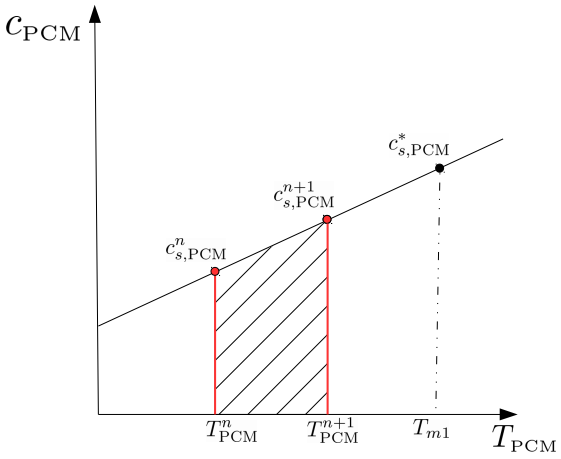

(a) solid region only

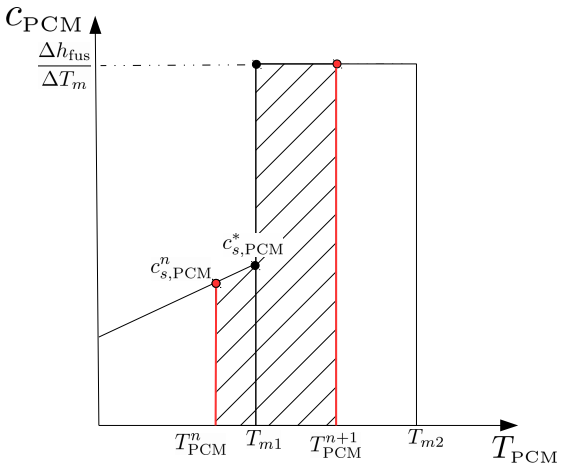

(b) stepping into the phase change region

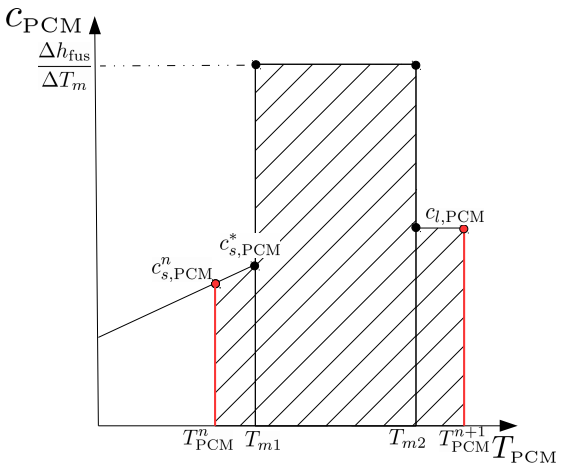

(c) skipping the phase change region

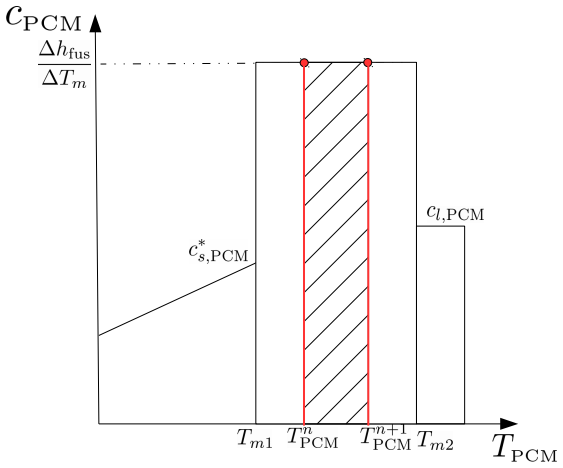

(d) phase change region only

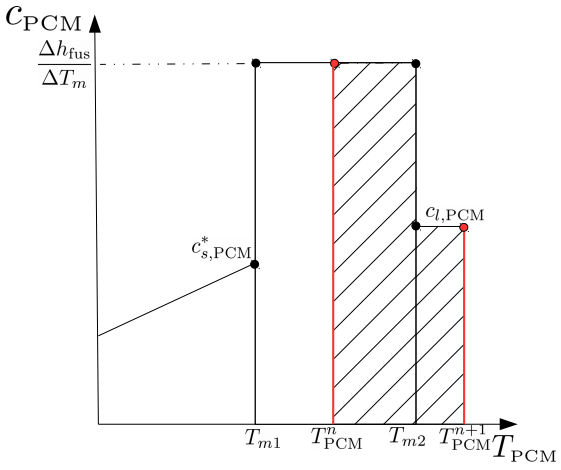

(e) stepping out of the phase change region

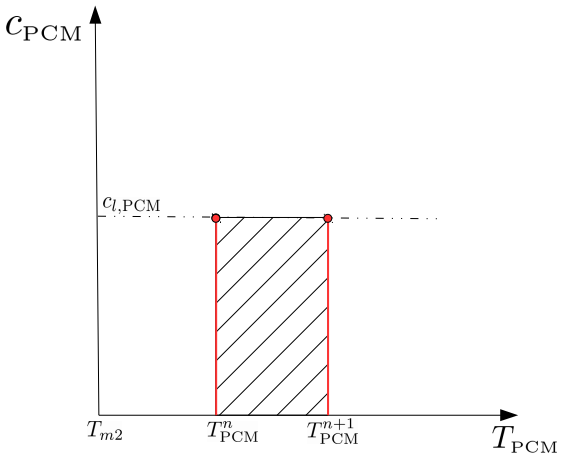

(f) liquid region only

Figure 3.7: Illustration of energy absorbed (shaded area) during melting of the PCM for possible combinations of T^{n}_{PCM} and T^{n+1}_{PCM}

The solid and liquid thermal conductivities of the PCM are modelled as constant in each phase. The recirculation of the liquid PCM, due to buoyancy forces, increases the rate of heat transfer through the PCM and can be modelled using an enhanced effective thermal conductivity model (Mathur et al., 2014). In this study the correlation provided by Xia et al. (2010) is implemented, to model the natural convection, where:

$$\frac{k_{l,\text{eff}}}{k_{l,\text{PCM}}} = 0.18\text{Ra}_p{}^{0.25} \tag{3.55}$$

According to Wu et al. (2014) the particle Rayleigh number is calculated by:

$$\text{Ra}_p = \frac{g\beta_{\text{PCM}}\left(T_{\text{sh}} - T_m\right)\left(d_p/2\right)^3}{\nu_{\text{PCM}}\alpha_{l,\text{PCM}}} \tag{3.56}$$

The numerical procedure for calculating the thermal conductivity of the PCM is based on the temperature of the PCM and is calculated as:

$$k_{\text{PCM}} = \begin{cases} k_{s,\text{PCM}}, & \text{if } T_{\text{PCM}} \leq T_{m1} \\ \dfrac{k_{s,\text{PCM}} - k_{l,\text{eff}},}{\Delta T_m}\left(T_{\text{PCM}} - T_{m1}\right) + k_{s,\text{PCM}}, & \text{if } T_{m1} < T_{\text{PCM}} \leq T_{m2} \\ k_{l,\text{eff}}, & \text{if } T_{m2} < T_{\text{PCM}} \end{cases} \tag{3.57}$$

3.5.1 Analytical validation for latent heat storage

The Neumann solution to the two-phase Stefan problem provides an excellent test case to validate the accuracy of the apparent heat capacity method implemented in this work. The two-phase Stefan problem models the conduction heat transfer in a semi-infinite slab undergoing a phase change. Figure 3.8 shows the problem layout for the melting and freezing of a PCM. During the melting of the PCM the solid slab is at an initial uniform temperature lower than the melting temperature of the PCM. The temperature at the wall is then raised to be higher than the melting temperature of the PCM. This initiates a phase change front that propagates through the material over time. The thermophysical properties of the liquid and solid regions are distinct, but constant over each region. The numerical solution to the Stefan problem is provided in Appendix D.

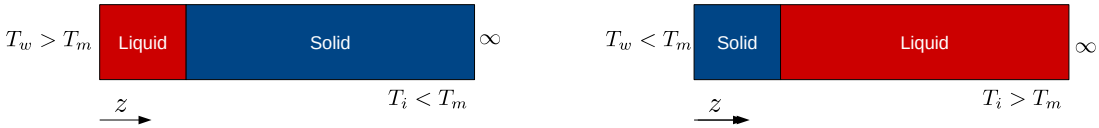

(a) Melting (b) Freezing

Figure 3.8: Stefan problem for the melting and solidification of a PCM

Figure 3.9 shows a comparison between the numerical and analytical solutions for the melting case of the Stefan problem. The results show that the phase change heat transfer is accurately modelled by the apparent heat capacity method. The PCM considered in this study is representative of an inorganic salt. The PCM is initially at a temperature ($T_m - 100$ °C), when the wall temperature is raised ($T_m + 100$ °C) at time $t = 0$.

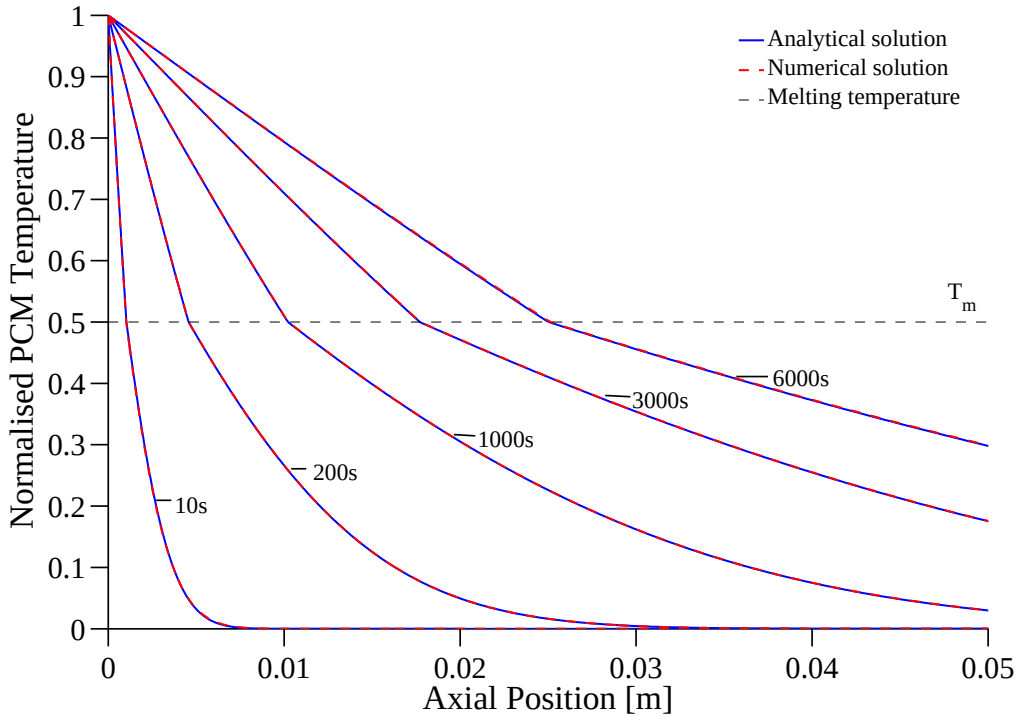

Figure 3.9: Comparison of the analytical and numerical solutions to the Stefan problem for a 200 °C melting range; $\alpha_{s,\mathrm{PCM}}$=2.98x10^{-7}m^2/s, $\alpha_{l,\mathrm{PCM}}$=2.19x10^{-7}m^2/s, St$_s$=0.90, St$_l$=0.86

3.6 Conclusions

Due to the complexity of the governing heat transfer and fluid flow equations a numerical solution is required. An implicit time stepping approach was implemented to discretise the transient terms in the C-S and D-C models. Spatial discretisation of the governing heat transfer and fluid flow equations was achieved using the numerical technique of OCFE, which allows for an efficient numerical solution. This chapter provided a general introduction to the OCFE methodology as well as its direct application to solving the governing equations considered in this study. The C-S and D-C heat transfer models were validated against the Klinkenberg (1948) analytical solution to the Schumann heat transfer model. The apparent heat capacity method was introduced to model the phase change for the EPCM particles. This approach was validated against the analytical solution to the Stefan problem.

Chapter 4

Experimental apparatus and method

4.1 Introduction

In order to validate the heat transfer modelling, a high temperature packed bed test facility was developed. The facility was designed to study the transient temperature profiles within a packed bed of ceramic or EPCM particles under forced convection conditions. This chapter details the design and operation of the experimental apparatus, including a description of the instrumentation utilised. Section 4.2 describes the high temperature packed bed test facility that was developed for this study. The sensible heat materials and testing are outlined in Section 4.3. The development of EPCM particles consisting of sodium sulphate (Na_2SO_4) is presented in Section 4.4.

4.2 Packed bed test facility

The laboratory scale test facility was developed to generate transient temperature profiles within a packed bed thermal storage system at atmospheric pressure. A diagram of the test facility is shown in Figure 4.1. The primary components included a blower, Liquefied Petroleum (LP) gas burner system and packed bed test section. Cold air was drawn into the system through a differential pressure flow meter. The cold air was then heated to the required temperature through the combustion of LP gas (in excess air) in the burner system. The high temperature flue gas was directed through the packed bed in order to transfer thermal energy to the packed particles. Due to the design of the system the flow direction could not be reversed during cooling. Therefore the bed was cooled in co-current heat recovery

mode. For comparison of the model with experimental data, the air properties were modified to account for the presence of combustion products in the flue gas stream. The calculation of the flue gas composition is outlined in Appendix A. Once the flue gas composition was calculated the software DeskTop Gas (available from www.techwareeng.com) was used to calculate the relevant gas properties. The fuel/air ratio of the burner was calculated by making regular mass measurements of the LP gas supply bottle.

The cylindrical test section had an internal diameter of 400 mm and was manufactured from 0.9 mm thickness Nimonic sheet metal. This material has an excellent resistance to oxidation at temperatures up to 1000 °C. The use of a thin metal wall is preferable to the approach of installing a refractory lining with a large thermal mass, as utilised by Nsofor (2005). High temperature ceramic gaskets were used to seal the flanged connections in the test facility. The particles were supported by a stainless steel mesh at the base of the packed bed. The test section was insulated with 150 mm thick ceramic fibre blanket insulation. Photographs of the test section with and without insulation are shown in Figure 4.2.

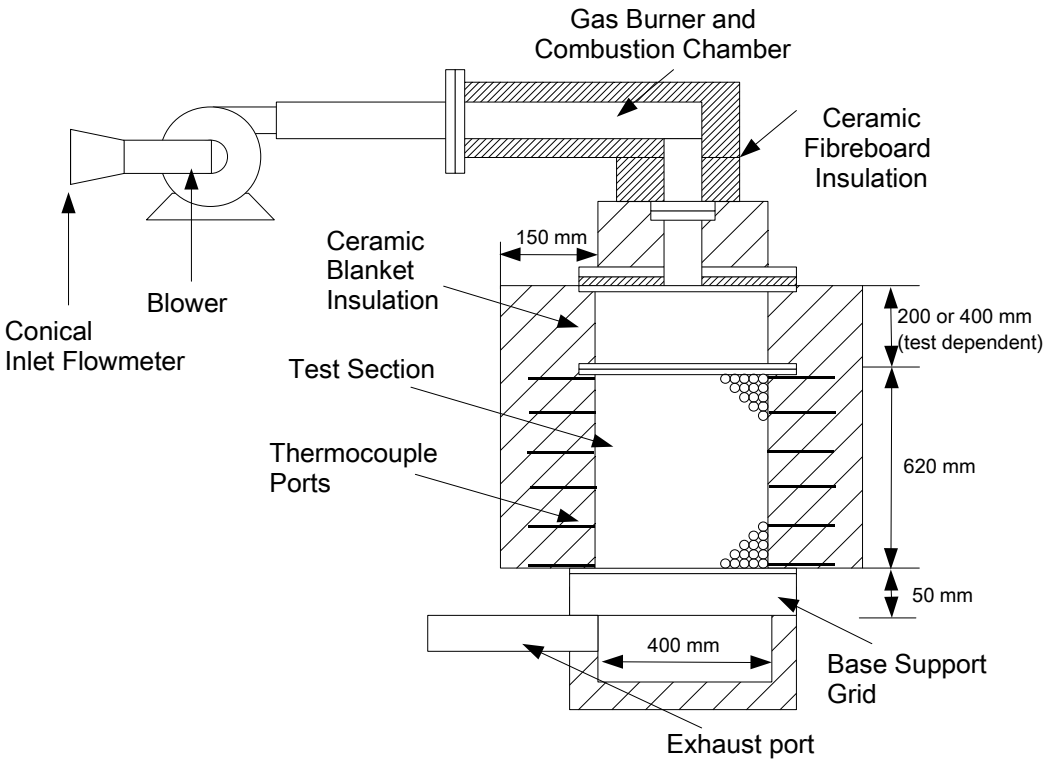

Figure 4.1: Diagram of the high temperature packed bed test facility (Klein et al., 2014)

(a) Nimonic test section with thermocouples installed

(b) Insulated test section

Figure 4.2: Photographs of the high temperature packed bed test facility

The mass flow rate through the blower was not regulated, instead the gas burner power was controlled to maintain the desired inlet air temperature. The air mass flow rate through the system was measured using a conical inlet, placed at the inlet to the packed bed blower. The conical inlet was manufactured according to the BS 848 standard (BSI, 2008). The geometry according to the standard is shown in Figure 4.3. An inlet diameter of 33 mm was chosen to ensure that the Reynolds number was above 20 000, which is a requirement from the BS 848 standard. In order to determine the mass flow rate, a differential pressure measurement was made between atmospheric pressure and the static pressure in the throat of the conical inlet. Due to equipment constraints two types of digital micromanometers were used during the sensible and latent heat testing campaigns. These were a DPM TT series and Air Ltd MP3KDS micromanometer. Both micromanometers were calibrated against a 5 kPa Betz manometer with a minimum pressure increment of 2 Pa. The mass flow rate is calculated according to:

$$\dot{m}_f = C_d \pi \frac{d_c^2}{4} \sqrt{2\rho_f \Delta P_c} \tag{4.1}$$

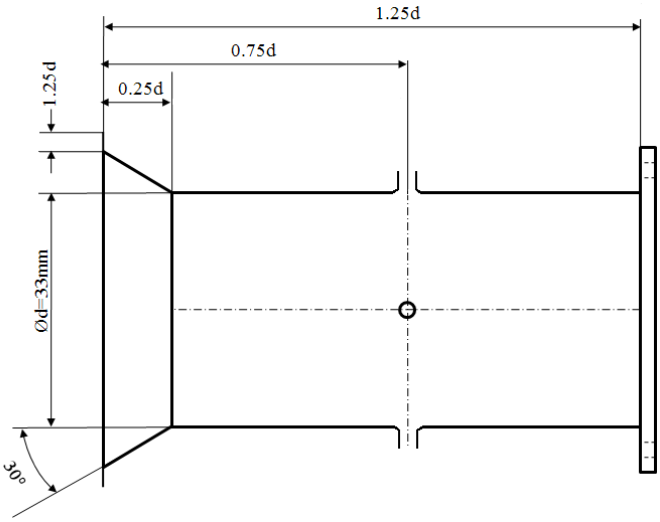

Figure 4.3: BS 848 geometry for the conical Inlet

The compound discharge coefficient C_d is Reynolds number dependent and is calculated using the following equation for an inlet diameter less than 0.5 m (BSI, 2008):

$$C_d = 0.01 \log_{10} \mathrm{Re}_c + 0.887 \tag{4.2}$$

Flow measurements were also conducted using a BS1042 orifice plate (BSI, 1981). The flow rate measurement was made between the blower outlet and the inlet to the LP gas burner system. This arrangement had a lower pressure drop than the conical inlet setup and allowed for an increase in the test flow rate. The sensible heat testing (heating and cooling) over the temperature ranges 20-600 °C and 600-900°C utilised the orifice plate, while all other sensible heat and latent heat tests utilised the conical inlet. An uncertainty analysis on the calculated mass flow rate for each experiment is presented in Appendix E. A numerical analysis is in also presented in Appendix E to demonstrate what the effect the uncertainty in mass flow rate has on the thermocline predictions from the modelling.

The National Instruments CompactDAQ (NI, 2014) system was used in conjunction with Labview SignalExpress (NI, 2004) to log the Type-K thermocouple signals from the packed bed and ambient surroundings. Two National Instruments 16 channel thermocouple cards (NI 9213) were used in the CompactDAQ chassis. These cards provided on-board cold junction compensation and 24 bit resolution of the analogue signal. Validation tests were performed on the thermocouples using a Fluke Thermocouple Furnace. The thermocouples were heated to a maximum temperature of 1000 °C. The measured temperature values were compared to the furnace readout, in order to verify that the readings were accurate to within standard Type-K thermocouple error limits (0.75% of the temperature reading in degrees Cel-

sius). The uncertainty on the thermocouple readings was taken as the standard thermocouple error for Type-K thermocouples.

One characteristic of the gas burner system was condensation during the initial phase of heating the packed bed. The flue gas from the burner contained water vapour which condensed on the cold particles in the packed bed. As shown in Figure 4.4 this caused a short thermal pulse to move through the packed bed at the dew point temperature of the flue gas. The packed bed was initially at a temperature of 15 °C but was rapidly heated to 32 °C due to the condensation.The small change in bed temperature was not found to noticeably influence the results.

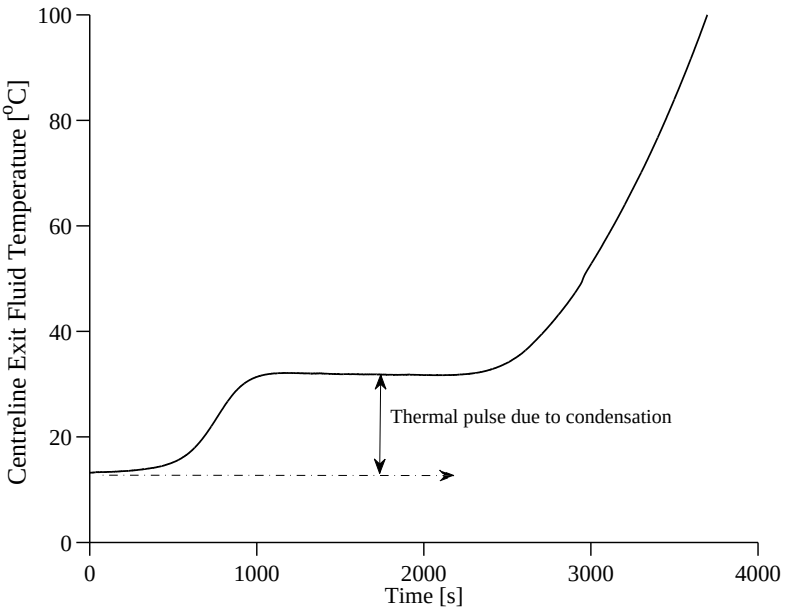

Figure 4.4: Thermal pulse observed at the packed bed exit during charging at 500°C

4.3 Sensible heat storage testing

4.3.1 Material properties

Sensible heat tests were conducted using 19 mm Denstone 2000 particles provided by Saint-Gobain NorPro (Norton, 1997). These alumino-silicate particles, shown in Figure 4.5, consist of 74.2% SiO_2, 19.2% Al_2O_3 and 6.6% other metal oxides and impurities. The Denstone product range has been designed as support media for catalyst beds and it is used in the refining, chemical and petrochemical engineering industries. The Denstone 2000 particles are able to withstand high rates of heat transfer. Samples were repeatedly heated to 600 °C and

then rapidly quenched in water, without any detectable deterioration or cracking. The particles have a maximum operating temperature of 982 °C and a particle density of 2200 kg/m^3. The 19 mm particles have a crush strength of 5.4 kN. Saint Gobain NorPro were able to provide data on the temperature dependent heat capacity and thermal conductivity of the Denstone particles. These properties are shown in Figure 4.6. Unfortunately the uncertainties associated with these property measurements could not be provided.

Figure 4.5: Denstone 2000 ceramic pebbles in test section

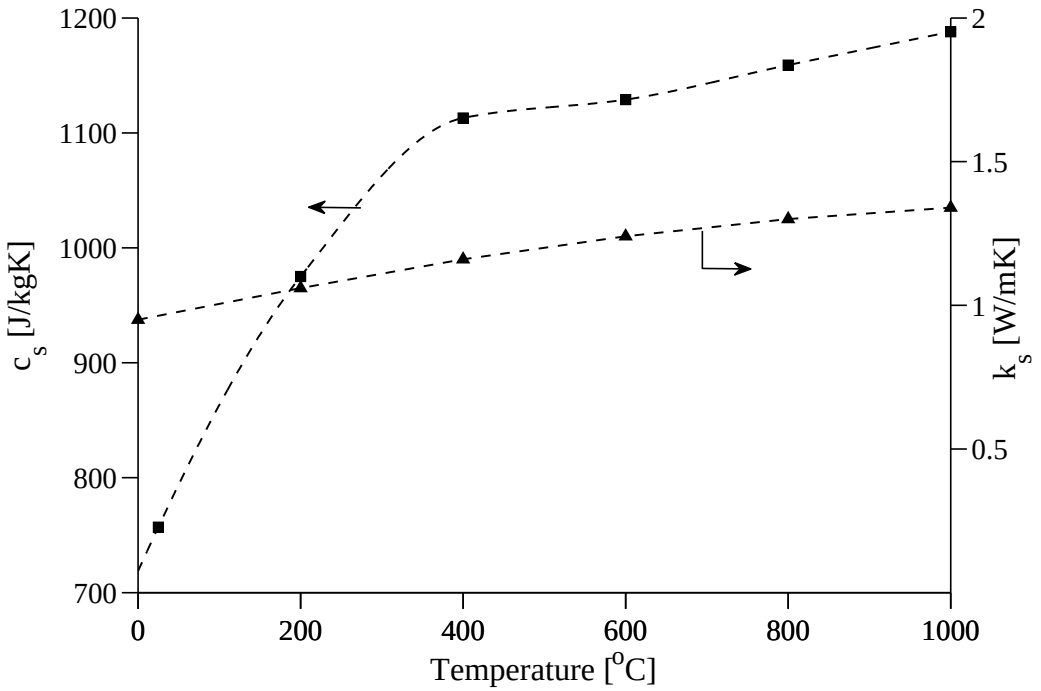

Figure 4.6: Temperature dependent specific heat capacity and thermal conductivity of the Denstone particles (Saint Gobain, personal communication Feb 27, 2012)

4.3.2 Low temperature sensible heat storage testing

Initial sensible heat testing was conducted at low temperature (160 °C) to study the convective heat transfer in the packed bed in the absence of radiation. As described by Balakrishnan and Pei (1979), radiation effects in the packed bed only need to be taken into account at temperatures above 250-300 °C. The test section for the initial testing was constructed from five Nimonic pipe sections, each of length 0.2 m and diameter 0.4 m. These pipe sections were bolted together to form the packed bed wall. The bed was packed to a depth of $L_z = 0.8$ m using the Denstone particles. Flanged sections were used to allow the large number of thermocouple wires to be placed inside the bed at set intervals with relative ease. High temperature ceramic gaskets were used at each flange connection and the packed bed was insulated with ceramic fibre blanket of 100 mm thickness. No preheating of the packed bed was completed for the low temperature testing. The packed bed was charged from an initial ambient temperature and then cooled with air at an ambient temperature.

A total of 24 Type-K thermocouples were placed in the packed bed for the low temperature testing. Ten thermocouples were used to measure the fluid temperatures at different axial and radial positions in the packed bed. Fourteen thermocouples were used to measure the axial and radial temperature profiles of the solid particles. The layout of thermocouples was aimed at resolving the axial thermocline along the centreline of the packed bed and also the radial temperature profiles at two levels in the bed. The positions of the thermocouple measurements are presented in Figure 4.7.

The measurement of the solid phase temperature required the insertion of a thermocouple into a solid particle. Initial attempts to drill into the brittle Denstone particles were unsuccessful. Therefore the solid phase temperature was measured using 19 mm stainless steel ball bearings. A small hole was spark eroded into each measurement particle and a thermocouple inserted. The ball bearings have a higher thermal conductivity than the Denstone particles, which helps to ensure that the thermocouple measures an average particle temperature. The ball bearings also have a higher heat capacity than the Denstone particles. Therefore the properties of the ball bearings were taken into account at each measurement position in the numerical modelling. This was done by modifying the heat capacity and density of the material at each position in the solid measurement location.

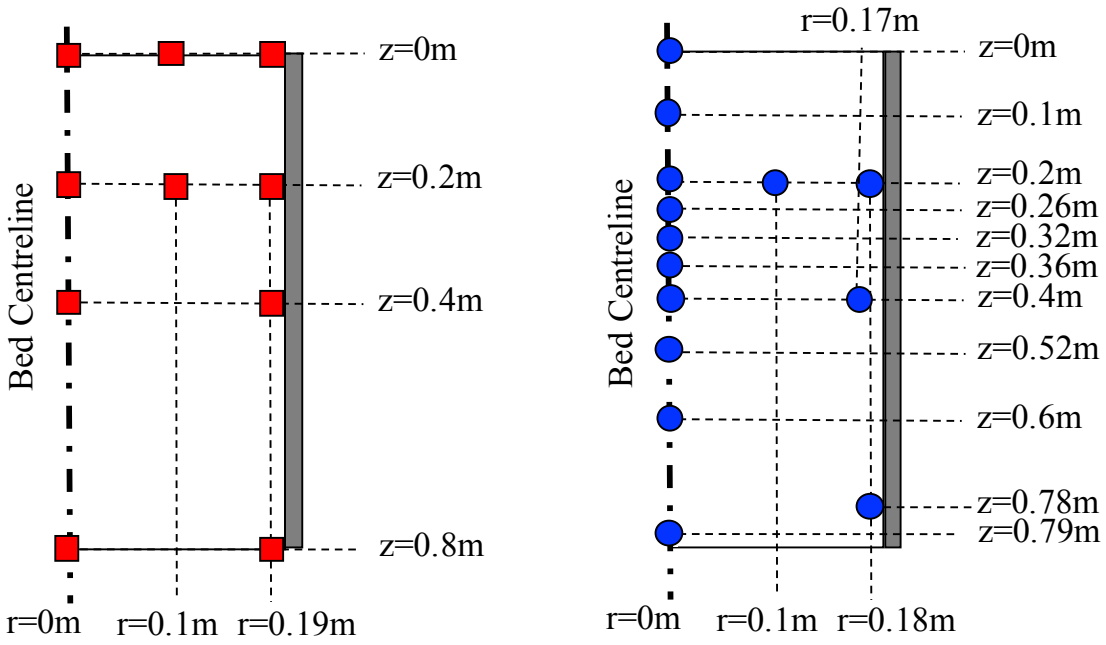

(a) Fluid phase

(b) Solid phase

Figure 4.7: Thermocouple layout for the low temperature, sensible heat storage testing

4.3.3 High temperature sensible heat storage testing

Subsequent testing was conducted at high temperature to generate packed bed temperature profiles across the operating temperature ranges of potential recuperated and non-recuperated gas turbine cycles. Detailed thermocline measurements from within a packed bed TES, across these temperature ranges, were not previously available in the literature consulted. In heating a packed bed to high temperatures (900 °C), alumino-silicate ceramics undergo large changes in specific heat capacity between ambient and 350 °C. However these changes are not significant over the temperature ranges of gas turbine cycles. Table 4.1 shows the normalised changes in solid heat capacity of the Denstone particles, over the temperature ranges considered in this study. These normalised changes were calculated using Eq.(4.3). The data presented in Table 4.1 shows the benefits of preheating the packed bed to above 350 °C before testing.

$$\Delta c_s = \frac{\mid c_s(T_s^{\max}) - c_s(T_s^{\min}) \mid}{c_s(T_s^{\text{avg}})} \times 100\% \tag{4.3}$$

Two important modifications were made to the packed bed test facility for the high temperature testing. These included changes to the gas burner system and the packed bed test section. The gas burner was upgraded to a 45 kW_{th} system capable of achieving a maximum flue gas

Table 4.1: Percentage variation in specific heat capacity, calculated using Eq.(4.3)

Material	25-350°C [%]	25-600°C [%]	25-900°C [%]	350-900°C [%]	600-900°C [%]
Air	5.0	10.5	15.2	10.1	4.8
Denstone	33.9	36.0	36.7	7.3	2.4

temperature of 1000 °C. The low temperature testing showed that the thermal capacitance of the wall flanges influenced the temperature measurements in the near wall region. For this reason the test section was redesigned to be a single section of Nimonic pipe of 0.4 m diameter. Due to the length of time required to preheat the packed bed and conduct testing at high temperature the length of the bed was reduced from $L_z = 0.8$ m to $L_z = 0.62$ m for further testing. The bed wall included welded thermocouple ports to allow thermocouple access. A high temperature sealant was used to ensure there was no leakage of flow between the thermocouples and the wall ports.

In order to generate thermal storage data covering the operating temperature ranges of gas turbine cycles the high temperature packed bed was preheated to 350 °C and 600 °C. Once the bed reached steady state, the inlet fluid temperature was raised to 900 °C. Preliminary high temperature tests were conducted at 1000 °C, but excessive degradation of the combustion chamber lining required the maximum test temperature to be reduced. Upon completion of the heating cycle, the cooling of the bed was initiated by reducing the inlet fluid temperature to either 350 °C or 600 °C. After the cooling cycle was complete, the gas burner was shut down and the bed cooled to ambient. A typical inlet fluid temperature profile for a 350-900 °C test is presented in Figure 4.8.

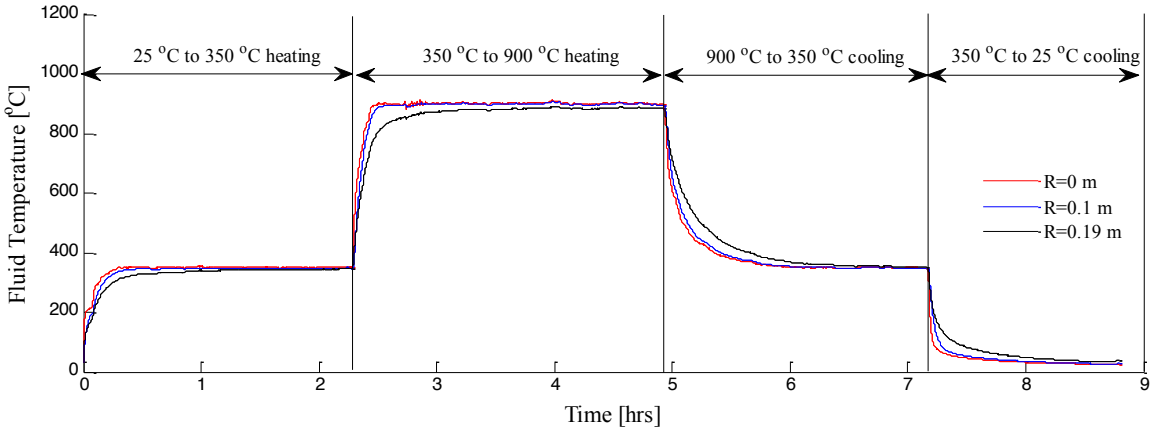

Figure 4.8: Inlet fluid temperature profile (Klein et al., 2014)

The fluid and solid temperatures were measured at seven axial levels within the packed bed using eighteen Type-K thermocouples. The temperature of the solid at the wall was measured at three of the axial levels to study the radial temperature profiles within the bed. The fluid and solid pebble thermocouples are shown in Figure 4.9. A perforated Nimonic tube was used to reduce the effects of radiation on the fluid thermocouples. Subsequent to the low temperature test campaign a method was developed to successfully drill into the brittle ceramic particles. This method involved the use of a specific diamond tipped drill bit for glass that did not cause cracking of the particles. Thermocouples were inserted into ten Denstone particles and sealed with a high alumina mortar. The layout of thermocouples is presented in Figure 4.10.

(a) Centre (b) Wall

Figure 4.9: Fluid and solid thermocouples in the packed bed (Klein et al., 2014)

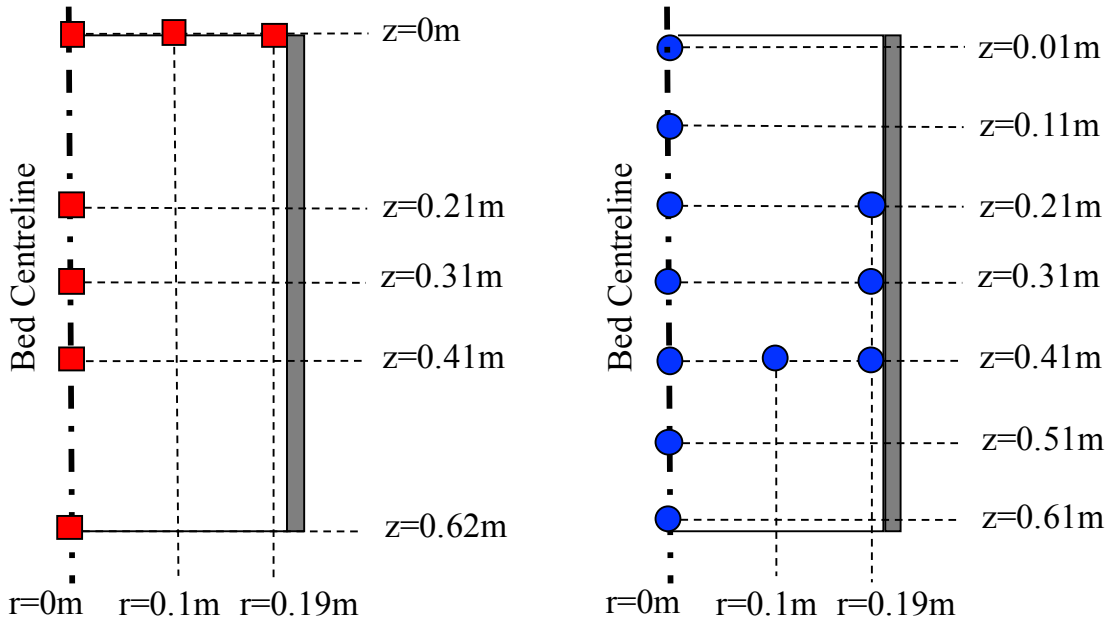

(a) Fluid phase (b) Solid phase

Figure 4.10: Thermocouple layout for the high temperature, sensible heat storage testing

4.4 Latent heat storage testing

This section describes the methods that were used to test latent heat storage in a packed bed of EPCM particles. The selection of a suitable high temperature PCM and compatible shell material are presented in Sections 4.4.1 and 4.4.2 respectively. The selection of an encapsulation technique is outlined in Section 4.4.3. Subsequent to the sensible heat testing, the test facility was further modified to include a diffuser at the inlet to the packed bed test section. The 400 mm long diffuser joined the 76 mm diameter pipe inlet to the 400 mm diameter test section.

4.4.1 Identification of suitable PCMs

Suitable high temperature PCMs were identified from the literature, based on melting temperature and latent heat of fusion. The melting temperature of the PCM should lie between 600-950 °C for the thermal storage system under consideration. Candidate materials include inorganic PCMs such as alkali-metal and alkaline-earth-metal fluoride, chloride, bromide, carbonate and sulphate salts, as well as metals and alloys. Table 4.2 lists the latent heat properties of various inorganic salts. The associated costs of various inorganic salt and metallic PCMs are shown in Tables 4.3 and 4.4 respectively.

Table 4.2: Properties of inorganic salt PCMs for high temperature TES (Kenisarin, 2010)

Metal	Fluoride	Sulphate	Carbonate	Chloride	Nitrate
			Melting Temperature [°C]		
Lithium	849	858	732	610	253
Potassium	858	1069	900	771	335
Sodium	996	884	858	801	307
Magnesium	1263	1137	990	714	426
Calcium	1418	1460	1330	772	560
			Latent heat of fusion [kJ/kg]		
Lithium	1041	84	509	416	373
Potassium	507	212	202	353	88
Sodium	794	165	279	482	177
Magnesium	938	122	698	454	N/A
Calcium	381	203	N/A	253	145

Table 4.3: Cost of inorganic salt PCMs based on Δh_{fus} only

Salt	T_m[1] [°C]	Δh_{fus}[1] [kJ/kg]	Cost [USD/kg]	Cost [USD/kW$_{\text{th}}$]
$NaNO_3$	308	177	0.2[2]	4.1
NaCl	801	482	0.15[2]	1.1
KCl	771	353	0.13[3]	1.3
Na_2CO_3	851	279	0.2[2]	2.6
K_2CO_3	891	202	0.6[2]	10.7
Na_2SO_4	884	165	0.26[4]	5.7
NaF	996	794	1.4[3]	6.3
KF	858	507	4.5[3]	32.0
LiF	849	1041	17[3]	59.8

[1] Kenisarin (2010)
[2] Herrmann and Kearney (2002)
[3] Mantz and de Electroquimica (2007)
[4] purchase price from CHC Resources in November 2013

Table 4.4: Cost of metallic PCMs based on Δh_{fus} only

Metal	T_m[1] [°C]	Δh_{fus}[1] [kJ/kg]	Cost[2] [USD/kg]	Cost [USD/kW$_{\text{th}}$]
Aluminium	660	397	2.2	19.9
Copper	1085	206	6.3	110.1
Silicon	1414	1789	3.2	6.4
Magnesium	650	369	1.9	18.5
Tin	232	59	18.2	1110.5
Lead	207	23	2.1	328.7
Zinc	420	113	2.3	73.3

[1] Barin et al. (1977)
[2] AMM (2015)

Recently metallic PCMs have been proposed as an alternative to inorganic salts, as they posses a high thermal conductivity and undergo a low volume expansion upon melting (less than 10%). These PCMs can be either pure metals such as aluminium or an alloy. The primary disadvantage of metallic PCMs is the higher cost of the material. Molten metals are also highly corrosive towards high temperature steel alloys. Due to the elevated cost of the metallic PCMs, inorganic salts were chosen for further research in this project. It is proposed that the high surface area of a packed bed of EPCMs can be used to negate the effects of the poor salt thermal conductivity. The sodium salts: NaCl, Na_2CO_3 and Na_2SO_4

were identified for further analysis as they are readily available at low cost. These salts have low material costs (0.15-0.26 USD/kg) with a latent heat of fusion ranging between 165-482 kJ/kg. Although fluoride salts have a higher latent heat capacity they were not considered due to their reactivity with engineering ceramic materials at high temperature.

Sodium sulphate ($T_m = 884$ °C) and sodium carbonate ($T_m = 858$ °C) have melting points closest to 950 °C and are therefore most applicable to the Brayton cycle TES. As described by Lide (2001), Na_2SO_4 will form a melt above 884 °C and will only decompose when heated to above 1100 °C. Thy and Jenkins (2006) analysed the thermal decomposition of $CaCO_3$, Na_2SO_4 and Na_2CO_3 and found that Na_2CO_3 shows appreciable decomposition just above the melting point. They heated a small sample of salt in a furnace to 1200 °C, and used a gas analyser to determine the decomposition of the material. The results showed that the maximum release of CO_2 for Na_2CO_3 occurs at 850 °C, indicating decomposition. In contrast Na_2SO_4 is stable below 1100 °C. Another benefit of Na_2SO_4 is that it has a very low vapour pressure once melted. Thus it will not easily evaporate from a micro-encapsulated system.

Table 4.5 shows the heat storage capacity of various sodium salts over the 600-950 °C temperature range, including sensible and latent heat energy stored. Although Na_2CO_3 has the highest overall heat capacity, it was not further considered due to decomposition and reaction problems. Even though Na_2SO_4 has a lower latent heat capacity than NaCl on a mass basis it has a higher volumetric heat capacity due to a higher density. Sodium sulphate also has a melting temperature that is closer to 950 °C than NaCl. Therefore Na_2SO_4 was chosen for further development. Anhydrous Na_2SO_4 was sourced locally from the company CHC Resources. The cost of the material in November 2013 was 2.75 ZAR/kg excluding taxes.

Table 4.5: Enthalpy change over 600-950°C temperature range for inorganic PCMs

Inorganic salt	$\rho_{s,\mathrm{PCM}}$ [g/cm^3]	$\rho_{l,\mathrm{PCM}}$[1] [g/cm^3] (950 °C)	$\rho_{s,\mathrm{PCM}}/\rho_{l,\mathrm{PCM}}$ [ ]	Δh_{PCM}[2] [kJ/kg] (600-950 °C)	$\rho_{l,\mathrm{PCM}}\Delta h_{\mathrm{PCM}}$ [MJ/m^3] (600-950 °C)
NaCl	2.17	1.48	1.47	871	1289
Na_2SO_4	2.66	2.04	1.30	660	1346
Na_2CO_3	2.54	1.93	1.32	835	1612

[1] Janz (1988)

[2] Barin et al. (1977)

Table 4.6 shows the energy storage density of alumino-silicate ceramic materials for comparison with the Na_2SO_4. On a mass basis Na_2SO_4 can store 660 kJ/kg, compared to 427 kJ/kg for the high alumina ceramic. However, the volumetric energy storage density of the Na_2SO_4 is 1346 MJ/m^3, compared to 1538 MJ/m^3 for the high alumina ceramic. Thus in order to store the same amount of energy, the Na_2SO_4 requires a 14.2 % increase in storage volume, resulting in increased containment costs. In comparison to the low alumina content ceramic, the Na_2SO_4 can achieve a potential 34.1% reduction in storage volume.

Table 4.6: Enthalpy change over 600-950°C temperature range for alumino-silicate ceramic materials

Inorganic salt	ρ_s [g/cm^3]	Δh_s [1] [kJ/kg]	$\rho_s \Delta h_s$ [MJ/m^3]
High alumina content	3.6	427	1538
Low alumina content	2.2	403	887

[1] Touloukian and Ho (1970*a*)

4.4.2 Compatibility of PCM and shell material

Due to the high temperature of the system and corrosive nature of the PCMs, only ceramic encapsulation materials were considered in this research. In order to analyse the stability of different salt/ceramic pairs an equilibrium composition analysis was conducted using the software HSC Chemistry 7 (Roine et al., 2009). The software determines the equilibrium composition using the Gibbs energy minimisation method. A 1:1 salt to ceramic mass ratio was used in the model. The results of this analysis are presented in Table 4.7. Figure 4.11(a) demonstrates how Na_2CO_3, for example although already discounted, will react with Al_2O_3 at temperatures above 300 °C. Thus this salt/ceramic pair is unstable and not viable. As shown in Figure 4.11(b) Na_2SO_4 and Al_2O_3 are stable across the 0-1000 °C temperature range and are therefore a viable working pair. The results of the equilibrium composition analysis are presented in Table 4.7. Alumina was chosen as the encapsulation material as it does not react with NaCl or Na_2SO_4. It is also a common engineering ceramic material.

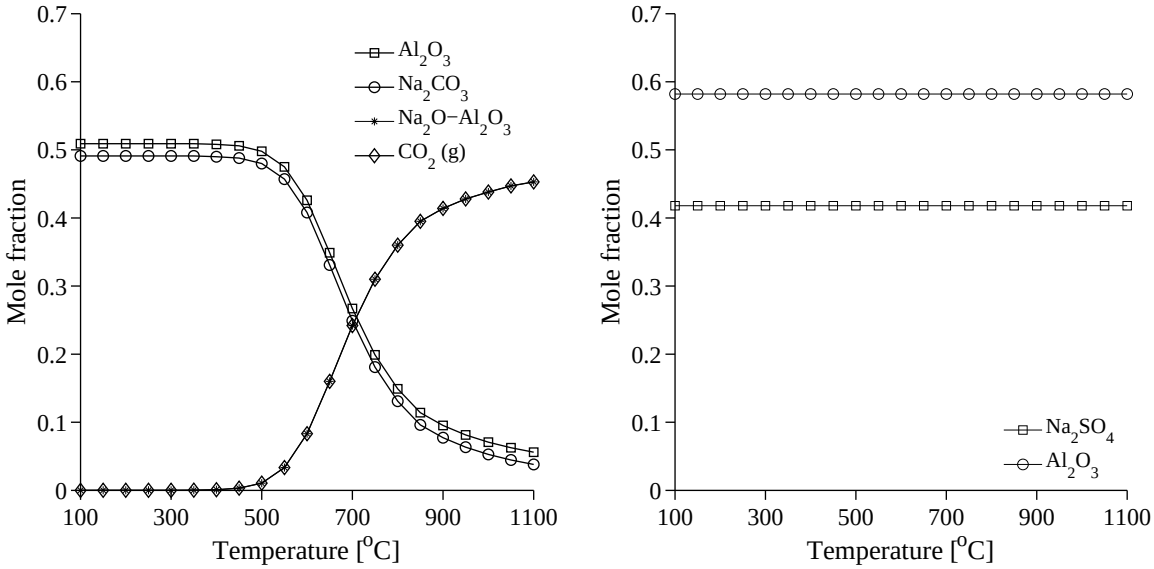

(a) Na_2CO_3 and Al_2O_3 (b) Na_2SO_4 and Al_2O_3

Figure 4.11: Equilibrium composition for 1:1 mass ratio of molten salts and alumina

Table 4.7: Results of the equilibrium composition analysis

	NaCl	Na_2CO_3	Na_2SO_4	NaF
Al_2O_3	✓	✗	✓	✗
MgO	✓	✓	✓	✓
SiO_2	✓	✗	✓	✗
ZrO_2	✓	✗	✓	✓

✓ no reaction ✗ reaction

4.4.3 Encapsulation of PCM

Figure 4.12 shows the EPCM concepts that were considered in this research. Two potential methods exist for encapsulating PCMs for latent heat storage in a packed bed. These are termed micro-encapsulation and macro-encapsulation. Micro-encapsulation technology involves the immobilisation of a PCM within the porous structure of a ceramic material. This is achieved by either infusing a porous ceramic with a molten PCM or by cold pressing and sintering a powdered mixture of the ceramic and PCM. As the composite material is heated/cooled the PCM melts/solidifies and absorbs/releases an increased amount of heat. The molten phase change material is retained within the ceramic pores by capillary and surface tension forces. The PCM to ceramic mass ratio is typically varied between 20-50% (Notter et al., 1993). Thus this system represents a combined sensible-latent heat storage concept.

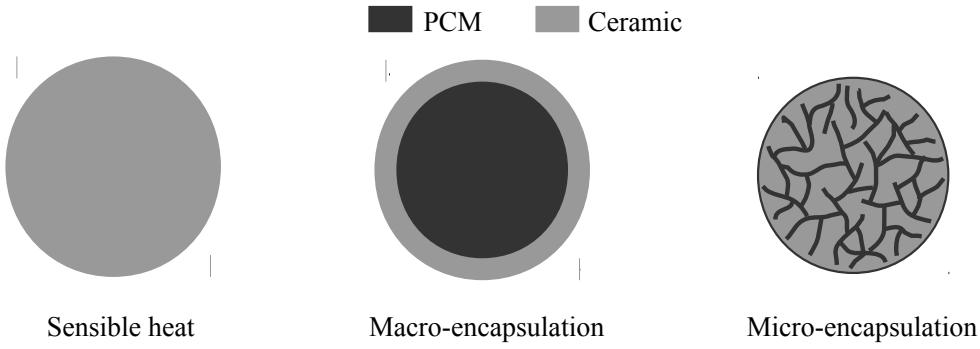

Figure 4.12: Encapsulation methods for EPCMs

Micro-encapsulation of PCMs was first developed by the Institute of Gas Technology in the 1980s (Claar and Petri, 1983, 1985). In 1988 the German Aerospace Centre (DLR), Didier Ceramics and Stuttgart University began a research programme to investigate composite salt-ceramic materials for thermal storage applications (Notter et al., 1993; Tamme et al., 1990). Na_2SO_4/SiO_2 was manufactured using the cold pressing method and extensively tested with respect to thermal, chemical and mechanical stability. The results indicated that the composite material was stable after repeated thermal cycling above the melting point of the Na_2SO_4. Thus the pore fraction of the matrix was large enough to allow for the expansion of the salt without cracking the ceramic (Notter et al., 1993). However, testing conducted by Jalalzadeh-Azar et al. (1997) indicated that a SiO_2/Na_2SO_4 material was inferior to zirconia in high temperature packed bed TES experiments. The testing of the packed bed revealed clumping of the material due to salt leakage out of the spheres.

The composite Na_2CO_3-$BaCO_3$/MgO was studied at the Oak Ridge National Laboratory (Martin, 1987). This material was also prepared by cold pressing and sintering. Although the material was mechanically stable, heat transfer testing showed that the molten salt could evaporate when subjected to high temperature gas flow. Although the overall loss of salt in the system was less than 1% during testing, there was redistribution of salt within the packed bed due to vaporization and condensation effects.

Kodama et al. (2004) describe the use of composite ceramic/PCMs to provide thermal storage for the solar reforming of methane. Porous Al_2O_3 and ZrO_2 ceramic balls were infused with alkali-metal chloride or carbonate PCMs. The results showed the addition of the PCM could extend the operation of the solar reformer in comparison to sensible heat storage. Gokon et al. (2008) developed a double wall reactor concept. The ceramic/PCM was placed in the annular region between two pipes. The inner pipe was filled with a catalyst and the outer pipe was heated by incident solar radiation.

In the macro-encapsulation approach the molten PCM is retained within a hollow shell. The shell can be preformed, filled with a molten PCM and sealed; or it can be formed by coating a solid PCM particle (Goswami, 2012). Macro-encapsulation allows for a higher percentage of PCM in the system, especially when thin shells are considered. Another advantage of macro-encapsulation is that the PCM is never in direct contact with the gas stream, thus eliminating any evaporation problems. However, the manufacturing process of macro-encapsulated PCMs introduces added complexity. As indicated in Table 4.5 inorganic salts undergo large changes in volume upon melting. The capsule design must therefore include a void to allow for the expansion of the PCM.

Pendyala (2012) investigated suitable methods of encapsulating $NaNO_3$ for use between 300 °C and 500 °C. Various techniques were considered, including electroless coatings, silicate coatings, SiO_2 coatings and sand encapsulation. A method for metal oxide coating was developed and the EPCMs were characterised with respect to cyclic stability and thermal performance. However, further extended testing was recommended.

Encapsulation of $NaNO_3$, NaCl, $MgCl_2$ and NaCl-$MgCl_2$ eutectic salts was studied by Zhao (2013). Cylindrical shells were manufactured from stainless steel 304L and sealed using welded end caps. A 20-30% void was included to allow for the expansion of the salt upon melting. Testing using an immersion calorimeter showed that multiple thermal cycles and long term exposure to the molten salt did not cause any measurable deterioration in the heat capacity of the salt.

Mathur et al. (2014) developed a manufacturing technique for macro-encapsulated $NaNO_3$ particles. A void was created within each particle using a sacrificial polymer coating as the middle layer between the PCM and the shell. The shell consisted of a mixture of kaolin and Montmorillanite clay. The projected cost of the storage media only is 5.8 USD/kWh_{th}, with a projected total specific storage cost of 16.4 USD/kWh_{th} (including storage media, containment, balance of plant and installation costs).

Goswami (2012) investigated two methods for macro-encapsulation of NaCl particles. The first method involved the use of preformed ceramic shells that were filled with NaCl. The second method used direct ceramic coating of NaCl particles. In both methods the ceramic shell with NaCl core was subsequently metal plated using electroless and electrochemical deposition techniques. A cost analysis showed that macro-encapsulated salt particles have a potential to store energy for steam cycles at a cost of 14 USD/kWh_{th}

4.4.4 Manufacturing of EPCM particles for testing

The ceramic engineering company cerAdvance was approached to manufacture the alumina ceramic materials for experimental testing of the EPCMs. The first concept that was pursued consisted of an alumina ceramic foam that was coated with a thin alumina shell. In order to impregnate the alumina foam, the particles were submerged in molten salt. Capillary action draws the liquid salt into the foam through a small filling hole. A diagram of the apparatus used to impregnate the particles is shown in Figure 4.13(a). The outer salt pot was manufactured from thick walled stainless steel 304 pipe. The salt pot was sealed with flanges and argon was used as a cover gas. A stainless steel basket within the salt pot was used to dip the pebbles into the salt and subsequently remove them. A sectioned view of one of the EPCM specimens is shown in Figure 4.13(b).

The results of the impregnation are presented in Table 4.8. On average each pebble consisted of 36.9% Na_2SO_4 on a mass basis. Although the impregnation test of the porous EPCM particles was successful, there were multiple technical challenges associated with the very high temperatures involved. The molten salt is highly corrosive towards the stainless steel pot in the presence of oxygen. This required the sealing of the pot, thus limiting the number of particles that could be impregnated for each firing of the furnace. This made the manufacture of a full packed bed of particles not feasible using the current apparatus.

Table 4.8: Results of the salt impregnation test

Filled particle mass [g]	Na_2SO_4 absorbed [g]	Mass fraction Na_2SO_4 [%]
169.6 (9.5)	62.5 (4.6)	36.9 (2.8)

bracketed values represent standard deviation

The primary disadvantage of the foam EPCM concept was the low mass fraction of salt in each particle. This significantly reduces the effectiveness of the latent heat storage design as the bulk of energy is stored in the alumina material. The small salt mass fraction does not justify the extra manufacturing cost of the particles. The dense shell of the material made the largest contribution to the mass. However, without the shell the alumina foam started to disintegrate.

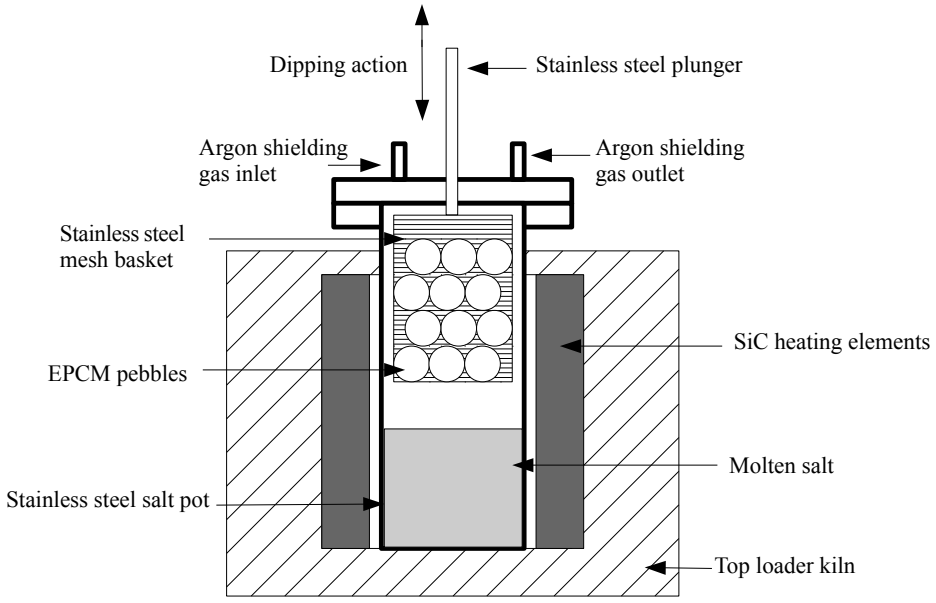

(a) Salt impregnation apparatus

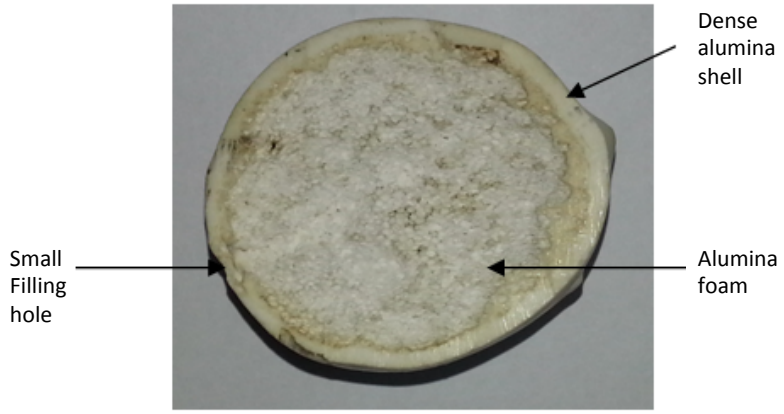

(b) Ceramic foam particle

Figure 4.13: Impregnation of Line-OX alumina foam EPCM particles

Due to the low salt mass fraction in the micro-encapsulated particles, further research efforts were based on a macro-encapsulation approach. Figure 4.14 shows that the macro-encapsulation allows for higher mass fractions of Na_2SO_4 in each EPCM particle, even when including a void to allow for the expansion of the salt. In order to conduct experimental testing hollow alumina shells of outer diameter 45 mm and 1.2 mm wall thickness were manufactured by cerAdvance. These shells were then filled with powdered Na_2SO_4 salt through a small filling hole and a furnace was used to melt and solidify the powdered salt. As the bulk density of the powdered salt is lower than the required effective density, the particles were then 'topped up' with a small amount of powder to get the correct mass of salt required. The hole in each particle was then plugged with another silica material that

was partially sintered. Approximately 800 particles were manufactured to allow preliminary testing in the laboratory scale packed bed test facility. The ceramic that was used to plug the filling hole did not fully seal during sintering. Therefore it was possible for salt to gradually leak out of the plug when molten. Once the particles were randomly packed in the bed, they were each rotated such that the hole was at the top. Future research should focus on getting an airtight seal for the macro-encapsulated particles. However, the aim of the present work is to first generate experimental data to validate the numerical model. As shown in Figure 4.15, on average approximately 70% of the mass of each particle in the packed bed consisted of the Na_2SO_4 PCM. Taking into account the void for the expansion of the salt upon melting, the apparent density of the the salt within the particles was 1862 kg/m^2.

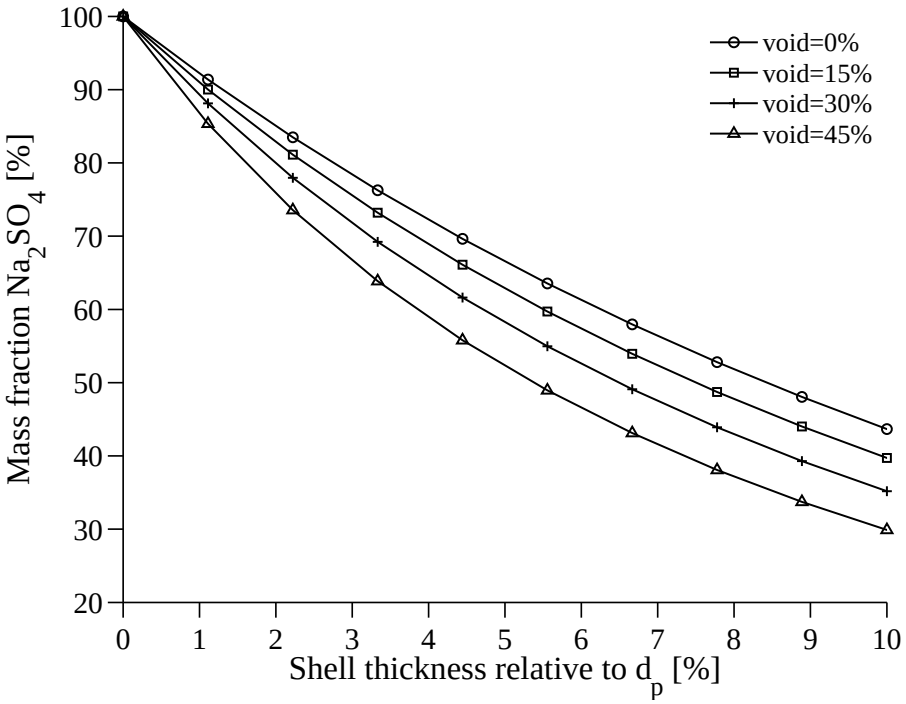

Figure 4.14: Mass fraction of Na_2SO_4 in 45 mm diameter macro-encapsulated particles

The macro-encapsulated particles were tested in the high temperature packed bed test facility. This equated to a packing depth of 0.51 m. The axial temperature and radial profiles of the air were measured by 18 Type-K thermocouples. Attempts were made to measure the PCM temperature within the particles. A 1.5 mm Type-K thermocouple probe was inserted into three EPCM particles. Unfortunately these thermocouples were quickly corroded by the molten salt in the presence of oxygen. Once the salt melted the thermocouples malfunctioned. Thus for validation purposes the air temperature in the packed bed needs to be utilised. The air temperature was measured along the centreline of the packed bed at five different axial levels. A photograph of the packed particles in the test section is shown in Figure 4.16 and a diagram of the thermocouple positions is presented in Figure 4.17.

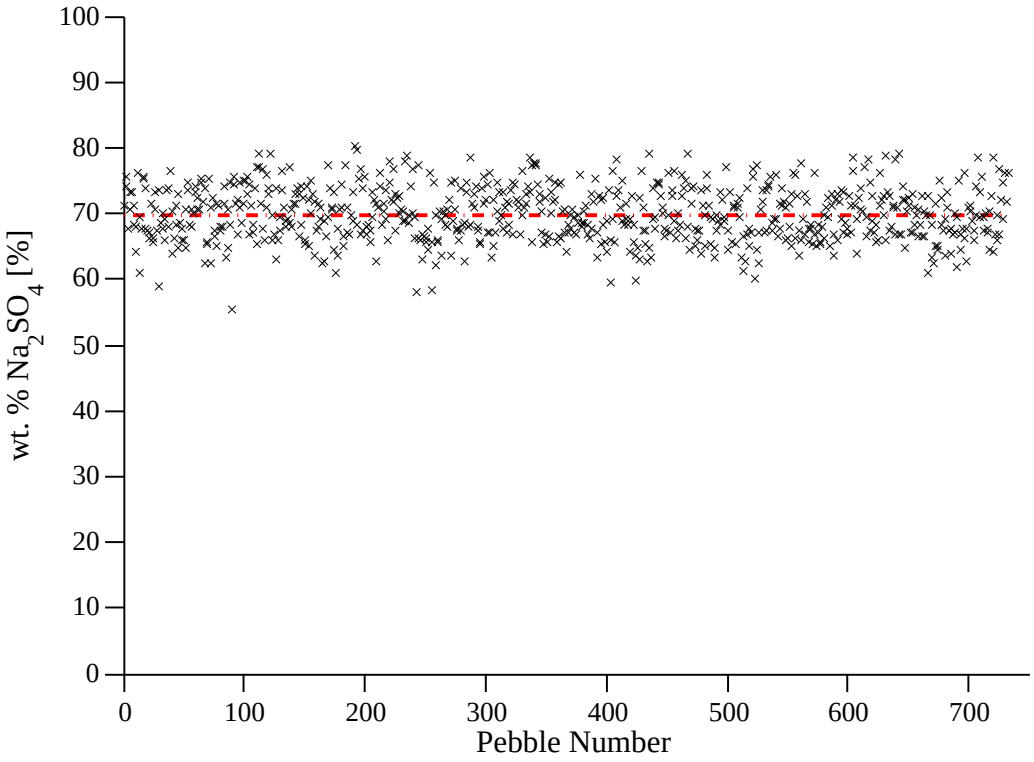

Figure 4.15: Mass fraction of Na_2SO_4 in the macro-encapsulated particles used for testing

Figure 4.16: Packed bed of macro-encapsulated Na_2SO_4 particles in alumina shells

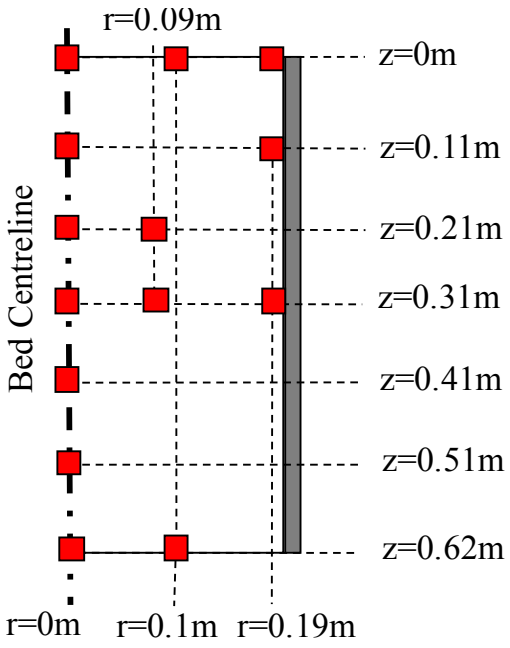

Figure 4.17: Fluid thermocouple positions for the latent heat storage testing

4.5 Conclusions

This chapter outlines the experimental methods that were utilised in this study. Experimental data was generated for both sensible and latent heat storage using a high temperature packed bed test facility. In order to analyse the sensible heat transfer system, the test facility was packed with 19 mm alumino-silicate particles (Denstone 2000). The temperature dependent heat capacity and thermal conductivity of this material were presented. Initial testing was conducted with a bed length of $L_z = 0.8$ m, at charging temperature of 160 °C. This data allows the packed bed to be studied in a predominantly convective heat transfer environment. Further high temperature sensible heat transfer experiments were conducted over the temperature ranges of representative gas turbine cycles (350-900 °C and 600-900 °C). The solid phase heat capacity of the alumino-silicate material was found to vary by up to 33.9% between ambient and 350 °C. Therefore the packed bed was preheated to 350 °C and 600 °C, to reduce the sharp changes in the solid heat capacity with temperature to generate representative storage conditions for a SGT cycle.

In order to analyse a latent heat transfer system an encapsulated Na_2SO_4 material was developed. This inorganic salt was selected due to its favourable heat storage properties, low cost, thermal stability and high melting temperature. In comparison to sensible heat storage in alumina, Na_2SO_4 has the potential to reduce the mass of storage material required by up to

35%. A materials analysis showed that alumina is a suitable ceramic encapsulation material that does not react with molten Na_2SO_4 at high temperature. Two encapsulation methods were discussed in this chapter. The development of a micro-encapsulated PCM particle was not pursued further due to a low mass fraction of salt in the particle. The manufacturing of a macro-encapsulated Na_2SO_4 particle for testing was described.

Chapter 5

Experimental validation: sensible heat storage

5.1 Introduction

This chapter describes the validation of the sensible heat thermal storage model that is utilised in this work. Section 5.2 describes the selection of the heat transfer model to analyse the sensible heat storage system. Preliminary thermal tests were conducted at low temperature (160 °C) to study the convective heat transfer in the packed bed of alumino-silicate particles. The validation of the sensible heat storage modelling over the low temperature range is presented in Section 5.3. Subsequent thermal tests were conducted at high temperature (900 °C), over the temperature ranges of representative recuperated and non-recuperated gas turbine cycles. The validation of the modelling at high temperature is presented in Section 5.4.

5.2 Model selection

In Chapter 2 the C-S and D-C heat transfer models were presented for the packed bed thermal storage system. The C-S model assumes a lumped capacitance approach for the internal particle heat transfer, while the D-C model solves an additional one dimensional temperature gradient within the spherical particles. The solutions of the C-S and D-C models were compared in order to determine which model is best suited to sensible heat storage in a packed bed. Although the D-C heat transfer model is comprehensive, it is more computationally

expensive than the C-S model. This is due to the added number of intra-particle temperature profiles that must be solved. It is therefore desirable to utilise the C-S model as it has a lower computational cost and simpler implementation. The use of the D-C model is only necessary when there exist large temperature gradients within the particles.

Heat transfer simulations of a packed bed of Denstone particles (alumino-silicate) were conducted using the C-S and D-C heat transfer models. The exit fluid temperature profiles from each model were compared for a full heating test to steady state. Under these conditions the temperature profiles at the bed exit are most sensitive to differences between the C-S and D-C models. In order to determine the effects of intra-particle temperature gradients the Biot number was varied. This was achieved by varying the thermal conductivity of the particles, based on the specified Biot number. At low Biot numbers the particles absorb/release energy isothermally and therefore the solutions of the C-S and D-C models converge. As described in Section 2.3.3, the C-S model can be corrected for intra-particle conduction effects by employing the Jeffreson (1972) correction factor.

As shown in Table 5.1, the C-S model can accurately reproduce the solution of the D-C model across all the Biot numbers that were tested, when employing the Jeffreson (1972) correction factor. At Biot numbers as high as 5, the Root Mean Square (RMS) deviation between the C-S and D-C model solutions is within 1 °C for the conditions analysed. The Biot numbers of the sensible heat storage systems analysed in this work are below 1. Under these conditions the C-S and D-C models yield solutions that are indistinguishable. The D-C model offers no improvements in accuracy over the C-S model for modelling sensible heat storage, and has a higher computational cost. Therefore the sensible heat storage modelling in this work was based on the C-S model, with the Jeffreson (1972) correction factor.

Table 5.1: Comparison of the fluid discharge temperature for the C-S and D-C models

Bi_p	RMS deviation uncorrected h_p [°C]	RMS deviation corrected h_p [°C]	Max. deviation uncorrected h_p [°C]	Max deviation corrected h_p [°C]
0.1	0.57	0.00	0.08	0.00
1	0.07	0.00	0.08	0.00
3	3.10	0.02	7.76	0.07
5	8.12	0.72	20.3	0.39

Calculated for $Re_p = 200$, $\Delta T = 350$ °C

5.3 Low temperature model validation

5.3.1 Axial temperature profiles

The low temperature testing was conducted at a charging temperature of 160 °C. This was the minimum temperature at which the LP gas burner could stably operate. The testing procedure involved heating the packed bed from a uniform ambient temperature to 160 °C. Once the packed bed was fully charged, the burner was shut down and the bed cooled with air flow at the ambient room temperature. The flow direction was not reversed during the cooling cycle (co-current cooling mode). The aim of this initial testing was to validate the packed bed modelling in a primarily convective heat transfer environment (minimal radiation). Convection is the dominant heat transfer mechanism in the packed bed storage system and needs to be accurately modelled. Due to the large changes in solid heat capacity across the test temperature range, temperature dependent thermophysical properties were utilised in the modelling.

Figures 5.1 and 5.2 present the measured and predicted fluid and solid temperature profiles along the centreline of the packed bed at different axial positions. An analysis of the charging and discharging profiles shows that the predictions of the C-S model match the measurements with acceptable accuracy. The shape of the transient temperature profiles is well captured by the model. Table 5.2 presents the RMS deviation between the model and the experimental measurements. This is a maximum of 7.4 °C for the fluid phase and 6.4 °C for the solid phase measurements. When normalised by the test temperature range the maximum Normalised Root Mean Square Deviations (NRMSD) are 5.3% and 4.7% respectively.

Table 5.2: RMS deviations between the measured and predicted temperature profiles along the packed bed centreline for the 160 °C test

		$z = 0$ m [°C]	$z = 0.2$ m [°C]	$z = 0.4$ m [°C]	$z = 0.6$ m [°C]	$z = 0.8$ m [°C]
Fluid	charging	N/A	1.3 (1.0%)	4.1 (3.0%)	N/A	7.2 (5.2%)
	discharging	N/A	1.3 (0.9%)	4.4 (3.2%)	N/A	7.4 (5.3%)
Solid	charging	6.4 (4.7%)	0.8 (0.6%)	3.0 (2.2%)	4.3 (3.2%)	5.6 (4.1%)
	discharging	4.5 (3.2%)	0.4 (0.3%)	2.6 (1.9%)	4.9 (3.5%)	5.4 (3.9%)

bracketed values indicate RMS deviation normalised by the test temperature range

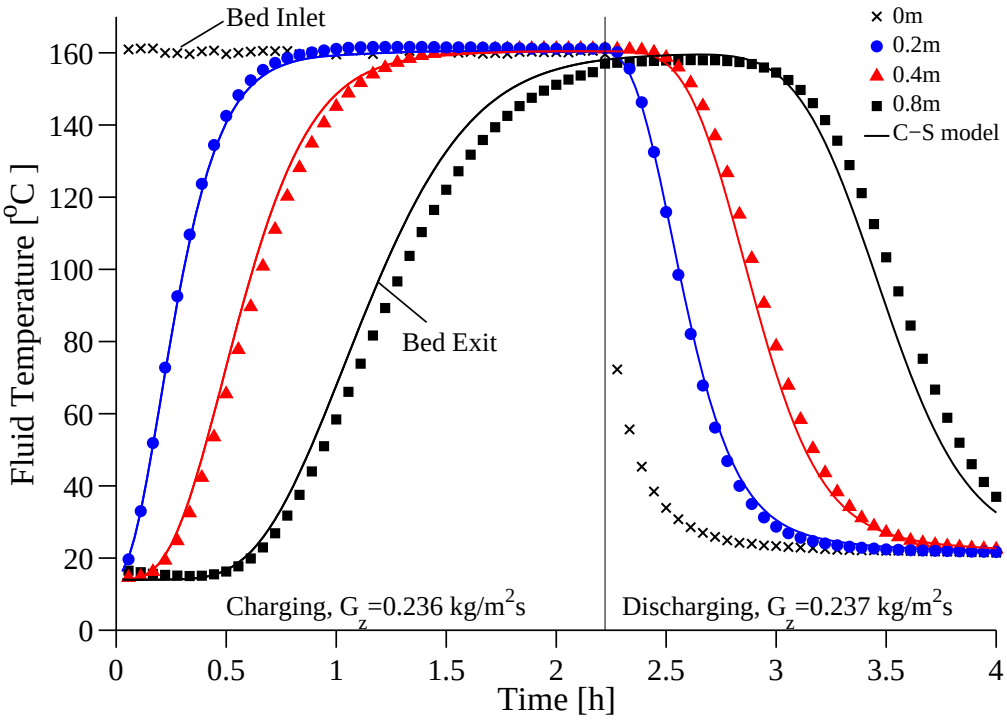

Figure 5.1: Comparison of the measured (markers) and predicted (curves) centreline fluid temperature profiles for the 160 °C test, using Denstone particles.

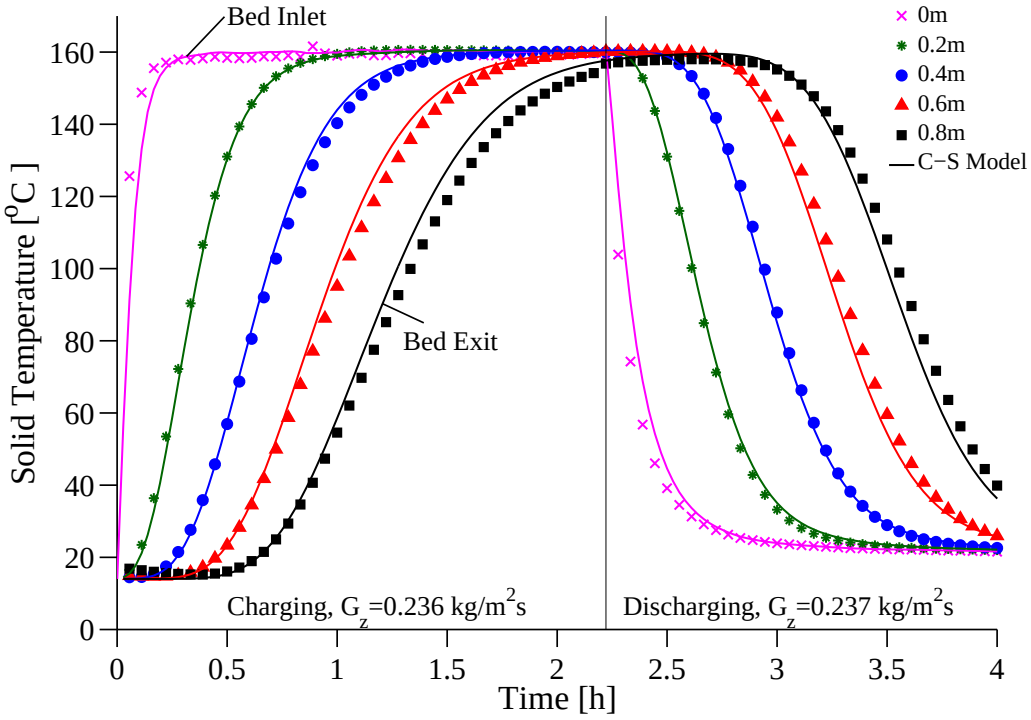

Figure 5.2: Comparison of the measured (markers) and predicted (curves) centreline solid temperature profiles for the 160 °C test, using Denstone particles.

The RMS deviations between the model and experiment increase with distance from the bed inlet. This indicates that the model over-predicts the thermocline velocity by a small amount. The speed of the thermocline is proportional to the following parameters:

$$U_{\text{therm}} \propto \frac{G_z c_f}{\rho_s c_s (1-\varepsilon)} \tag{5.1}$$

As presented in Figure 4.6, the heat capacity of the Denstone particles varies strongly with temperature below 300 °C. However, only two data points were provided from Saint Gobain for temperatures below 200 °C. The interpolation of the solid heat capacity across this temperature range is a potential cause for the deviations between the model and experimental data. The modelling of the velocity channelling profile could also influence the velocity of the thermocline in the core region of the packed bed. However, overall the agreement of the model with the experimental data is satisfactory.

5.3.2 Sensitivity analysis on inter-phase heat transfer coefficient

As the focus of the low temperature testing was on the convective heat transfer in the packed bed, a sensitivity study was conducted on the inter-phase convection heat transfer coefficient. There are a variety of empirical correlations that predict this parameter for packed beds. Four popular correlations from Wakao et al. (1979), KTA (1983), Yoshida et al. (1962) and Gunn (1978), are discussed in Section 2.3.3. Figure 2.3 presents a comparison of these correlations up to a Reynolds number of 1000. A variation of approximately 20% exists between the Gunn and Wakao et al. correlations and a variation of approximately 35% exists between the Gunn and Yoshida et al. correlations.

In order to determine the sensitivity of the temperature profiles to variations in the heat transfer coefficient, the Gunn correlation was chosen as the reference case and h_p was varied by $\pm 50\%$ of the nominal value. As shown in Figure 5.3, increasing the heat transfer coefficient does not significantly change the predicted axial temperature profiles in the packed bed. It appears that there is a limiting value, above which further increasing the inter-phase heat transfer coefficient does not affect the heat transfer. Decreasing h_p by 50% has the most influence on the heat transfer in the packed bed, resulting in a decrease in the thermocline gradient. The numerical predictions using the different values of heat transfer coefficient are compared to the experimental data in Table 5.3. The use of the Gunn (1978) convective correlation provides the lowest RMS deviations with the experimental data and validates its use for the packed bed thermal storage.

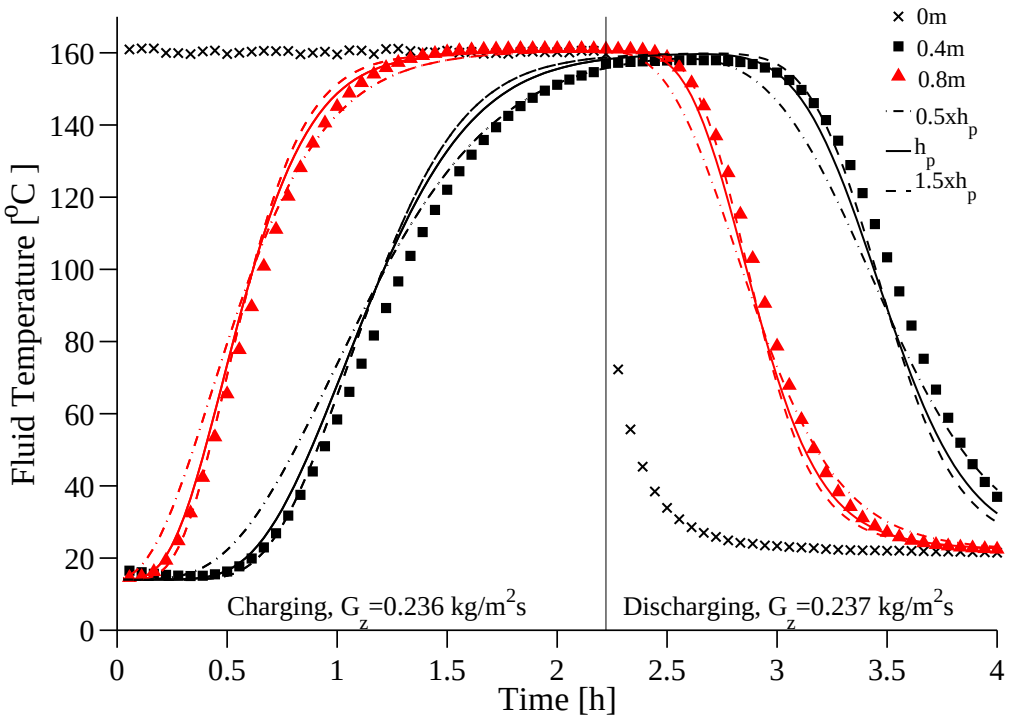

Figure 5.3: Sensitivity of the C-S model to variations in the inter-phase heat transfer coefficient, with h_p calculated according to Gunn (1978). Markers indicate experimental data and curves indicate numerical model.

Table 5.3: Effect of the inter-phase heat transfer coefficient on the RMS deviation between the measured and predicted fluid centreline temperature profiles for the 160 °C test

	RMS deviation $z = 0.2$ m [°C]	RMS deviation $z = 0.4$ m [°C]	RMS deviation $z = 0.8$ m [°C]
Gunn (1978) reference h_p	1.3	4.4	7.4
1.5 x h_p	1.5	4.7	8.2
0.5 x h_p	4.5	7.0	8.9

5.3.3 Radial temperature profiles

During the initial low temperature testing, radial fluid temperature profiles were recorded at bed depths of $z = 0.2$ m and $z = 0.4$ m. These temperature profiles allow the imposed fluid-wall boundary condition to be analysed and the near wall heat transfer to be studied. Figure 5.4 presents the results for the test conducted at 160 °C.

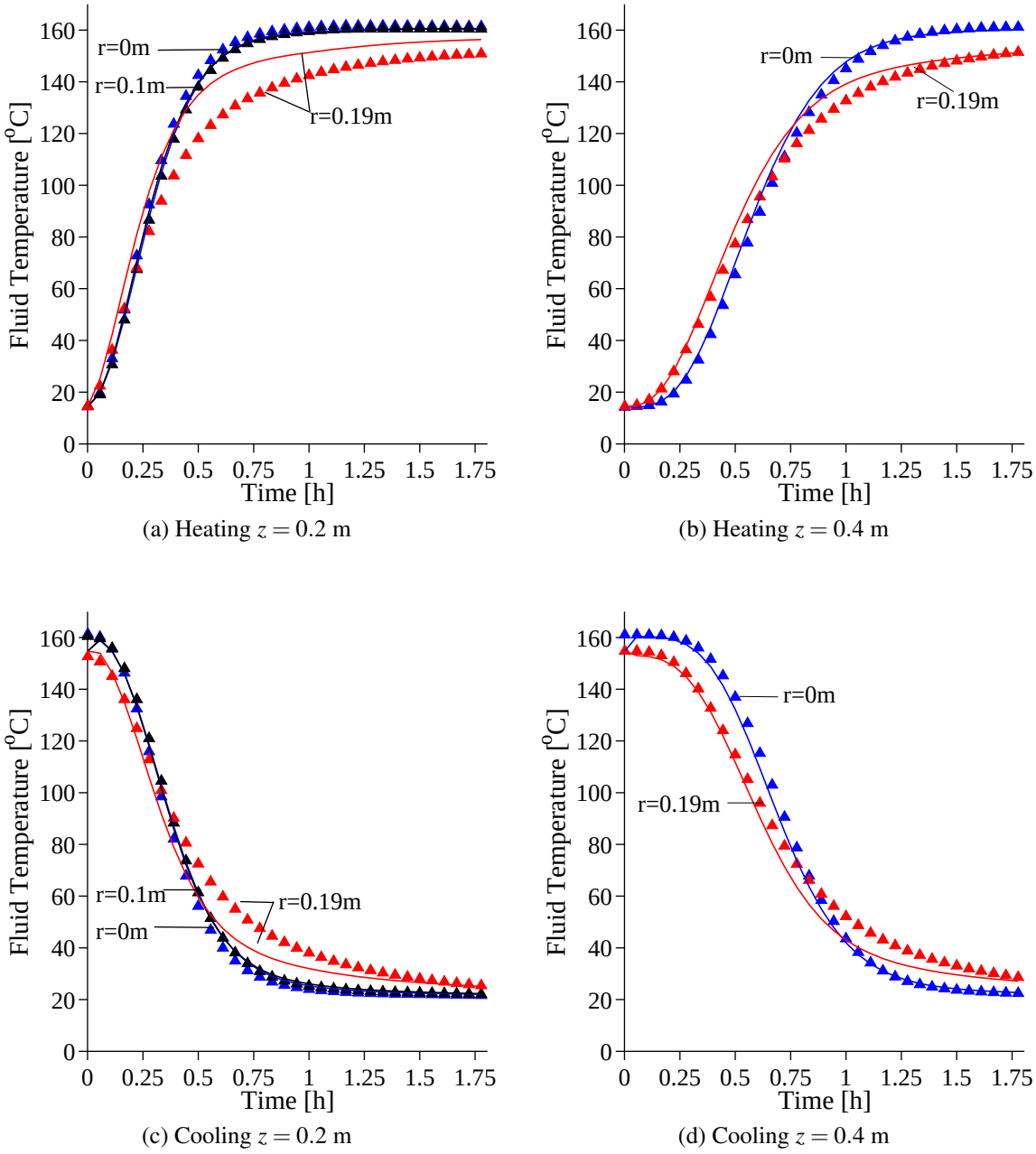

(a) Heating $z = 0.2$ m

(b) Heating $z = 0.4$ m

(c) Cooling $z = 0.2$ m

(d) Cooling $z = 0.4$ m

Figure 5.4: Comparison of measured (markers) and predicted (curves) radial fluid temperature profiles for the 160 °C test, using Denstone particles.

The heat transfer in the near wall region is difficult to quantify accurately as there are a number of different heat transport phenomena present. However, there is good agreement between the C-S model and the experimental data. This indicates that the heat transfer mechanisms at the wall are correctly modelled in the absence of radiation, or at least that the result is empirically the same. During heating, the measurements show that the temperature of the fluid at the wall ($r = 0.19$ m) rises faster than in the centre of the bed ($r = 0.02$

m). This is due to the wall channelling effect, as the velocity in the near wall region is higher than in the core region of the bed. The higher void fraction near the wall also results in a lower solid mass to absorb thermal energy. As the temperature in the near wall fluid temperature rises, the heat losses to the wall increase. Therefore there is a shift in the temperature profiles, whereby the fluid in the near wall region is cooler than in the centre of the bed. During cooling of the packed bed, wall channelling and heat losses both preferentially cool the solid at the wall, causing a larger deviation between the centreline and near wall temperature measurements. The trends in experimental data are correctly reproduced by the model, and validate the wall channelling approach that is utilised in this work. Table 5.4 shows that the maximum NRMSD in the near wall region ($r = 0.19$ m) is 7.1% at the axial level $z = 0.2$ m.

The fluid temperature in the near wall region is 10-15 °C lower than at the centre of the bed at the end of the heating test. As the packed bed was well insulated and charged to a relatively low temperature, this trend is related to the thermal capacitance of the wall. The initial test section design consisted of flanged sections of 200 mm in length that were bolted together. The fluid temperature measurements were taken in close proximity to these flanges. The metal wall, although well insulated, responds to the heating of the packed bed slower than the fluid in the adjacent near wall region. Therefore the hot fluid loses energy to heat the metal wall and flanges. This causes a lower fluid temperature in the near wall region than in the centre of the packed bed. As shown in Figure 5.4(a), after one hour of heating the temperature difference between the fluid in the near wall region and bed centre decreases as the wall temperature rises.

Table 5.4: RMS deviations between measured and predicted radial fluid temperature profiles

	$r = 0.02$ m [°C]	$r = 0.1$ m [°C]	$r = 0.19$ m [°C]
Heating $z = 0.2$ m	1.7 (1.2%)	0.8 (0.6%)	9.8 (7.1%)
Cooling $z = 0.2$ m	1.8 (1.3%)	1.1 (0.8%)	7.1 (5.2%)
Heating $z = 0.4$ m	3.5 (2.6%)	N/A	3.3 (2.4%)
Cooling $z = 0.4$ m	3.8 (3.8%)	N/A	5.1 (3.7%)

5.4 High temperature model validation

As discussed in Section 4.3.3, the high temperature sensible heat testing involved the preheating of the packed bed to 350 °C or 600 °C prior to heating to 900 °C. In this section

the experimental data generated from these high temperature experiments is compared to the predictions from the C-S model. An analysis of the axial and radial temperature profiles is presented, and the effect of temperature dependent thermophysical properties is studied. As argued in Section 5.2, the D-C model offers no improvements in accuracy over the C-S model for sensible heat storage. Therefore the only the C-S model is considered in this section. The predictions from the D-C model are in good agreement with those from the C-S model.

5.4.1 Axial solid temperature profiles

The successful design and operation of a packed bed thermal storage system requires a detailed understanding of the movement of the thermocline along the length of the bed during charging and discharging cycles. Therefore it is important that the numerical model can correctly predict the transient axial temperature distributions in the packed bed. The regular placement of centreline thermocouples along the length of the bed allows for the axial thermocline to be measured. The advantage of analysing the thermocline with respect to the normalised bed position z/L_z is that the movement of the thermocline through the bed can be intuitively studied. Figure 5.5 presents the validation of the C-S heat transfer model across the preheating temperature ranges of ambient-350 °C and ambient-600 °C. Figures 5.6 and 5.7 show the validation of the C-S model across the temperature ranges of non-recuperated gas turbines (350-900 °C) and recuperated gas turbines (600-900 °C). For completeness, temperature dependent thermophysical properties were utilised in the C-S model across all of the temperature ranges.

During the 600-900 °C heating test the pipe between the blower and burner became dislodged, requiring the brief shut down of the burner. Once the pipe connection was repaired the burner was relighted and charging continued until the bed reached steady state at 900 °C. Due to the non uniform conditions in the packed bed, the experimental data for the reheating to 900 °C is not conducive for comparison with the numerical model. Therefore heating data for this test is only available for first hour of charging, prior to the burner shut down.

Figures 5.5-5.7 demonstrate that the shape and position of the thermocline is accurately predicted for heating and cooling tests, conducted over a range of temperatures and mass fluxes. The results validate the use of the C-S model for analysing sensible heat transfer in a packed bed of alumino-silicate particles at high temperature. Therefore the proposed model can be used to conduct further numerical investigations into sensible heat storage in a high temperature packed bed.

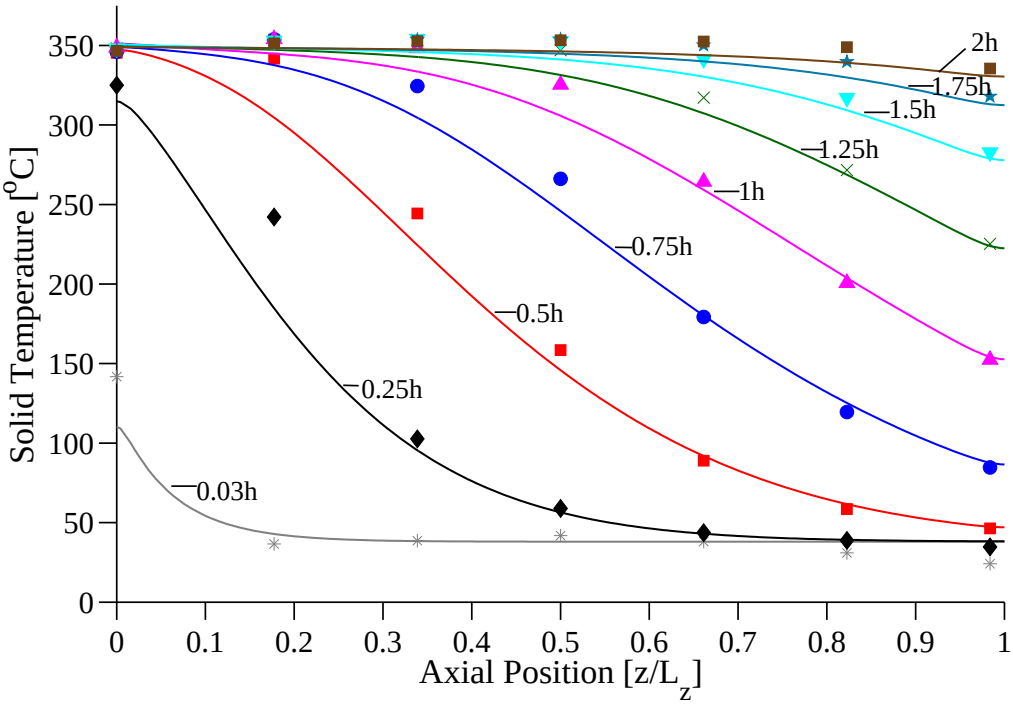

(a) Non-recuperated gas turbine cycle: ambient-350 °C, G_z=0.216 kg/m^{2}s

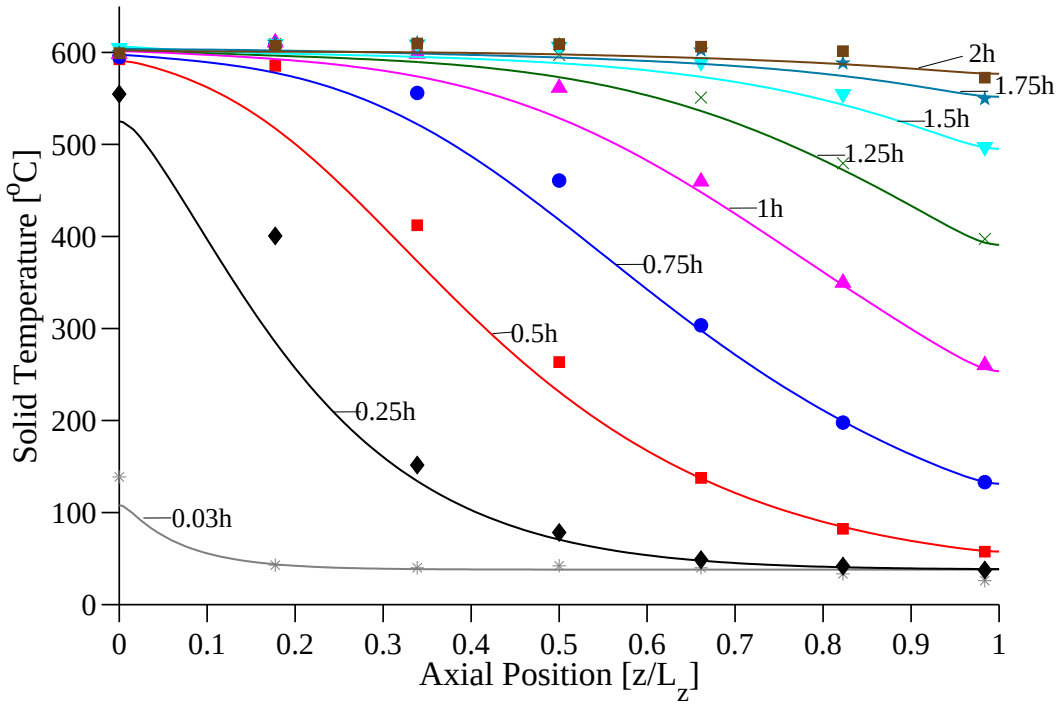

(b) Recuperated gas turbine cycle: ambient-600 °C, G_z=0.237 kg/m^{2}s

Figure 5.5: Comparison of the measured (markers) and predicted (curves) centreline solid temperature profiles for preheating the packed bed, using Denstone particles

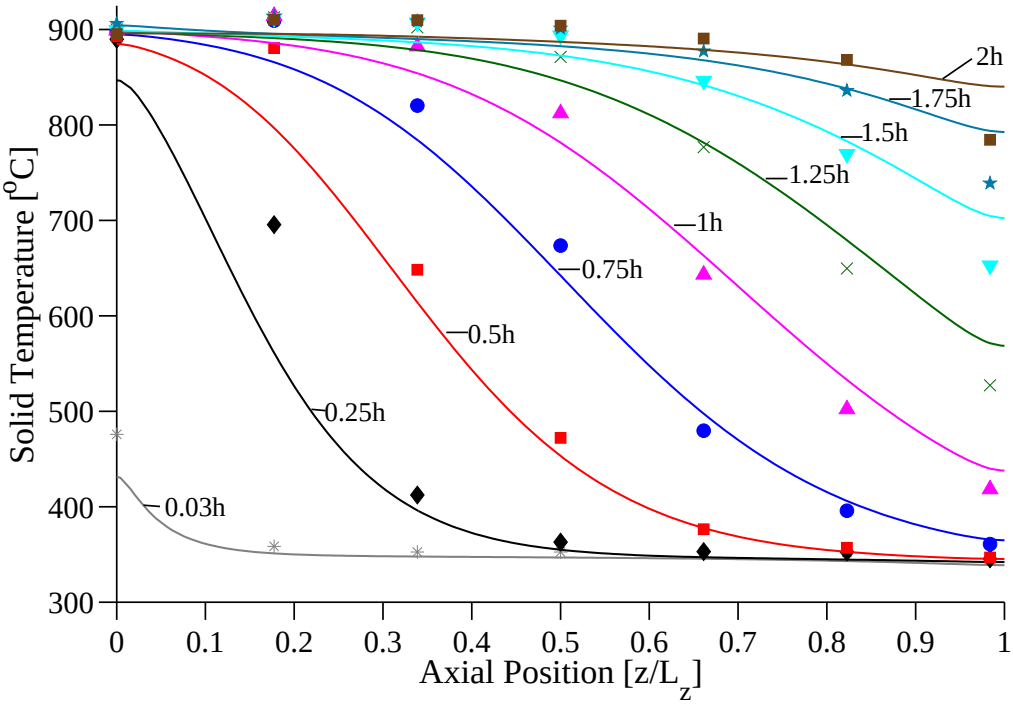

(a) Non-recuperated gas turbine cycle: 350-900 °C, G_z=0.186 kg/m^{2}s

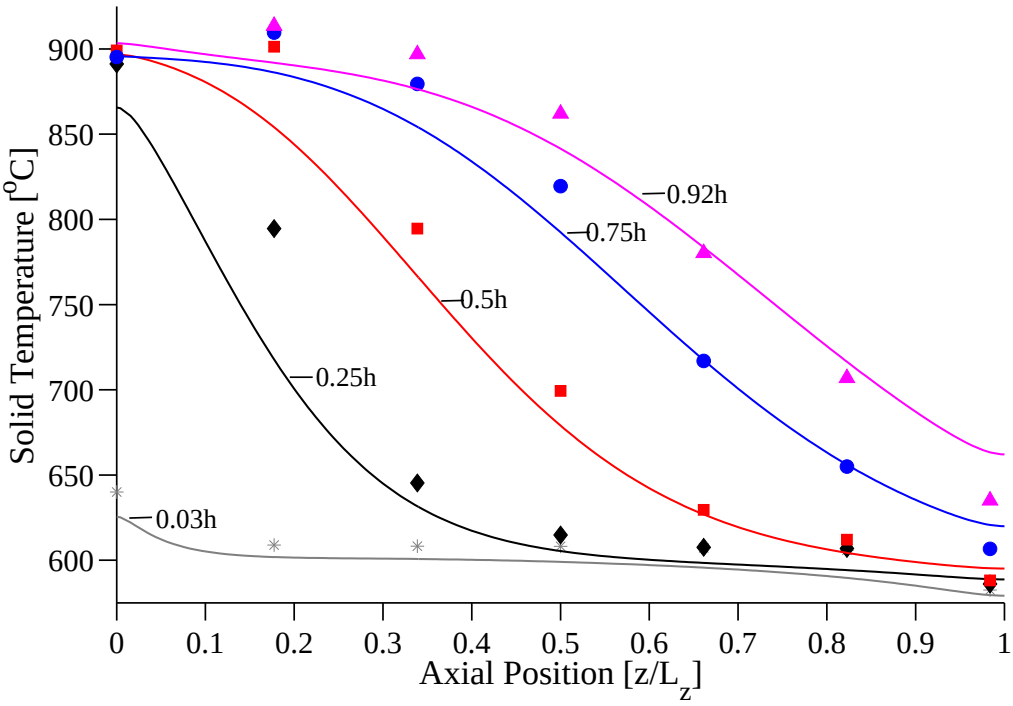

(b) Recuperated gas turbine cycle: 600-900 °C, G_z=0.225 kg/m^{2}s

Figure 5.6: Comparison of the measured (markers) and predicted (curves) centreline solid temperature profiles for the high temperature heating tests, using Denstone particles

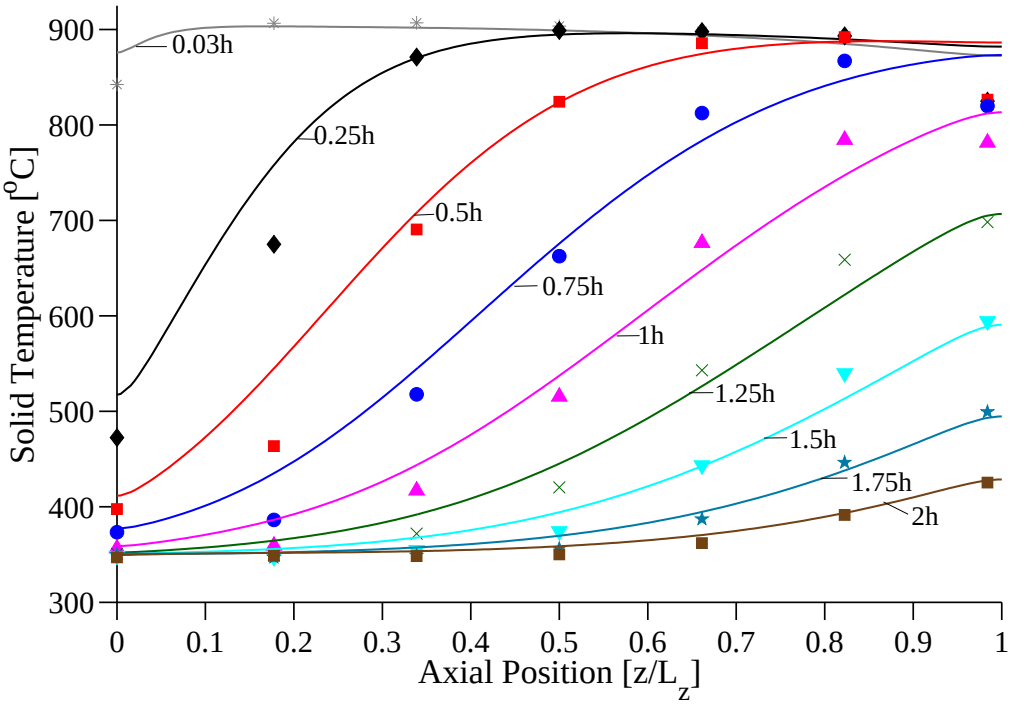

(a) Non-recuperated gas turbine cycle: 900-350 °C, G_z=0.201 kg/m^{2}s

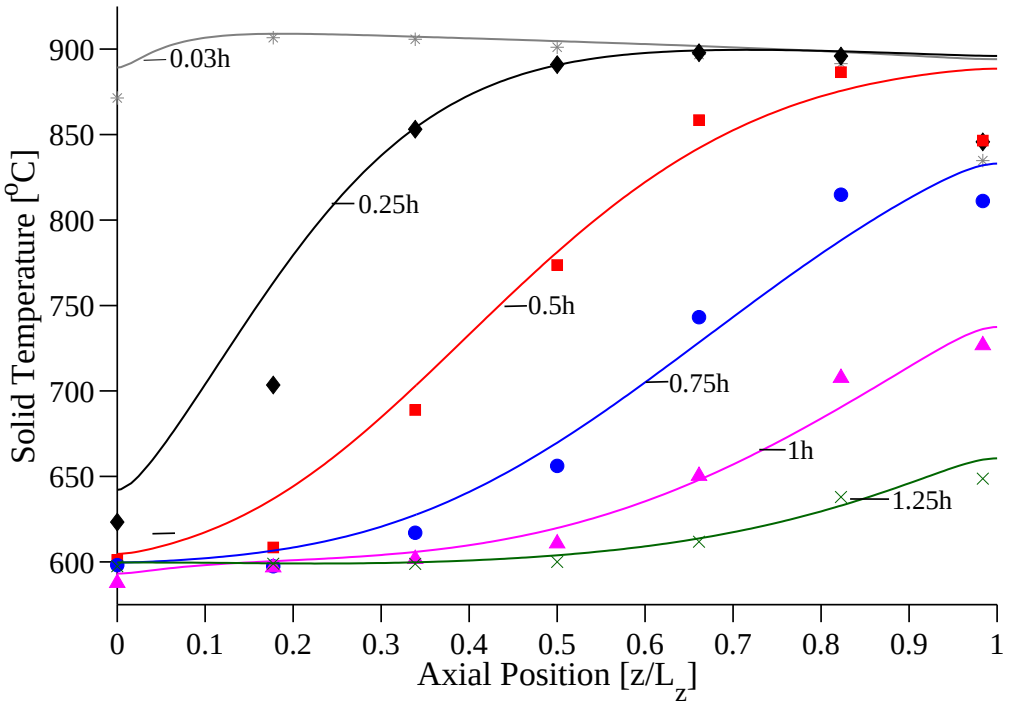

(b) Recuperated gas turbine cycle: 900-600 °C, G_z=0.280 kg/m^{2}s

Figure 5.7: Comparison of the measured (markers) and predicted (curves) centreline solid temperature profiles for the high temperature cooling tests, using Denstone particles

In order to quantify the accuracy of the C-S model, the NRMSD is used. The RMS deviation between the measured and predicted temperatures is normalised by the test temperature range. This allows a direct comparison of the results for the four temperature ranges that were analysed. The results of this analysis are shown in Figure 5.9. The highest NRMSD for each test was located at the measurement position $z/L_z = 0.18$. It is believed that this is caused by the design of the test facility, which did not include a diffuser at the bed inlet. The sudden expansion from the combustion chamber pipe (76 mm diameter) to the test section (400 mm diameter) creates a jet effect onto the unpacked region above the packed bed. This jet flow increases the rate of heat transfer in the proximity of the inlet, at the bed centre. This effect dissipates as the flow propagates further into the bed, resulting in a decrease in NRMSD from the position $z/L_z = 0.33$ onwards. For the preheating tests, presented in Figure 5.8 the NRMSD continues to decrease towards the bed outlet. However, as shown in Figure 5.9 the NRMSD increases at the bed outlet at high temperatures. This is caused by heat losses from the base of the test facility, which are not taken into account in the modelling. During the high temperature tests the base only reached temperatures between 847-867 °C at a charging temperature of 900 °C. A steady state temperature of 891 °C was measured at a height of 110 mm above the base, indicating that this heat loss does not affect the packed bed upstream from the base when there is convective flow.

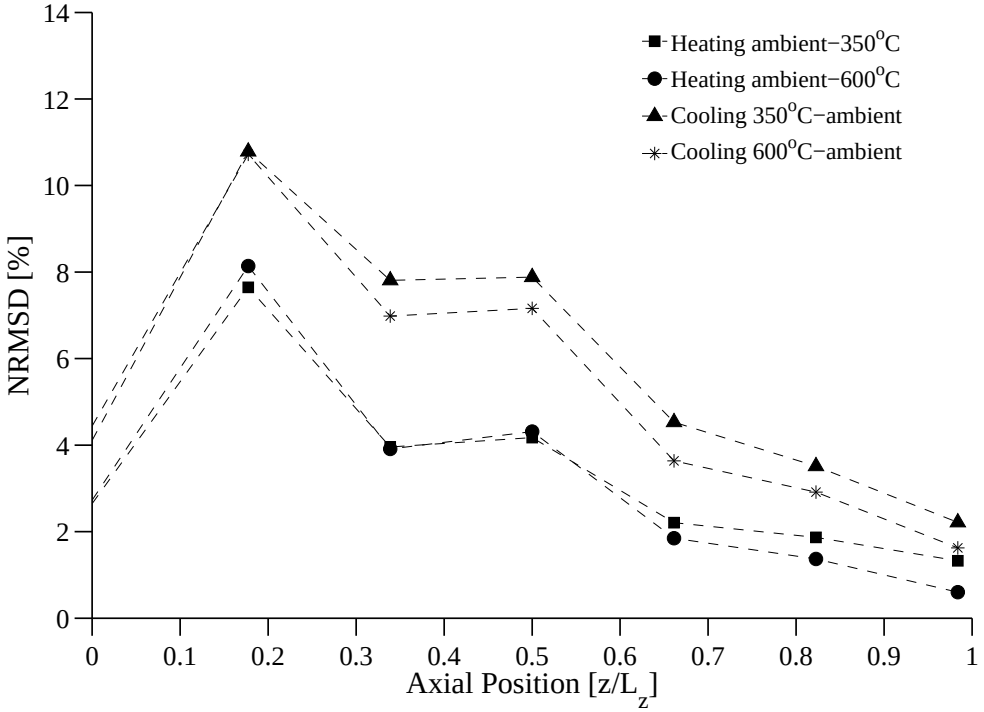

Figure 5.8: Normalised RMS deviations between the measured and predicted solid centreline temperature profiles for the preheating and post cooling testing

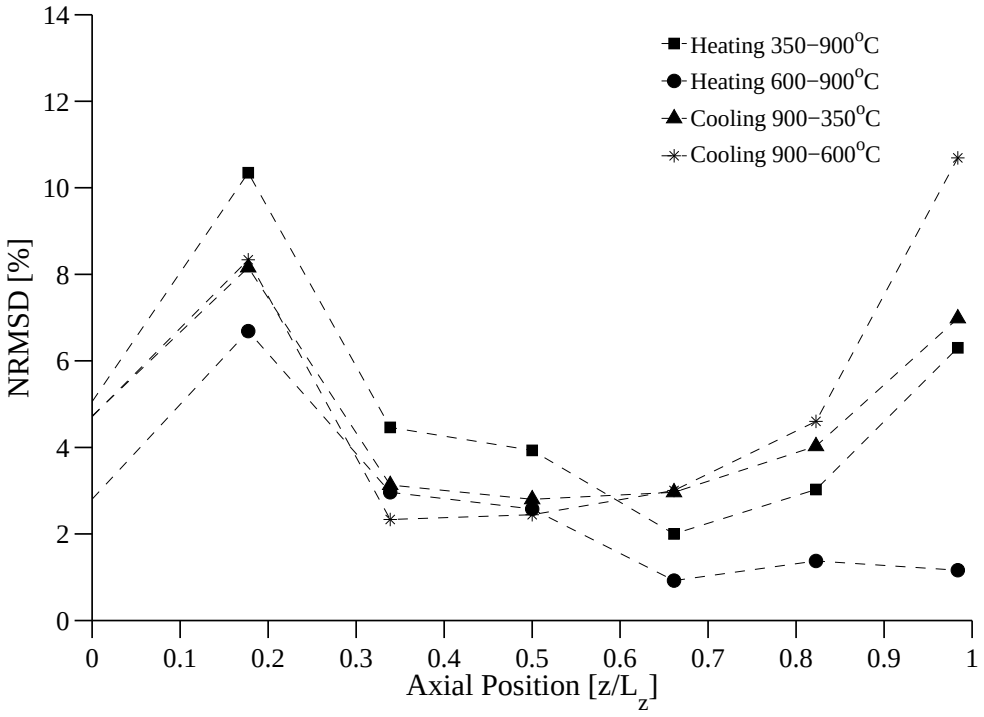

Figure 5.9: Normalised RMS deviations between the measured and predicted solid centreline temperature profiles for the high temperature testing

Effect of temperature dependent thermophysical properties

This section demonstrates the effect of temperature dependent thermophysical properties on the predicted shape of the axial thermocline. The use of variable properties in the C-S model increases the simulation time. Thus it is beneficial to implement constant thermophysical properties, evaluated at an average temperature, for design studies that require a large number of parametric simulations. However, the use of constant properties should not affect the accuracy of the model predictions. Therefore it is important to determine when the constant property assumption is applicable to sensible heat storage systems based on ceramic materials.

As stated in Section 4.3.3, the solid phase heat capacity is the dominant temperature dependent property in a sensible heat thermal storage system (Zanganeh et al., 2012). The data presented in Table 4.1 shows that the heat capacity of the Denstone exhibits a strong temperature dependence below 350 °C and a weak temperature dependence between 350 °C and 900 °C. This trend is common to ceramic materials (MgO, Al_2O_3, mullite, and SiC), and is described by the Debye theory, which assumes that the main contribution to the specific heat of a solid is atomic vibrations (Surendranatha, 2015). This theory introduces the concept of

the Debye temperature, above which the isochoric heat capacity is approximately constant and the isobaric heat capacity exhibits a weak temperature dependence. Below the Debye temperature modes of vibration are frozen out and the heat capacity tends to 0 J/mol.K as the temperature approaches 0 K. Thus at temperatures significantly below the Debye temperature a strong temperature dependence in heat capacity is expected. Materials such as copper have a low Debye temperature (343 K, Kittel (1976)), and therefore have a constant isochoric heat capacity when heated from room temperature. In contrast, many ceramic materials have a high Debye temperature. For example the Debye temperature of Al_2O_3 is 1045 K (Anderson, 1963).

Experimental data from two heating tests was selected to demonstrate the effect of the temperature dependent variations in the solid heat capacity. The 20-600°C heating test ($\Delta T = 580$ °C) and 350-900 °C ($\Delta T = 550$ °C) were utilised. The C-S model was solved using both temperature dependent and constant thermophysical properties. The solutions are compared to the experimental data in Figures 5.10 and 5.11. Figure 5.10 demonstrates that the constant property model does not accurately predict the thermocline shape from the preheating experiment. The thermocline from the variable property model penetrates deeper into the cooler region of the packed bed than the constant property model, and best represents the measured thermocline shape. Therefore under these conditions the constant property assumption should not be implemented as it will lead to inaccuracies in the predicted results.

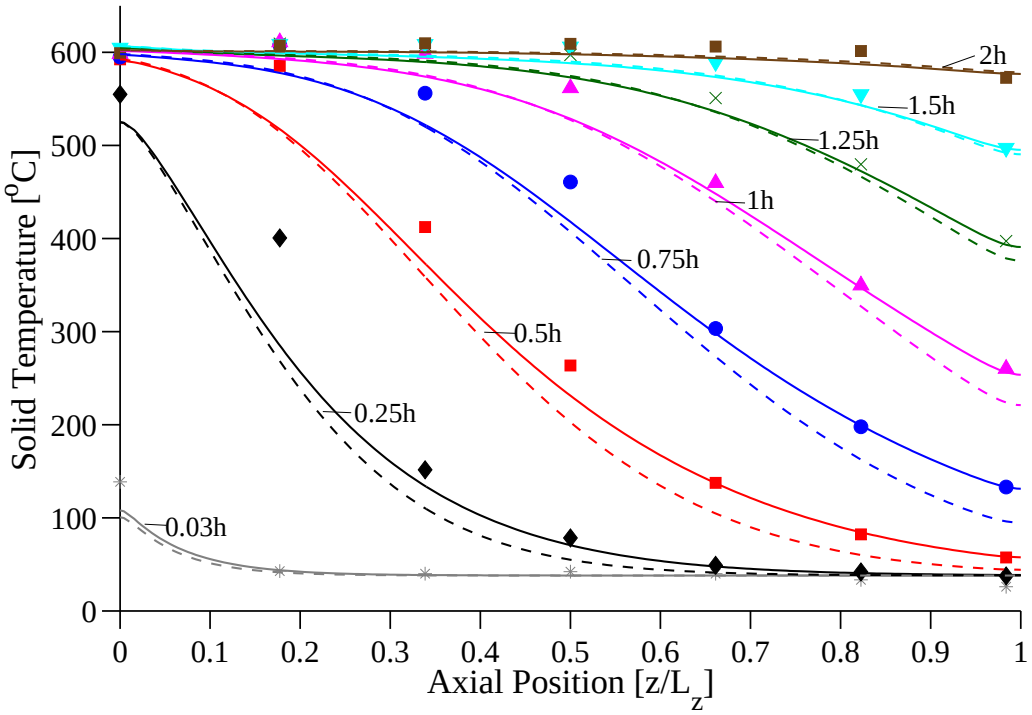

Figure 5.10: Comparison of constant property (dashed curve) and variable property (solid curved) modelling with experimental data (markers) for the 20-600 °C heating test

Figure 5.11 shows that there is a small difference between the constant and variable property models, despite a temperature range of 550 °C. Therefore the constant property model is applicable if the minimum temperature in the packed bed is higher than 350 °C. These results are also applicable to other ceramic materials such as Al_2O_3. The constant property modelling can be used for design studies of thermal storage systems for both recuperated and non-recuperated gas turbine cycles.

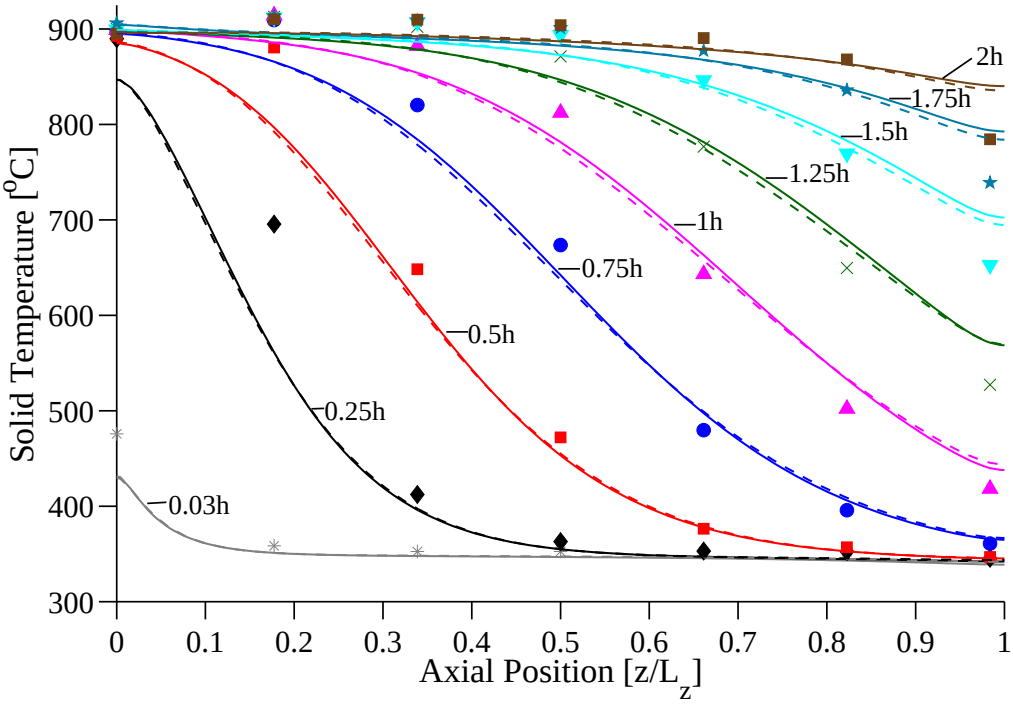

Figure 5.11: Comparison of constant property (dashed curve) and variable property (solid curved) modelling with experimental data (markers) for the 350-900 °C heating test

5.4.2 Radial solid temperature profiles

The solid temperatures at the packed bed wall were measured on three axial levels to analyse the radial temperature profiles. The results for the radial temperature profiles are presented in Figures 5.12 and 5.13. The trends in the radial temperature profiles are consistent with the low temperature tests that are presented in Section 5.3.3. The solid in the near wall region is preferentially heated and cooled by the wall channelling effect. The test section wall was redesigned subsequent to the low temperature tests and the flanged connections were removed, reducing the wall heat capacity. Thus the heat loss profile that developed was most likely caused by thermal losses through the insulated bed wall. Due to the high temperature nature of the testing, radiation heat exchange occurred between the solid and

the bed wall. This added heat transfer mechanism was included in the modelling. The results show that during heating and cooling tests there is good agreement between the C-S model and the experimental data, with a maximum NRMSD below 3%. The trends in radial temperature profiles are predicted with a high degree of accuracy during the high temperature tests, validating the modelling of the near wall region at high temperature.

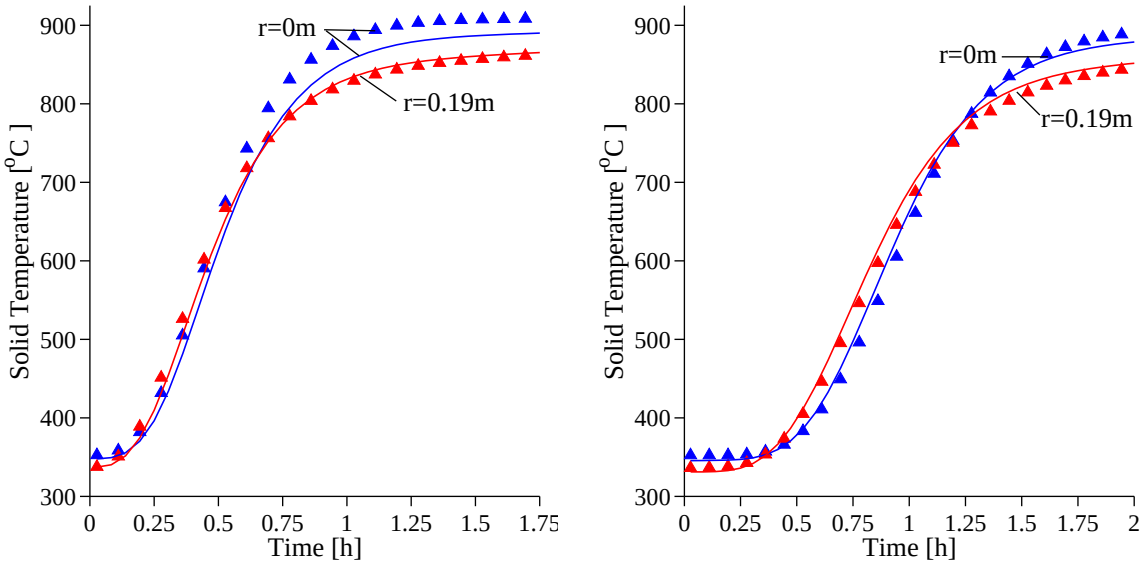

(a) Heating $z = 0.21$ m

(b) Heating $z = 0.41$ m

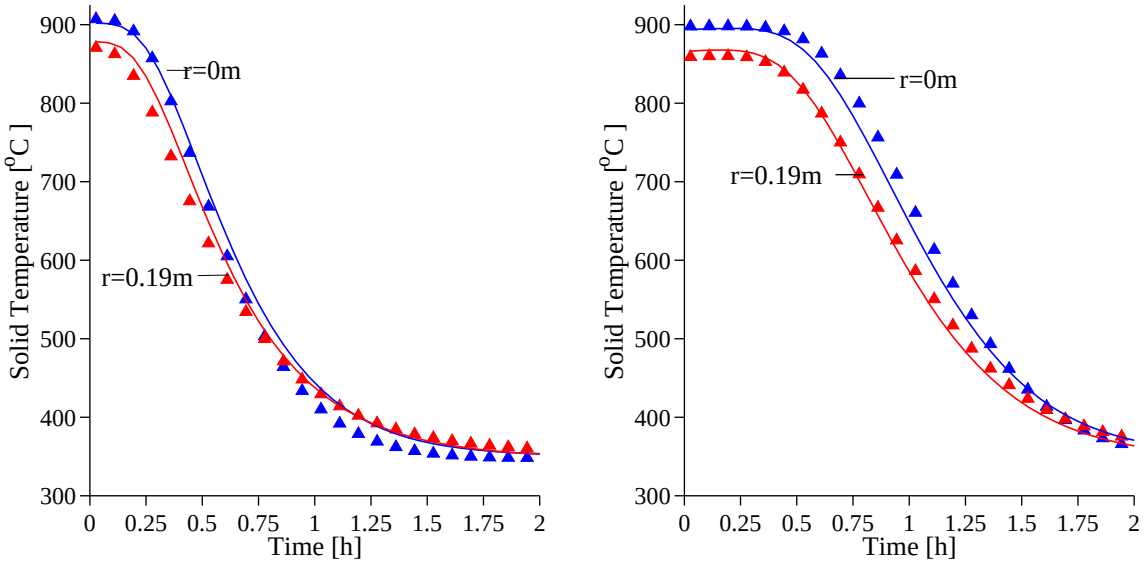

(c) Cooling $z = 0.21$ m

(d) Cooling $z = 0.41$ m

Figure 5.12: Comparison of the measured (markers) and predicted (curves) radial solid temperature profiles over the non-recuperated gas turbine temperature range, using Denstone particles

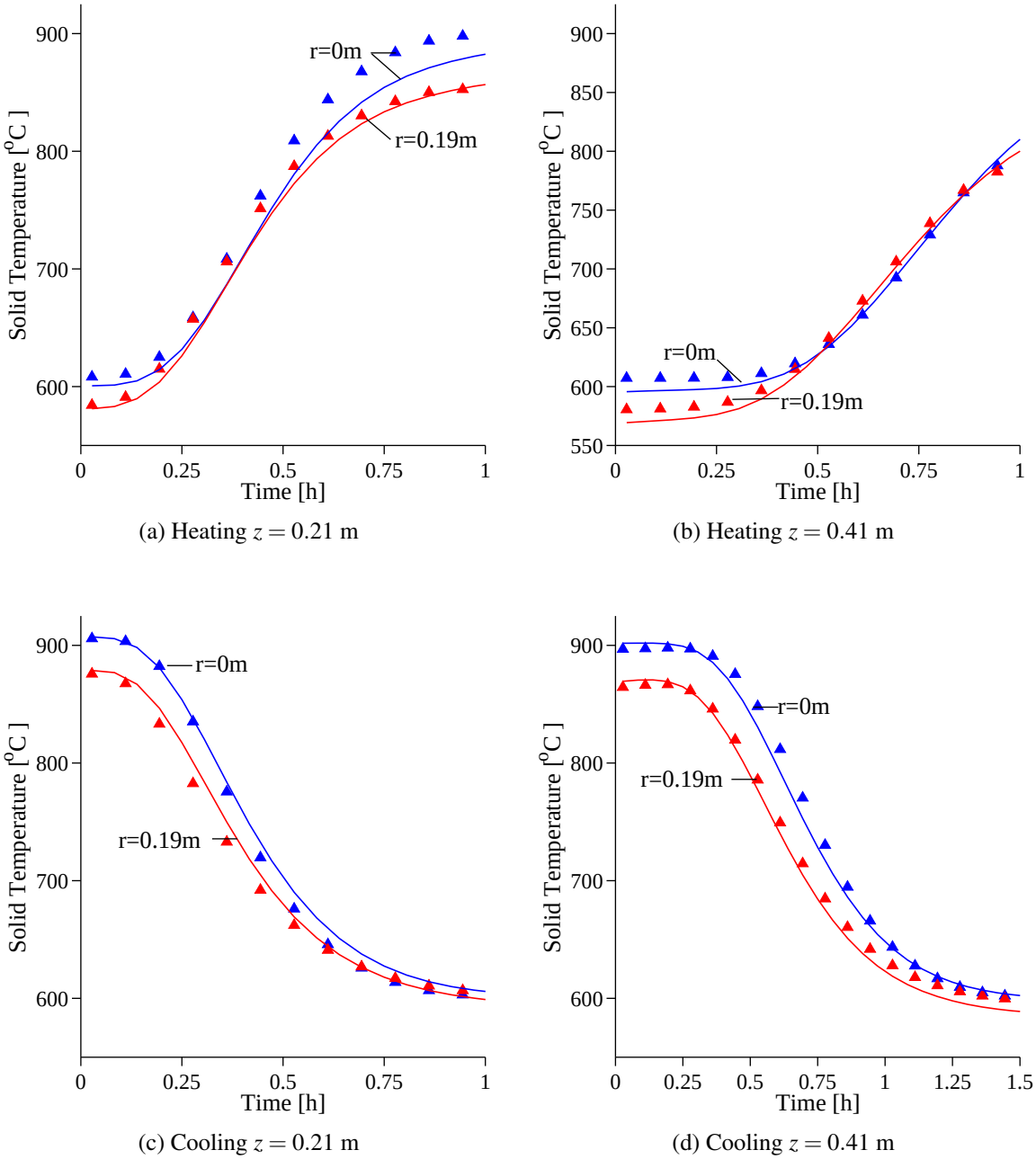

(a) Heating $z = 0.21$ m

(b) Heating $z = 0.41$ m

(c) Cooling $z = 0.21$ m

(d) Cooling $z = 0.41$ m

Figure 5.13: Comparison of the measured (markers) and predicted (curves) radial solid temperature profiles over the recuperated gas turbine temperature range, using Denstone particles

5.5 Conclusions

This chapter presents the extensive validation of the C-S model for sensible heat storage in a packed bed. The axial and radial temperature profiles within a packed bed of alumino-silicate

particles were used to verify the accuracy of the C-S model across a variety of temperature ranges, mass fluxes and bed configurations ($L_z = 0.62$ m and $L_z = 0.8$ m). The following conclusions are made:

- The D-C model is more complex to implement and has a higher computational cost than the C-S model. A Biot number analysis demonstrated that for sensible heat storage modelling the D-C model offers no significant improvement in accuracy over the C-S model. Therefore, for solid ceramic particles, intra-particle temperature gradients do not need to be explicitly modelled and can be taken into account in the C-S model through the use of the Jeffreson (1972) correction factor. Thus the C-S model is recommended for modelling sensible heat storage systems.

- The C-S model accurately describes the convective and conductive heat transfer in the packed bed test facility for a bed length of 0.8 m and charging temperature of 160 °C. A maximum NRMSD of 5.3% and 4.7% were recorded for the fluid and solid phase temperatures respectively along the packed bed centreline during heating and cooling tests where radiation effects are small.

- Wall channelling causes the preferential heating and cooling of the packed bed in the near wall region and a small decrease in thermocline velocity in the bed centre. The modelling correctly predicts trends in the near wall fluid temperature. A maximum NRMSD of 7.1% and 3.7% were recorded at bed depths of $z = 0.2$ m and $z = 0.4$ m for the 160 °C testing.

- The centreline temperature profiles are not strongly influenced by large changes in the inter-phase heat transfer coefficient. The Gunn (1978) correlation is validated for the packed bed of spherical particles.

- The C-S model, based on variable thermophysical properties, accurately predicts the thermocline shape and position for the high temperature testing conducted across temperature ranges of 20-350 °C, 350-900 °C, 20-600 °C, 600-900 °C. Along the bed centreline the maximum NRMSD was below 11 % for all the high temperature tests conducted.

- During the high temperature testing the highest NRMSD was located in the proximity of the bed inlet at $z = 0.11$ m. It is believed that this is caused by the inlet into the packed bed test facility, which did not include a diffuser. At high temperature a second peak in NRMSD was present at the bed exit due to thermal losses from the base of the test facility, which were not taken into account in the model.

- The trends in radial temperature profiles for the high temperature testing are consistent with the low temperature tests. The radial temperature profiles within the packed bed are accurately modelled at high temperature, with a maximum solid phase NRMSD of 3% being measured in the near wall region at $r = 0.19$ m.

- Temperature dependent changes in the solid phase heat capacity can influence the shape of the thermocline, depending on the temperature range of the analysis. The solid phase heat capacity of many ceramic heat storage materials exhibits a strong temperature dependence below 350 °C but a weak temperature dependence between 350 °C and 1000 °C. Variable property modelling should be used for modelling ceramic heat storage materials if the operating temperature range is below 350 °C but the constant property assumption is valid over the temperature ranges of non-recuperated and recuperated SGT cycles.

Overall the C-S model is shown to accurately predict the axial and radial temperature profiles within the packed bed test facility. Therefore this model can be used with confidence to conduct parametric design studies.

Chapter 6

Experimental validation: latent heat storage

6.1 Introduction

This chapter describes the selection of the latent heat storage model and its subsequent validation against experimental data for EPCMs. The C-S and D-C modelling approaches are analysed in Section 6.2, for EPCMs. The most suitable model is chosen to analyse the latent heat thermal storage system.

The fundamental difference between packed beds of solid ceramic and EPCM particles is the intra-particle heat transfer process. As stated by Akiyama et al. (1992), the thermal performance of a latent heat packed bed thermal storage system is dependent on the thermal performance of a single EPCM particle. The validation of the latent heat storage model is presented in Section 6.3, for a single EPCM particle, heated and cooled by convection. The validation of the full storage model is presented in Section 6.4 for a packed bed of macro-encapsulated Na_2SO_4 particles.

6.2 Model selection

The sensible heat storage model, validated in Chapter 5, accounts for the finite thermal conductivity of the ceramic particles by modifying the inter-phase heat transfer coefficient (Jeffreson, 1972). Beasley et al. (1989) and Zanganeh et al. (2014) proposed a form of the C-S

model to study the heat transfer in a packed bed of EPCM particles. The temperature gradients within the EPCM particles were not taken into account, instead the Bradshaw et al. (1970) correlation was used to correct the convective heat flux at the particle surface. It is not clear if the Jeffreson (1972) and Bradshaw et al. (1970) correlations can be applied directly to packed particles that undergo a phase change. Therefore a numerical study was conducted to determine the effects of intra-particle temperature gradients within a single EPCM particle. If the lumped capacitance approach adequately describes the heat transfer within a single EPCM particle, then the C-S model is suited to modelling the packed bed. However, if this approach is not accurate then the D-C heat transfer model needs to be utilised, taking into account intra-particle temperature gradients.

$$\Theta_{\mathrm{PCM}}(\zeta) = \frac{T_{\mathrm{PCM}}(\zeta) - (T_m - 100)}{(T_m + 100) - (T_m - 100)} \tag{6.1}$$

$$= \frac{T_{\mathrm{PCM}}(\zeta) - T_m + 100}{200} \tag{6.2}$$

The analysis was based on a 40 mm diameter EPCM particle, with a negligible shell thickness that is heated by a gas stream (h_p fixed at 40 W/m^{2}K). The thermal conductivity of the liquid and solid phases were assumed equal and calculated according to the specified Biot number. The initial temperature of the sphere was ($T_m - 100$ °C) and it was heated by a gas stream at ($T_m + 100$ °C). The normalised PCM temperature Θ_{PCM} is calculated by Eq.(6.2). Under the prescribed initial and gas heating temperatures, $\Theta_{\mathrm{PCM}} = 0.5$ at the melting point T_m. The latent heat for the particle was based on Na_2SO_4 at 162 kJ/kg (Barin et al., 1977). Figure 6.1 shows the PCM temperature profiles at the centre and surface of the particle. At a Biot number of 0.01 the particle melts isothermally. Thus this temperature profile represents the lumped capacitance solution. At a Biot number of 0.1 there is a small difference between the surface and centre temperatures of the particle. The effect of intra-particle conduction becomes more prominent at Biot numbers greater than 0.5, where the surface temperature of the PCM rises faster than the centre temperature.

In order to determine the accuracy of the lumped capacitance approach for EPCM particles, Eq.(2.23) from the D-C model was compared to the lumped capacitance solution for a single sphere, given by:

$$\rho_{\mathrm{PCM}} c_{\mathrm{PCM}} \frac{\partial T_{\mathrm{PCM}}}{\partial t} = \frac{6h_p^*}{d_p}\left(T_f - T_{\mathrm{PCM}}\right) \tag{6.3}$$

where h_p^* was calculated according to Jeffreson (1972) and $h_p = 40$ W/m^{2}K.

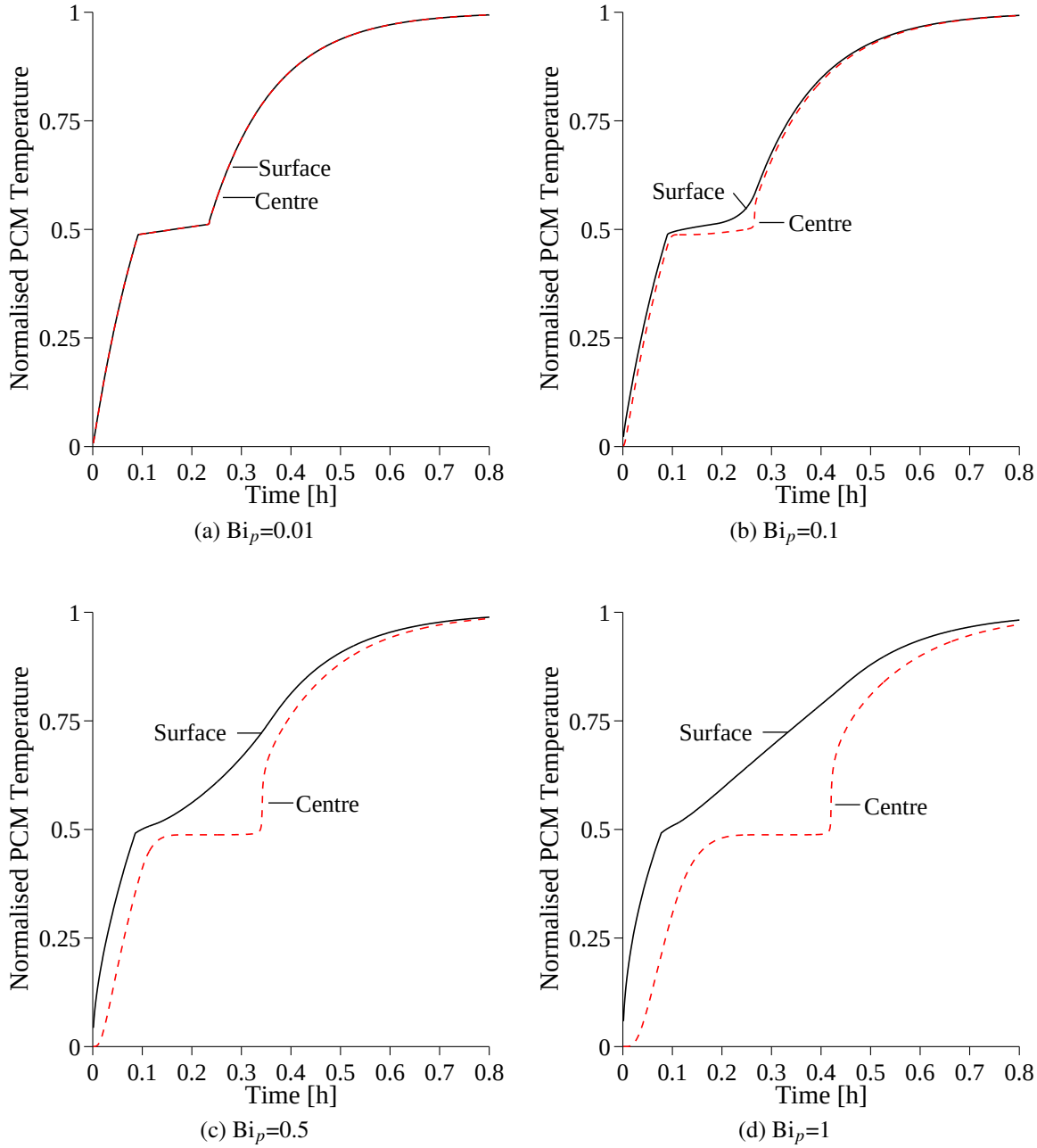

(a) Bi_p=0.01 (b) Bi_p=0.1

(c) Bi_p=0.5 (d) Bi_p=1

Figure 6.1: Comparison of the predicted surface ($\zeta = 0.02$ m) and centre ($\zeta = 0$ m) temperatures for a single EPCM sphere heated by convection

The accuracy of the lumped capacitance solution was determined by examining the rate that energy is stored within the EPCM particle. Figure 6.2(a) shows the calculated convective flux for the heating of a solid particle. Across the range of Biot numbers tested, there is excellent agreement between the calculated heat fluxes of Eqs.(2.23) and (6.3). Thus the modified heat transfer coefficient h_p^* allows for the C-S model to predict the same solution as the D-C model for sensible heat transfer. The case of the PCM undergoing a phase change is

presented in Figure 6.2(b). At Biot numbers exceeding 0.1, there is poor agreement between the calculated heat flux values. The lumped capacitance approach predicts a mean temperature for the particle. However, as shown in Figure 6.1, there is a large difference between the particle surface and centre temperatures for Biot numbers greater than 0.1. As the convective heat flux is a function of the particle surface temperature, this leads to errors in the lumped capacitance approach. Figure 6.2(b) shows that the Jeffreson (1972) correction factor, is not recommended for EPCM particles where the Biot number exceeds 0.1. Due to the low thermal conductivity of the inorganic salts considered in this work, the Biot numbers are larger than 0.1. Thus the D-C model was chosen to study the latent heat transfer in the packed bed.

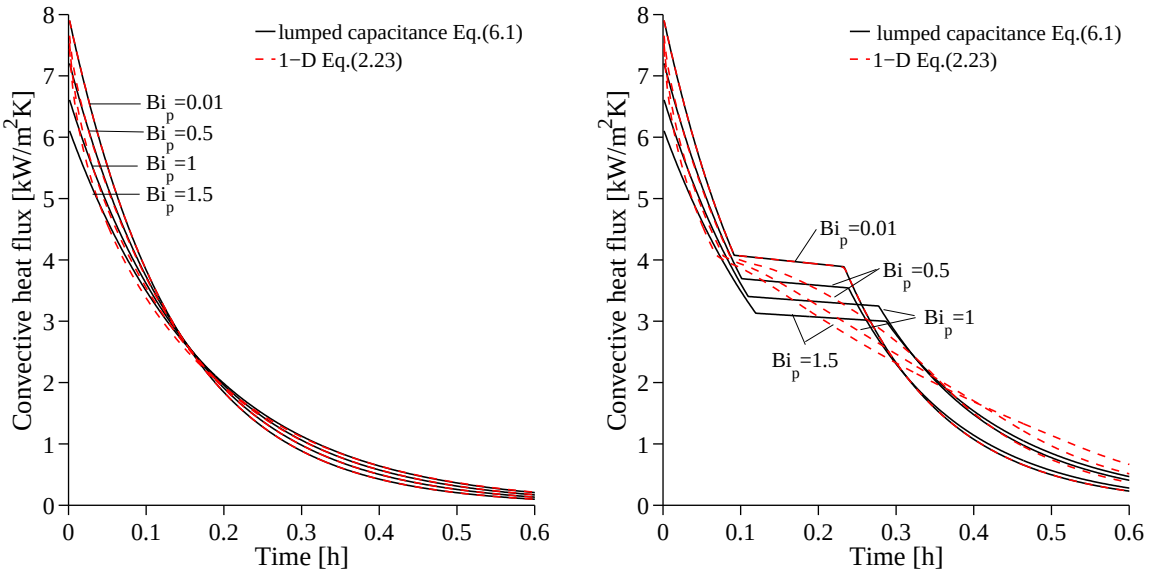

(a) Heating solid PCM

(b) Melting PCM

Figure 6.2: Effects of intra-particle temperature gradients on a single PCM sphere heated by convection

6.3 Single particle testing

6.3.1 Model validation

Akiyama et al. (1992) and Yagi and Akiyama (1995) conducted numerical and experimental tests to study the internal heat transfer within an EPCM sphere. Both inorganic PCMs (KNO_3-$NaNO_3$ and NaCl) and metallic PCMs (Al, Pb, Al-12Si) were tested using nitrogen as the heat transfer fluid. The EPCM sphere was manufactured by filling a hollow stainless steel sphere (OD 40 mm, ID 36 mm) with liquid PCM. The temperature of the sphere surface

($\zeta = 0.02$ m), midpoint (ζ=0.01 m) and centre ($\zeta = 0$ m) were measured using thermocouples, while a micro-suction pyrometer was used to measure the fluid temperature.

A diagram of the test apparatus is provided in Figure 6.3. In order to reduce the radiation heat transfer between the sphere and surroundings a radiation shield was developed. The thermal capacitance of the radiation shield was designed to minimise the temperature difference between the sphere surface and the shield. Both the sphere surface and radiation shield were coated with a high temperature paint of known emissivity. As described by Yagi and Akiyama (1995) the inclusion of the radiation shield reduced the energy transferred by radiation from 50% to 10%.

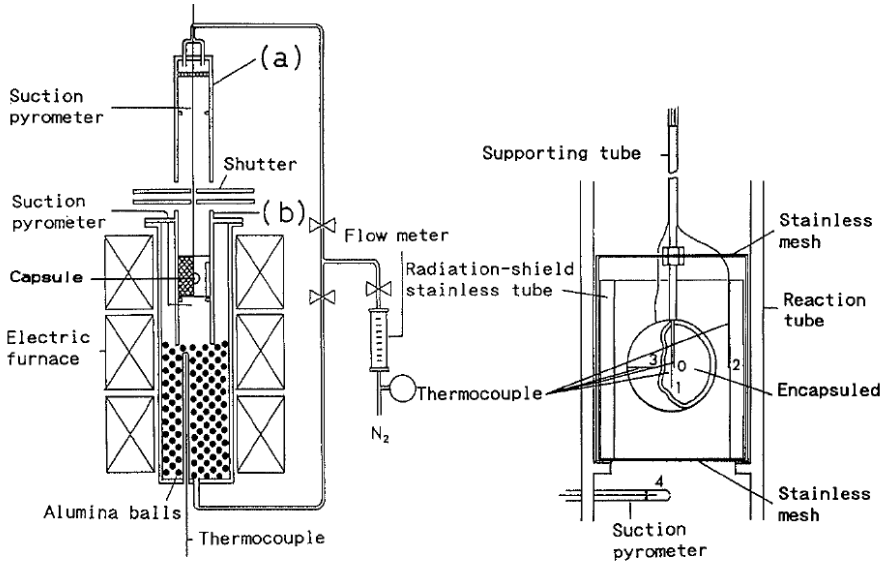

Figure 6.3: Test apparatus for heating a cooling a single PCM sphere in a convective gas stream (Yagi and Akiyama, 1995). Permission for reuse obtained from Elsevier.

Akiyama et al. (1992) do not provide the convection coefficients that they applied to their model for comparison with the experimental data. However, they do provide the predicted surface temperature profiles from their model. Using this information and the experimental data provided it is possible to recalculate the heat transfer coefficient for each test. This was achieved by using an energy balance method, as outlined in Appendix F. The average heat transfer coefficient that was calculated from the Akiyama et al. model and was then applied to the current model. This approach of calculating an average heat transfer coefficient yielded good agreement between the current model and the Akiyama et al. model.

The modelling of the EPCM particle includes the stainless steel shell, which exchanges energy with the PCM at the inner surface of the shell via conduction. In Figures 6.4 to 6.9 the particle surface temperature (outer stainless steel shell) is labelled as PCM ($\zeta = 0.02$ m).

The results for aluminium as a PCM are presented in Figures 6.4 and 6.5. This metallic PCM has a very high thermal conductivity (greater than 100 W/mK), which ensures isothermal melting and solidification. Therefore because aluminium does not exhibit internal temperature gradients it provides a simple test case to experimentally validate the apparent heat capacity method that is used in the D-C model. The high thermal conductivity of the PCM also ensures that circumferential variations in the local heat transfer coefficient do not influence the results.

Overall there is excellent agreement between the current model and the data presented by Akiyama et al. (1992), both experimental and numerical. During the melting of the PCM (Figure 6.4) the temperature plateau at 660 °C is notably larger than during the solidification cycle (Figure 6.5). This is caused by the driving temperature difference between the PCM melting temperature and the nitrogen gas flow temperature. During the heating cycle, the nitrogen gas temperature is approximately 40 °C higher than the melting temperature of the aluminium. However, during cooling the nitrogen gas temperature is approximately 590 °C below the melting temperature, resulting in a significantly higher rate of solidification. Thus for the design of an EPCM packed bed it is important to carefully consider the driving temperature difference for the melting and solidification, as this will affect the rate that latent heat energy is stored and released.

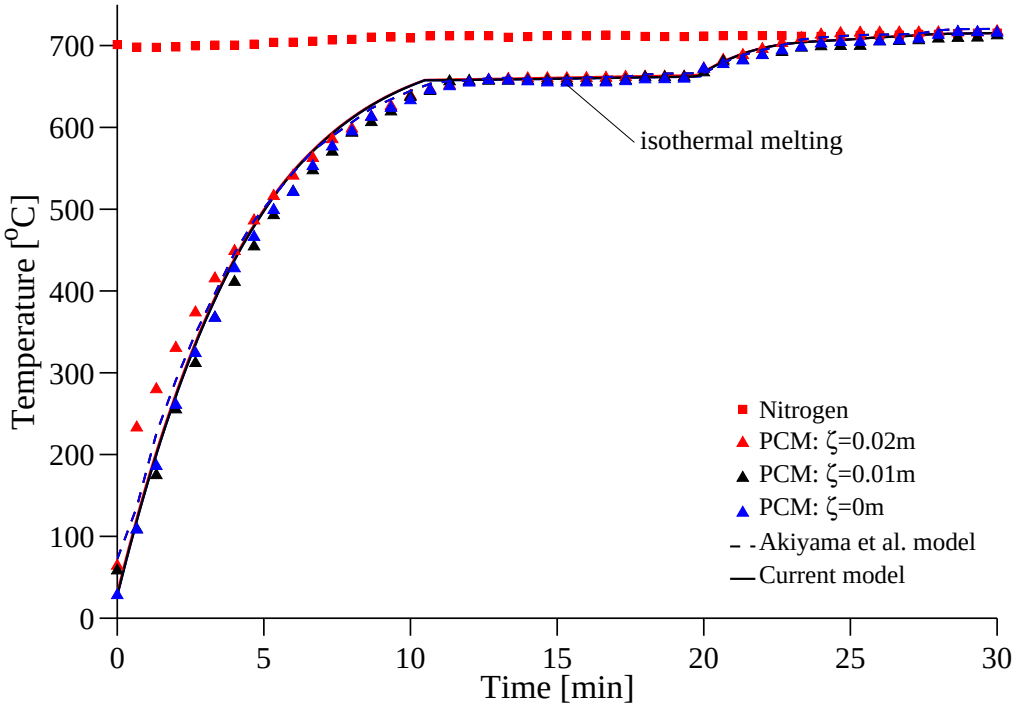

Figure 6.4: Comparison of the measured (markers) and predicted (curves) temperature profiles for the melting of an Aluminium EPCM sphere

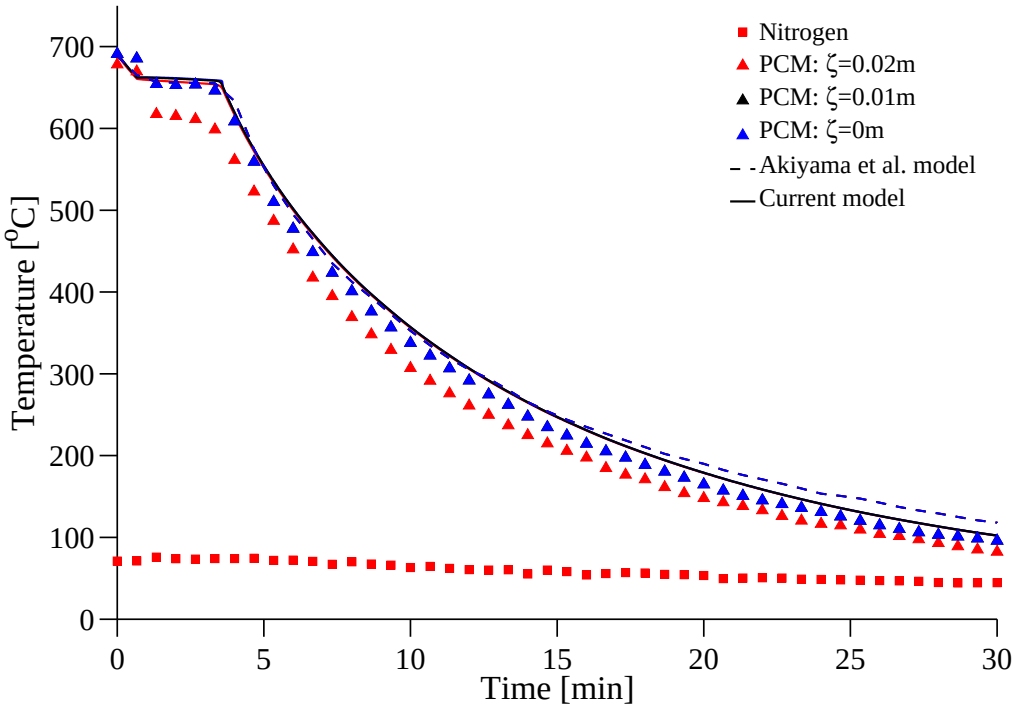

Figure 6.5: Comparison of the measured (markers) and predicted (curves) temperature profiles for the solidification of an Aluminium EPCM sphere

Figures 6.6 and 6.7 present the heating and cooling of a eutectic mixture of KNO_3 and $NaNO_3$ inorganic salts. Both the measured and predicted temperature profiles show that this PCM does not melt isothermally. Due to the low thermal conductivity of the PCM, there is a large temperature difference between the particle surface and centre.

According to Akiyama et al. (1992), the KNO_3-$NaNO_3$ undergoes a phase transition at 105 °C ($\Delta h_{pt} = 27.3$ kJ/kg), and it melts at 222 °C ($\Delta h_{fus} = 94$ kJ/kg). Therefore this PCM exhibits two periods of constant temperature upon heating and cooling. The agreement between the current model and the experimental data is satisfactory for the initial heating phase. Subsequent to the phase transition, the accuracy of the model deteriorates. The deviations between the measured and predicted temperature profiles occur before the surface temperature of the particle exceeds the melting temperature of the salt ($t \approx 12$ min). This shows that the differences are related to the heat transfer in the solid salt between 100 °C and 200 °C. During melting, the lack of a defined plateau in the measured temperature profiles indicates that salt does not melt concentrically. Due to the change in density between the solid and liquid salt, the solid sinks to the bottom of the particle during melting. As the intra-particle heat transfer model is only one-dimensional these effects are excluded, which is a possible cause for the differences between the numerical and experimental data.

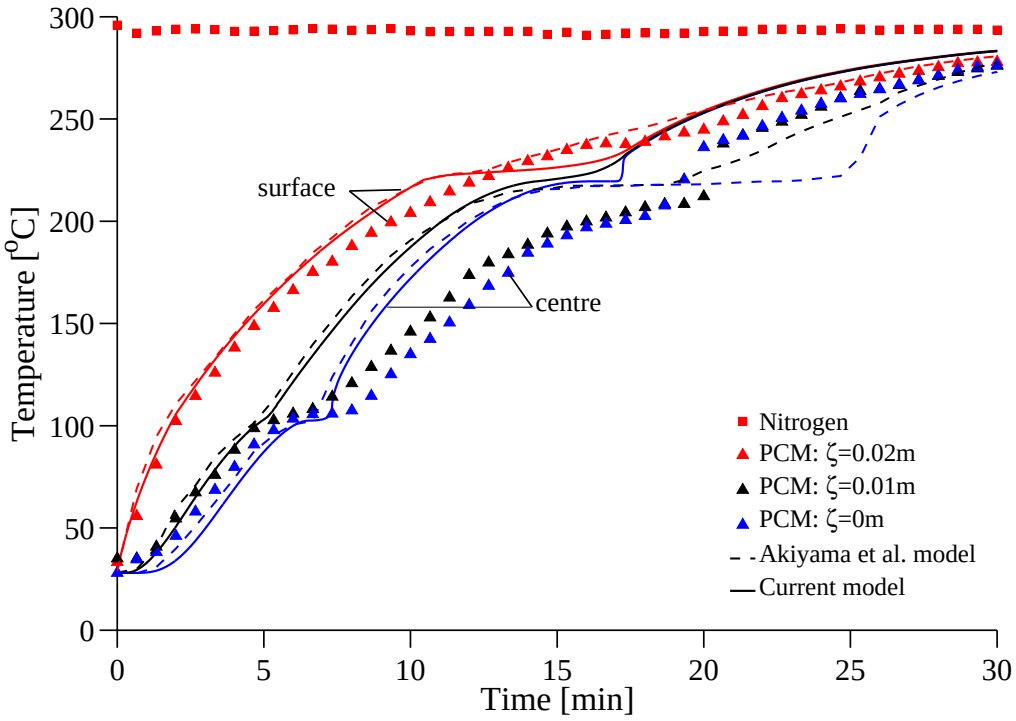

Figure 6.6: Comparison of the measured (markers) and predicted (curves) temperature profiles for the melting of a KNO_3-$NaNO_3$ EPCM sphere

While the KNO_3-$NaNO_3$ is in solid form, the predictions from current model are in good agreement with the Akiyama et al. model. The small temperature difference between the models is related to the use of an average heat transfer coefficient in the current work. Once the salt starts to melt, natural convection effects become more prominent and increase the rate of melting within the particle. The current model includes natural convection, through Eq.(3.55). Therefore it predicts a melting time that is in better agreement with the experimental data than the Akiyama et al. model. If this effect is excluded from the current model the temperature profiles are in good agreement with the Akiyama et al. model for the full heating test.

As shown in Figure 6.7, the use of a one-dimensional heat transfer model provides a better prediction of the experimental data during cooling. The salt solidifies inwards from the particle shell in a concentric process, therefore the differences in density between the liquid and solid salt does not influence the results. In contrast to the heating test there is a well defined plateau in the measured temperature profiles during the solidification of the salt. Xia et al. (2010) state that natural convection effects are not important for the solidification of the liquid PCM. However, as shown in Figure 6.7 this statement contradicts the experimental data. The Akiyama et al. model under-predicts the cooling rate of the liquid PCM. This

indicates that natural convection currents exist that increase the rate of heat transfer through the liquid PCM. Therefore as a first order approximation Eq.(3.55) was used to model the melting and solidification of the PCM. The driving temperature difference for the Rayleigh number calculation was $(T_m - T_p(\zeta = 0))$ for the cooling cycle. This provides an accurate prediction of the cooling rate of the liquid PCM.

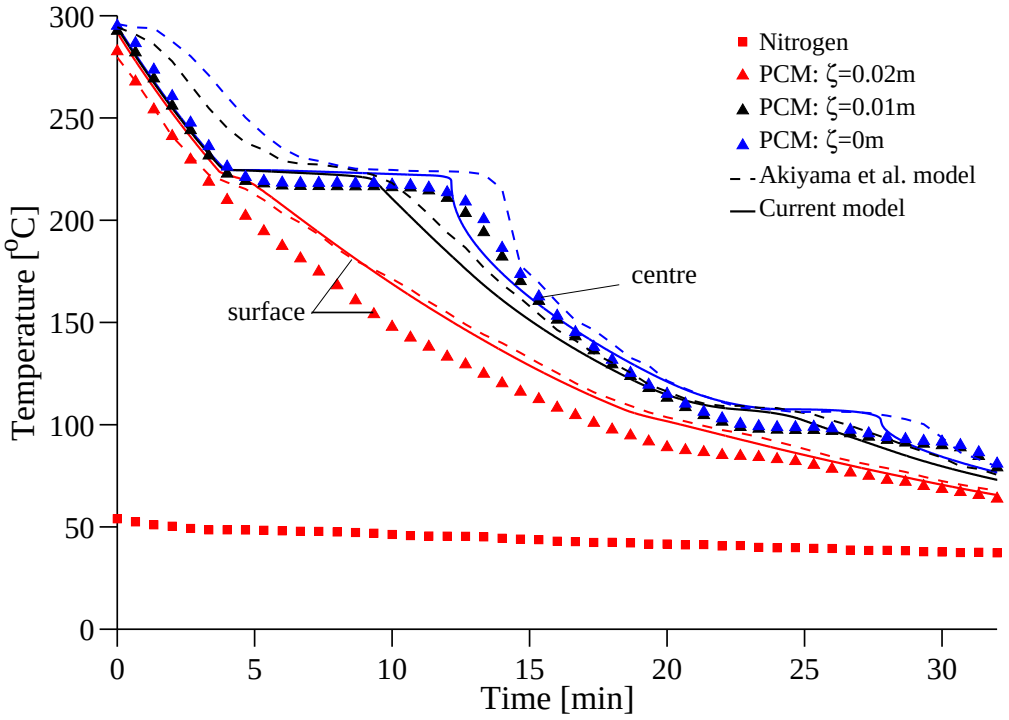

Figure 6.7: Comparison of the measured (markers) and predicted (curves) temperature profiles for the solidification of a KNO_3-$NaNO_3$ EPCM sphere

For the NaCl, shown in Figures 6.8 and 6.9, there are no solid-solid phase transitions. The trends in the predicted temperature profiles from the current model are consistent with those from the Akiyama et. al model. Again, the inclusion of natural convection in the current model reduces the melting time. It should be noted that a thermal conductivity of 4 W/mK was applied by Akiyama et al. in their model for both the solid and liquid NaCl phases. This value is not realistic for the thermal conductivity of liquid NaCl, which according to Galamba et al. (2004), is 0.6 W/mK. If this value was used in the Akiyama et al. model the errors would be larger.

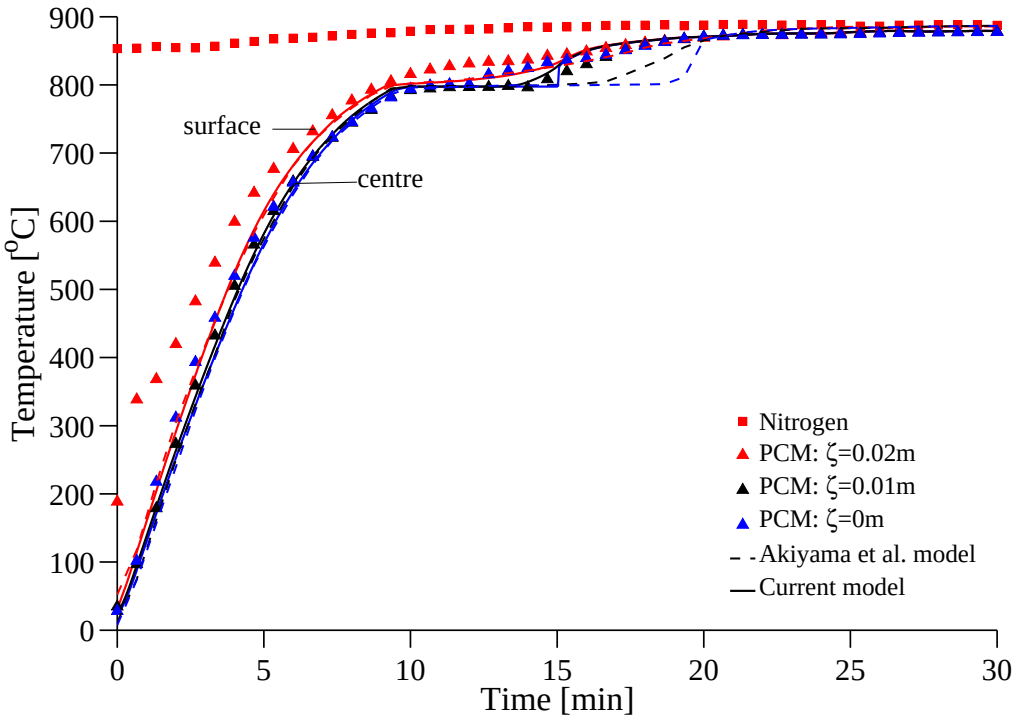

Figure 6.8: Comparison of the measured (markers) and predicted (curves) temperature profiles for the melting of a NaCl EPCM sphere

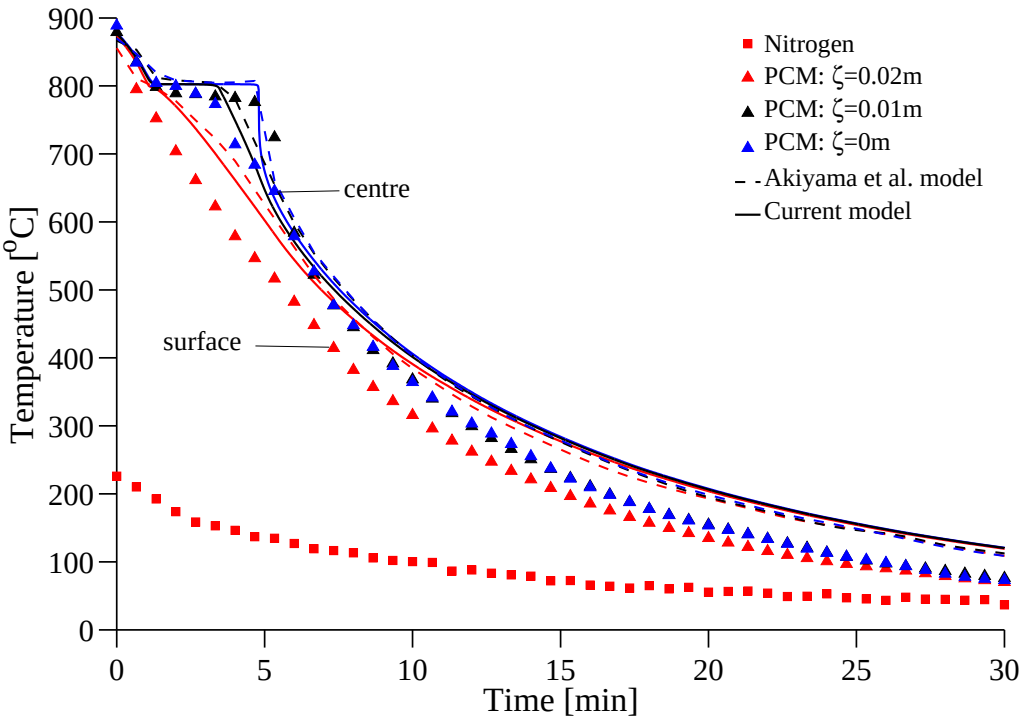

Figure 6.9: Comparison of the measured (markers) and predicted (curves) temperature profiles for the solidification of a NaCl EPCM sphere

It should be noted that there is an anomaly present in the experimental data, where the temperature profiles at $\zeta = 0$ m respond to heating and cooling faster than at $\zeta = 0.01$ m.Yagi and Akiyama (1995) state that this is possibly caused by the sinking of the solid during the melting of the PCM. It is not clear why this would affect the results for the solidification process. It is also possible that radiation energy exchange through the liquid salt could influence the measurements at high temperature. The current model predicts a temperature plateau width at 801 °C that agrees well with the experimental measurements during the heating and cooling tests.

6.3.2 Conclusions for the single EPCM analysis

This section provided the validation of the intra-particle heat transfer component of the D-C model for metallic and inorganic salt EPCMs. Despite the complex heat transfer process within the EPCM particle, the model provides an acceptable prediction of the intra-particle temperature profiles during melting and solidification. The following conclusions are made:

- When natural convection effects are excluded, the predicted temperature profiles from the current model are in good agreement with the Akiyama et al. model.
- Metallic PCMs melt and solidify isothermally and can be accurately modelled using the lumped capacitance assumption.
- The apparent heat capacity method accurately models the phase change process. This is demonstrated by the excellent agreement between the current model and the experimental data for the aluminium PCM.
- The driving temperature difference between the fluid and the PCM melting temperature can significantly affect the length of time required to melt and solidify the PCM.
- Inorganic salts exhibit strong intra-particle temperature gradients during melting and solidification, which should be taken into account in the modelling. Therefore the D-C model is best suited to modelling a packed bed TES using inorganic salt EPCM particles.
- Natural convection currents in the liquid inorganic salts increase the phase change rate. By implicitly accounting for natural convection through an effective conductivity term, the current model provides a better representation of the measured temperature profiles than the Akiyama et al. model.

6.4 Packed bed testing

In order to further validate the D-C model, experiments were conducted using a packed bed of macro-encapsulated Na_2SO_4 particles. The development of these particles, along with their thermal properties, is discussed in Section 4.4. The accuracy of the D-C model is determined by comparing the predicted fluid temperature profiles with the experimental measurements made within the Na_2SO_4 bed. Initial testing was conducted with a packed bed length of 0.51 m of Na_2SO_4 particles . However, a number of particle shells cracked during cooling, once the salt had solidified. This cracking phenomenon reduced the number of particles available for testing. Therefore a second bed configuration was subsequently tested with a bed length of 0.4 m of Na_2SO_4 particles. A discussion of the particle cracking is provided in Section 6.4.3.

6.4.1 Low temperature testing

Initial testing of the packed bed of macro-encapsulated Na_2SO_4 particles was conducted at a maximum charging temperature of 230 °C. Over this temperature range the energy is stored in sensible heat form only. This low temperature testing was conducted to verify the accuracy of the D-C model for the new packed bed configuration of 45 mm particles and 0.51 m bed length. A comparison between the measured and predicted fluid temperature profiles along the centreline of the packed bed is presented in Figures 6.10 and 6.11.

Due to the low bed-to-particle diameter ratio ($D/d_p = 8.9$) wall channelling is more prevalent for this bed configuration. The previous sensible heat testing, conducted using 19 mm Denstone particles, had a bed-to-particle diameter ratio of 21. Therefore it is important to verify the D-C model for the simpler sensible heat storage case, prior to testing the latent heat storage. Figures 6.10 and 6.11 show that the fluid temperature profiles are accurately predicted by the D-C model. This test case provides further validation of the wall channelling approach utilised in this work. For the 45 mm particles, the flow modelling indicates that the velocity within the core region of the packed bed, decreased by 18% compared to the plug flow velocity. Figure 6.11 demonstrates that the shape and position of the thermocline is predicted with a high degree of accuracy during the heating cycle, while the model overestimates the initial rate of cooling. However, as the thermocline moves deeper into the bed, the shape is predicted correctly.

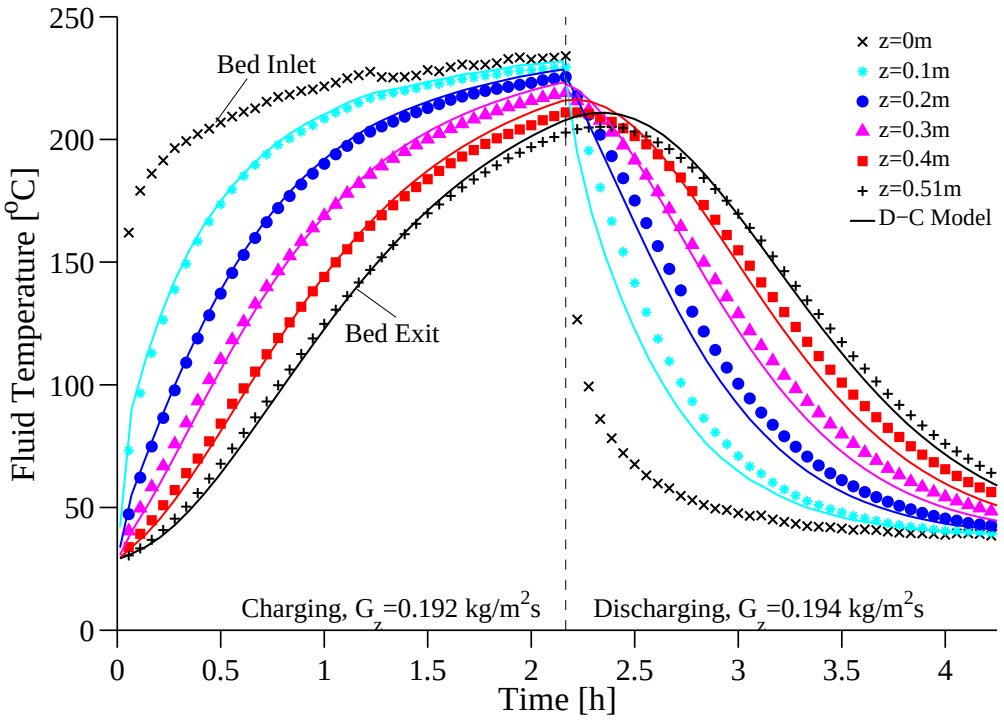

Figure 6.10: Comparison of the measured (markers) and predicted (curves) centreline fluid temperature profiles for the low temperature test, using Na_2SO_4 EPCM particles.

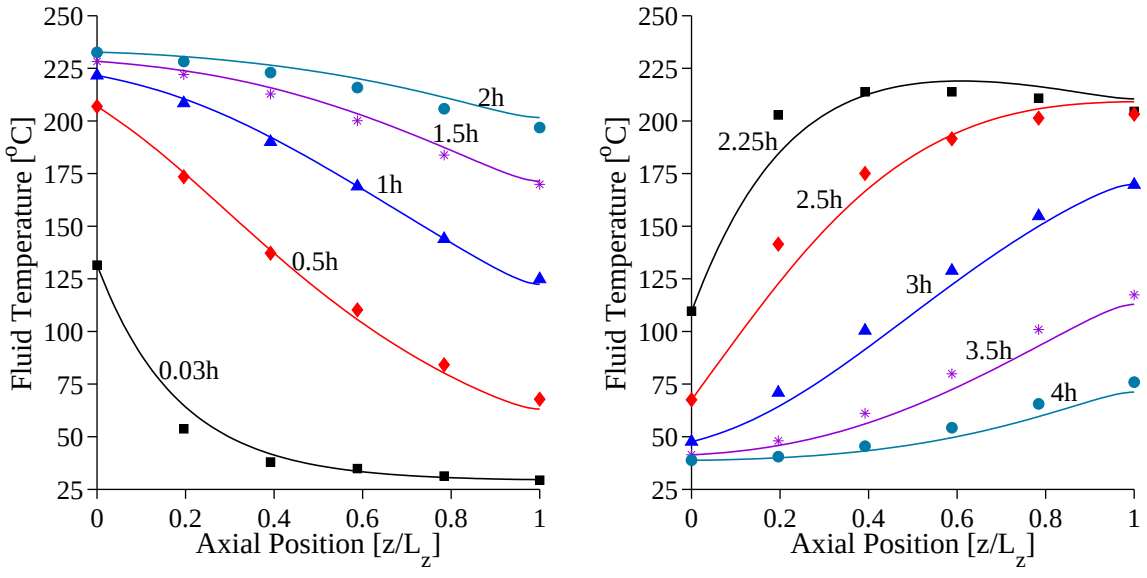

(a) Heating packed bed

(b) Cooling packed bed

Figure 6.11: Comparison of the measured (markers) and predicted (curves) centreline fluid thermoclines for the low temperature test, using Na_2SO_4 EPCM particles.

Figure 6.12 presents the NRMSD between the measured and predicted fluid temperature profiles for the low temperature test. The maximum NRMSD is 5.2% for the low temperature heating and cooling of the packed bed. Therefore the D-C model provides an accurate prediction of the fluid temperature profiles for the new packed bed configuration and it is suitable for further analysis of the melting and solidification of the Na_2SO_4.

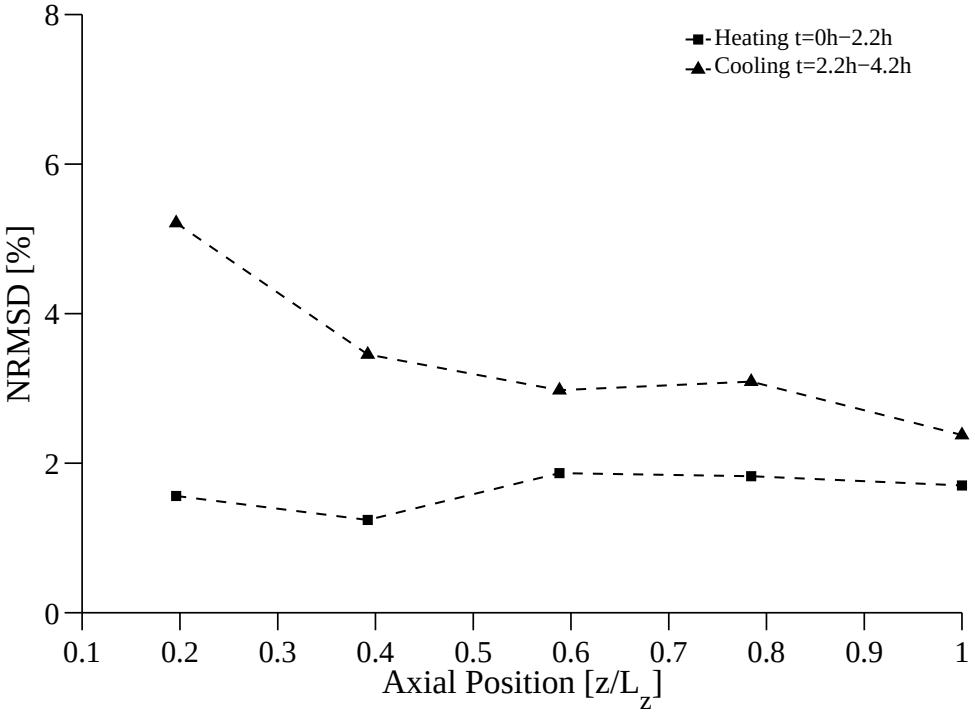

Figure 6.12: Normalised RMS deviations between the measured and predicted fluid centreline temperature profiles for the low temperature test

6.4.2 High temperature testing

The high temperature testing involved heating the macro-encapsulated particles to above the melting temperature of the Na_2SO_4. The measured fluid temperature profiles for the first high temperature test are presented in Figure 6.13. Attempts were made to measure the PCM temperature within a series of Na_2SO_4 particles. However, the high test temperature, combined with the corrosive molten salt led to failures of these thermocouples. Therefore only the fluid temperature profiles could be utilised. During the heating cycle an electrical fault required the blower and burner to be shut down for a brief period. This caused the inlet fluid temperature to drop rapidly before the burner could be relighted and the heating cycle

continued. There were no disruptions during the cooling cycle. This specific test could not be repeated due to the particle breakage, as no more EPCM particles were available within a reasonable time frame. The results for this test are analysed in three distinct regions, namely the preheating cycle (prior to burner shut down), the heating cycle and the cooling cycle. These regions of the test are illustrated in Figure 6.13.

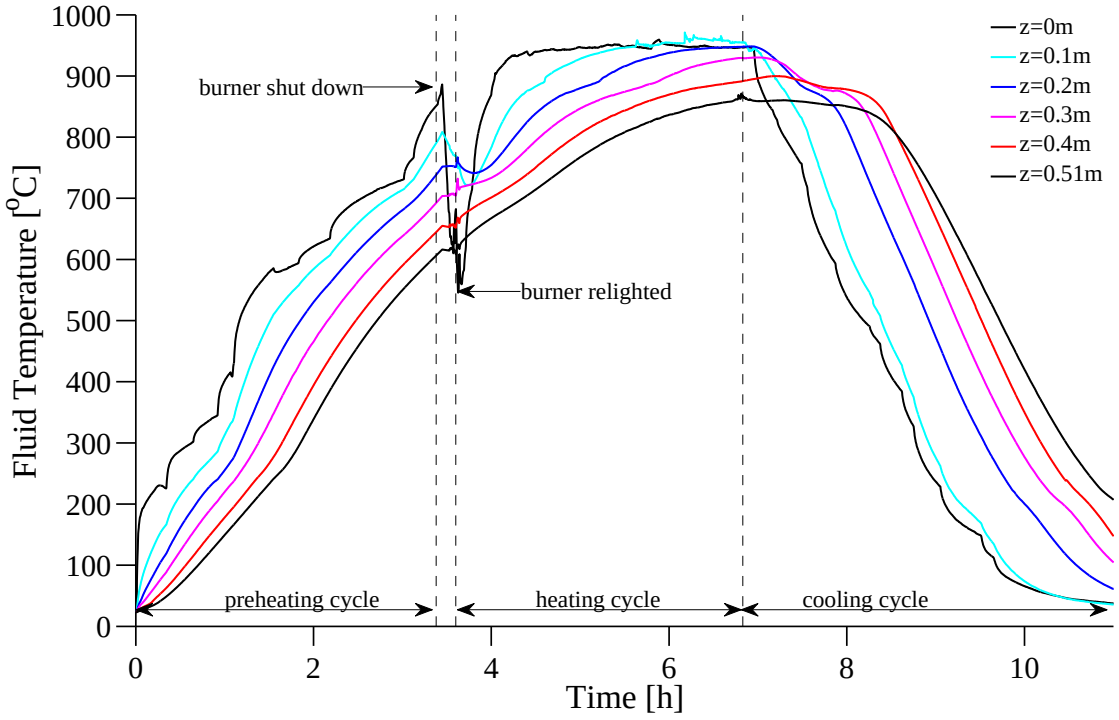

Figure 6.13: Measured centreline fluid temperature profiles from the packed bed of 45 mm macro-encapsulated Na_2SO_4 particles for the first high temperature test

Figure 6.14 presents the results for the preheating cycle. In order to reduce the thermal stresses on the EPCM particles the inlet gas temperature was steadily increased at an average of approximately 4 °C/min. The predicted fluid temperature profiles exhibit good agreement with the experiment over the preheating cycle. At 249 °C the Na_2SO_4 undergoes a solid-solid phase transition where 76 kJ/kg of energy is absorbed (Barin et al., 1977). The phase transition appears to have a stronger influence on the predicted temperature profiles than the measured profiles. This indicates that the material tested absorbs a lower amount of energy during the phase transition than predicted by the literature.

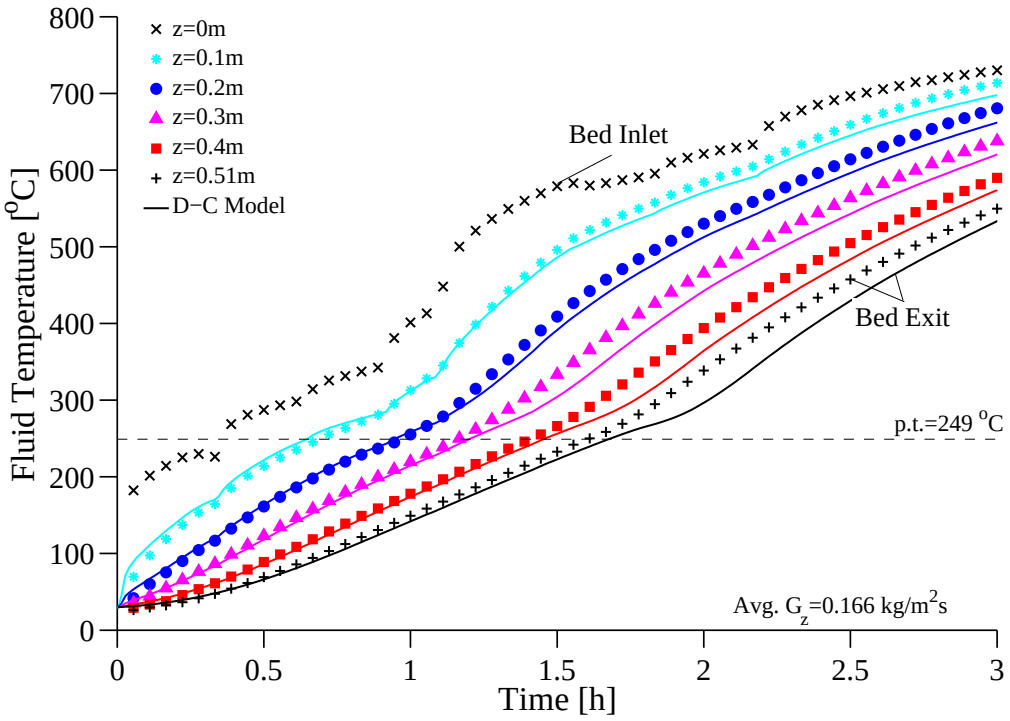

Figure 6.14: Comparison of the measured (markers) and predicted (curves) centreline fluid temperature profiles for the first preheating test, using Na_2SO_4 EPCM particles.

Figure 6.15 presents the results for the melting of the Na_2SO_4 particles, up to a maximum temperature of 950 °C. The effect of the phase change at 884 °C is shown in the measured and predicted temperature profiles. Between 650 °C and 884 °C, there is good agreement between the D-C model and the measured temperature profiles. After the salt begins to melt, the measured temperature profiles at each axial location increase temperature at a higher rate than predicted by the D-C model. This is potentially caused by the melting process within each particle. As shown by Goswami (2012) the solid salt sinks to the bottom of the particle and presses up against the shell. This contact increases the rate of melting within the particle. It is also possible that the literature value for the liquid specific heat capacity from Barin et al. (1977) differs from the Na_2SO_4 that was tested. A number of institutions in South Africa were contacted to test the heat storage properties of the materials used in this work. Unfortunately the maximum operating temperature of the available DSCs (Differential Scanning Calorimeter) was below 884 °C. Future work should focus on verifying these properties for the Na_2SO_4 supplied by CHC Resources.

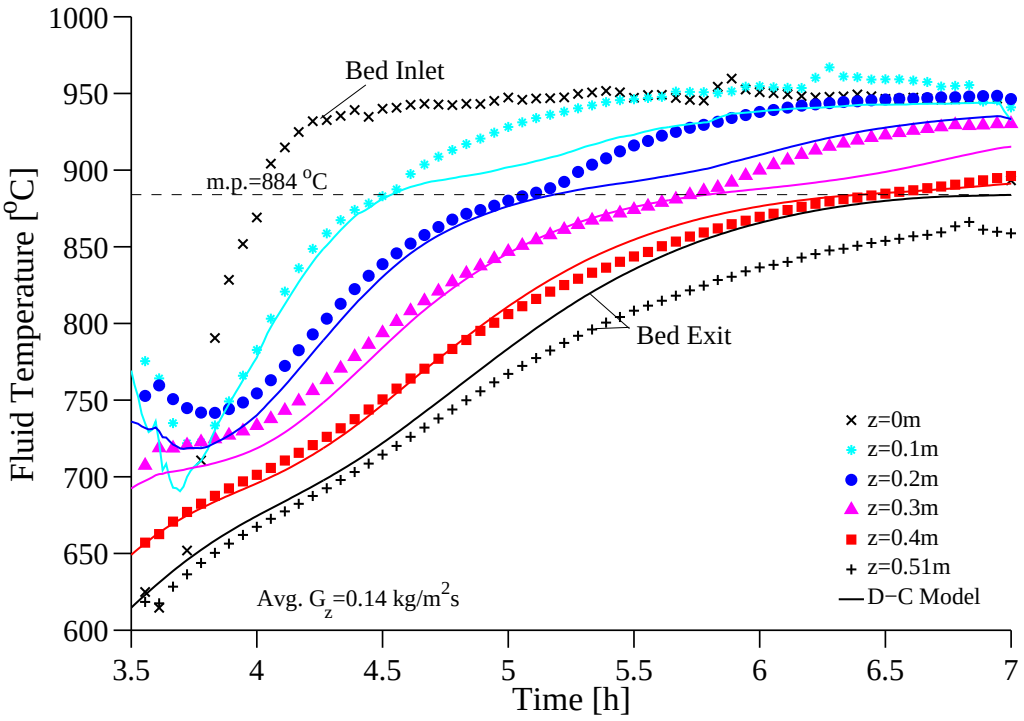

Figure 6.15: Comparison of the measured (markers) and predicted (curves) centreline fluid temperature profiles for the first heating test, using Na_2SO_4 EPCM particles.

Figures 6.16 and 6.17 show the cooling of the packed bed with molten Na_2SO_4 within the particles. Both the model and experiment demonstrate the desired effect of utilising a latent heat storage system. During cooling the fluid temperature decreases until the molten Na_2SO_4 begins to solidify at 884 °C. This causes the fluid temperature in the packed bed to stabilise (remain constant). Once the Na_2SO_4 has solidified the fluid temperature starts to decrease as sensible heat thermal energy is withdrawn from the packed bed. During the cooling cycle it is more likely that the PCM solidifies concentrically. As the PCM solidifies inwards from the shell, there is no sinking of the solid PCM within the particles. This is suggested to be the reason for the increase in precision of the model during cooling. The D-C model under-predicts the rate of cooling at the measurement position $z = 0.1$ m. Figure 6.18(b) shows that the shape of the measured thermocline is in good agreement with the D-C model during cooling. However, the measured temperature at $z = 0.1$ m is not consistent with the overall measured thermocline shape. A potential cause for this discrepancy is inlet flow effects into the packed bed. Figure 6.18(a), shows that the model accurately predicts the thermocline shape across the full heating test. The deviation between the model at $z = 0.1$ m is not present during the heating cycle.

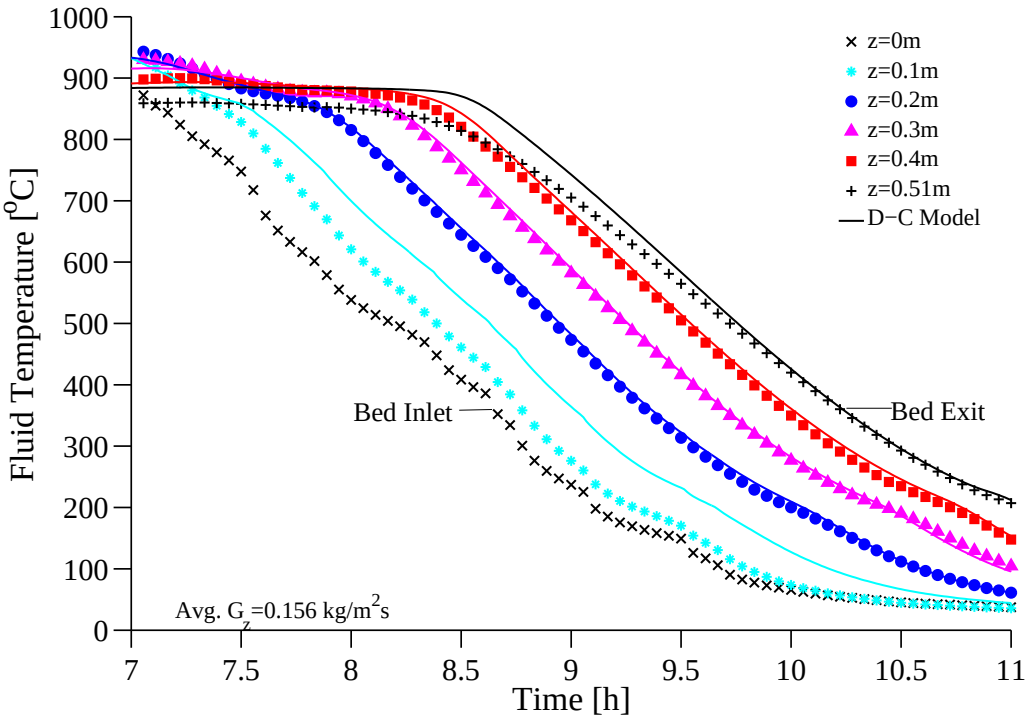

Figure 6.16: Comparison of the measured (markers) and predicted (curves) centreline fluid temperature profiles for the first cooling test, using Na_2SO_4 EPCM particles (extended).

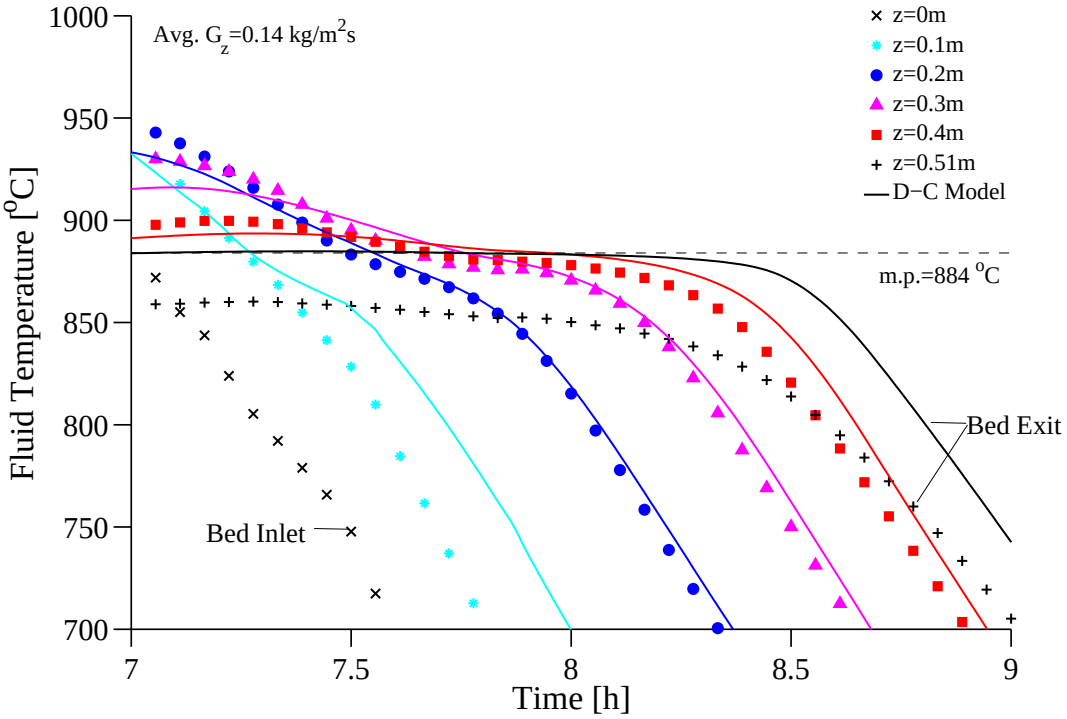

Figure 6.17: Comparison of the measured (markers) and predicted (curves) centreline fluid temperature profiles for the first cooling test, using Na_2SO_4 EPCM particles.

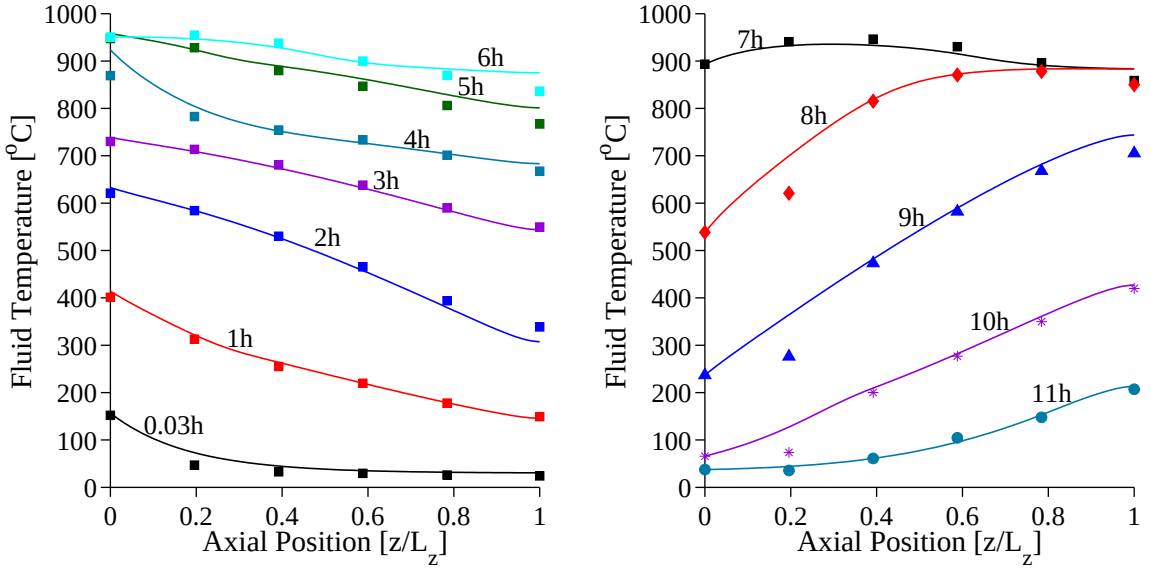

(a) Heating

(b) Cooling

Figure 6.18: Comparison of the measured and predicted fluid thermoclines for the first high temperature test, using Na_2SO_4 EPCM particles.

Figure 6.19 presents the NRMSD during the high temperature testing. The calculations are based on five distinct testing regions. For the preheating of the packed bed (0-3.4 h) the maximum NRMSD is 3.5%. As the bed did not reach steady state across the preheating temperature range, the NRMSD were calculated using the preheating temperature range at each measurement position. During the melting of the PCM (3.7-6.8 h) the maximum NRMSD increases to 9%. If the entire heating range is considered (0-6.8 h), the NRMSD is below 3%. Considering the solidification of the PCM (6.8-8.5 h), there is a 23% normalised RMS deviation at the packed bed exit. This is caused by heat losses from the base of the test facility at high temperature, which are not taken into account in the modelling.

Considering the full cooling range (6.8-11 h), the maximum NRMSD decreases to 6.3%. If the exit of the packed bed is excluded the D-C model predicts the measured temperature profiles to within a NRMSD of 10%, for the melting and solidification of the PCM. Considering the complexity of the heat transfer, this is a good result and validates the use of the model to conduct further parametric design studies.

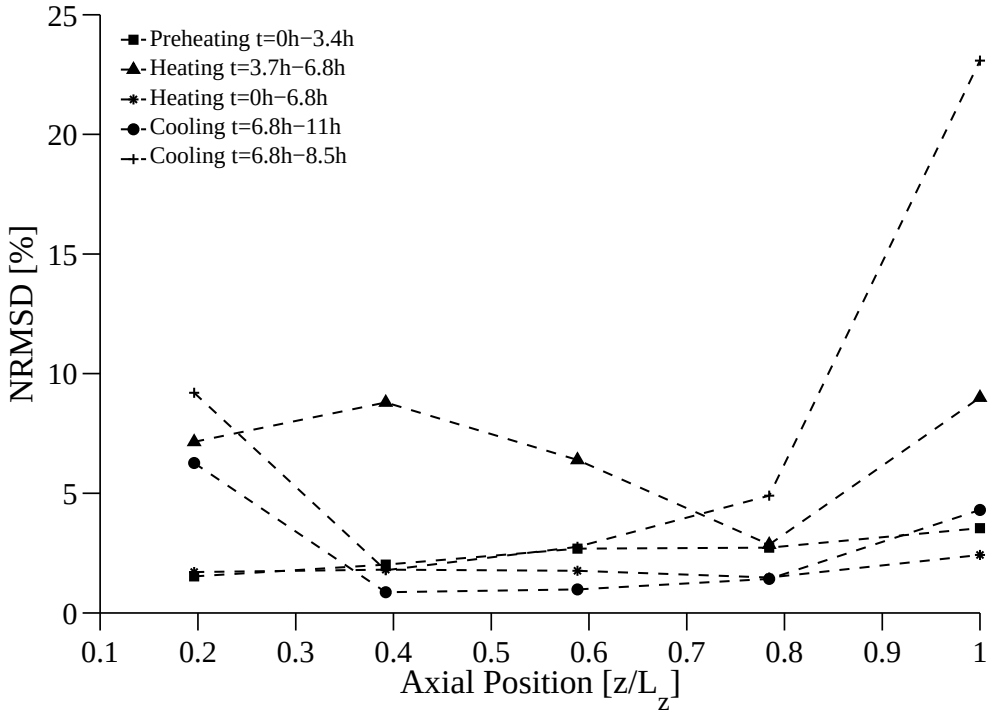

Figure 6.19: Normalised RMS deviations between the measured and predicted fluid centreline temperature profiles for the first high temperature test, using Na_2SO_4 EPCM particles.

The thermocline extends across the full length of the packed bed during the latent heat testing. This is related to the relatively large size of the particles in comparison to the test section length, $L_z/d_p = 11.3$. It should be cautioned that due to the packing of the particles against the mesh support there exist axial variations in the void fraction, within half a particle diameter from the bed exit. For the sensible heat storage testing presented in Section 5.4, this effect is negligible as $L_z/d_p = 31.1$. However for the larger EPCM particles the higher void fraction at the mesh support could have a localised effect on the heat transfer at the bed exit. The axial variation in the bed void fraction was not included in the modelling due to the added complexity required. This could be considered in further modelling work, in conjunction with modelling the thermal capacity of the mesh support and heat losses from the base of the bed. However, due to the low effective thermal conductivity of the packed bed, the exit temperature profiles do not have a significant influence on the temperature profiles in the core region of the packed bed. Therefore the model is still successfully validated. It should also be noted the higher void fraction at the bed exit leads to a lower mass to absorb energy, which is counteracted by the added thermal inertia of the mesh support.

The particles that cracked upon cooling from the high temperature tests were removed. The remaining particles were used to fill 0.4 m of the packed bed length. In order to maintain the full bed length of L_z=0.51 m the PCM particles were packed on top of a 0.11 m layer of solid Denstone particles. This layer of sensible heat particles at the base reduced heat losses at the last layer of the PCM particles. The properties of the Denstone particles were also included in the numerical model.

Figures 6.20 and 6.21 show the melting and solidification of the PCM. The results from this test are consistent with the first high temperature test conducted with a bed depth of 0.51 m of Na_2SO_4 particles. During the solidification of the molten Na_2SO_4 the fluid temperature in the packed bed remains constant at approximately 884 °C. The bottom layer of Denstone particles reduced the heat losses from the Na_2SO_4 particles through the base of the test facility. Therefore the deviation between the model and the experimental data does not increase at $z = 0.4$ m. Figure 6.22 shows that the NRMSD is below 5.5% for the heating and cooling in the second high temperature test.

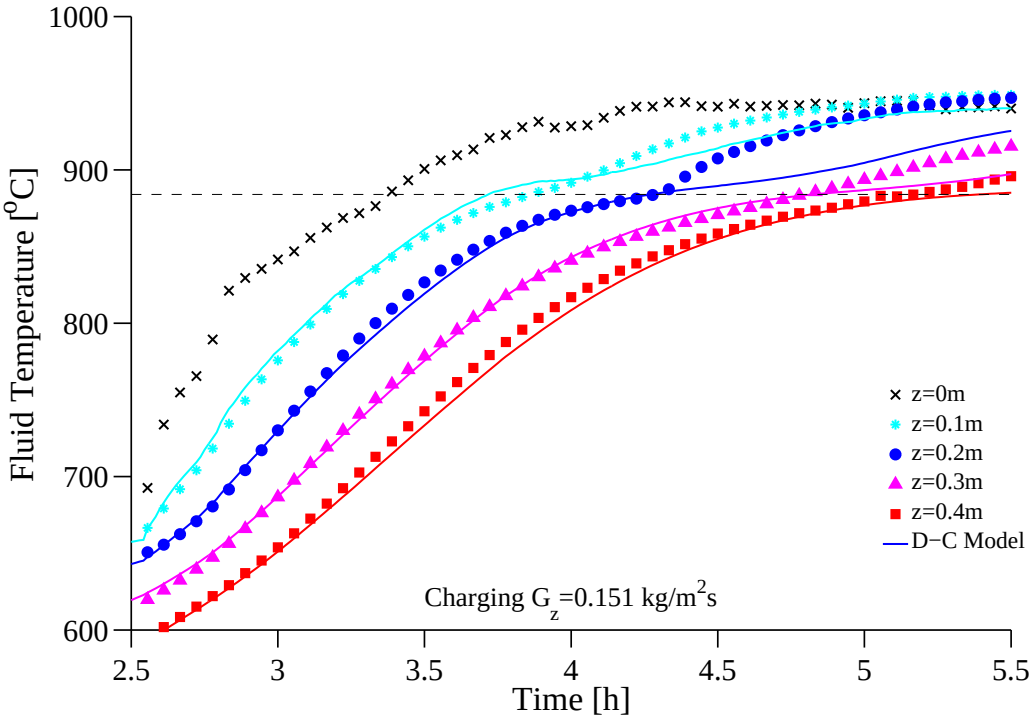

Figure 6.20: Comparison of the measured (markers) and predicted (curves) centreline fluid temperature profiles for the second heating test, using Na_2SO_4 EPCM particles.

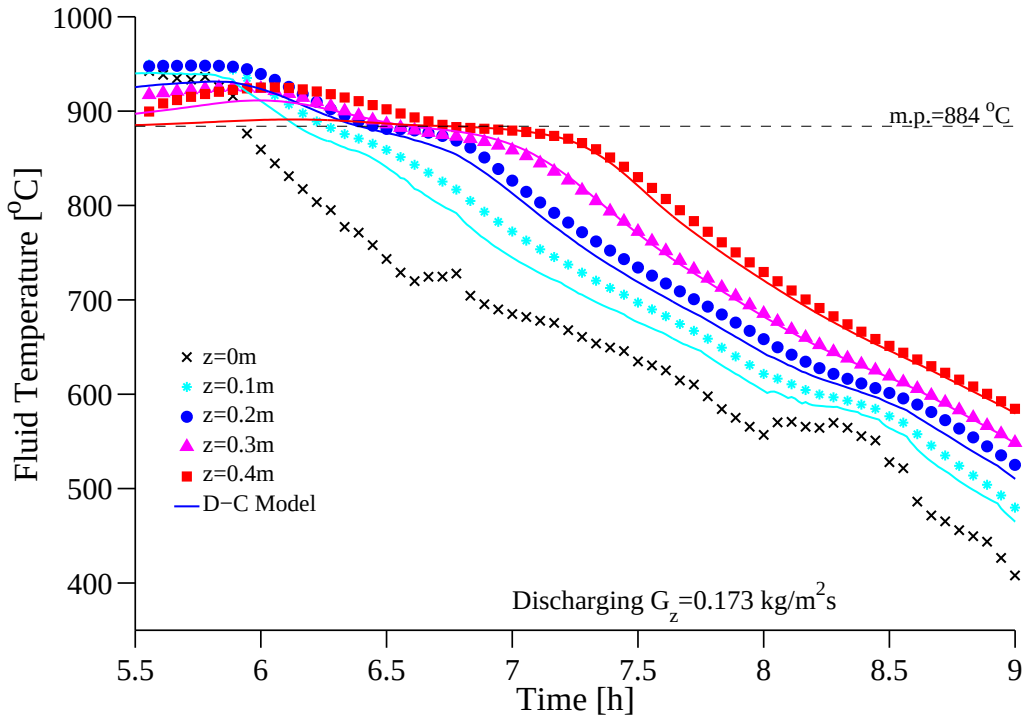

Figure 6.21: Comparison of the measured (markers) and predicted (curves) centreline fluid temperature profiles for the second cooling test, using Na_2SO_4 EPCM particles.

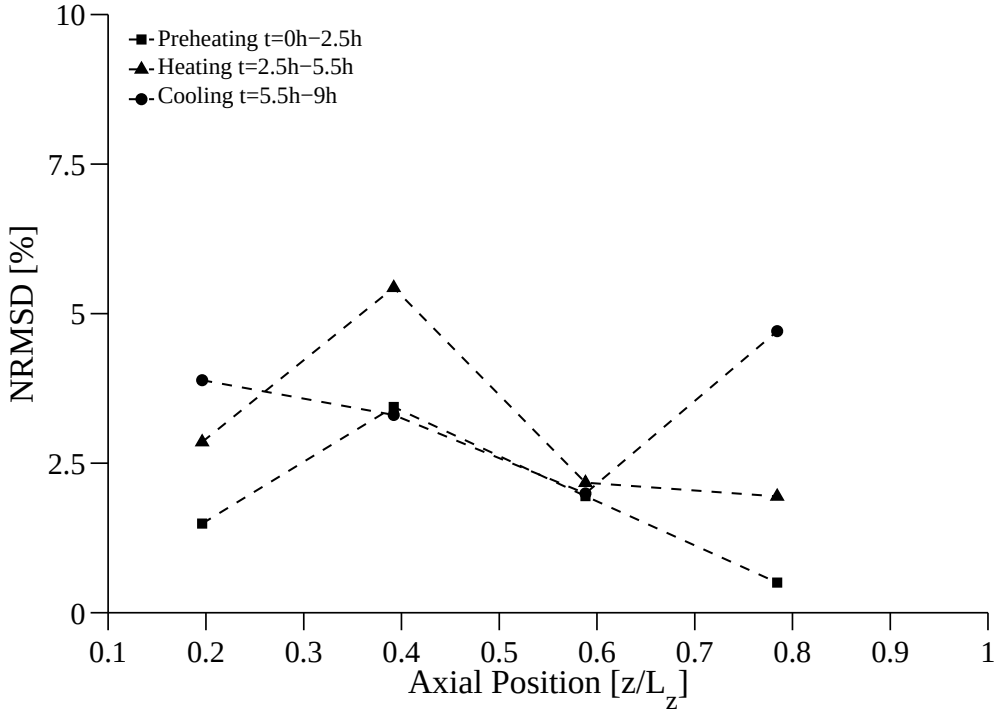

Figure 6.22: Normalised RMS deviations between the measured and predicted fluid centreline temperature profiles for the second high temperature test, using Na_2SO_4 EPCM particles. (Note that a 0.11 mm layer of Denstone particles was placed under the 0.4 m layer of EPCM)

6.4.3 Cracking of EPCM particles

During the cooling of the packed bed from high temperature a series of cracking sounds were audible from the test section at temperatures below 600 °C. A subsequent examination of the test section showed that a number of the EPCM particles (≈15%) had cracked during the heat transfer testing. Through an examination of the broken particles it was possible to determine at what stage of testing the alumina shell cracked. A limited number of broken shells were empty, showing that the shell failed before or during the period when the salt was liquid. Once the shell cracked the liquid salt drained to the base of the packed bed. The bulk of the broken particles cracked once the liquid salt had already solidified. Figure 6.23 shows an example of the cracked shell and solid Na_2SO_4 that remained. As the shells cracked after the particles were cooled to below 600 °C the results presented above for the melting and solidifying of the PCM are not notably affected. Therefore the results are still acceptable for the validation of the numerical model.

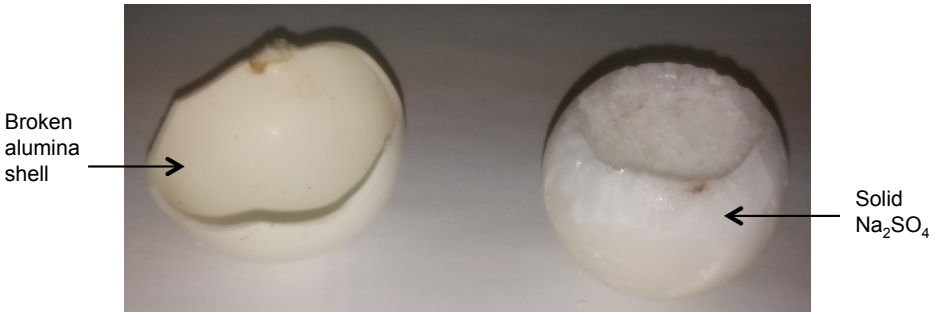

Figure 6.23: Broken EPCM particle after the high temperature testing

There are various factors that could cause the cracking of the particle shells. Thermal shock in the Al_2O_3 may play an important role, as dense Al_2O_3 is susceptible to failure in this mode. There is also a mismatch between the thermal expansion coefficients of the solid Na_2SO_4 ($5.5x10^{-5}$/°C, Notter et al. (1993)) and the Al_2O_3 ($5.4x10^{-6}$/°C, Auerkari (1996)). This could introduce added thermal stresses. However, the ability of the EPCM particles to survive heating and cooling above the melting temperature of Na_2SO_4 was checked prior to testing in the packed bed. Samples were rapidly heated and cooled (15 °C/min) using a small test furnace. These particles did not show signs of cracking. Therefore it is likely that the packing of the particles also contributes to the shell failures. If the cracking was purely related to thermal stresses, the inlet of the packed bed should have the highest number of shell failures, as this region experiences the highest transient thermal gradients. However, it was found that the frequency of the cracked particles increased towards the bottom of the packed bed. This indicates that the added mechanical loadings on the shell due to the mass of particles above also contributed to the shell failures. It is also possible that thermal

ratcheting stresses could be a contributing factor in the packed bed. As the hot packed bed wall expands upon heating, the particles settle in the test section. Then, upon cooling, the wall contracts and induces additional stress in the particle shells. Thus it is concluded that there is a combination of thermal and mechanical stresses in the alumina shell that lead to failure.

In each particle the small filling hole was plugged with a silica ceramic. It should be noted that this plug did not fully seal each particle. As the Na_2SO_4 melts it expands its volume by 28%. The porous plug allowed the build up of pressure within each particle to be released. However, the lack of sealing also meant that each particle had to be arranged with the hole at the top of the sphere. This is not practical for a large packed bed. In a pilot scale design this plug would need to be fully sealed. Thus the build up of pressure within each particle will place an added stress on the particle shell when the salt melts.

Further materials research is required to analyse the EPCM particles and determine a better method for encapsulating the inorganic salt. From this initial heat transfer testing thin Al_2O_3 shells do not appear suited to a packed bed of EPCM particles. One potential option is to increase the thickness of the shells to see if they can withstand the stresses. However, this would decrease the mass percentage of salt in the system as Al_2O_3 has a high density. Therefore other encapsulation materials such as SiO_2 should be investigated. Goswami (2012) developed a combination of a ceramic shell that was used to encapsulate NaCl. The ceramic shell was subsequently coated with a Nickel shell for added strength using electroless and electroplating methods. The aim of the current research is to present a preliminary analysis of the heat transfer within a packed bed of EPCMs. Further development of the EPCM particles is beyond the scope of the testing.

6.4.4 Conclusions from packed bed testing

The D-C model was compared to fluid temperature measurements taken from within a packed bed of 45 mm Na_2SO_4 particles. Considering the complexity of the heat transfer within the bed, the D-C model is shown to perform well and is able to accurately predict the measured temperature profiles. Therefore it can be used with confidence to conduct further design studies for a SGT cycle based on EPCMs. The following conclusions are made:

- Due to the low bed-particle diameter ratio of 8.9, wall channelling is more prevalent in the Na_2SO_4 packed bed experiments. Modelling shows that the core velocity decreases by up to 18% due to the bypass flow around the edges of the packed bed.

- Low temperature testing, conducted at 230 °C, confirmed that the convective heat transfer in the Na_2SO_4 bed is accurately modelled in the absence of a phase change. The predicted fluid temperature measurements were in good agreement with the experimental data, with a maximum NRMSD of 5.2%. The shape of the predicted axial thermocline was in good agreement with the experimental data.

- High temperature testing, conducted at 950 °C, showed that the D-C model underestimated the rate of melting within the Na_2SO_4 packed bed. It is suggested that this is caused by non-concentric melting of the PCM, or a lower heat capacity of the liquid Na_2SO_4 that was tested, than given in the literature. For the first high temperature experiment, with a depth 0.51 m Na_2SO_4 particles, the maximum NRMSD was 9% for the melting test. For the second high temperature experiment, with a reduced depth of 0.4 m Na_2SO_4 particles, the maximum NRMSD for the melting test was 5.5%.

- During cooling, the fluid temperature profiles, exhibit a period of constant temperature while the Na_2SO_4 solidifies. This stabilisation of the fluid temperature is the desired effect of using a EPCM packed bed. This was demonstrated experimentally for Na_2SO_4.

- For the first high temperature experiment, within the region 0.2 m$\leq z \leq$ 0.4 m the NRMSD was below 5%. For the second high temperature experiment, with a reduced depth of 0.4 m of Na_2SO_4 particles, the maximum NRMSD was 5.5%.

- A problem was encountered with the cracking of the EPCM particle shells during cooling. Therefore further research is required to develop an EPCM particle. Alumina was chosen as a shell material as it does not react with the Na_2SO_4. However, from this initial heat transfer testing it appears that Al_2O_3 shells are not suited for the application of EPCM particles. The aim of the research was to generate heat transfer data. If the concept of EPCMs is shown to be promising further investigations into the material development are proposed.

Chapter 7

Thermal storage design studies[a]

7.1 Introduction

This chapter describes the use of the sensible heat and latent heat storage models to simulate the performance of a packed bed thermal storage system for the T100 gas turbine cycle. Section 7.2 outlines the plant parameters and model input data for the simulations. The analysis presented in this chapter demonstrates how the C-S and D-C models can be utilised to develop optimal thermal storage designs.

Due to the complexity of integrating a high temperature, pressurised packed bed into a gas turbine cycle, it is desirable to reduce the complexity of the storage material. Therefore sensible heat storage is proposed as a suitable 'first generation' storage technology for the SGT cycle. Section 7.3 describes the parametric optimisation of a nominal six hour thermal storage system (1.55 MWh_{th}). The C-S model, validated in Chapter 5, is used to analyse the storage of sensible heat energy in a packed bed of Al_2O_3 particles. This study includes an analysis of suitable ceramic materials, as well as the optimisation of the bed aspect ratio (L_z/D) and particle diameter, for a fixed storage volume. In Section 7.4, an auxiliary design study is included that compares the thermal performance of different heat regenerator geometries for sensible heat thermal storage.

[a]Material from this chapter has been published in Klein, P., Roos, T.H. and Sheer, T.J. 2015, Parametric analysis of a high temperature packed bed thermal storage design for a solar gas turbine, *Solar Energy* **118**, 59–73.

A potential 'second generation' storage material is based on latent heat storage in EPCMs. Section 7.5 presents a second design study for a latent heat storage system. The thermal storage performance of a packed bed of encapsulated Na_2SO_4 particles is benchmarked against solid Al_2O_3 particles. An estimate cost comparison for the storage technologies is also presented. The concept of a Multi-Layered Packed Bed (MLPB) is proposed, aimed at improving the energy storage density of the packed bed. The latent heat simulations are based on the D-C model, which was validated in Chapter 6.

7.2 Model input data

The input into the thermal storage model is the DNI data taken from the Typical Meteorological Year (TMY2) for Johannesburg (Marion and Urban, 1995). A TMY is an artificial but statistically representative year that has been constructed from data sets of solar radiation and surface meteorological measurements recorded on an hourly basis over 30 years. These weather files were created for the simulation of solar energy supply systems and represent the hourly local solar conditions at a specific location for each day in the year. Figure 7.1 demonstrates how the data from the TMY is used to calculate the energy surplus/deficit that is used to charge/discharge (heat/cool) the thermal storage system.

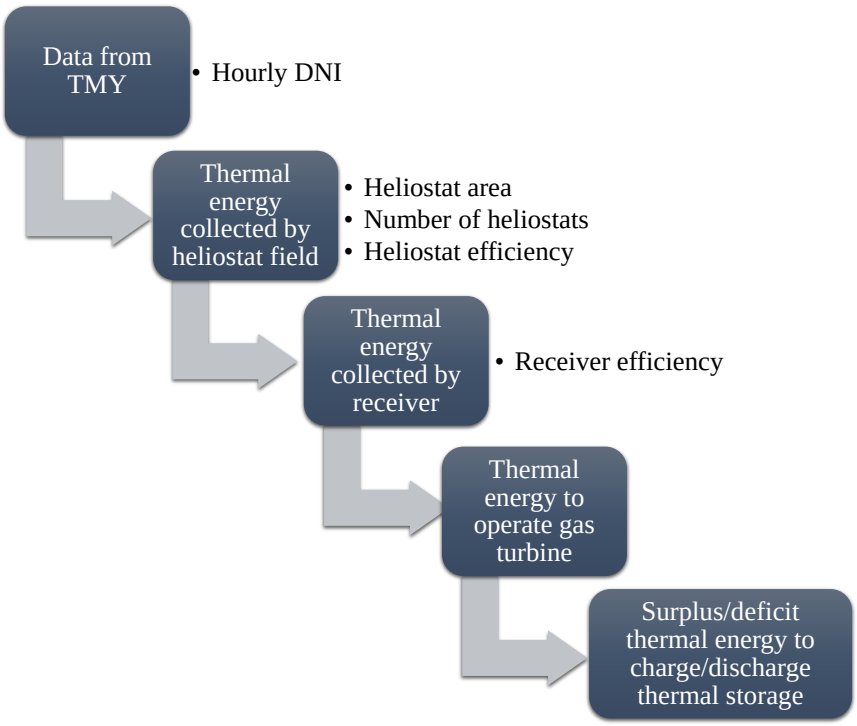

Figure 7.1: Flow chart for the input energy to the thermal storage design model

In order to calculate the thermal power provided by the collector system, the quantity of heliostats, area of each heliostat, efficiency of the heliostat field and the efficiency of the receiver must be known. The excess/deficit thermal power to charge/discharge the thermal storage is calculated according to Eq.(7.2). A positive value of $\dot{Q}_{\text{st}}$ indicates that the thermal storage is being charged (energy stored) and a negative value indicates that the storage is being discharged (energy withdrawn).

$$\dot{Q}_{\text{st}} = \text{DNI} \times A_{\text{helio}} \text{N}_{\text{helio}} \eta_{\text{helio}} \eta_{\text{rec}} - \dot{Q}_{\text{turb}} \tag{7.1}$$

$$= \dot{Q}_{\text{solar}} - \dot{Q}_{\text{turb}} \tag{7.2}$$

The excess energy collected for the storage is a function of the choice of Solar Multiple (SM). This is defined as the thermal power generated by a given solar field at design point, relative to the thermal power required to operate the turbine at the design point. A SM greater than one is required when implementing thermal storage. The plant design used in this research is based on work conducted by the Council for Scientific and Industrial Research (CSIR) and the German Aerospace Center (DLR) as part of the Integrated Resource Infrastructure Platform (IRIP) (Roos et al., 2015). The power block parameters for the Turbec T100PH gas turbine are:

- Compressor inlet air temperature and pressure: 25 °C and 88 kPa
- Turbine power at operating conditions: 73 kW_e
- Turbine efficiency at operating conditions: 28.2%

The reduction in turbine power from 100 kW_e is due to the operating conditions. Although the altitude is constrained by location, the turbine power and efficiency could be increased to 83 kW_e and 29.7% respectively by implementing inlet air cooling to 15 °C. This is not considered at present. The solar collection system parameters are:

- Heliostat area: 13.4 m^2
- Annual heliostat field efficiency: 67%
- Design point Direct Normal Irradiance (DNI): 950 W/m^2
- High temperature receiver efficiency: 70%
- Receiver and storage inlet pressure: 396 kPa_abs (4.5 compressor pressure ratio)

Four SMs were investigated to determine a viable plant design (excluding cost analysis), able to incorporate the proposed thermal storage system. The DNI profile for each day in the TMY was analysed and the excess energy available for storage was calculated using Eq.(7.2). The thermal energy was then converted into a nominal hourly value using the turbine thermal power requirement $\dot{Q}_{\text{turb}}$. As shown in Figure 7.2, six hours of thermal storage is not feasible with a solar multiple of 1.5 or 1.8. For a SM of 2.1, 31% of days in the TMY will supply six or more hours of thermal storage, while 52% of days will supply three or more hours of thermal storage. If the SM is increased to 2.4, 41% of days will supply six or more hours of thermal storage, and 57% of days will provide three or more hours of thermal storage.

From an energy yield perspective it is naturally beneficial to maximise the SM. However the overall capital cost of the plant is strongly dependent on the choice of SM. This is primarily related to the size of the required heliostat field. A detailed financial optimisation of the SM with respect to the Levelised Cost of Electricity (LCOE) is beyond the scope of this work. Therefore the chosen SM is based on energy considerations alone. Figure 7.2 indicates that for a SM of 2.4 a large number of days in the TMY are able to supply more than six hours of storage. However, once the TES is fully charged any further excess energy cannot be stored.

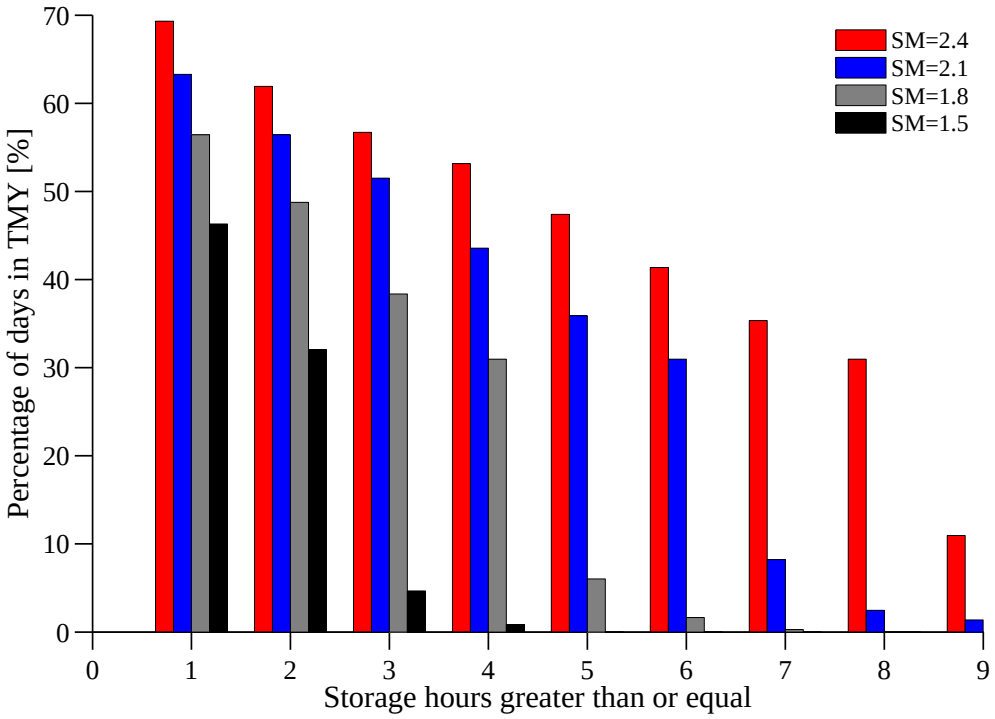

Figure 7.2: Percentage of days in the TMY with storage hours greater than or equal to hourly values between 1 and 9 hours

Figure 7.3 presents the annual energy stored for six hours of storage, compared to the energy available for storage. The results reveal that the level of wasted energy is significantly higher for the SM of 2.4 than the solar multiple of 2.1. Therefore a SM of 2.1 was chosen for this work. For comparison Amsbeck et al. (2010) chose a solar multiple of 2.7 for a nine hour storage system for the T100 gas turbine at a plant location that receives an annual DNI of 2015 kWh/m^2/yr (Amsbeck et al., 2008). The total sum of the DNI profiles taken from the TMY for the current plant location amounts to 1782 kWh/m^2/yr. The use of an annual heliostat field efficiency in Eq.(7.1) is an approximation, as the actual efficiency will vary according to the relative position of the sun to the field. A more detailed plant model would take this into account. As the aim of this study is to investigate the storage component, this approximation is deemed to be acceptable.

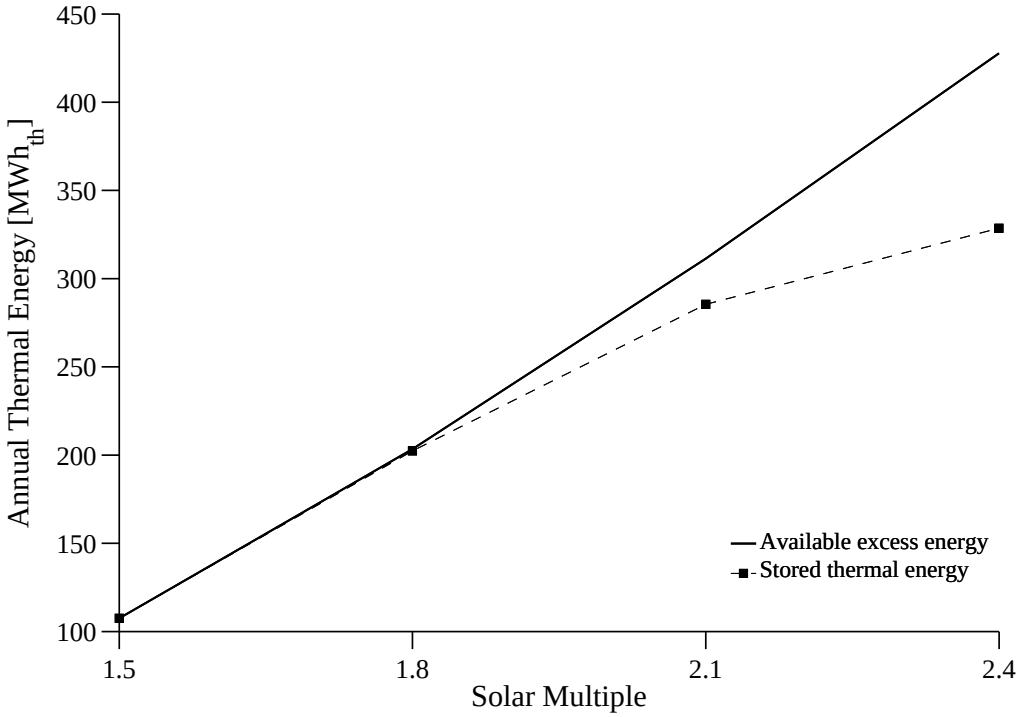

Figure 7.3: Analysis of the of annual energy available for storage as a function of SM, excluding partial discharging

Figure 7.4 shows the DNI profile taken from the TMY for typical clear summer and winter days. The summer day has a higher peak and wider spread across the day. However, an analysis of the TMY showed that the plant location experiences a higher number of clear days in winter than summer, due to cloud cover. Thus the clear winter day DNI profile was chosen for the design study. This day is able to fill the storage to maximum capacity.

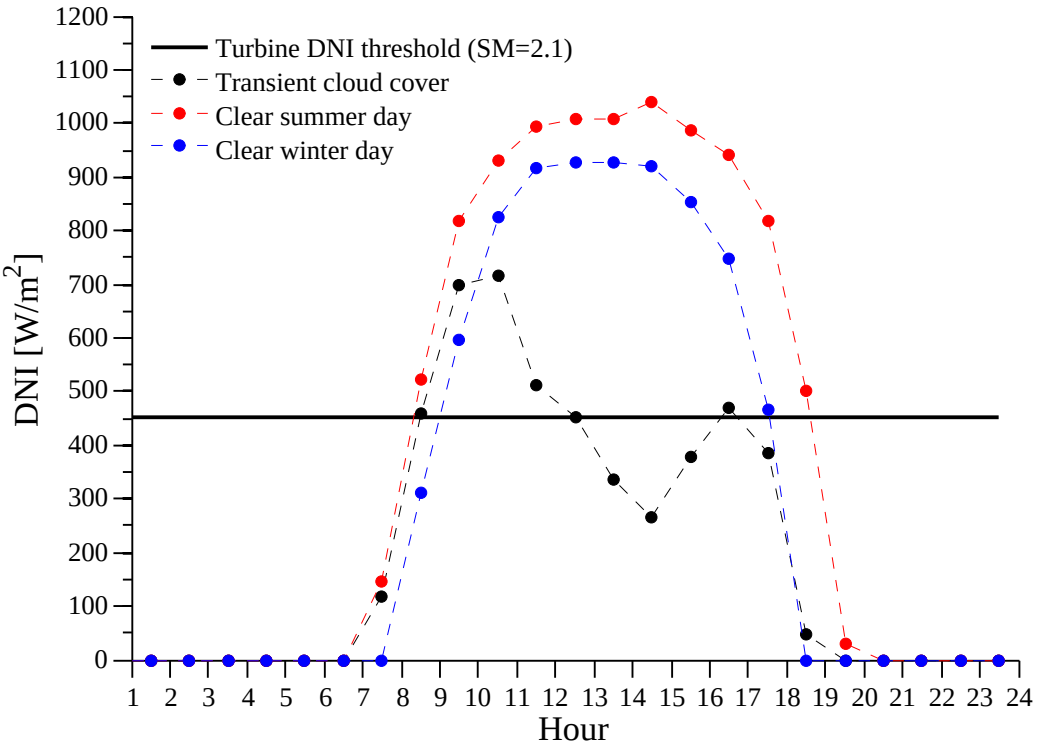

Figure 7.4: DNI profile for clear summer and winter days

Once the power input to the thermal storage has been calculated the transient thermal conditions of the storage can be simulated. The excess/deficit solar energy at the receiver is controlled by circulating a portion of the mass flow through the packed bed using a blower and valve system. Figure 7.5 shows the flow path of air between the receiver and the packed bed during charging and discharging cycles. Once the available solar power exceeds the turbine power threshold, the charging of the thermal storage is initiated by starting the packed bed blower. The blower circulates a portion of the flow through the packed bed and receiver, maintaining the exit temperature of the receiver at 950 °C. As the excess solar thermal power rises, the flow through the packed bed increases. When the solar power drops below the turbine power threshold the blower is bypassed and the flow is diverted through the thermal storage. The air flow rate through the thermal storage is calculated by:

$$\dot{m}_{f,\mathrm{st}} = \frac{\dot{Q}_{\mathrm{st}}}{c_f \Delta T_{\mathrm{rec}}} \tag{7.3}$$

As illustrated by Figure 7.5, a negative value of $\dot{m}_{f,\mathrm{st}}$ indicates discharging of the thermal storage. This is representative of the flow direction, which is reversed during discharging. The inlet air temperature to the packed bed during charging of the packed bed is 950 °C, which represents the turbine inlet temperature and therefore maximum solar receiver outlet

temperature. The inlet air temperature during discharging is 600 °C, which represents the temperature of the air exiting the recuperator. The temperature change across the receiver, ΔT_{rec} is 350 °C.

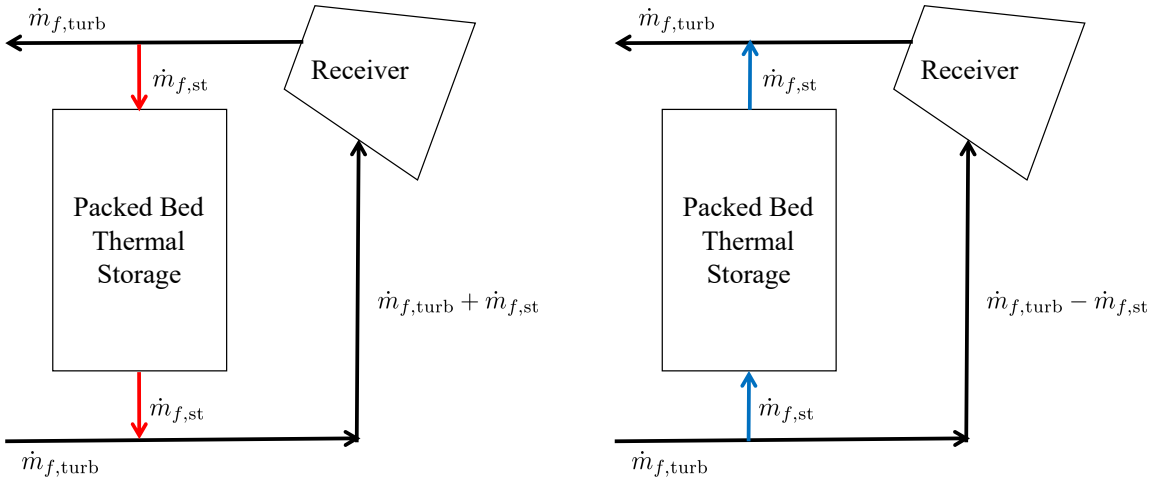

(a) Charging thermal storage

(b) Discharging thermal storage

Figure 7.5: Mass flow rate through the thermal storage during charging and discharging

7.3 Sensible heat thermal storage[b]

7.3.1 Material selection

Prior to conducting the design study a material analysis was completed to determine a suitable solid packing medium for the sensible heat storage system. Due to the high temperature nature of the system only ceramic filler materials were considered in this analysis. Suitable storage materials have the following characteristics: (1) high volumetric heat capacity; (2) high operating temperature capability (1000 °C); (3) good thermal conductivity; (4) resistance to thermal shock; (5) low cost.

[b]The modelling presented in this section is based on constant fluid and solid thermophysical properties across the temperature range 600-950 °C. This approach is shown in Chapter 5 to be valid for the temperature range of the analysis.

In the literature Al_2O_3 and ZrO_2 are recommended as high temperature thermal storage materials (Mongibello et al., 2013; Avila-Marin et al., 2014). The thermophysical properties of these candidate materials are presented in Table 7.1. Alumino-silicate spheres can be sourced in different grades of purity. High purity Al_2O_3 spheres typically have an Al_2O_3 content greater than 92%, while lower purity alumina spheres are predominantly SiO_2. In order to be concise the high alumina material is referred to as Al_2O_3 in this work, despite the possible presence of other impurities in the ceramic. Jalalzadeh-Azar et al. (1996) and Adebiyi et al. (1998) advocated ZrO_2 as an efficient high temperature thermal storage medium.

Table 7.1: Heat storage properties of candidate ceramic core materials

Material	ρ_s [kg/m^3]	Q_m [kWh$_{th}$/tonne]	Q_v [kWh$_{th}$/m^3]	Cost [ZAR/kg]	Cost [ZAR/kWh$_{th}$]
Al_2O_3	3600	119	256	14.1	119
ZrO_2	5400	60	195	273	4536

Calculated assuming $\varepsilon = 0.4$, $\Delta T = 350$ °C, 1 ZAR=10.85 USD (SARB, n.d.)

In order to estimate the costs of each material a series of quotes were obtained from ceramic manufacturers, including Tipton Ceram (Japan) and Pingxiang Funeng Chemical (China). The costs provided in Table 7.1 represent an average of the quotes obtained (F.O.B.). Bindra et al. (2013) estimate the cost of Al_2O_3 spheres for TES at 100 USD/ft^3 ($\varepsilon = 0.35, \rho_s = 3900$ kg/m^3). This equates to a cost of approximately 1.4 USD/kg (15.2 ZAR/kg), which is in line with the estimation made in this work. High purity Al_2O_3 has a density between 3600 kg/m^3 and 3900 kg/m^3, while Yttria stabilised ZrO_2 has a density between 5400 kg/m^3 and 6000 kg/m^3. As a heat storage material, ZrO_2 is more expensive than Al_2O_3 for two reasons, namely: the higher cost of the raw material and the lower specific heat capacity. In order to store the same amount of energy the storage mass of a ZrO_2 bed would be double that of Al_2O_3, while the Al_2O_3 bed maintains a better volumetric energy storage density. Thus even if the cost of the ZrO_2 material per kilogram was comparable with the Al_2O_3, the overall material cost would be double that of the Al_2O_3 bed. Therefore, Al_2O_3 was chosen as the storage material for analysis due to its high volumetric heat capacity and moderate cost.

Alternative alumino-silicate materials could also be considered, as decreasing the Al_2O_3 content results in a lower material cost per kWh$_{th}$. However, the density of alumino-silicates with a low Al_2O_3 content ranges between 2200 kg/m^3 and 2400 kg/m^3. The use of this material would require a storage volume that is up to 1.8 times larger than the high purity Al_2O_3 material. Due to the pressurised nature of the storage this increase in storage volume

would significantly increase the containment costs. Therefore the benefits of the higher density Al_2O_3 ($\geq 92\%$) are likely to outweigh the added material cost. The reduced volume of the packed bed also decreases the parasitic energy losses from the blower. This should be confirmed in future work through a detailed economic analysis.

7.3.2 Estimated size of packed bed

As the thermal storage system is based on sensible heat storage, the starting point for the simulation requires an estimation of the storage mass that would be required to provide a nominal six hours of thermal storage for the gas turbine. This was completed by conducting an energy balance, assuming a full turbine load of 73 kW_e for six hours:

$$\begin{aligned} Q_{st} &= \dot{Q}_{turb} \times (t) \\ &= 5592 \times 10^6 \text{ J} \end{aligned} \tag{7.4}$$

If the thermal storage were isothermal and had no losses a total of 5592 MJ (1.55 MWh_{th}) of energy would be required. However, sensible heat storage is not isothermal and a portion of the packed bed will not undergo the full 350 °C temperature change. For this reason the system must be oversized. Based on initial estimate calculations, it was assumed that 86% of the maximum theoretical stored energy could be discharged. Therefore the required storage size is estimated at 6502 MJ, equating to a storage mass of:

$$\begin{aligned} m_{st} &= \frac{Q_{st}}{c_s \Delta T_{rec}} \\ &= 15.2 \text{ tonnes} \end{aligned} \tag{7.5}$$

The storage mass can be used to calculate the required storage volume, assuming an average bed void fraction of 0.4:

$$\begin{aligned} V_{st} &= \frac{m_{st}}{\rho_s (1-\varepsilon)} \\ &= 7.05 \text{ m}^3 \end{aligned} \tag{7.6}$$

Therefore an internal bed volume of 7 m^3 was chosen for this analysis.

7.3.3 Optimisation of packed bed parameters

Once the material and bed volume are selected, the only design parameters that can be optimised are the aspect ratio of the packed bed (L_z/D) and the particle diameter. Five aspect ratios for the packed bed were analysed: $L_z/D = 1,2,3,4,5$. For each aspect ratio four particle diameters were simulated: $d_p = 10,16,25,50$ mm. These are standard particle sizes available from the consulted ceramic manufacturers. In order to determine the optimal storage design two design parameters are introduced, namely the utilisation factor and the storage efficiency. The calculation of these parameters is described in the subsequent sections.

Utilisation factor

Unlike latent heat TES, sensible heat TES is non-isothermal. Therefore these systems must be over-sized, in order to account for the storage material that does not undergo the full temperature change between the charge and discharge temperatures. The efficient use of the storage material is vital to cost reductions, as over-sizing of the system increases the storage mass and volume. This is particularly important in a pressurised environment where a premium is placed upon the storage volume. The concept of a utilisation factor is introduced to benchmark the amount of thermal energy that is recovered from each storage configuration, relative to the total theoretical maximum that can be stored:

$$\mathrm{UF} = \frac{Q_d}{m_s c_s \Delta T_{\mathrm{rec}}} \tag{7.7}$$

Equation 7.7 does not take into account the energy stored in the fluid phase, which is negligible compared to the solid phase for the ceramic/air working pair. As described by Mongibello et al. (2013) the energy extracted from the packed bed is calculated by:

$$Q_d = \int_{t_c}^{t_d} \dot{m}_d c_f \left(T_d(t) - T_{\mathrm{in},d}\right) \mathrm{d}t \tag{7.8}$$

The fluid discharge temperature T_d takes into the account radial gradients in the fluid temperature and velocity profile:

$$T_d(t) = \frac{2\pi\rho_f}{\dot{m}_d} \int_0^R U_z(r) T_f(0,r) r \,\mathrm{d}r \tag{7.9}$$

$$T_{\mathrm{in},d} = 873 \text{ K} \tag{7.10}$$

There are three factors that affect the utilisation factor: (1) the maximum allowable temperature that the packed bed base ($z = L_z$) reaches during the charging cycle; (2) the maximum allowable decrease in discharge temperature; (3) heat losses through the storage wall.

In an ideal storage system the base of the packed bed would reach 950 °C during the charging cycle, thus maximising the amount of thermal energy stored. However, the hot air exiting the packed bed is in direct contact with the mesh support grid for the ceramic particles and the blower. In order to avoid the use of costly nickel based super-alloys, these components should not exceed 700 °C (Glück et al., 1991). Figure 7.6 shows the effect of the maximum base temperature on utilisation factor, for a packed bed configuration of $L_z/D = 3$, with 10 mm and 50 mm particles. Raising the allowable base temperature from 650 °C to 750 °C increases the utilisation factor by a maximum of 6% and 15% for the 10 mm and 50 mm particles respectively.

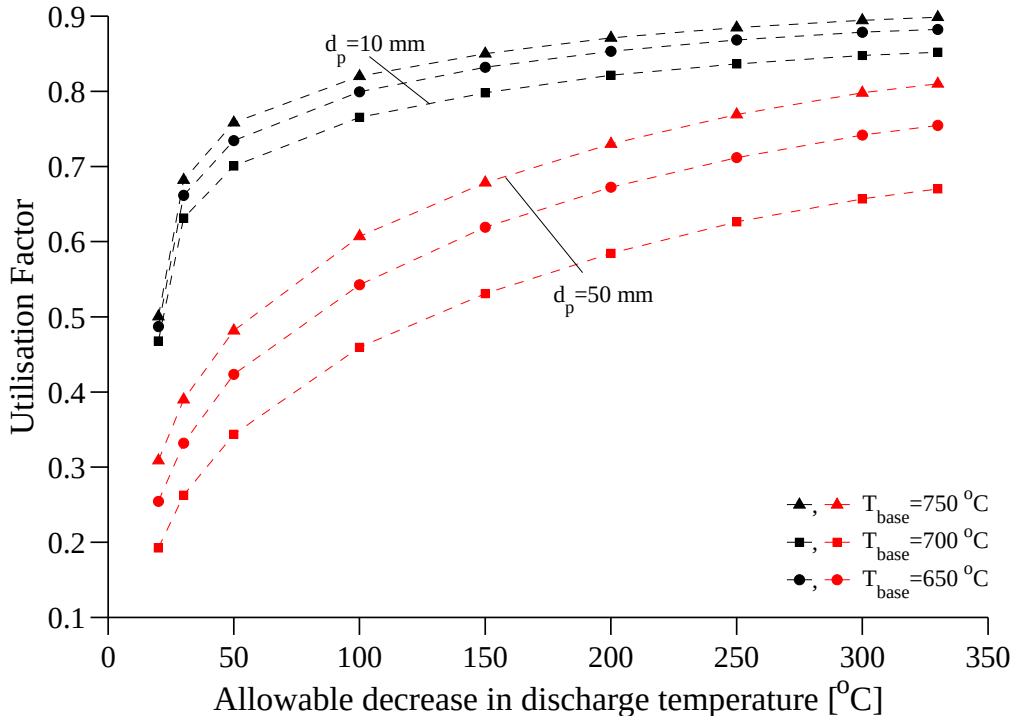

Figure 7.6: Utilisation factor as a function of maximum base temperature and allowable decrease in discharging temperature

During the discharge cycle the exit temperature of the fluid (discharge temperature) starts to decrease over time as the thermocline approaches the bed exit. This is a characteristic of all sensible heat TES systems. Once the discharging temperature decreases to below the specified limit the storage is considered to be depleted and the discharging cycle is stopped. The allowable decrease in discharge temperature is dependent on the choice of operating strategy

for the SGT. If the system is designed to operate on solar energy only (no hybridisation), the discharge temperature should remain close to 950 °C and not decrease below 850 °C. At 850 °C the turbine power is already significantly reduced (52 kW_e assuming 28.2% conversion efficiency). If hybridisation is included then the combustion chamber can be used to boost the turbine inlet temperature to 950 °C. As shown in Figure 7.6, increasing the allowable drop in discharge temperature results in higher the utilisation factors, as more thermal energy can be extracted from the packed bed before discharging is halted. Therefore by boosting the storage discharging temperature with hybridisation, the utilisation factor from the storage can be maximised.

Thermocline shape

The thermocline represents the spatial temperature gradient between hot (950 °C) and cold (600 °C) regions of the packed bed. The gradient of the thermocline strongly influences the utilisation factor. The amount of energy sensible heat stored is dependent on the temperature change of the material. In order to maximise the energy stored, a large percentage of the storage material should undergo the full temperature swing between the charging and discharging cycles. At the point when the charging cycle is halted, the storage material in the thermocline region undergoes a partial temperature change between 600 °C and 950 °C. Therefore this material does not store its maximum capacity of energy.

In an ideal storage system there would be no thermocline region and instead a step change between the hot and cold regions of the packed bed. Although this cannot be achieved in a real storage system, the design should minimise the size of the thermocline region. During charging, if the thermocline region is large, the base temperature will rise to the specified limit and charging will be stopped before a large region of the storage material has reached 950 °C. This reduces the amount of energy stored, thus decreasing the utilisation factor. Figure 7.7 presents the shape of the thermocline for various packed bed configurations at the point when the charging cycle is complete. The level of energy stored is related to the area under the fluid and solid axial temperature profiles. In the current research a conservative temperature limit of 650 °C was imposed on the base.

The gradient of the thermocline is dependent on the convective heat transfer between the fluid and solid particles. As the rate of convective heat transfer increases, the fluid transfers energy more rapidly to the solid, which decreases the size of the thermocline region. The convective heat transfer in the packed bed is dependent on the surface area for heat exchange and inter-phase heat transfer coefficient. The interstitial surface area is inversely proportional to the particle diameter. Therefore, as shown in Figure 7.7, decreasing the particle diameter increases the gradient of the thermocline. The inter-phase heat transfer coefficient

is Reynolds number dependent. Therefore increasing the mass flux in the system improves the convective heat transfer. Storage designs with a high aspect ratio result in a steeper thermocline gradient due to the increase in convective heat transfer.

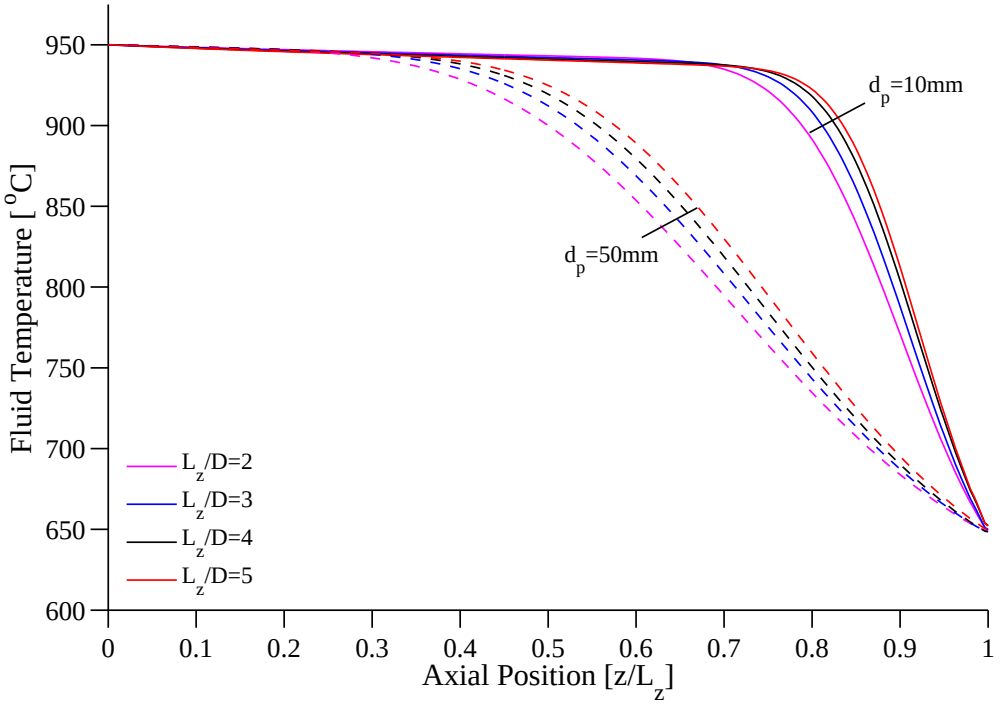

Figure 7.7: Charging thermocline shape at the point when the base temperature limit of 650 °C is exceeded (clear winter day)

Storage efficiency

The cost of improved convective heat transfer is an increase in the storage pressure drop. High aspect ratio packed beds also have higher thermal losses. Therefore the improved heat transfer must be balanced against the increase in energy losses.

The second parameter that can be used to optimise the thermal storage design is the storage efficiency (ξ). This parameter is defined as the energy that is extracted from the packed bed during discharging, compared to the total input energy during the charging cycle. The energy supplied to the packed bed takes into the account blower electrical energy that is required to circulate the mass flow through the packed bed. The blower electrical energy is converted into thermal energy using the efficiency of the gas turbine ($\eta_{\text{turb}} = 0.282$ at specified

conditions). The efficiency of each storage configuration is calculated using Eq.(7.11).

$$\xi = \frac{Q_d}{Q_c + Q_{\Delta P}} \tag{7.11}$$

where Q_d is calculated according to Eq.(7.8) and the energy supplied to the packed bed is given by:

$$Q_c = \int_0^{t_c} \dot{m}_c c_f \Big(T_{\text{in},c} - T_b(t) \Big) \, \mathrm{d}t \tag{7.12}$$

$$Q_{\Delta P} = \int_0^{t_c} \dot{Q}_{\Delta P}(t) \, \mathrm{d}t \tag{7.13}$$

where:

$$T_b(t) = \frac{2\pi\rho_f}{\dot{m}_c} \int_0^R U_z(r) T_f(L_z, r) r \, \mathrm{d}r \tag{7.14}$$

$$T_{\text{in},c} = 1223 \text{ K} \tag{7.15}$$

$$T_{\text{in},d} = 873 \text{ K} \tag{7.16}$$

Pressure drop and blower power requirement

The increase in convective heat transfer in the packed bed must be balanced against the increase in pressure drop, as the gas turbine performance is sensitive to this parameter. One of the benefits of the pressurised system is the density related decrease in the volumetric flow rate. Figure 7.8 shows the effect of aspect ratio and particle diameter on the pressure drop during the discharging phase. In discharging mode the pressure drop is shown to be below 4.5 kPa for all bed configurations that were simulated. Under worst case scenario of $L_z/D = 5$ and $d_p = 10$ mm, the pressure drop is close to that of the benchmark receiver (4 kPa). Thus the pressure drop during discharging is acceptable for all configurations, under discharging conditions.

In charging mode the blower must circulate the air between the packed bed and the receiver. Neglecting buoyancy effects, the electrical power requirement for the blower is calculated using:

$$\dot{Q}_{\Delta P} = \frac{1}{\eta_{\text{blower}} \eta_{\text{turb}}} \frac{\dot{m}_c}{\rho_f} \Big(\Delta P_{\text{bed}} + \Delta P_{\text{rec}} \Big) \tag{7.17}$$

The pressure drop across the packed bed is calculated using Eq.(2.32). Due to the lack of a detailed receiver design an initial estimate of the receiver pressure drop was made based on

measurements taken during testing of the SOLGATE receiver (Heller et al., 2006). As a first order estimate, the receiver pressure drop was calculated by scaling the conditions relative to the SOLGATE receiver (Spelling, 2013). In the current study the pressure drop was linearly scaled according to the superficial flow velocity in the receiver, where:

$$\frac{\Delta P_{\text{rec}}}{\Delta P_{\text{SOLGATE}}} = \left(\frac{U_{\text{rec}}}{U_{\text{SOLGATE}}}\right) \tag{7.18}$$

$$= \left(\frac{G_{\text{rec}}}{G_{\text{SOLGATE}}}\right)\left(\frac{\rho_{\text{SOLGATE}}}{\rho_{\text{rec}}}\right) \tag{7.19}$$

$$= \left(\frac{G_{\text{rec}}}{G_{\text{SOLGATE}}}\right)\left(\frac{P_{\text{SOLGATE}}}{P_{\text{rec}}}\right)\left(\frac{T_{\text{rec}}}{T_{\text{SOLGATE}}}\right) \tag{7.20}$$

The conditions for the SOLGATE are given by Spelling (2013), as: $\Delta P_{\text{SOLGATE}} = 40$ mBar, $G_{\text{SOLGATE}} = 1.063$ kg/sm^2, $P_{\text{SOLGATE}} = 6.5$ bar, $T_{\text{SOLGATE}} = 700$ °C.

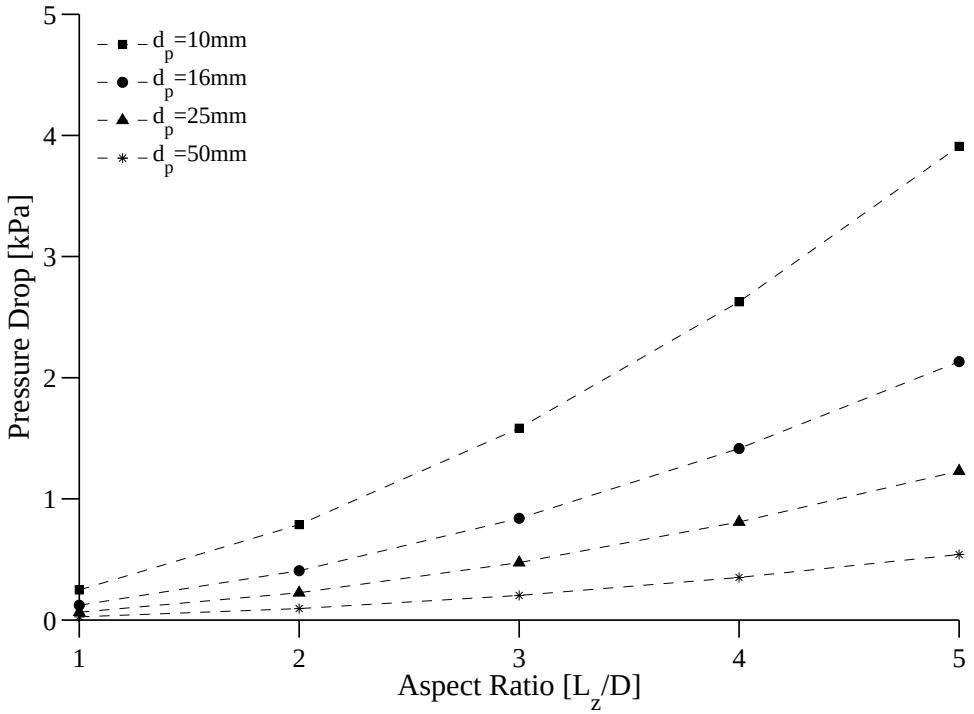

Figure 7.8: Pressure drop across the packed bed for $\dot{m}_f = 0.64$ kg/s

Figure 7.9 shows that most of the blower power is used to circulate the air through the receiver. For $L_z/D = 5$ and $d_p = 10$ mm the blower power reaches 7.3 kW_e, which is 10% of the electrical power produced by the turbine. The sudden decrease in power requirements, shown in Figure 7.9, occurs when the storage charging is stopped as the base temperature limit is reached. Even with very low pressure drop across the packed bed, the blower power requirements reach 5 kW_e due to the receiver pressure drop. This could be overcome by

including a secondary receiver to charge the storage. Using this configuration the primary receiver would be used to power the gas turbine cycle. The excess energy from the heliostat field would be absorbed by the secondary receiver to charge the storage in a separate flow loop. This would avoid the increased mass flow through a single receiver setup, therefore decreasing the pressure drop. However, this approach would likely increase the system complexity and the receiver costs.

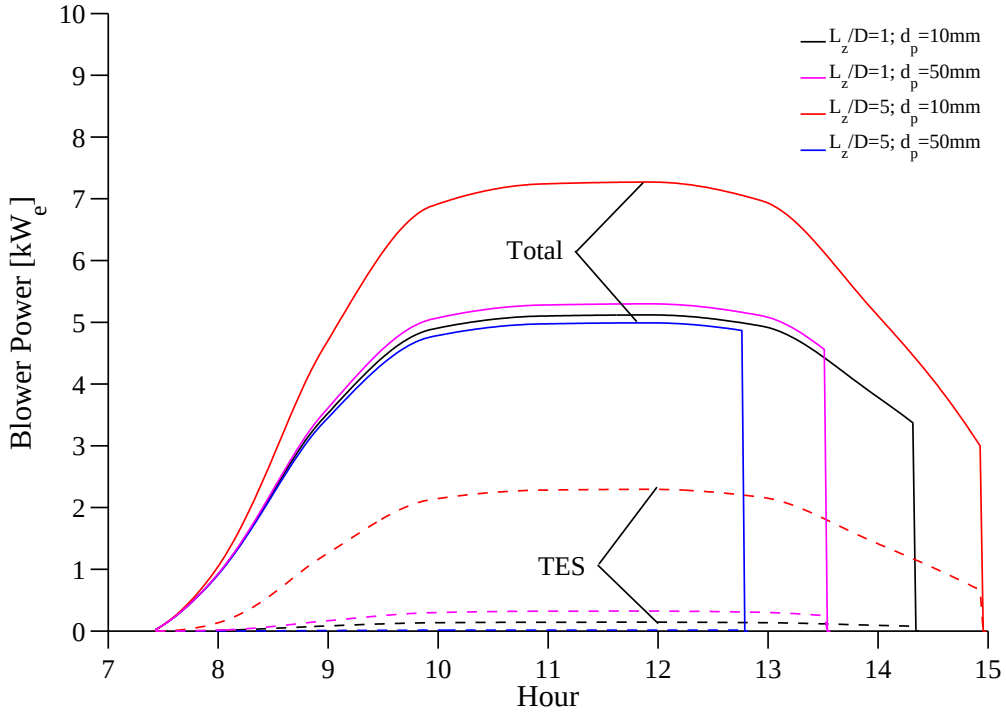

Figure 7.9: Blower power requirements during the charging cycle on a clear winter day

Optimisation results

Figure 7.10 shows the discharge temperature profiles for five aspect ratios and two particle diameters of 10 mm and 50 mm. The results from the simulations show that the smaller 10 mm particles are able to sustain a higher discharge temperature than the larger 50 mm particles. Therefore the smaller particles are able to supply a higher amount of thermal energy during the discharge cycle. As shown in Figure 7.11, for a fixed aspect ratio, decreasing the particle size increases the maximum amount of energy that can be stored before the base temperature limit is reached and the charging cycle completed. For an aspect ratio of $L_z/D = 3$, decreasing the particle diameter from 50 mm to 10 mm results in an increase in the energy stored in the packed bed from 1.31 MWh_{th} to 1.64 MWh_{th}.

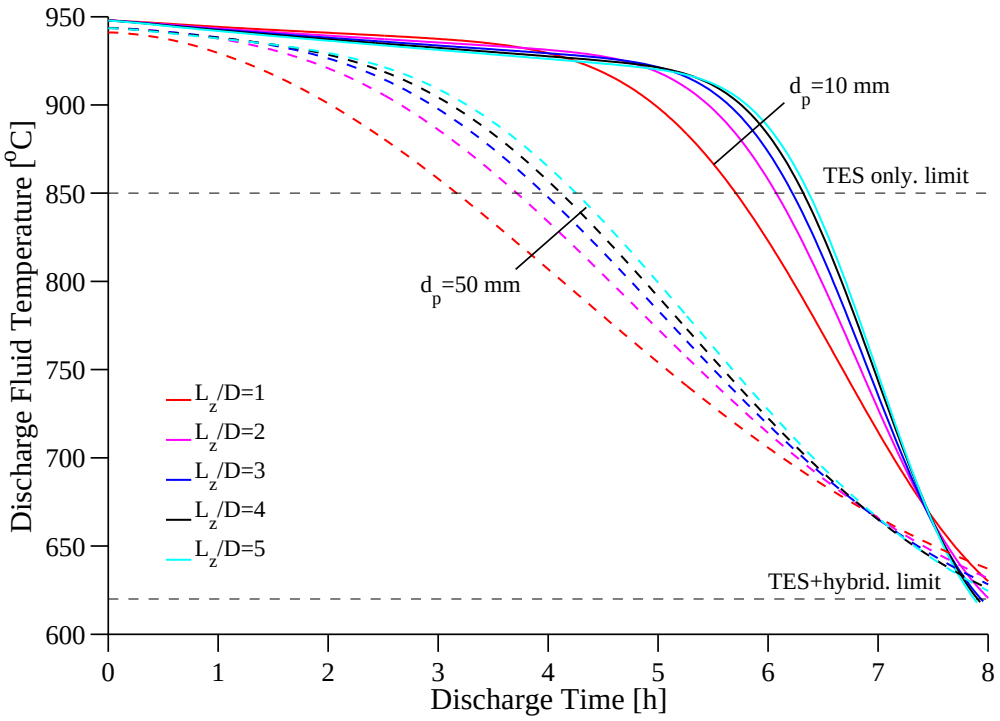

Figure 7.10: Discharge temperature profiles from the Al_2O_3 packed bed. Discharging initiated 8.6 h after the start of charging.

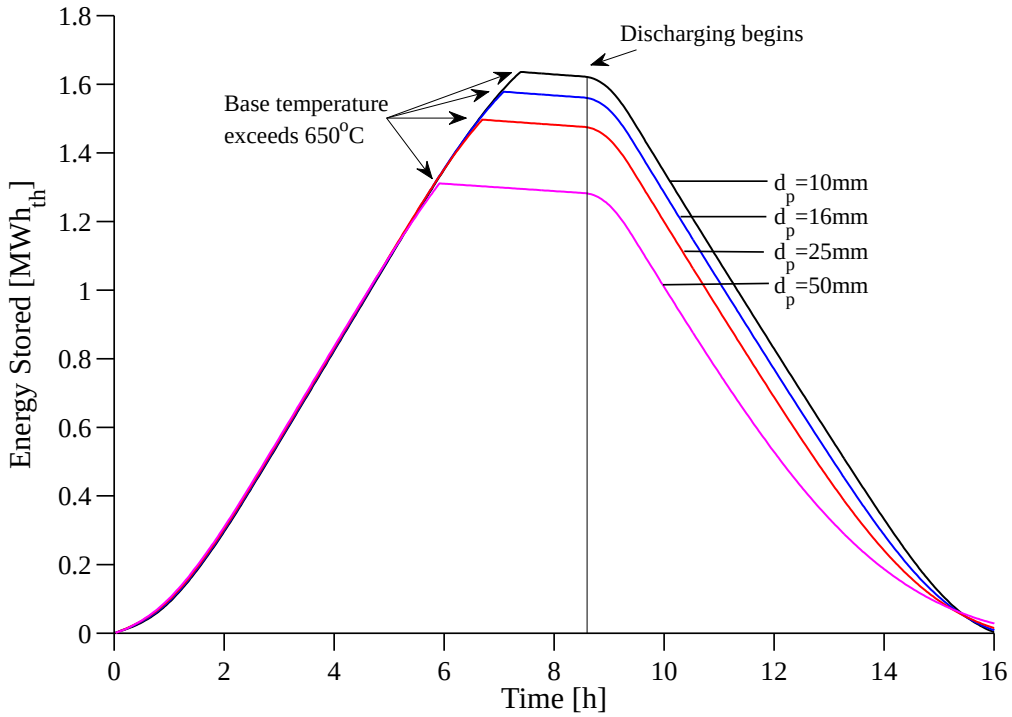

Figure 7.11: Sensible heat energy stored for different particle diameters, for $L_z/D = 3$

The parametric design study includes the operation of the storage with and without hybridisation. During the discharging cycle the storage is considered to be depleted when the discharge temperature drops below 620 °C for TES+hybridisation; and below 850 °C for TES only. Figure 7.10 indicates the position at which the discharge temperature profiles drop below the specified limits. The results for the storage efficiencies and utilisation factors are presented in Figures 7.12 and 7.13 respectively.

The advantages of combining TES with fossil fuel hybridisation are clear. The boosting of the discharge temperature allows for more energy to be extracted from the storage before it is considered depleted. This results in an increase in storage efficiency and utilisation factor. As shown in Figure 7.12, the storage efficiency decreases with increasing aspect ratio for TES+hybridisation. This is caused by the increase in pressure drop and heat losses through the wall. The particle diameter does not have a large influence on the efficiency for this case. The largest 50 mm particles have efficiencies between 0.4% and 1.4% lower than the 10 mm particle diameters for various aspect ratios. Increasing the aspect ratio from 1 to 5 decreases the efficiency by between 4.1% and 5%, depending on the particle diameter.

For the case of TES only, the decrease in convective heat transfer at low aspect ratios results in lower storage efficiencies. The choice of particle diameter has a more pronounced effect on storage efficiency for the TES only case. Using the 10 mm particles improves the efficiency, by up to 27%, when compared to the 50 mm particles. Both test cases exhibit small improvements in utilisation factor with increasing aspect ratio. The choice of particle diameter plays a more important role, with the smallest 10 mm particles maximising the utilisation factor for both TES+hybridisation and TES only.

Table 7.2 provides a summary of the optimal storage configurations for the case of TES only and TES+hybridisation. For each analysed storage configuration the level of stored energy increases with increasing the aspect ratio and decreasing the particle diameter. For the case of TES+hybridisation the configuration of $L_z/D = 2$ and $d_p = 10$ mm is determined to be optimal, yielding 1.56 MWh_{th} of energy discharged at a storage efficiency of 88% and utilisation factor of 85%. If hybridisation is not allowed for the optimal configuration is $L_z/D = 4$ and $d_p = 10$ mm, yielding 1.44 MWh_{th} energy discharged at a storage efficiency of 78% and utilisation factor of 78%.

Table 7.2: Results of the parametric optimisation of a sensible heat TES design

Configuration	L_z/D	d_p [mm]	Q_c [kWh_{th}]	Q_d [kWh_{th}]	$Q_{\Delta P}$ [kWh_{th}]	ξ [%]	UF [%]
Hybrid.+TES	2	10	1656	1559	114	88	85
TES only	4	10	1705	1435	124	78	78

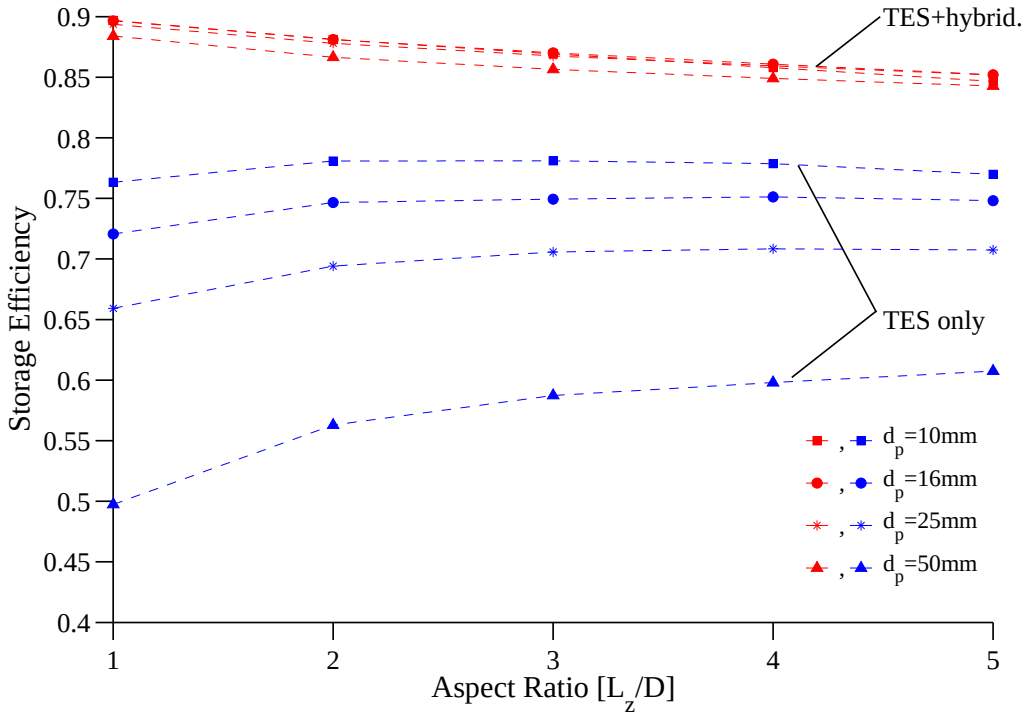

Figure 7.12: Storage efficiencies from parametric design study

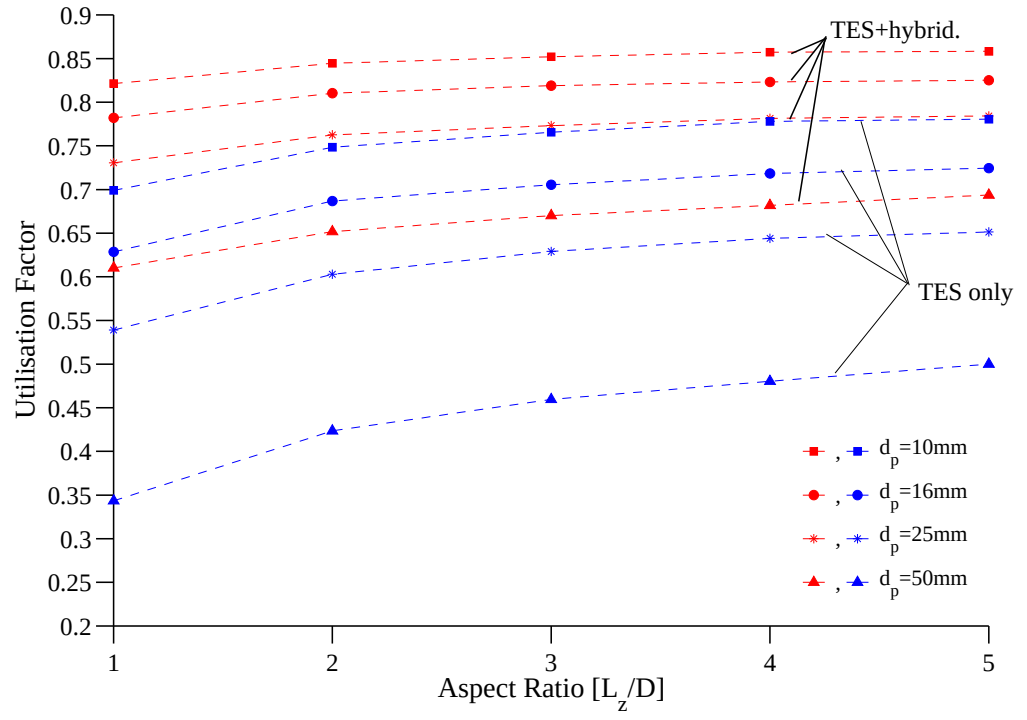

Figure 7.13: Utilisation factors from the parametric design study

7.3.4 Conclusions for sensible heat storage

This section presented the use of the validated C-S model to conduct a detailed parametric design study of a sensible heat, packed bed TES. The aim of this study was to determine optimal storage configurations, based on a nominal six hour TES for a T100 gas turbine (at specified operating conditions). The main findings are:

- Due to its high volumetric energy storage density, Al_2O_3 is a suitable sensible heat storage material for pressurised TES applications. The cost of this material is estimated to be 119 ZAR/kWh$_{th}$ (11 USD/kWh$_{th}$) for a 350 °C temperature range.
- The maximum temperature of the packed bed base should to be limited in order to avoid the use of costly materials for the mesh support and packed bed blower. A conservative temperature limit of 650 °C was used in the modelling. Increasing the base temperature limit improves the amount of energy that can be stored before the charging cycle is stopped.
- Increasing the aspect ratio of the storage (L_z/D) and decreasing the particle diameter improves the convective heat transfer between the fluid and solid phases. The storage efficiency and utilisation factors were maximised by utilising 10 mm particles. However, the increase in convective heat transfer must be balanced against the associated increase in pressure drop across the packed bed. Therefore a small particle diameter should be used and the aspect ratio of the bed decreased to reduce the pressure drop.
- The thermal performance of the storage can be improved by utilising hybridisation to boost the discharge temperature from the storage. Employing hybridisation can increase the storage efficiency by 10% and the utilisation factor by 7%.
- The blower power reaches 7.3 kW$_e$ for the configuration $L_z/D = 5$ and $d_p = 10$ mm, equating to 10% of the turbine power. Alternative receiver concepts should be investigated to reduce the required blower power.

7.4 Auxiliary investigation into optimal inventory geometries for sensible heat storage[c]

As described by Zunft et al. (2014) regenerator heat storage provides a high degree of design flexibility. Parameters that can be optimised include the inventory material and geometry, and the aspect ratio of the containment. Typical off-the-shelf inventories that are used in industrial applications are based on either a random packing of particles, or a structured packed bed. The research presented in the current study is focused on a packed bed of spherical particles to provide thermal storage for a gas turbine cycle. However, various other packing geometries could also be utilised. Therefore an auxiliary study was conducted to compare the thermal performance of a packed bed of spheres to other available inventory types, including ceramic saddles, checker bricks and honeycomb monoliths. Table 7.3 provides the geometric properties of the different core materials that were considered in the analysis. Honeycomb monoliths and saddles have the highest surface area for heat exchange, at the penalty of a higher void fraction.

A one dimensional form of the C-S model was used to conduct parametric simulations for storage systems for two sizes of gas turbines, namely: micro-turbine (100 kW_e) and pilot scale (4 MW_e). Details of the modelling are presented in Appendix G. The micro-turbine system is termed Storage A and the pilot scale system is termed Storage B. The micro-turbine storage is designed to provide a maximum discharge power of 0.37 MW_{th}, with a storage capacity of 1.9 MWh_{th}. The pilot scale storage is designed to provide a maximum discharge power of 8.2 MW_{th}, with a storage capacity of 42 MWh_{th}.

For the analysis, the storage system was discharged with air at 600 °C from an initial uniform temperature of 1000 °C. Therefore no temperature limit was placed on the base of the bed, nor were thermal losses taken into consideration. For these reasons the predicted utilisation factors are higher than predicted in the Section 7.3. The aim of the modelling was to benchmark the different core geometries against each other, for an allowable decrease of 50 °C in the discharge fluid temperature. For each core geometry, the aspect ratio (L_z/D) of the packed bed was varied up to a maximum of 5. The pressure drop and utilisation factor were calculated for each simulated aspect ratio. Increasing the aspect ratio and decreasing the particle/channel size increases the utilisation factor while also increasing the pressure drop.

[c]Material from this section has been published in Klein, P., Roos, T.H and Sheer, T.J 2014, Analysis of regenerative thermal storage geometries for solar gas turbines, *in Proceedings of the 15th International Heat Transfer Conference, IHTC-15*, Kyoto Japan, IHTC15-9580.

Table 7.3: Properties of regenerator inventories

nominal size	a_p [m^2/m^3]	ε [ ]	$(1-\varepsilon_{\text{sphere}})/(1-\varepsilon)$
Randomly packed spheres			
6 mm	600	0.4	1
13 mm	280	0.4	1
19 mm	190	0.4	1
25 mm	144	0.4	1
Randomly packed saddles[1]			
6 mm	900	0.6	1.5
13 mm	465	0.62	1.58
19 mm	280	0.65	1.71
25 mm	250	0.68	1.88
Honeycomb monolith[2]			
68 cpsi	1005	0.6	1.5
42 cpsi	825	0.65	1.71
18 cpsi	540	0.67	1.82
Checker bricks			
5/10 mm	181	0.23	0.78
10/20 mm	91	0.23	0.78
20/40 mm	45	0.23	0.78

[1] Amelio and Morrone (2007)

[2] Green and Perry (2008)

In order to determine the performance of each inventory type the utilisation factor is shown as a function of pressure drop. The results for Storage A and B are presented in Figures 7.14 and 7.15 respectively. The results for Storage A and B are consistent. Due to the pressurised nature of the storage systems, the volumetric flow rate is reduced. For this reason the pressure drop is not a limiting factor. All of the core geometries are able to achieve pressure drops of below 1% of the compressor delivery pressure. These limits are 4.5 kPa for Storage A and 9.9 kPa for Storage B.

For the randomly packed particles the saddles yield higher utilisation factors and lower pressure drops than the spheres. This is due to their higher specific surface area for heat exchange and higher void fraction. For both packed beds of spheres and saddles the smallest particles have the highest thermal performance. Packed beds of 6 mm spheres have a utilisation factor that is competitive with saddles but at a higher pressure drop.

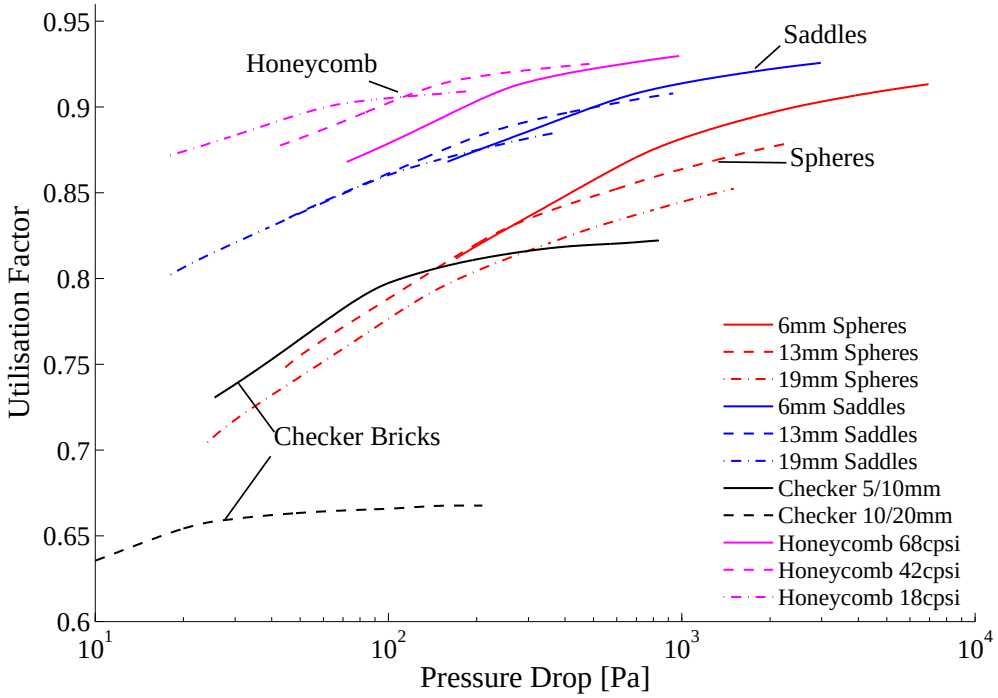

Figure 7.14: Utilisation factor as a function of pressure drop for the micro-turbine case study, Storage A

The honeycomb shapes have the highest utilisation factors of the four inventory types that were tested. This is due to their large specific surface area for heat exchange. The pressure drop associated with the honeycombs is also significantly lower than the randomly packed beds. Using a ceramic honeycomb it is possible to achieve utilisation factors over 90% at pressure drops lower than 1 kPa for both Storage A and B. The checker brick geometry is shown to have the lowest thermal performance of the inventory types analysed. This is due to the low specific surface area and low heat transfer coefficient. The 20/40 mm (hole diameter/spacing) checker bricks have a utilisation factor that is below 40%. Only the 5/10 mm checker brick can produce a utilisation factor that is above 80%. The pressure drop through the checker bricks is below 1 kPa under maximum mass flux conditions for both Storage A and B.

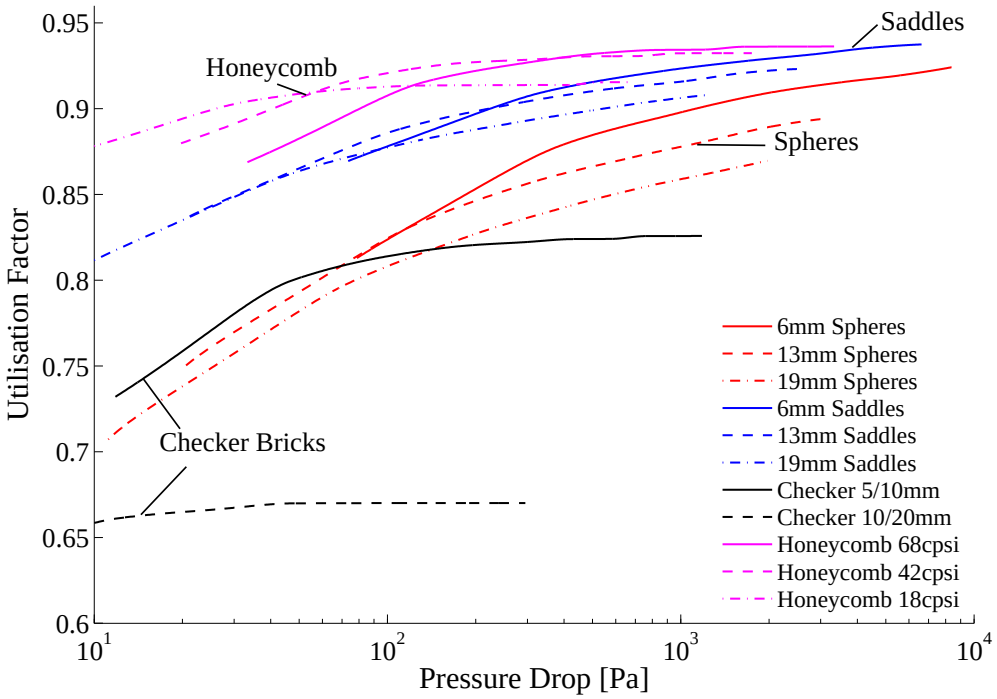

Figure 7.15: Utilisation factor as a function of pressure drop for the pilot scale turbine case study, Storage B

From a thermal design perspective the honeycomb monoliths and packed bed of saddles generate the highest utilisation factors. Therefore these inventory types provide the optimal usage of a fixed ceramic mass for thermal storage. However, as shown in Table 7.3 the void fractions of these inventories are higher than for a packed bed of spheres or checker bricks. A packed bed of saddles or honeycomb monolith requires a storage volume that is 1.5-1.88 times larger than packed bed of spheres (equal mass). This increase in volume would increase the costs of the pressure vessel and inventory container. The increase in thermal performance over the packed bed of spheres does not justify this large increase in the storage volume. From a thermal design perspective the packed bed of spheres is an efficient design selection. It can provide much higher utilisation factors than the checker bricks whilst maintaining a high energy storage density. Due to the pressurised nature of the storage, the pressure drop across the spheres is not significant.

It should however be noted that this analysis does not take into account thermal ratcheting effects which are avoided by using a structured bed packing. Thermal ratcheting is characterised by the cyclic expansion and contraction of the containment walls, which causes the settling of particles in the bed. The settling of the particles leads to added stresses on the packing material and the inner wall/insulation. Thermal ratcheting stresses are problem-

atic for large scale packed beds, but it is likely that they will be manageable for the size of packed bed proposed for the SGT. However, these stresses need to be addressed through a thermo-mechanical analysis, using tools such as Discrete Element Modelling (DEM).

7.5 Latent heat storage

This section presents a design study to compare the thermal storage performance of a packed bed of EPCM particles to that of solid Al_2O_3 particles. The D-C model, which was validated in Chapter 6 was used to analyse both packed bed systems for a configuration of $L_z/D = 3$ and $d_p = 16$ mm. The DNI design day, described in Section 7.2, was applied to the D-C model.

In Section 7.5.1 the chosen base temperature limit for the TES is discussed. Section 7.5.2 compares a packed bed of macro-encapsulated Na_2SO_4 particles to solid Al_2O_3 particles. In order to improve the energy storage density of the system, a hybrid Multi-Layered Packed Bed (MLPB) concept is studied in Section 7.5.3. This concept combines the advantages of sensible and latent heat storage materials. The MLPB consists of three layers of storage materials, namely: encapsulated Na_2SO_4, solid Al_2O_3 and encapsulated NaCl-KCl particles.

7.5.1 Selection of base temperature limit

In the previous design study for sensible heat storage (Section 7.3.3), a temperature limit of 650 °C was imposed on the base of the packed bed. Once this limit is exceed the charging cycle of the system is stopped and the TES cannot store any further energy. For the modelling presented in Section 7.5 the base temperature limit was increased to 670 °C. For the MLPB concept, a PCM with a melting temperature between 600 °C and the base temperature limit is used. It was noted that suitable PCMs such as aluminium ($T_m = 660$ °C) and NaCl-KCl ($T_m = 657$ °C) have a melting temperature slightly higher than 650 °C. Therefore the imposed base temperature limit was raised to 670 °C. The limit of 670 °C was applied to all the simulations presented in this section to allow a direct comparison of the results for the different types of storage materials.

7.5.2 Packed bed of Na_2SO_4 EPCM particles

The EPCM particles are based on macro-encapsulated Na_2SO_4, in a thin Al_2O_3 shell. The effective density of the salt within the Na_2SO_4 particles is 1862 kg/m^3, which incorporates a void within the particles to allow for the expansion of the salt upon melting. The mass fraction of Na_2SO_4 in the packed bed is 76%.

The thermal performance of a packed bed is a function of the energy that can be discharged during the cooling cycle. Figure 7.16 compares the discharge temperature profiles from the Na_2SO_4 bed to the Al_2O_3 bed. For the Na_2SO_4 the discharge temperature decreases until the melting temperature of 884 °C is reached. The discharge temperature then remains constant (stabilised) until the salt has fully solidified. Once the latent heat energy has been extracted from the Na_2SO_4, the discharge temperature quickly decreases. For an equivalent volume packed bed, the discharge temperature from the Na_2SO_4 bed decreases faster than for the Al_2O_3 bed. This indicates that the Na_2SO_4 bed is capable of storing less thermal energy than the Al_2O_3 bed, resulting in a lower thermal storage performance.

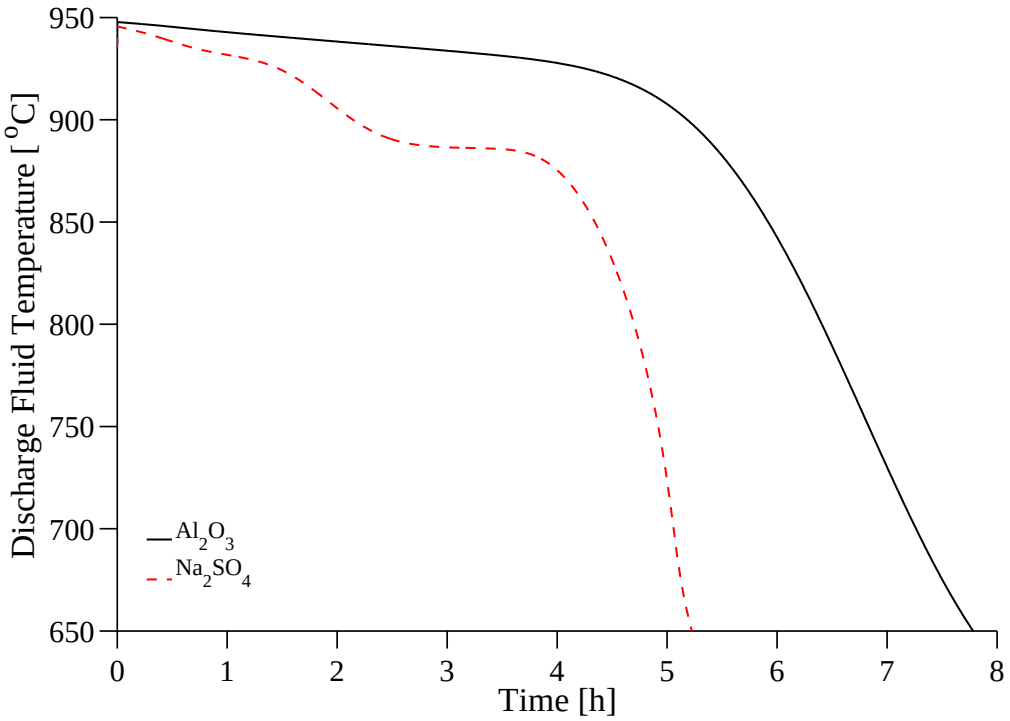

Figure 7.16: Discharge temperature profiles from packed beds of Na_2SO_4 and Al_2O_3 particles for $V = 7$ m^3, $d_p = 16$ mm. Discharging initiated 8.6 h after the start of charging.

The energy that can be withdrawn from the thermal storage during discharging is naturally a function of the maximum energy that is stored during the charging cycle. As a PCM it is necessary for the material to melt in order to achieve a high energy storage density. For the Na_2SO_4, 162 kJ/kg (24.5% of total) is stored when the salt melts and 92 kJ/kg (13.9% of total) is stored heating the liquid salt from 884 °C to 950 °C (Barin et al., 1977). The parameter of melt fraction (MF) is introduced to quantify the amount of salt that undergoes a phase change. There are three regions in the melting process, namely: solid ($MF = 0$), melting ($0 < MF < 1$) and liquid ($MF = 1$). At the point when the charging cycle is complete the melt fraction within each particle is calculated using Eq.(7.21). The mass averaged values of melt fraction are presented in Figure 7.17 as a function of normalised axial position.

$$MF(r,z,\zeta) = \begin{cases} 1 & \text{if } T_{\text{PCM}}(r,z,\zeta) > T_{m2} \\ \dfrac{T_{\text{PCM}}(r,z,\zeta) - T_{m1}}{\Delta T_m} & \text{if } T_{m1} < T_{\text{PCM}}(r,z,\zeta) \leq T_{m2} \\ 0 & \text{if } T_{\text{PCM}}(r,z,\zeta) \leq T_{m1} \end{cases} \tag{7.21}$$

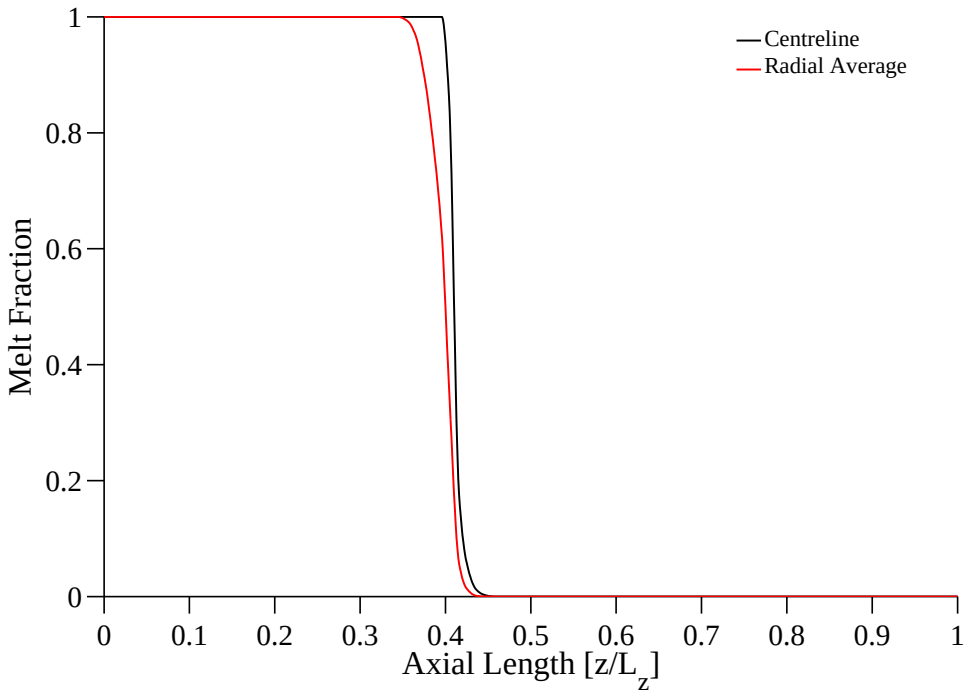

Figure 7.17: Fraction of Na_2SO_4 mass that is molten for V=7 m^3, L_z/D=3, d_p=16 mm

The melt fraction analysis shows that only 33.6% of the Na_2SO_4 mass is liquid, 10.8% is melting, and 55.6% is solid when the base temperature limit is exceeded. The large percentage of PCM that does not undergo a phase change results in a significant decrease in the amount of thermal energy that can be stored in the packed bed. In order to determine the cause of the low melt fraction, the axial thermoclines from the Na_2SO_4 and Al_2O_3 beds are compared at different charging times in Figure 7.18.

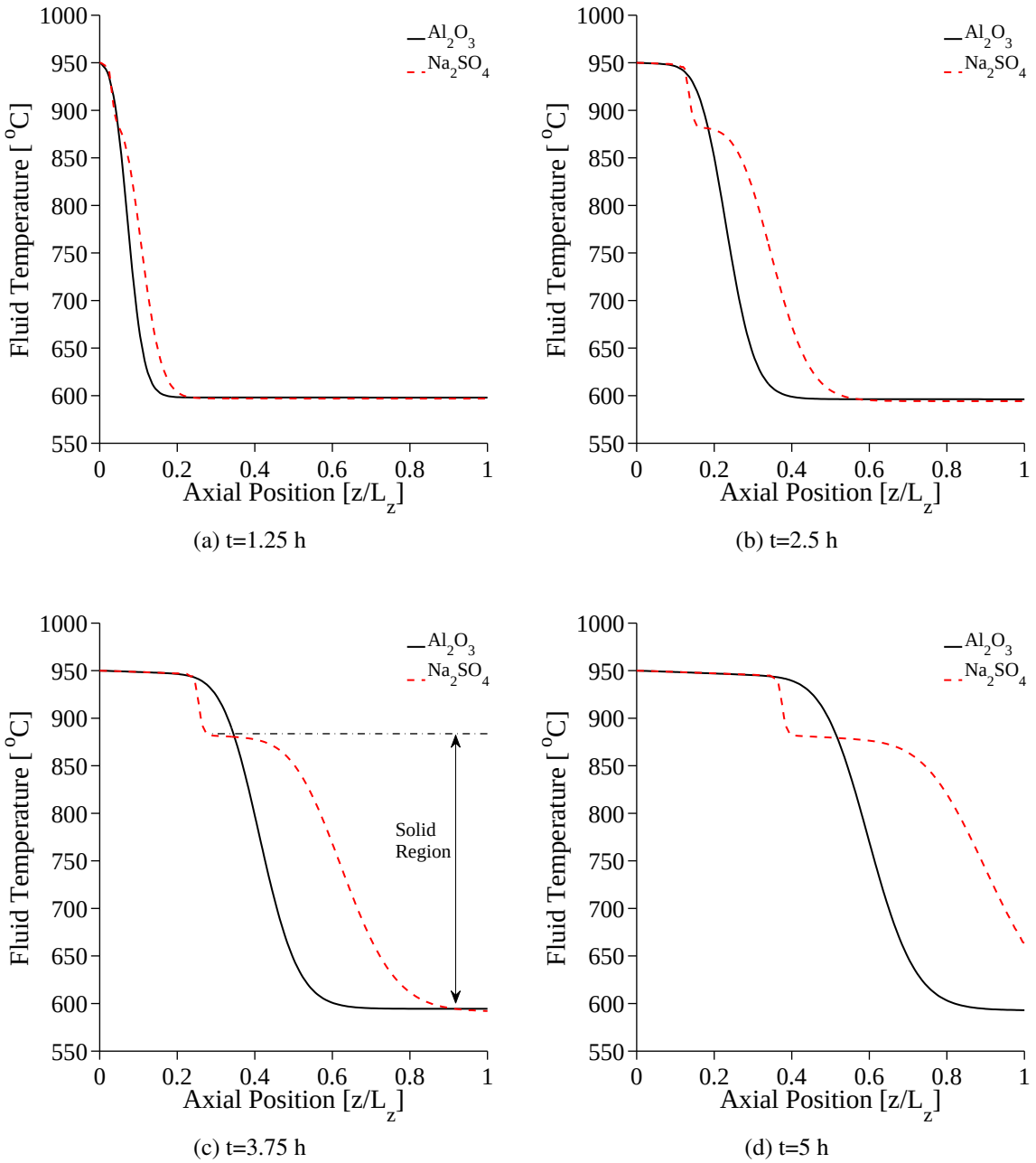

Figure 7.18: Axial thermocline comparison for Na_2SO_4 and Al_2O_3 packed particles, for $V = 7$ m^3, $L_z/D = 3$, $d_p = 16$ mm

The melting of the Na_2SO_4 introduces a plateau in the thermocline shape at approximately 884 °C. Over time, while the salt in the top region of the packed bed is melting, a temperature front propagates through the solid region of the packed bed. This temperature profile in the solid region is labelled in Figure 7.18(c). As a solid sensible heat storage material the Na_2SO_4 is less effective at storing thermal energy than the Al_2O_3. This is due to its lower effective density of 1862 kg/m^3 compared to 3600 kg/m^3 for Al_2O_3. Therefore as shown in Figure 7.18(d), the thermocline in the Na_2SO_4 bed penetrates deeper into the packed bed over time than for the Al_2O_3 bed. This leads to a reduction in the charging time, thus limiting the maximum energy that can be stored in the Na_2SO_4 bed.

Figure 7.19 presents the transient profile of energy that is stored in each packed bed configuration. During the initial stages of charging, energy is stored at the same rate in the Na_2SO_4 and Al_2O_3 packed beds. For the Na_2SO_4 particles the base temperature limit is exceeded after 5.1 hours of charging and only 1.05 MWh_{th} is stored. In comparison, the base temperature limit for the Al_2O_3 bed is reached after 7.4 hours of charging, with 1.59 MWh_{th} of energy stored. Therefore the Na_2SO_4 bed can only store 66% of the energy stored in the Al_2O_3 bed.

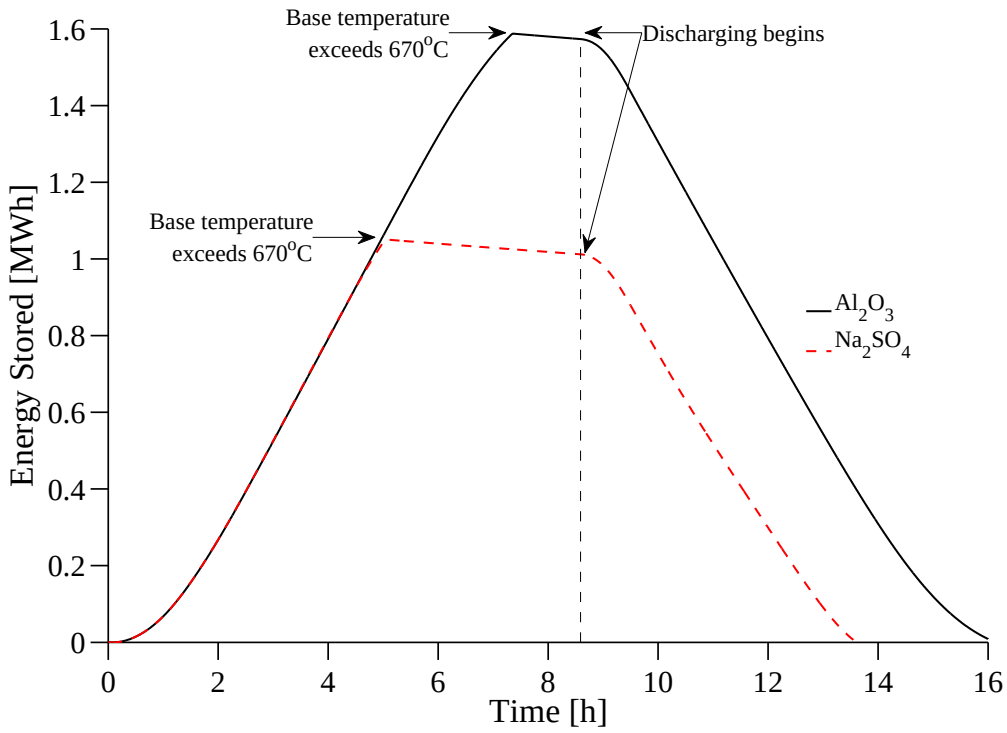

Figure 7.19: Energy stored in Na_2SO_4 and Al_2O_3 packed beds, for $V = 7$ m^3, $L_z/D = 3$, $d_p = 16$ mm

As a PCM, Na_2SO_4 has a relatively low latent heat capacity of 162 kJ/kg (compared to NaCl at 482 kJ/kg). However, as shown in Figure 7.20, even if the latent heat capacity of the PCM is doubled from 162 kJ/kg to 324 kJ/kg, the results for the discharge temperature profiles are very similar. Therefore it is the sensible heat transfer in the packed bed of Na_2SO_4 that limits the thermal storage performance and not the latent heat storage capacity of the salt. In order to improve the energy storage density, a higher density PCM could be considered. However, of the inorganic salts analysed in this work, Na_2SO_4 has the highest liquid density of 2069 kg/m^3 at melting point. In comparison NaCl has a liquid density of 1556 kg/m^3 at melting point (Janz, 1988). Due to the volume change of the salt upon melting it is necessary to include an extra void in each particle. The gas in this void is pressurised to account for the expansion of the liquid salt. When the salt is fully molten there must remain a small void in the particle, which is assumed to be 10% of the internal particle volume. This further reduces the effective density of the Na_2SO_4 to 1862 kg/m^3 and the NaCl to 1400 kg/m^3.

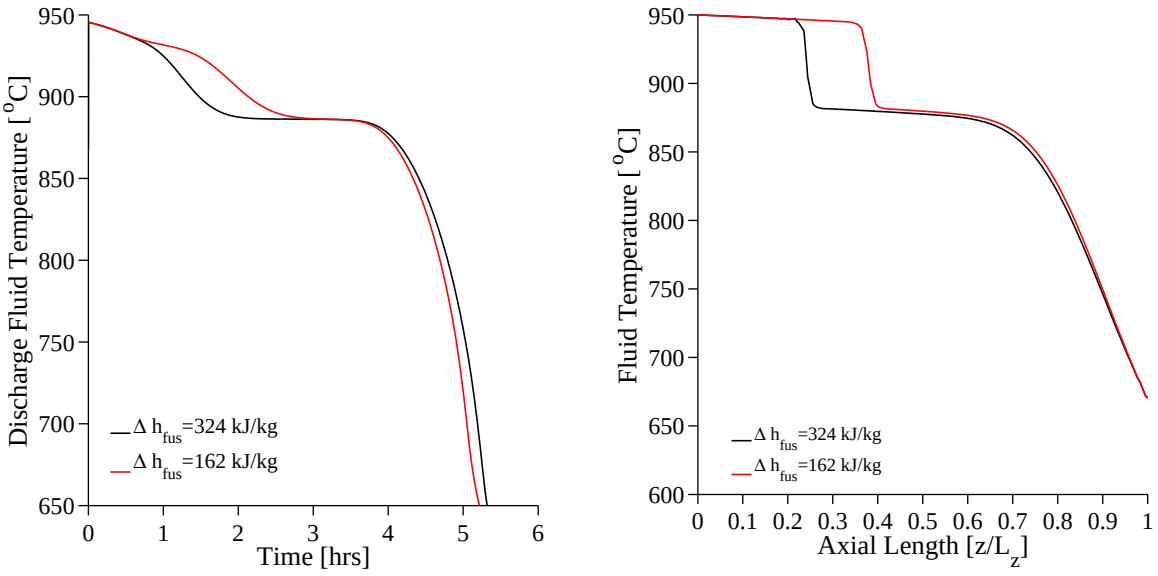

(a) Discharge temperature profile

(b) Thermocline shape at the end of charging cycle

Figure 7.20: Effect of doubling the latent heat capacity of Na_2SO_4, for V=7 m^3, L_z/D=3, d_p=16 mm

Due to the pressurised nature of the thermal storage it is desirable to minimise the storage volume. The results presented in Figures 7.16-7.19 demonstrate that for a fixed volume, the use of Al_2O_3 is preferable to Na_2SO_4 as it provides a higher volumetric energy storage density. This is due to the high density of the Al_2O_3 particles. However, as a storage material the cost of Al_2O_3 is an order of magnitude more expensive than Na_2SO_4 (14.1 ZAR/kg compared to 2.75 ZAR/kg). Therefore a packed bed of Na_2SO_4 particles has the potential to remain cost competitive with Al_2O_3 even if a larger packed bed volume is required. Figures 7.21 and 7.22 demonstrate the effect of increasing the packed bed volume from 7 m^3 to 9.1 m^3 (30% increase) and 10.5 m^3 (50 % increase). The results show that an increase in the packed bed volume to 10.5 m^3 is required to provide a thermal storage performance that is competitive with Al_2O_3. The larger bed will have an increased pressure drop, resulting in an increase in the blower power consumption, which is currently not taken into account in the analysis. However, pressure drop across the packed bed is generally much lower than across the receiver. Therefore the increase in bed volume will not have a large effect on the storage efficiency.

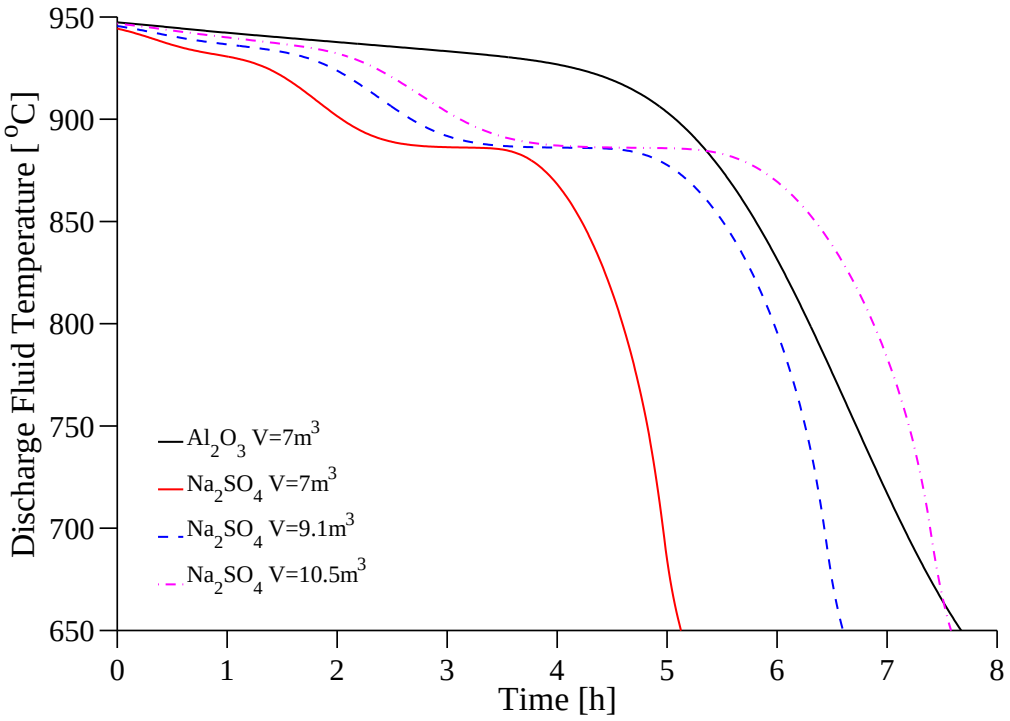

Figure 7.21: Discharge temperature profiles from packed beds of Na_2SO_4 and Al_2O_3 particles for different bed volumes. Discharging initiated 8.6 h after the start of charging.

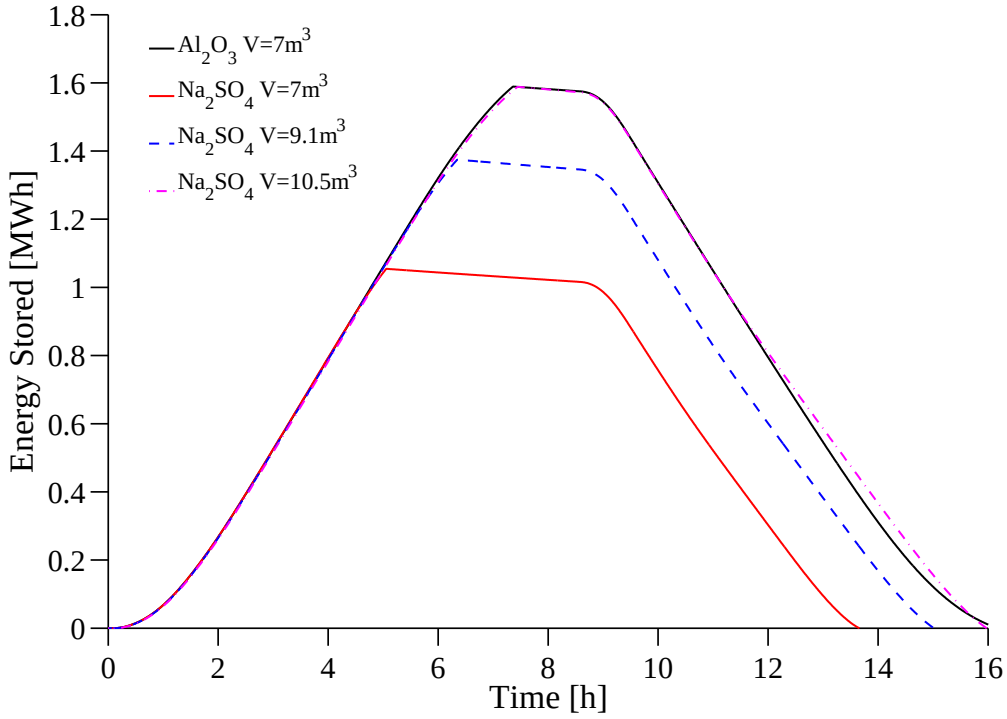

Figure 7.22: Energy stored in Na_2SO_4 and Al_2O_3 beds, for storage volumes of 7 m^3, 9,1 m^3 and 10.5 m^3, and $L_z/D = 3$, $d_p = 16$ mm

Table 7.4 provides a cost estimate of the Na_2SO_4 storage materials based on the different bed volumes. At a storage volume of 10.5 m^3 the overall mass of the Na_2SO_4 bed is 12% lower than that of the Al_2O_3 packed bed. Based on the assumptions made for encapsulating the Na_2SO_4 particles, the storage material cost for the 10.5 m^3 packed bed of Na_2SO_4 is 53% lower than a 7 m^3 packed bed of solid Al_2O_3. However, the added cost of the larger pressure vessel needs to be taken into account. Therefore the viability of increasing the storage volume depends on the cost of increasing the storage containment.

Table 7.4: Cost comparison of Al_2O_3 and encapsulated Na_2SO_4 design concepts

material	V [m^3]	$m_{Al_2O_3}$ [kg]	$m_{Na_2SO_4}$ [kg]	m_{tot} [kg]	$C_{Al_2O_3}$ [1] [ZAR]	$C_{Na_2SO_4}$ [2] [ZAR]	C_{encap} [3] [ZAR]	C_{tot} [ZAR]
solid Al_2O_3	7	15511	0	15511	219k	0	0	219k
Na_2SO_4	7	2212	6878	9090	31k	19k	19k	69k
Na_2SO_4	9.1	2876	8942	11818	41k	25k	24k	90k
Na_2SO_4	10.5	3318	10317	13636	47k	28k	28k	103k

[1] Calculated assuming an Al_2O_3 cost of 14.1 ZAR/kg
[2] Calculated assuming a Na_2SO_4 cost of 2.75 ZAR/kg
[3] Calculated assuming an encapsulation cost of 2.71 ZAR/kg (Mathur et al., 2014)

The estimated pressure vessel cost for the 7 m^3 packed bed is based on a quote received from Latham Engineering Africa. The cost of this vessel is 159k ZAR excluding taxes and installation. The internal volume of the pressure vessel is larger than the packed bed volume to account for the 50 mm insulation layer, which is constructed from microporous insulation. This material is typically a blend of ceramic powders and fibres and maintains a low thermal conductivity for high temperature applications.

The pressure vessel volumes are 8.0 m^3, 10.3 m^3 and 11.8 m^3 for the packed bed volumes of 7 m^3, 9.1 m^3 and 10.5 m^3 respectively. In order to calculate the cost of increasing the pressure vessel volume, Eq.(7.22) is used with a cost exponent of 0.6 for a vertical pressure vessel (Green and Perry, 2008). Therefore the cost of increasing the packed bed volume by 50% equates to a 26.2% increase in the estimated cost of the pressure vessel. The cost of the microporous insulation was quoted at 1980 ZAR/m^2 for a 25 mm thickness. Therefore the cost for a 50 mm inside thickness is estimated at 3960 ZAR/m^2. This price was used to calculate the cost of the insulation for the various configurations. Figure 7.23, illustrates the cost breakdown for the 7 m^3 Al_2O_3 bed and the 10.5 m^3 Na_2SO_4 bed.

$$C_2 = C_1 \left(\frac{V_2}{V_1} \right)^{0.6} \tag{7.22}$$

$$\frac{C_{9.1\text{m}^3}}{C_{7\text{m}^3}} = 1.162 \tag{7.23}$$

$$\frac{C_{10.5\text{m}^3}}{C_{7\text{m}^3}} = 1.262 \tag{7.24}$$

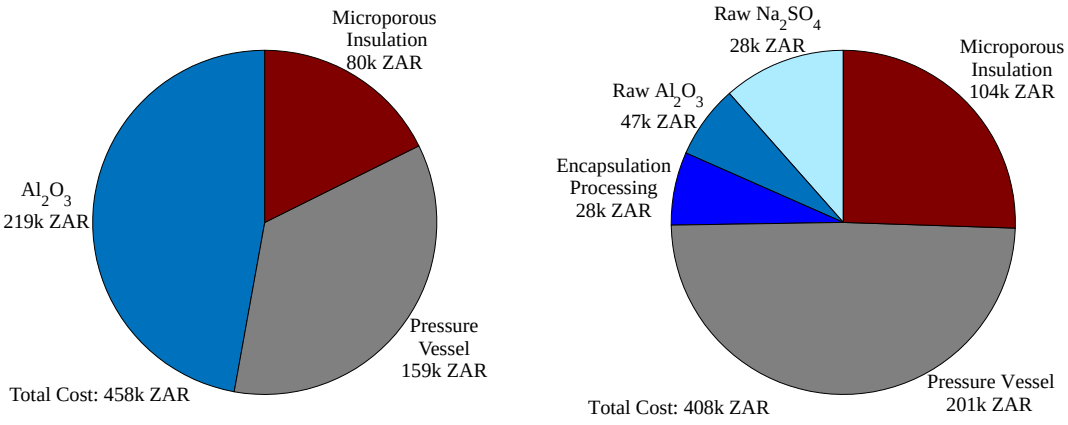

(a) 7 m^3 Al_2O_3 packed bed

(b) 10.5 m^3 Na_2SO_4 packed bed

Figure 7.23: Breakdown of the storage costs for Al_2O_3 and Na_2SO_4 packed beds, excluding installation costs and balance of plant equipment such as blower, piping and valves.

For the packed bed of Al_2O_3 particles the dominant cost is the storage material. For the Na_2SO_4 packed bed the dominant costs are the pressure vessel and insulation. The total estimated cost for the 10.5 m^3 Na_2SO_4 bed is 408k ZAR, while the total estimated cost for the 7 m^3 Al_2O_3 is 458k ZAR. At present the Al_2O_3 shell material and encapsulation processing cost account for a combined 75k ZAR, while the cost of the Na_2SO_4 is only 28k ZAR. Therefore further cost savings could be achieved if a low cost encapsulation process could be developed. Alternative shell materials could be considered with a lower density. This would allow for a higher mass fraction of Na_2SO_4 in the system. Metallic PCMs could also be considered, as the dominant costs are not the material costs for the PCM.

7.5.3 Multi-layered packed bed concept

The simulations presented in Section 7.5.2 demonstrate that less than 40% of the Na_2SO_4 particles in the packed bed, will undergo a phase change before the base temperature limit is reached. The added cost of encapsulating the particles that do not change phase is disadvantageous. In order to address this issue a Multi-Layered Packed Bed (MLPB) concept is proposed that combines the use of sensible heat storage in solid Al_2O_3 particles, with latent heat storage in EPCMs. As shown in Figure 7.24, the concept consists of three layers of storage materials, namely: encapsulated Na_2SO_4, solid Al_2O_3 and encapsulated NaCl-KCl eutectic. The MLPB materials were selected to increase the thermal storage performance for a fixed storage volume of 7 m^3. The combination of sensible heat and latent heat storage was previously proposed by Zanganeh et al. (2014) to stabilise the discharge temperature from a packed bed of rocks.

The sensible heat energy stored in the Al_2O_3 particles is dependent on the temperature change of the material between the charging and discharging cycles. Due to the temperature limit imposed on the base of the packed bed, the particles in this region do not undergo the full 350 °C temperature swing. Therefore, as shown in Figure 7.25(a), more thermal energy can be stored in the base region of the packed bed if an EPCM is used with a melting temperature between 600 °C and 670 °C. The chosen PCM for the bottom region of the MLPB concept is a eutectic mixture of NaCl-KCl salts. This PCM has a melting temperature of 657 °C and a latent heat capacity of 338 kJ/kg. At temperatures between 657 °C and 770 °C this PCM achieves a higher volumetric energy storage density than the solid Al_2O_3 particles. As discussed in Section 7.5.1, the base temperature limit for these simulations was increased to 670 °C so that the low cost material NaCl-KCl could be considered.

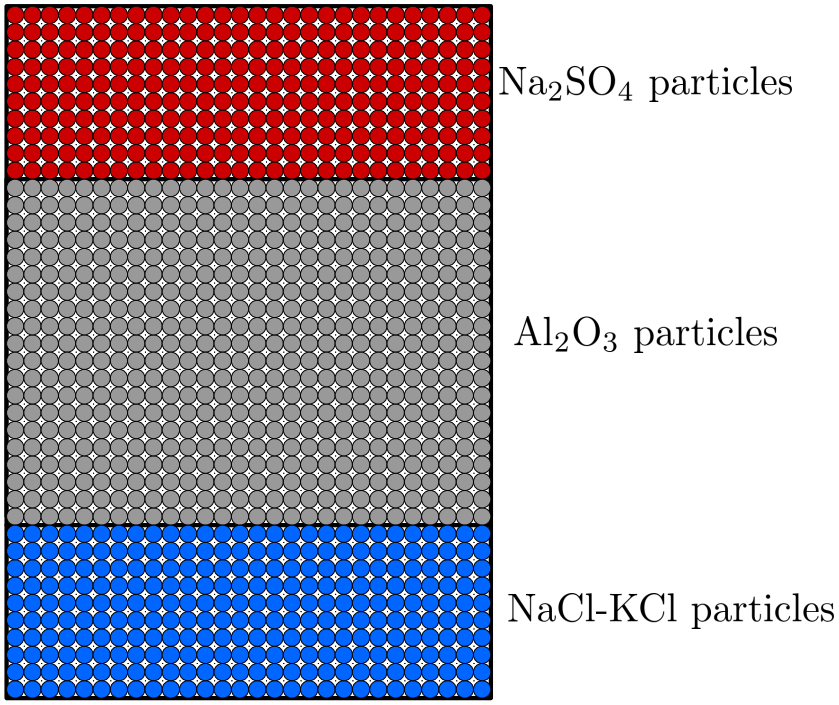

Figure 7.24: Multi-layered packed bed concept

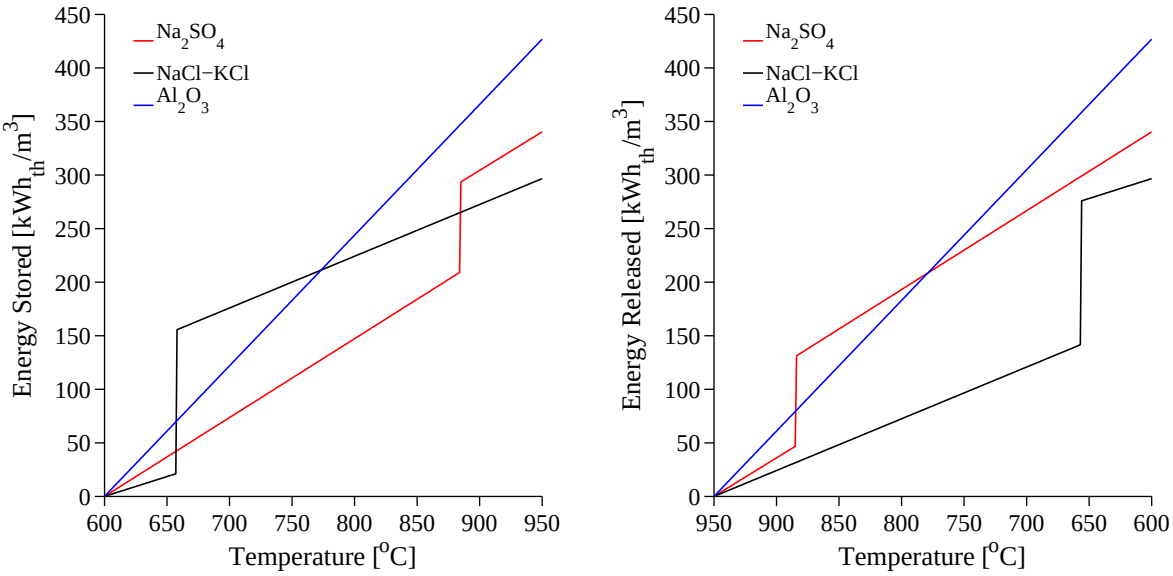

(a) Heating from 600 °C to 950 °C

(b) Cooling from 950 °C to 600 °C

Figure 7.25: Energy stored and released at different temperature ranges. Energy change based on a 600 °C reference temperature, excluding the packed bed void fraction.

During the charging cycle, the top region of the packed bed experiences a 350 °C temperature change. Across this temperature range the volumetric energy storage density of the Al_2O_3 is higher than that of the Na_2SO_4 salt. However, the advantage of placing the top layer of Na_2SO_4 is shown during the cooling cycle. Extracting energy from the Al_2O_3 particles causes the discharge temperature to decrease over time. This results in a drop in the thermal power output from the packed bed, requiring added hybridisation. In cases where hybridisation should be limited, it is beneficial to discharge thermal energy at a high temperature from the packed bed. As shown in Figure 7.25(b) the Na_2SO_4 is able to discharge more thermal energy than the Al_2O_3 at temperatures between 884 °C and 780 °C. This allows the MLPB to discharge energy at a higher rate than if only Al_2O_3 is utilised.

Table 7.5 presents four MLPB concepts that were considered in the analysis. A comparison of the discharge temperature profiles from the MLPBs is presented in Figure 7.26. The results show that decreasing the volume percentage of EPCMs in the system maximises the thermal storage performance. The MLPB 3 and MLPB 4 concepts provide a small increase the amount of energy discharged above 850 °C in comparison to the Al_2O_3 bed (5.3%). The thermal performance of the MLPB 4 concept is equivalent to the MLPB 3 concept, despite reducing the volume of EPCMs in the system from 20% to 10%.

The result that a small volume of EPCMs yields the best thermal storage performance indicates that low cost PCMs with low/moderate latent heat capacities are not an optimal material choice for the MLPB concept. Instead high cost PCMs with much higher heat capacities such as metallic PCMs and fluoride salts should be considered. These PCMs could further increase the thermal performance of the packed bed in comparison to the Al_2O_3 only bed. As the volume percentage of EPCM in the system is low the benefit of the high latent heat capacity would likely outweigh the added material costs. Therefore further work should investigate the potential of a MLPB with such PCMs.

Table 7.5: Composition of MLPB concepts

	EPCM: Na_2SO_4 [% vol.]	solid Al_2O_3 [% vol.]	EPCM: NaCl-KCl [% vol.]
MLPB 1	25	50	25
MLPB 2	20	60	20
MLPB 3	10	80	10
MLPB 4	5	90	5

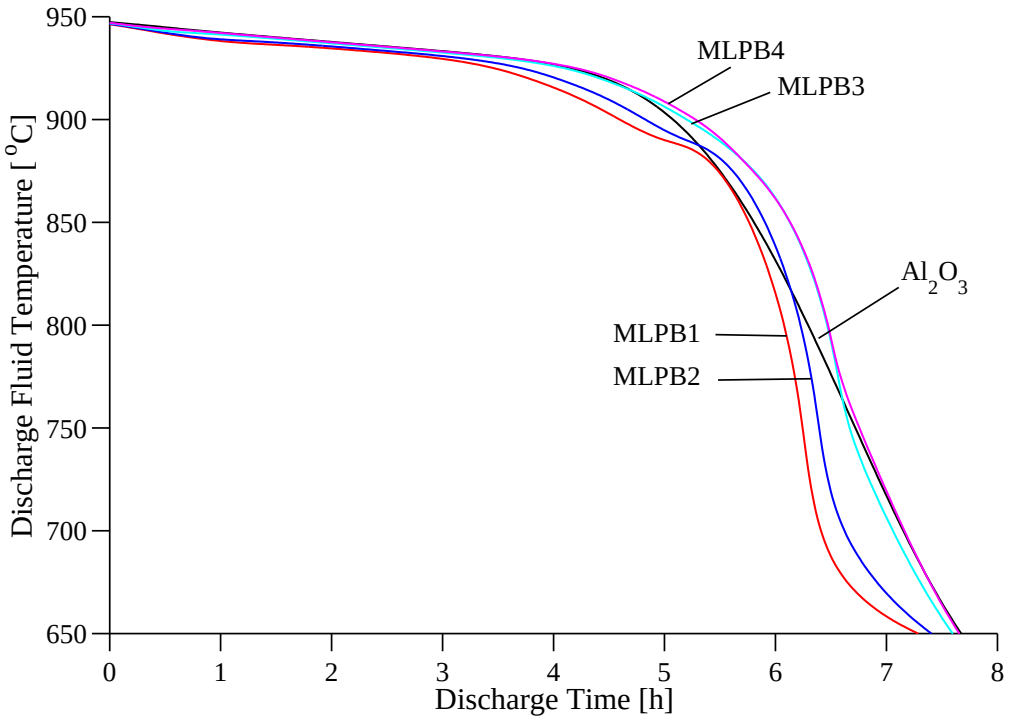

Figure 7.26: Discharge temperature profiles from MLPBs for $V = 7$ m^3, $d_p = 16$ mm. Discharging initiated at $t = 8.6$ h.

7.5.4 Conclusions for latent heat storage

The thermal performance of a packed bed of macro-encapsulated Na_2SO_4 particles was analysed using the D-C heat transfer model and the results compared to a packed bed of solid Al_2O_3 particles ($L_z/D = 3$ and $d_p = 16$ mm). In order to improve the energy storage capacity, a second MLPB concept was studied that combines sensible heat storage in Al_2O_3 particles with latent heat storage in EPCM particles. The proposed top layer of the MLPB consisted of encapsulated Na_2SO_4 particles, the middle layer solid Al_2O_3 particles and the bottom layer encapsulated NaCl-KCl particles. The main findings from the latent heat storage design studies are:

- For an equivalent 7 m^3 packed bed volume, the Na_2SO_4 EPCM particles could only store 66% of the thermal energy stored by the solid Al_2O_3 particles. At the end of the charging cycle only 33.6% of the Na_2SO_4 mass had fully melted, which significantly reduced the heat storage capacity of the packed bed.

- The sensible heat storage capacity of the Na_2SO_4 limits the energy stored during the charging cycle. Due to the low density of the salt at 1862 kg/m^3 the thermocline

penetrated through the solid region of the packed bed, causing the base temperature limit to be exceeded before a significant fraction of the salt had melted.

- Doubling the latent heat capacity of the Na_2SO_4 did not improve the thermal storage performance.
- If the volume of the Na_2SO_4 packed bed was increased to 10.5 m^3, the thermal storage performance was comparable to a 7 m^3 Al_2O_3 bed. A preliminary cost analysis indicated that the 10.5 m^3 Na_2SO_4 bed has the potential to achieve a 11% decrease in the storage cost and a 12% decrease in the storage mass compared to the 7 m^3 Al_2O_3 bed. This analysis was based on an assumed encapsulating cost (processing and shell material) of 7.24 ZAR/kg of Na_2SO_4. The cost of the Na_2SO_4 packed bed could be further reduced if a low cost encapsulation method is developed that does not use high density Al_2O_3 as the shell material.
- Decreasing the volume percentage of EPCM layers in the MLPB improves the overall energy storage density. A packed bed with 5% vol. Na_2SO_4 particles, 90% vol. solid Al_2O_3 particles and 5% vol. NaCl-KCl particles, provided a small increase in the thermal storage performance compared to an equivalent volume Al_2O_3 bed.
- In order to further increase the energy storage alternative PCMs should be considered for the MLPB. Due to the low volume fraction of PCMs in the MLPB concept, the use of more expensive PCMs with higher latent heat capacities than Na_2SO_4 and NaCl-KCl are recommended. Metallic PCMs or fluoride salts, with high heat storage capacities and would further improve the thermal storage performance of the MLPB concept without significantly increasing the overall storage cost.

Table 7.6 provides a summary of the thermal storage performances of the Al_2O_3 and EPCM particles that were analysed. In conclusion the thermal storage performance (energy discharged and utilisation factor) of the solid Al_2O_4 packed bed is difficult to significantly improve upon with the EPCMs that were tested in this work. Therefore in order for this technology to be viable, the cost of manufacturing the EPCM particles should be significantly lower than the cost of solid Al_2O_3 particles. The MLPB concept shows some promise in improving the energy storage density of the packed bed, although for the EPCMs tested the gains were not significant (5.3% increase in energy discharged above 850 °C).

Table 7.6: Comparison of sensible heat, latent heat and hybrid storage configurations for L_z/D=3 and d_p=16 mm

Packed bed type	V [m^3]	m_s [tonnes]	Q_c [MWh_{th}]	Q_d[1] [MWh_{th}]	Q_d[2] [MWh_{th}]	UF[1] [%]	UF[2] [%]
Al_2O_3 bed	7	15.51	1.67	1.54	1.32	83.5	74.8
Na_2SO_4 bed	7	9.09	1.11	0.99	0.87	65.3	57.5
Na_2SO_4 bed	9.1	11.82	1.45	1.31	1.16	66.4	59.1
Na_2SO_4 bed	10.5	13.64	1.69	1.52	1.36	66.8	59.8
MLPB 1 bed	7	11.90	1.58	1.45	1.29	88.2	78.4
MLPB 2 bed	7	12.62	1.62	1.48	1.32	88.3	79.0
MLPB 3 bed	7	14.07	1.69	1.55	1.39	87.9	78.9
MLPB 4 bed	7	14.79	1.71	1.56	1.39	86.7	77.4

[1] TES+hybridisation: energy extracted while T_d is above 620 °C.
[2] TES only: energy extracted while T_d is above 850 °C.

Chapter 8

Conclusions and Recommendations

Thermal storage in a pressurised packed bed provides a technology to increase the solar share of Solar Gas Turbine (SGT) plants. The thermal energy recovered from the storage system can be used to offset the usage of costly diesel fuel in off-grid plants. The overall objective of this thesis was to investigate two packed bed thermal storage concepts for SGT cycles. This was achieved through the development and validation of detailed numerical tools that simulate the forced convection heat transfer in a high temperature packed bed.

8.1 Sensible heat storage

The first storage concept was based on sensible heat storage in a packed bed of spherical ceramic particles. The main contributions from this research are:

- The development and validation of two comprehensive heat transfer models to study sensible heat thermal storage in a ceramic packed bed;
- The rigorous mathematical derivation of the heat transfer models in terms of fluid and solid phase temperatures,which was not previously reported;
- The finding that for sensible heat packed bed storage, the temperature gradients within the ceramic particles do not need to be explicitly modelled to yield accurate results;
- The new application of Orthogonal Collocation on Finite Elements (OCFE), using cubic Hermite splines, to model sensible heat thermal storage in a high temperature ceramic packed bed;

- The generation of high temperature experimental data from an alumino-silicate packed bed over the temperature ranges of recuperated and non-recuperated gas turbine cycles, which was not previously available;
- The provision of design recommendations for a six hour (1.55 MWh_{th}) sensible heat TES system for a SGT.

8.1.1 Modelling and experimental validation

Two types of heat transfer models were formulated in an axisymmetric domain for the packed bed TES, namely the Continuous-Solid (C-S) and Dispersion-Concentric (D-C) models. For modelling sensible heat storage, the more complex D-C model, which includes intra-particle temperature gradients, provided no increase in accuracy over the C-S model. Therefore the C-S model was utilised to analyse the ceramic packed bed. In comparison to previous models in the literature, the current modelling is more comprehensive, taking into account near wall flow effects that are present in small scale packed beds, as well as high temperature radiation heat exchange between particles and at the inner bed wall. The thermal storage modelling re-contextualises a broad range of constitutive empirical correlations (void fraction, flow channelling, effective fluid and solid conductivities, inter-phase heat transfer coefficient) that were developed primarily for packed bed reactors in the chemical engineering field.

In order to account for variable thermophysical properties, the governing energy equations for the C-S and D-C models were derived in terms of fluid enthalpy and solid internal energy. To facilitate an efficient numerical solution, the energy equations were rigorously reformulated in terms of fluid and solid temperatures. Relevant high temperature storage models (Jalalzadeh-Azar et al., 1996; Adebiyi et al., 1998; Nsofor, 2005), do not provide the derivation from fluid enthalpy and solid internal energy to fluid and solid temperatures. Therefore it was not known whether these models maintain the correct energy balance when using temperature dependent thermophysical properties. The derivation given in the current work verifies that these previous models are valid, providing a mathematical basis for their use with variable properties.

The governing energy equations for the C-S model were solved by the numerical technique of OCFE, using cubic Hermite splines as the basis functions. From the literature reviewed, this technique has not been previously used to study sensible heat thermal storage in a ceramic packed. Therefore the current work presents a new application of this numerical technique. Due to the fourth order accuracy of the finite elements, OCFE is an efficient method that

yields accurate solutions even on relatively coarse meshes. This allows rapid approximate solutions that can be used in a future real time predictive capability for an operational TES.

The proposed C-S model was validated against experimental data from a packed bed test facility that was developed as part of this study. Low temperature thermal tests (160 °C) were used to validate the model for convective heat transfer in the absence of significant radiation. The axial temperature profiles demonstrate the importance of accounting for the decrease in the core velocity due to wall channelling in small scale packed beds. The predicted axial temperature profiles from the packed bed were not sensitive to variations in the inter-phase heat transfer coefficient, and the use of the Gunn (1978) correlation was validated. Along the centreline of the packed bed a comparison of the C-S model and experimental data yielded a maximum Normalised Root Mean Square Deviation (NRMSD) of 5.3% and 4.7% for the fluid and solid phases respectively. Both the simulations and the experiments demonstrated the preferential heating and cooling of the fluid in the near wall region due to wall channelling. Despite the complex heat transfer at the bed wall, the maximum NRSMD for the model predictions in the near wall region was 7.1%, thus validating the modelling approach.

High temperature thermal tests were conducted over the operating temperature ranges of representative non-recuperated (350-900 °C) and recuperated (600-900 °C) SGT cycles. This was achieved through a new approach of preheating the packed bed, which has not been previously considered for high temperature experiments. Experimental data and simulations using the C-S model confirmed the result from Zanganeh et al. (2012) that temperature dependent variations in the solid heat capacity can influence the thermocline shape. Common ceramic heat storage materials undergo large changes in heat capacity below 350 °C but exhibit small changes if the temperature range is between 350 °C and 1000 °C. A comparison of the C-S model with the high temperature experimental data showed that the shape and position of the thermocline was accurately predicted. Along the bed centreline the NRMSD for the predicted solid phase temperature was below 11% for all the high temperature tests. The predicted solid phase temperatures in the near wall region were in good agreement with the measured values, with a maximum NRMSD below 3%. Therefore the near wall region of the packed bed was accurately modelled at high temperature.

8.1.2 Design studies

Previous design studies of SGT thermal storage systems are limited to a preliminary analysis conducted by Amsbeck et al. (2010). In order to determine the viability of this concept, more detailed investigations are required. A design study was conducted for a 1.55 MWh_{th}

storage system to provide a nominal six hours of thermal storage for the Turbec T100 gas micro-turbine. Alumina was selected as the storage material due to its high volumetric heat capacity. In contrast to previous design studies, a variable charging and discharging mass flow rate was used. This was based on a typical DNI profile for a clear day from the TMY for the plant location. Parameters that were varied included the particle size and aspect ratio (L_z/D) of the packed bed. For each analysed storage configuration the level of stored energy improved with increasing the aspect ratio and decreasing the particle diameter. The increase in performance was related to the improved convective heat transfer between the fluid and solid phases. This results in a steep thermocline gradient, allowing more energy to be stored and recovered.

Due to the nature of sensible heat thermal storage systems, the discharge temperature decreases as energy is extracted. The results of the storage optimisation demonstrated that the storage performance was maximised by utilising hybridisation with fossil fuels to boost the storage discharge temperature to 950 °C. By allowing more energy to be extracted from the storage, this operating strategy significantly improves the utilisation factor and storage efficiency. For the case of TES+hybridisation the configuration of aspect ratio $L_z/D = 2$ and $d_p = 10$ mm was determined to be optimal, yielding 1.56 MWh_{th} of discharged energy at a storage efficiency of 88% and utilisation factor of 85%. If hybridisation was not provided the preferable configuration was $L_z/D = 4$ and $d_p = 10$ mm, yielding 1.44 MWh_{th} energy discharged at a storage efficiency of 78% and utilisation factor of 78%.

Regenerative heat storage in solid media is not only limited to packed beds of spherical particles. An auxiliary design study compared the thermal performance of spherical particles to other commercially available inventory packings, including a random packing of saddles, and structured packings of honeycomb monoliths and checker bricks. Parametric simulations showed that the honeycomb monoliths and saddles have the highest thermal storage performance and the lowest pressure drop. However, the energy storage densities of these inventories are lower than spheres, requiring an increase in the storage volume of between 50% and 88%. Checker bricks have the highest energy storage density but the lowest thermal storage performance. A packed bed of spheres was identified as the most promising inventory type for SGT thermal storage, as this inventory type provides a good balance between energy storage density and thermal performance.

8.2 Latent heat storage

Although effective, sensible heat storage in ceramics requires a large mass that is energy intensive and costly to manufacture. By utilising Phase Change Materials (PCM), the energy storage density of the packed bed (mass basis) can be improved by storing latent heat and sensible heat energy. Another desired effect of using PCMs is the stabilisation of the discharge temperature at the PCM melting point during cooling.

Due to the high cost of alumina as a storage material, a second storage concept was investigated, based on a packed bed of Encapsulated Phase Change Materials (EPCM). This concept was analysed in order to determine if EPCM particles can provide an improved thermal storage performance or decreased storage costs, compared to solid Al_2O_3 particles. The EPCM packed bed is a novel storage concept for a SGT cycle, although it has been previously proposed for lower temperature systems (Zanganeh et al., 2014). The main contributions from this research are:

- The development and validation of a comprehensive heat transfer model to study latent heat thermal storage in a packed bed of EPCM particles;
- The new application of the numerical method of OCFE, using cubic Hermite splines, to model latent heat storage in a packed bed EPCMs;
- The novel extension of the conservative apparent heat capacity method of Gong (1996) for solving phase change problems;
- The generation of high temperature experimental data from a packed bed of macro-encapsulated Na_2SO_4 particles, which was not previously available;
- The first design study to consider macro-encapsulated PCM particles to provide thermal storage (1.55 MWh_{th}) for a SGT.
- The analysis of a three layered combined solid ceramic and EPCM storage concept, which has not previously been considered for a SGT cycle.

8.2.1 Modelling and experimental validation

A Biot number analysis for a single EPCM particle demonstrated that when the Biot number exceeds 0.5, the intra-particle temperature profiles are not accurately modelled using the lumped capacitance assumption. Therefore, due to the low thermal conductivity of inorganic

salts, the D-C model was utilised to model the EPCM packed bed. The melting and solidification of the PCM was modelled using the conservative effective heat capacity method, as originally proposed by Gong (1996). A novel extension to this method was developed to take into account a linear temperature dependence in the solid PCM heat capacity. The conservative heat capacity method avoids convergence problems and allows for stable implicit time stepping. The D-C model was solved using OCFE. No previous studies were found that have used this specific method, with cubic Hermite splines, to solve a phase change problem in a packed bed of EPCMs.

In comparison to previous models of EPCM packed beds, the D-C model is more detailed. It includes radial variations in temperature (axisymmetic), wall channelling, inter-particle heat transfer via conduction and radiation, and intra-particle heat transfer via conduction and convection (in liquid PCM). In the current work the inter-particle heat transfer via conduction and radiation is modelled by an equation that links the surface temperature of the particles in the packed bed. This is a more physically representative approach than the models proposed by previous authors such as Wakao and Kaguei (1982), who added the fluid and solid effective conductivities in the fluid energy equation.

A cost comparison of inorganic salts and metallic PCMs showed that sodium salts have the potential for a low cost storage material. The heat storage properties of the three sodium salts, Na_2SO_4, NaCl and Na_2CO_3 were compared. Sodium sulphate was selected as a suitable PCM for the gas micro-turbine cycle due to its favourable energy storage density, high melting temperature of 884 °C and stability up to 1100 °C. Macro-encapsulation of the Na_2SO_4 was selected in order to maximise the mass fraction of PCM in the packed bed. Alumina was chosen as a shell material, as it does not react with the molten Na_2SO_4 at high temperature. Therefore the packed bed design for the purpose of experimental validation consisted of macro-encapsulated Na_2SO_4 particles in a thin spherical Al_2O_3 shell.

The intra-particle heat transfer component of the D-C model was validated against experimental data from Akiyama et al. (1992) for a single EPCM sphere heated and cooled by convection. The experimental data included Al, KNO_3-$NaNO_3$ and NaCl. For the inorganic salts, the current model predicted the measured PCM temperatures with a higher degree of accuracy than the Akiyama et al. model. This was due to inclusion of natural convection effects in the liquid PCM. The modelling and experimental data showed that metallic PCMs melt isothermally, while inorganic salts exhibit notable intra-particle temperature gradients.

Previous models of EPCM packed beds are frequently validated against low temperature experimental data for PCMs such as paraffin wax (Beasley and Clark, 1984). Due to the difficulties encountered with testing high temperature PCMs there is a limited amount of experi-

mental data available. Temperature measurements from a packed bed of macro-encapsulated Na_2SO_4 particles were not available in the literature that was reviewed. Therefore, for the purpose of model validation experiments were conducted using a packed bed test facility consisting of 45 mm macro-encapsulated Na_2SO_4 spherical particles.

Sensible heat testing, conducted at 230 °C, validated the D-C model in the absence of a phase change. The predicted fluid temperature measurements were in good agreement with the experimental data, with a maximum NRMSD of 5.2%. The D-C model was further validated against high temperature experimental data (950 °C) for the melting and solidification of the packed bed of Na_2SO_4 particles. The heating of the solid salt was predicted with good accuracy, while the model under-estimated the rate of melting for the EPCM packed bed. This is potentially caused by a combination of non-concentric melting of the PCM and contact melting. The maximum NRMSD was 9% for the melting of the packed particles. During the cooling cycle the fluid temperature profiles remain constant at approximately 884 °C while the salt solidifies. This is the desired effect of using PCMs and it was demonstrated experimentally and numerically. Excluding the base of the test facility, where thermal losses influenced the results, the maximum NRMSD for the solidification of the PCM was 9.2%. In central region of the packed bed ($0.2\text{m} \leq z \leq 0.4\text{m}$, $r = 0$ m), where entrance effects and heat losses do not affect the results the NRMSD was below 5% for the solidification of the salt.

The experimental testing revealed a cracking problem with the EPCM particle shells. Once the salt had solidified, a number of particles cracked upon cooling, due to a combination of thermal and mechanical stresses. Therefore further research is required to develop an EPCM particle. Subsequent to the removal of the broken particles in the packed bed, a second heat transfer test was conducted to analyse the melting and solidification of the salt, for a reduced bed length of 0.4 m of Na_2SO_4 particles. The results of this test were consistent with the previous test. The D-C model predictions yielded a maximum NRMSD of 5.5% for the second latent heat storage test.

Considering the complexity of the heat transfer within the packed bed of EPCMs, the D-C model is shown to perform well and is able to accurately predict the measured temperature profiles in the EPCM bed. Therefore it can be used with confidence to conduct further design studies for a SGT cycle.

8.2.2 Design studies

In order to compare the thermal performance of EPCM particles to solid Al_2O_3 particles a design study was conducted using the validated D-C model for a fixed bed configuration of V=7 m^3, $L_z/D = 3$ and $d_p = 16$ mm. The results demonstrated that the Na_2SO_4 packed bed provided a 36% lower energy storage capacity than the Al_2O_3 bed. Even if the latent heat capacity of the PCM was doubled the heat storage capacity would not be improved.

The modelling revealed that the sensible heat storage capacity of the EPCM particles restricts the thermal storage performance when a limit is placed on the base temperature of the packed bed. During heating the thermocline penetrates through the solid region of the Na_2SO_4 bed faster than for the Al_2O_3 bed. This is caused by the apparent density of the encapsulated Na_2SO_4, which is 48% lower than than the Al_2O_3 density. Thus only 33.6% of the mass of salt in the packed bed was fully molten before the base temperature limit was exceeded and the charging cycle halted. Simulations indicated that if the EPCM packed bed volume was increased to 10.5 m^3 it could provide an equivalent thermal storage performance of a 7 m^3 Al_2O_3 bed, with a potential decrease in the overall storage cost of 11% (dependent on encapsulation cost).

The concept of a Multi Layer Packed Bed (MLPB) was introduced to combine the benefits of EPCM and solid particles in a single packed bed. The aim of this concept was to maximise the energy storage density for a 7 m^3 packed bed. The three proposed layers of storage were Na_2SO_4/Al_2O_3/NaCl-KCl. Simulations showed that reducing the volume fraction of EPCMs in the packed bed to 5% Na_2SO_4, 90% Al_2O_3, and 5% NaCl-KCl provided a small improvement in the heat storage capacity (5.3%) compared to solid Na_2SO_4 particles only. As the maximum energy storage density was achieved by minimising the volume of PCM in the packed bed, it is beneficial to investigate alternative PCMs that have a higher material cost but also a higher heat storage capacity. The melting temperatures of the top and base layers should be close to 950 °C and 600 °C respectively. Potential PCMs with high heat capacities include fluoride salts, aluminium, and a magnesium-silicon eutectic. In particular metals with a high silicon content have favourable thermal storage properties.

In conclusion, the EPCM particles considered in this work do not offer a significant improvement the thermal storage performance, compared to solid Al_2O_3 particles. Therefore the EPCMs should only be further considered for SGT cycles if they can be manufactured at very low cost. The use of EPCMs are better suited to non-pressurised TES applications, where the cost of increasing the storage volume is lower than for a pressurised packed bed.

8.3 Recommendations for further research

Further research is required to develop the high temperature packed bed thermal storage technology for SGT cycles. This section presents recommendations for the continuation of the research presented in this thesis.

The potential of thermal storage as an alternative to diesel fuel hybridisation in a SGT is dependent on the associated costs of the system. This thesis provides an in-depth thermodynamic analysis of the energy storage concept, which forms the foundation for future cost modelling. It is recommended that further detailed LCOE studies are performed to accurately quantify costs and determine the viability of the proposed thermal storage technology.

The focus of this study was on the investigation of heat transfer in high temperature packed beds. The pressure drop and flow modelling that was utilised was based on the Ergun (1952) and extended Brinkman (1949) equations. Parasitic energy losses due to the pressure drop across the packed bed influence the storage efficiency. The friction factor predicted by the Ergun equation should be validated for the transient heating and cooling of the packed bed between 600 °C and 950 °C.

This study demonstrated that with the correct choice of mass flux, the pressure drop across the packed bed is significantly lower than across the receiver. Therefore alternative concepts should be developed to reduce the receiver pressure drop while charging the packed bed. One potential concept is to utilise a secondary receiver for the charging of the storage. This would reduce the flow rate and pressure drop across each receiver.

The recommendation of Al_2O_3 particles as a sensible heat storage material is based on thermal considerations only. Further analysis of the material stability under thermal cycling is required. Ceramic and EPCM particles should be subjected to rapid thermal cycling tests as part of the development of this technology. Mathur et al. (2014) recommend that particles for CSP thermal storage should be able to withstand 10000 cycles for a typical plant lifespan of 30 years. In general, the ability of the alumino-silicate material to withstand thermal shock increases with SiO_2 content. However, decreasing the Al_2O_3 content also reduces the density of the material.

This thesis has presented a preliminary material analysis of EPCMs. Inorganic salts were studied due to their potential for low cost storage. The development of workable EPCMs requires further research into encapsulation methods. The primary difficulty of the macro-encapsulation approach is the expansion of the PCM upon melting. The Na_2SO_4 particles that were tested in this study were not hermetically sealed and therefore did not address

this issue. This is a major technical challenge that must be overcome before viable EPCMs can be developed. Research in this area was conducted by Goswami (2012) for NaCl. The results from that approach could potentially be transferred to other inorganic salts such as Na_2SO_4. Alternative shell materials should also be investigated. The thin Al_2O_3 shells that were utilised in the packed bed testing in this investigation exhibited cracking upon cooling and are therefore not suitable in their current form to EPCMs. The development of low cost shells would reduce the cost of the EPCMs. At present the estimated encapsulation cost of the Na_2SO_4 is 270% higher than the raw cost of the salt.

Alternative PCMs to Na_2SO_4 should be explored to improve the thermal storage performance of the packed bed. The testing presented in this thesis demonstrated that the sensible heat storage in the solid PCM has a strong influence on the amount of energy that can be stored. If a PCM has a high latent heat capacity but low sensible heat capacity the thermocline will penetrate through the solid region of the bed before a significant amount of PCM has melted. Therefore the density and sensible heat storage capacity of a PCM should be carefully considered in the search for improved PCMs.

From a thermal design perspective packed beds have the potential to provide efficient thermal storage for a SGT cycle. However, packed beds are subject to thermal ratcheting stresses which need to be addressed prior to the commercialisation of this technology. Thermal ratcheting is characterised by the cyclic expansion and contraction of the containment walls, which causes the settling of particles in the bed. The successive settling of the particles leads to added stresses on the inventory material and the inner wall/insulation. The design of the packed bed containment must account for thermal ratcheting stresses, which should be studied through a thermo-mechanical analysis, using tools such as Discrete Element Modelling (DEM).

The development of a pilot plant is required to reduce the technical risks associated with incorporating a pressurised, high temperature packed bed into a gas turbine cycle. It is recommended that the pilot plant should employ sensible heat storage as near term storage solution. Subsequent to the successfully integration of an Al_2O_3 packed bed storage system, the use of EPCMs could be considered.

.

References

Achenbach, E. (1995), Heat and flow characteristics of packed beds, *Experimental Thermal and Fluid Science* **10**(1), 17–27.

Adebiyi, G.A. (1991), A second-law study on packed bed energy storage systems utilizing phase-change materials, *Journal of Solar Energy Engineering* **113**(3), 146–156.

Adebiyi, G.A., Hodge, B.K., Steele, W.G., Jalalzadeh-Azar, A. and Nsofor, E.C. (1996), Computer simulation of a high-temperature thermal energy storage system employing multiple families of phase-change storage materials, *Journal of Energy Resources Technology* **118**(2), 102–111.

Adebiyi, G.A., Nsofor, E.C., Steele, W.G. and Jalalzadeh-Azar, A.A. (1998), Parametric study on the operating efficiencies of a packed bed for high-temperature sensible heat storage, *Journal of Solar Energy Engineering* **120**(1), 2–13.

Akiyama, T., Ashizawa, Y. and Yagi, J. (1992), Storage and release of heat in a single spherical capsule containing phase-change material with a high melting point, *Heat Transfer Japanese Research* **21**(2), 199–217.

Allen, K.G. (2014), Rock bed thermal storage for concentrating solar power plants, PhD thesis, Stellenbosch University.

Amelio, M. and Morrone, P. (2007), Numerical evaluation of the energetic performances of structured and random packed beds in regenerative thermal oxidizers, *Applied Thermal Engineering* **27**(4), 762–770.

Amiri, A. and Vafai, K. (1994), Analysis of dispersion effects and non-thermal equilibrium, non-Darcian, variable porosity incompressible flow through porous media, *International Journal of Heat and Mass Transfer* **37**(6), 939–954.

AMM (2015). American Metal Market, Daily AMM, Retrieved March 25, 2015, from www.amm.com.

Amsbeck, L., Buck, R., Heller, P., Jedamski, J. and Uhlig, R. (2008), Development of a tube receiver for a solar-hybrid microturbine system, *in Proceedings of the 14th SolarPACES Conference*, Las Vegas, pp. 4–7.

Amsbeck, L., Denk, T., Ebert, M., Gertig, C., Heller, P., Herrmann, P.. and Rehn, J.. (2010), Test of a solar-hybrid microturbine system and evaluation of storage deployment, *in Proceedings of the 16th SolarPACES Conference,* Perpignan.

Anderson, O.L. (1963), A simplified method for calculating the debye temperature from elastic constants, *Journal of Physics and Chemistry of Solids* **24**(7), 909–917.

Aora (2012). Tulip DST unit - Features summary.

Auerkari, P. (1996), *Mechanical and physical properties of engineering alumina ceramics*, Technical Research Centre of Finland.

Avila-Marin, A.L., Alvarez-Lara, M. and Fernandez-Reche, J. (2014), A regenerative heat storage system for central receiver technology working with atmospheric air, *Energy Procedia* **49**, 705–714.

Balakrishnan, A.R. and Pei, D.C. (1979), Heat transfer in gas-solid packed bed systems. 1. A critical review, *Industrial and Engineering Chemistry Process Design and Development* **18**(1), 30–40.

Barin, I., Kubaschewski, O. and Knacke, O. (1977), *Thermochemical properties of inorganic substances, Supplement*, Springer-Verlag, Berlin.

Beasley, D.E. and Clark, J.A. (1984), Transient response of a packed bed for thermal energy storage, *International Journal of Heat and Mass Transfer* **27**(9), 1659–1669.

Beasley, D.E., Ramanarayanan, C. and Torab, H. (1989), Thermal response of a packed bed of spheres containing a phase-change material, *International Journal of Energy Research* **13**(3), 253–265.

Benenati, R.F. and Brosilow, C.B. (1962), Void fraction distribution in beds of spheres, *American Institute of Chemical Engineers Journal* **8**(3), 359–361.

Benmansour, A., Hamdan, M.A. and Bengeuddach, A. (2006), Experimental and numerical investigation of solid particles thermal energy storage unit, *Applied Thermal Engineering* **26**(5), 513–518.

Benyahia, F. (2004), On the modelling of flow in packed bed systems, *Particulate Science Technology Journal* **22**(4), 367–378.

Bindra, H., Bueno, P., Morris, J.F. and Shinnar, R. (2013), Thermal analysis and exergy evaluation of packed bed thermal storage systems, *Applied Thermal Engineering* **52**(2), 255–263.

Bird, R.B., Stewart, W.E. and Lightfoot, E.N. (2002), *Transport phenomena*, John Wiley & Sons.

Bischof-Niemz, T. (2015), Financial costs and benefits of renewables in South Africa in 2014, Technical report, CSIR, CSIR/02400/RD Core/IR/2015/0001/B.

Bongwe, K. (2013), Overview of universal energy access strategy, Presentation from Department of Energy IEP planning workshop.

Borbely, A.M. and Kreider, J.F. (2001), *Distributed generation: the power paradigm for the new millennium*, CRC press.

Botterill, J.S. and Denloye, A.O. (1978), A theoretical model of heat transfer to a packed or quiescent fluidized bed, *Chemical Engineering Science* **33**(4), 509–515.

Boyse, F., Causevic, A., Duwe, E., Orthofer, M. and Cullinen, M.S. (2014), Implementing renewable energy for off-grid operations.

Bradshaw, A.V., Johnson, A., McLachlan, N.H. and Chiu, Y.T. (1970), Heat transfer between air and nitrogen and packed beds of non-reacting solids, *Transactions of the Institute of Chemical Engineers* **48**, T77–T84.

Brinkman, H.C. (1949), A calculation of the viscous force exerted by a flowing fluid on a dense swarm of particles, *Applied Scientific Research* **1**(1), 27–34.

BSI (1981), Measurement of fluid flow in closed conduits. Part 1: Pressure differential devices. British Standard Institution.

BSI (2008), Industrial fans-Performance testing using standardized airways. BS EN ISO 5801:2008, British Standards Institute.

Burke, S.P. and Plummer, W.B. (1928), Gas flow through packed columns, *Industrial & Engineering Chemistry* **20**(11), 1196–1200.

Carman, P.C. (1937), Fluid flow through granular beds, *Transactions-Institution of Chemical Engineeres* **15**, 150–166.

Chang, P.W. and Finlayson, B.A. (1978), Orthogonal collocation on finite elements for elliptic equations, *Mathematics and Computers in Simulation* **20**(2), 83–92.

Cheng, P. and Hsu, C.T. (1986), Fully-developed, forced convective flow through an annular packed-sphere bed with wall effects, *International Journal of Heat and Mass Transfer* **29**(12), 1843–1853.

Claar, T.D. and Petri, R.J. (1983), High-temperature direct-contact thermal energy storage using phase-change media. US Patent 4,421,661.

Claar, T.D. and Petri, R.J. (1985), High-temperature direct-contact thermal energy storage using phase-change media. US Patent 4,512,388.

Comini, G., Del Guidice, S., Lewis, R.W. and Zienkiewicz, O.C. (1974), Finite element solution of non-linear heat conduction problems with special reference to phase change, *International Journal for Numerical Methods in Engineering* **8**(3), 613–624.

Creffield, G.K. and Wickens, A.J. (1975), Thermal conductivity of anhydrous borax, boric oxide, and sodium sulfate, *Journal of Chemical and Engineering Data* **20**(3), 223–225.

Daszkowski, T. and Eigenberger, G. (1992), A reevaluation of fluid flow, heat transfer and chemical reaction in catalyst filled tubes, *Chemical Engineering Science* **47**(9), 2245–2250.

DME (2003), White paper on the renewable energy policy of the Republic of South Africa. Department of Minerals and Energy, Pretoria.

Du Plessis, J.P. and Woudberg, S. (2008), Pore-scale derivation of the ergun equation to enhance its adaptability and generalization, *Chemical Engineering Science* **63**(9), 2576–2586.

Du Toit, C.G. (2008), Radial variation in porosity in annular packed beds, *Nuclear Engineering and Design* **238**(11), 3073–3079.

Du Toit, C.G., Rousseau, P.G., Greyvenstein, G.P. and Landman, W.A. (2006), A systems CFD model of a packed bed high temperature gas cooled nuclear reactor, *International Journal of Thermal Sciences* **45**(10), 70–85.

Eberhard, A. (2011), The future of South African coal: Market, investment, and policy challenges, *Programme on Energy and Sustainable Development* .

Ergun, S. (1952), Fluid flow through packed columns, *Chemical Engineering Progress* **48**(2), 89–94.

Fahien, R.W. and Stankovic, I.M. (1979), An equation for the velocity profile in packed columns, *Chemical Engineering Science* **34**(11), 1350–1354.

Fand, R.M., Kim, B.Y.K., Lam, A.C.C. and Phan, R.T. (1987), Resistance to the flow of fluids through simple and complex porous media whose matrices are composed of randomly packed spheres, *Journal of Fluids Engineering* **109**(3), 268–273.

Faris, W.G. (2004), Lectures on partial differential equations. University of Arizona.

Finlayson, B.A. (1980), Orthogonal collocation on finite elements - progress and potential, *Mathematics and Computers in Simulation* **22**(1), 11–17.

Fluri, T.P. (2009), The potential of concentrating solar power in South Africa, *Energy Policy* **37**(12), 5075–5080.

Forsberg, C.W., Peterson, P.F. and Zhao, H. (2007), High-temperature liquid-fluoride-salt closed-Brayton-cycle solar power towers, *Journal of Solar Energy Engineering* **129**(2), 141–146.

Galamba, N., Nieto de Castro, C.A. and Ely, J.F. (2004), Thermal conductivity of molten alkali halides from equilibrium molecular dynamics simulations, *The Journal of Chemical Physics* **120**(18), 8676–8682.

Gheribi, A.E., Salanne, M. and Chartrand, P. (2015), Thermal transport properties of halide solid solutions: Experiments vs equilibrium molecular dynamics, *The Journal of chemical physics* **142**(12), 124109.

Giese, M., Rottschäfer, K. and Vortmeyer, D. (1998), Measured and modeled superficial flow profiles in packed beds with liquid flow, *American Institute of Chemical Engineers Journal* **44**(2), 484–490.

Glück, A., Tamme, R., Kalfa, H. and Streuber, C. (1991), Investigation of high temperature storage materials in a technical scale test facility, *Solar Energy Materials* **24**(1), 240–248.

Gokon, N., Nakano, D., Inuta, S. and Kodama, T. (2008), High-temperature carbonate/MgO composite materials as thermal storage media for double-walled solar reformer tubes, *Solar Energy* **82**(12), 1145–1153.

Gong, Z.X. (1996), Time-dependent melting and freezing heat transfer in multiple phase change materials, PhD thesis, McGill University Montreal, Quebec, Canada.

Goswami, D.Y. (2011), Development of low cost industrially scalable PCM capsules for thermal energy storage in CSP plants, Technical report, University of South Florida. Presentation.

Goswami, D.Y. (2012), Development and demonstration of an innovative thermal energy storage system for baseload power generation, Technical report, University of South Florida. DE-EE0003590.

Grange, B., Dalet, C., Falcoz, Q., Siros, F. and Ferrière, A. (2014), Simulation of a hybrid solar gas-turbine cycle with storage integration, *Energy Procedia* **49**, 1147–1156.

Green, D.W. and Perry, R.H. (2008), *Perry's chemical engineers' handbook*, 8th edn, McGraw-hill New York.

Gunn, D.J. (1978), Transfer of heat or mass to particles in fixed and fluidised beds, *International Journal of Heat and Mass Transfer* **21**(4), 467–476.

Gunn, D.J. and De Souza, J.F. (1974), Heat transfer and axial dispersion in packed beds, *Chemical Engineering Science* **29**(6), 1363–1371.

Hänchen, M., Brückner, S. and Steinfeld, A. (2011), High-temperature thermal storage using a packed bed of rocks–heat transfer analysis and experimental validation, *Applied Thermal Engineering* **31**(10), 1798–1806.

Hartnady, C.J. (2010), South Africa's diminishing coal reserves, *South African Journal of Science* **106**(9-10), 1–5.

Heller, P., Pfänder, M., Denk, T., Tellez, F., Valverde, A., Fernandez, J. and Ring, A. (2006), Test and evaluation of a solar powered gas turbine system, *Solar Energy* **80**(10), 1225–1230.

Herrmann, U. and Kearney, D.W. (2002), Survey of thermal energy storage for parabolic trough power plants, *Journal of Solar Energy Engineering* **124**(2), 145–152.

Hu, H. and Argyropoulos, S.A. (1996), Mathematical modelling of solidification and melting: a review, *Modelling and Simulation in Materials Science and Engineering* **4**(4), 371.

Hunt, M.L. and Tien, C.L. (1990), Non-Darcian flow, heat and mass transfer in catalytic packed-bed reactors, *Chemical Engineering Science* **45**(1), 55–63.

IAEA (2001), Heat transport and afterheat removal for gas-cooled reactors under accident conditions-technical report IAEA-TECDOC-1163, Technical report, International Atomic Energy Agency.

IEA (2011), Energy for all - Financing access for the poor., IEA. Special early excerpt of the World Energy Outlook 2011, International Energy Agency.

Incropera, F.P. and Dewitt, D.P. (2002), Fundamentals of mass and heat transfer.

Ismail, K.A. and Stuginsky, R. (1999), A parametric study on possible fixed bed models for PCM and sensible heat storage, *Applied Thermal Engineering* **19**(7), 757–788.

Jalalzadeh-Azar, A.A., Steele, W.G. and Adebiyi, G.A. (1996), Heat transfer in a high-temperature packed bed thermal energy storage system - roles of radiation and intraparticle conduction, *Journal of Energy Resources Technology* **118**(1), 50–57.

Jalalzadeh-Azar, A.A., Steele, W.G. and Adebiyi, G.A. (1997), Performance comparison of high-temperature packed bed operation with PCM and sensible heat pellets, *International Journal of Energy Research* **21**(11), 1039–1052.

Janz, G.J. (1988), Thermodynamic and transport properties for molten salts: Correlation equations for critically evaluated density, surface tensions, electrical conductance, and viscosity data, *Journal of Physical and Chemical Reference Data* **17**.

Janz, G.J., Tomkins, R.P.T., Allen, C.B., Downey Jr, J.R., Garner, G.L., Krebs, U. and Singer, S.K. (1975), Molten salts: Volume 4, part 2, chlorides and mixtures - electrical conductance, density, viscosity, and surface tension data, *Journal of Physical and Chemical Reference Data* **4**(4), 871–1178.

Jeffreson, C.P. (1972), Prediction of breakthrough curves in packed beds: 1. Applicability of single parameter models, *American Institute of Chemical Engineers Journal* **18**(2), 409–416.

Kaviany, M. (1995), *Principles of heat transfer in porous media*, 2 edn, Springer-Verlag.

Kenisarin, M.M. (2010), High-temperature phase change materials for thermal energy storage, *Renewable and Sustainable Energy Reviews* **14**(3), 955–970.

Kittel, C. (1976), *Introduction to solid state physics*, 5th edn, John Wiley & Sons.

Klein, P., Roos, T.H. and Sheer, T.J. (2014), Experimental investigation into a packed bed thermal storage solution for solar gas turbine systems, *Energy Procedia, 49, 840-849.* **49**, 840–849.

Klein, P., Roos, T.H. and Sheer, T.J. (2015), Parametric analysis of a high temperature packed bed thermal storage design for a solar gas turbine, *Solar Energy* **118**, 59–73.

Klinkenberg, A. (1948), Numerical evaluation of equations describing transient heat and mass transfer in packed solids, *Industrial & Engineering Chemistry* **40**(10), 1992–1994.

Kodama, T., Isobe, Y., Kondoh, Y., Yamaguchi, S. and Shimizu, K.I. (2004), Ni/ceramic/molten-salt composite catalyst with high-temperature thermal storage for use in solar reforming processes, *Energy* **29**(5), 895–903.

Koning, G.W. (2002), Heat and mass transport in tubular packed bed reactors at reacting and non-reacting conditions, PhD thesis, Twente University Press.

KTA (1981), Reactor core design of high temperature gas-cooled reactors. Part 3: Loss of pressure through friction in pebble bed cores. KTA3102.3. German Nuclear Safety Standards Commission.

KTA (1983), Reactor core design of high temperature gas-cooled reactors. Part 2: Heat transfer spherical fuel elements, KTA3102.2. German Nuclear Safety Standards Commission.

Kumar, K.P. (1998), Heat transfer characteristics of air heater heating elements, Master's thesis, University of the Witwatersrand.

Kunii, D. and Smith, J.M. (1960), Heat transfer characteristics of porous rocks, *American Institute of Chemical Engineers Journal* **6**(1), 71–78.

Laguerre, O., Amara, S.B., Alvarez, G. and Flick, D. (2008), Transient heat transfer by free convection in a packed bed of spheres: Comparison between two modelling approaches and experimental results, *Applied Thermal Engineering* **28**(1), 14–24.

Lemmon, E.C. (1981), Multidimensional integral phase change approximations for finite element conduction codes, *in* R. W. Lewis, K. Morgan and O. C. Zienkiewicz, eds, 'Numerical methods in heat transfer', Wiley, Chichester, pp. 201–213.

Lide, D.R., ed. (2001), *CRC handbook of physics and chemistry*, 82nd edn, CRC Press.

Longe, O.M., Ouahada, K., Ferreira, H.C. and Chinnappen, S. (2014), Renewable energy sources microgrid design for rural area in South Africa, *in Innovative Smart Grid Technologies Conference (ISGT), 2014 IEEE PES*, IEEE, pp. 1–5.

Macdonald, I.F., El-Sayed, M.S., Mow, K. and Dullien, F.A. (1979), Flow through porous media-the Ergun equation revisited, *Industrial & Engineering Chemistry Fundamentals* **18**(3), 199–208.

Mantz, R.A. and de Electroquimica, S.M. (2007), Molten salts 15: In memory of Robert Osteryoung, Electrochemical Society.

Marion, W. and Urban, K. (1995), Users manual for TMY2s: Derived from the 1961–1990 national solar radiation data base, Technical report, National Renewable Energy Laboratory (NREL), USA.

Martin, H. (1978), Low Peclet number particle-to-fluid heat and mass transfer in packed beds, *Chemical Engineering Science* **33**(7), 913–919.

Martin, J.F. (1987), Thermal energy storage. Technical progress report, April 1985-March 1986, Technical report, Oak Ridge National Lab., TN (USA). ORNL/TM-10247.

Mathur, A., Kasetty, R., Oxley, J., Mendez, J. and Nithyanandam, K. (2014), Using encapsulated phase change salts for concentrated solar power plant, *Energy Procedia* **49**, 908–915.

McGreavy, C., Foumeny, E.A. and Javed, K.H. (1986), Characterization of transport properties for fixed bed in terms of local bed structure and flow distribution, *Chemical Engineering Science* **41**(4), 787–797.

Meier, A., Winkler, C. and Wuillemin, D. (1991), Experiment for modelling high temperature rock bed storage, *Solar Energy Materials* **24**(1), 255–264.

Mills, O.F. (1992), *Heat Transfer*, Irwing, Boston.

Mongibello, L., Atrigna, M. and Graditi, G. (2013), Parametric analysis of a high temperature sensible heat storage system by numerical simulations, *Journal of Solar Energy Engineering* **135**(4), 041010.

Nag, P.K. (2007), *Heat and Mass Transfer*, 2nd edn, McGraw Hill, New Delhi.

NI (2004), SignalExpress: Getting started with SignalExpress. National Instruments, 373873A-01.

NI (2014), NI CompactDAQ datasheet. National Instruments.

Niessen, H.F. and Stöcker, B. (1997), Data sets of the SANA experiment 1994-1996, Technical report, JUEL-3409. Forschungszentrum Jülich GmbH.

Nithyanandam, K., Pitchumani, R. and Mathur, A. (2014), Analysis of a latent thermocline storage system with encapsulated phase change materials for concentrating solar power, *Applied Energy* **113**, 1446–1460.

Norton (1997), Denstone catalyst bed support media. Norton Chemical Process Products Corporation.

Notter, W., Lechner, T., Groß, U. and Hahne, E. (1993), Thermophysical properties of the composite ceramic-salt system (SiO_2/Na_2SO_4), *Thermochimica Acta* **218**, 455–463.

Nsofor, E.C. (2005), Investigations on the packed bed for high-temperature thermal energy storage, *International Journal of Green Energy* **2**(4), 337–351.

Pendyala, S. (2012), Macroencapsulation of phase change materials for thermal energy storage, Master's thesis, University of South Florida.

Pham, Q.T. (1986), The use of lumped capacitance in the finite-element solution of heat conduction problems with phase change, *International Journal of Heat and Mass Transfer* **29**(2), 285–291.

Pitz-Paal, R., Dersch, J. and Milow, B. (2005), European concentrated solar thermal roadmapping (ECOSTAR), *European Commission, Coordinated action sustainable energy systems SES6-CT-2003-502578, Cologne* .

Quero, M., Korzynietz, R., Ebert, M., Jiménez, A.A., del Río, A. and Brioso, J.A. (2014), Solugas–operation experience of the first solar hybrid gas turbine system at MW scale, *Energy Procedia* **49**, 1820–1830.

Rahman, M.S. (2009), *Food properties handbook*, CRC press.

Ranz, W.E. and Marshall, W.R. (1952), Evaporation from drops, *Chemical Engineering Progress* **48**(3), 141–146.

Regin, A.F., Solanki, S.C. and Saini, J.S. (2009), An analysis of a packed bed latent heat thermal energy storage system using PCM capsules: Numerical investigation, *Renewable Energy* **34**(7), 1765–1773.

Rohsenow, M., Hartnett, J.P. and Cho, Y. (1998), *Handbook of Heat Transfer*, 3rd edn, New York, McGraw-Hill.

Roine, A., Lamberg, P., Katiranta, T. and Salminen, J. (2009), HSC Chemistry 7 Simulation. Outotec Research, Finland.

Roos, T.H., Rubin, N., Maliage, M., Klein, P., Dunn, D. and Perumal, S. (2015), DPSS IRIP Progress Report for 2010/2011 and 2011/2012, *CSIR Report, DPSS ASC2011/046* .

SARB (n.d.). South African Reserve Bank, Retrieved September 21, 2015, from https://www.resbank.co.za.

Schumann, T.E. (1929), Heat transfer: a liquid flowing through a porous prism, *Journal Franklin Institute* **208**(3), 405–416.

Schwartz, C.E. and Smith, J.M. (1953), Flow distribution in packed beds, *Industrial & Engineering Chemistry* **45**(6), 1209–1218.

Schwarzbözl, P., Buck, R., Sugarmen, C., Ring, A., Crespo, M.J., Altwegg, P. and Enrile, J. (2006), Solar gas turbine systems: Design, cost and perspectives, *Solar Energy* **80**(10), 1231–1240.

Sergeev, D., Kobertz, D. and Müller, M. (2015), Thermodynamics of the NaCl-KCl system, *Thermochimica acta* **606**, 25–33.

Skaare, S.H. (1993), Reaction and heat transfer in a wall-cooled fixed bed reactor, PhD thesis, Norwegian University of Science and Technology, Trondheima.

Smirnov, M.V., Khokhlov, V.A. and Filatov, E.S. (1987), Thermal conductivity of molten alkali halides and their mixtures, *Electrochimica acta* **32**(7), 1019–1026.

Spelling, J. (2013), Hybrid Solar Gas-Turbine Power Plants: A Thermoeconomic Analysis, PhD thesis, KTH University.

Stine, W.B. and Geyer, M. (2001), Power from the sun. Retrieved April 15, 2011, from www.powerfromthesun.net/book.html.

Suleiman, B.M., Lundén, A. and Karawacki, E. (2000), Heat transfer and ion migration in the system Li_2SO_4-Na_2SO_4, *Solid state ionics* **136**, 325–330.

Surendranatha, A.O. (2015), *An Introduction to ceramics and refractories*, CRC Press, Boca Raton.

Tamme, R., Grozinger, U., Gluck, A., Kanwischer, H. and Neitzel, U. (1990), Advanced regenerator media for industrial and solar thermal applications, *in* Energy Conversion Engineering Conference, Vol. 4, pp. 218–221.

Tamme, R., Taut, U., Streuber, C. and Kalfa, H. (1991), Energy storage development for solar thermal processes, *Solar Energy Materials* **24**(1), 386–396.

Thy, P. and Jenkins, B.M. (2006), Use of sodium sulfate separated from agricultural drainage water in glass making, *Final Report. Department of Water Resources, Sacramento, California* .

Too, S., Olivares, R., Benito, R., Kim, J.S., Duffy, G. and Edwards, J. (2012), High temperature thermal energy storage systems for open-cycle solar air Brayton plant.

Touloukian, Y.S. and Ho, C.Y. (1970*a*), Thermophysical properties of matter-the TPRC data series: Specific heat of nonmetallic solids, Technical report, DTIC Document.

Touloukian, Y.S. and Ho, C.Y. (1970*b*), Thermophysical properties of matter-the TPRC data series: Thermal conductivity of nonmetallic solids, Technical report, DTIC Document.

Tsotsas, E. (2002), *Heat exchanger design handbook*, Begell House. Section 2.8.2., G. F. Hewitt (ed.).

Tsotsas, E. and Schlünder, E.U. (1988), Some remarks on channelling and on radial dispersion in packed beds, *Chemical Engineering Science* **43**(5), 1200–1203.

Tsotsas, E. and Schlünder, E.U. (1990), Heat transfer in packed beds with fluid flow: remarks on the meaning and the calculation of a heat transfer coefficient at the wall, *Chemical Engineering Science* **45**(4), 819–837.

Vafai, K. (1984), Convective flow and heat transfer in variable-porosity media, *Journal of Fluid Mechanics* **147**, 233–259.

Van Antwerpen, W. (2009), Modelling the effective thermal conductivity in the near-wall region of a packed pebble bed, PhD thesis, North-West University, Potchefstroom Campus.

Varone, A., Pili, P. and Murgia, G. (2010), A thermocline, two-phases, solar heat storage tank: modelling, parametric simulations and design for a real case, *in Proceedings of the 16th SolarPACES Conference*, Perpignan.

Visser, C.J. (2007), Modelling heat and mass flow through packed pebble beds: a heterogeneous volume-averaged approach, Master's thesis, University of Pretoria.

Vorayos, N., Tippayawong, N. and Thanapiyawanit, B. (2008), Thermo-fluid characterization of flue gas flows through a packed bed, *Journal of Mechanical Science and Technology* **22**(5), 973–980.

Vortmeyer, D. and Haidegger, E. (1991), Discrimination of three approaches to evaluate heat fluxes for wall-cooled fixed bed chemical reactors, *Chemical Engineering Science* **46**(10), 2651–2660.

Vortmeyer, D. and Schuster, J. (1983), Evaluation of steady flow profiles in rectangular and circular packed beds by a variational method, *Chemical Engineering Science* **38**(10), 1691–1699.

Wakao, N. and Kaguei, S. (1982), *Heat and mass transfer in packed beds*, Vol. 1, Taylor & Francis.

Wakao, N., Kaguei, S. and Funazkri, T. (1979), Effect of fluid dispersion coefficients on particle-to-fluid heat transfer coefficients in packed beds: correlation of Nusselt numbers, *Chemical Engineering Science* **34**(3), 325–336.

Williams, D.F. (2006), Assessment of candidate molten salt coolants for the NGNP/NHI heat-transfer loop, *ORNL/TM-2006/69, Oak Ridge National Laboratory, Oak Ridge, Tennessee* .

Winterberg, M. and Tsotsas, E. (2000), Impact of tube-to-particle-diameter ratio on pressure drop in packed beds, *American Institute of Chemical Engineers Journal* **46**(5), 1084–1088.

Winterberg, M., Tsotsas, E., Krischke, A. and Vortmeyer, D. (2000), A simple and coherent set of coefficients for modelling of heat and mass transport with and without chemical reaction in tubes filled with spheres, *Chemical Engineering Science* **55**(5), 967–979.

Wu, M., Xu, C. and He, Y.L. (2014), Dynamic thermal performance analysis of a molten-salt packed-bed thermal energy storage system using PCM capsules, *Applied Energy* **121**, 184–195.

Xia, L., Zhang, P. and Wang, R.Z. (2010), Numerical heat transfer analysis of the packed bed latent heat storage system based on an effective packed bed model, *Energy* **35**(5), 2022–2032.

Yagi, J. and Akiyama, T. (1995), Storage of thermal energy for effective use of waste heat from industries, *Journal of Materials Processing Technology* **48**(1), 793–804.

Yoshida, F., Ramaswami, D. and Hougen, O.A. (1962), Temperatures and partial pressures at the surfaces of catalyst particles, *American Institute of Chemical Engineers Journal* **8**(1), 5–11.

Yu, J., Zhang, M., Fan, W., Zhou, Y. and Zhao, G. (2002), Study on performance of the ball packed-bed regenerator: experiments and simulation, *Applied Thermal Engineering* **22**(6), 641–651.

Zanganeh, G., Commerford, M., Haselbacher, A., Pedretti, A. and Steinfeld, A. (2014), Stabilization of the outflow temperature of a packed-bed thermal energy storage by combining rocks with phase change materials, *Applied Thermal Engineering* **70**(1), 316–320.

Zanganeh, G., Pedretti, A., Zavattoni, S., Barbato, M. and Steinfeld, A. (2012), Packed-bed thermal storage for concentrated solar power-pilot-scale demonstration and industrial-scale design, *Solar Energy* **86**(10), 3084–3098.

Zehner, P. and Schlünder, E.U. (1970), Wärmeleitfähigkeit von schüttungen bei mäßigen temperaturen, *Chemie Ingenieur Technik* **42**(14), 933–941.

Zhao, W. (2013), Characterization of Encapsulated Phase Change Materials for Thermal Energy Storage, PhD thesis, Lehigh University.

Zunft, S., Hänel, M., Krüger, M. and Dreißigacker, V. (2009), High-temperature heat storage for air-cooled solar central receiver plants: a design study, *in Proceedings of the 15th SolarPACES Conference*, Berlin, pp. 15–18.

Zunft, S., Hänel, M., Krüger, M. and Dreißigacker, V. (2014), A design study for regenerator-type heat storage in solar tower plants–results and conclusions of the hotspot project, *Energy Procedia* **49**, 1088–1096.

Appendix A

Thermophysical properties

A.1 Flue gas properties

The LP gas that was utilised is a mixture of 60% Butane (C_4H_{10}) and 40% Propane (C_3H_8). The flue gas properties were calculated based on a stoichiometric analysis, assuming an approximation for air as O_2+3.76N_2. Once the gas composition was determined the software DeskTop Gas was utilised to calculate the relevant thermodynamic properties.

For Propane:

$$C_3H_8 + 5\mathbf{X}(O_2 + 3.76N_2) \rightarrow 3CO_2 + 4H_2O + 5(\mathbf{X} - 1)O_2 + 5\mathbf{X}(3.76N_2) \tag{A.1}$$

For Butane:

$$C_4H_{10} + 6.5\mathbf{X}(O_2 + 3.76N_2) \rightarrow 4CO_2 + 5H_2O + 6.5(\mathbf{X} - 1)O_2 + 6.5\mathbf{X}(3.76N_2) \tag{A.2}$$

X is the defined as the percentage of excess air. It is calculated by the ratio of actual air:fuel ratio to the stoichiometric air:fuel ratio

$$\mathbf{X} = \frac{\dot{m}_{\text{air}}/\dot{m}_{\text{fuel}}}{(\dot{m}_{\text{air}}/\dot{m}_{\text{fuel}})_{\text{stoich}}} \tag{A.3}$$

A.2 Ceramic properties

A.2.1 Denstone 2000

$$\rho = 2200 \text{ [kg/m}^3\text{]} \tag{A.4}$$

$$c = 8.6376\text{x}10^{-16}T^6 - 3.9395\text{x}10^{-12}T^5 + 6.1492\text{x}10^{-9}T^4 - 3.054\text{x}10^{-6}T^3 - 1.1792\text{x}10^{-3}T^2 + 1.6276T + 716.334 \text{ [J/kgK]} \tag{A.5}$$

$$k = -2.2768\text{x}10^{-7}T^2 + 7.4485T + 0.7618 \text{ [W/mK]} \tag{A.6}$$

$$\tag{A.7}$$

where T is in [°C]. Equations were derived from the data provided by the material manufacturer Saint Gobain.

A.2.2 Alumina

$$\rho = 3600 \text{ [kg/m}^3\text{]} \tag{A.8}$$

$$c = 1.034\text{x}10^{-24}T^6 + 7.5080\text{x}10^{-13}T^5 - 3.4842\text{x}10^{-9}T^4 + 6.1857\text{x}10^{-6}T^3 - 5.2831\text{x}10^{-3}T^2 + 2.3780T + 717.48 \text{ [J/kgK]} \tag{A.9}$$

$$k = 6.8319\text{x}10^{-11}T^4 - 1.9344\text{x}10^{-7}T^3 + 2.1815\text{x}10^{-4}T^2 - 0.1261T + 39.467T \text{ [W/mK]} \tag{A.10}$$

where T is in [°C]. Equations were derived from the data provided in the sources: Touloukian and Ho (1970*a*), Touloukian and Ho (1970*b*)

A.3 PCM properties

A.3.1 Na_2SO_4

$$\rho_{\text{PCM}} = 1862 \text{ [kg/m}^3\text{]} \tag{A.11}$$

$$\Delta h_{\text{pt}}(522 \text{ K}) = 76 \text{ [kJ/kg]} \tag{A.12}$$

$$\Delta h_{\text{fus}}(1157 \text{ K}) = 162 \text{ [kJ/kg]} \tag{A.13}$$

$$c_{\text{PCM}} = \begin{cases} 579.85 + 1.0872 T_{\text{PCM}} & \text{if } \text{T}_{\text{PCM}} < 528 \text{ K} \\ 994.6 + 0.4224 T_{\text{PCM}} & 528 \text{ K} < \text{if } \text{T}_{\text{PCM}} < 1157 \text{ K} \\ 1390.4 & \text{if } \text{T}_{\text{PCM}} > 1157 \text{ K} \end{cases} \tag{A.14}$$

$$k_{\text{PCM}} = \begin{cases} 0.9 & \text{if } \text{T}_{\text{PCM}} < 1157 \text{ K} \\ 0.6 & \text{if } \text{T}_{\text{PCM}} > 1157 \text{ K} \end{cases} \tag{A.15}$$

Equations were derived from the data provided in the sources: Touloukian and Ho (1970*a*), Touloukian and Ho (1970*b*), Barin et al. (1977), Suleiman et al. (2000), Notter et al. (1993), and Creffield and Wickens (1975).

A.3.2 KCl-NaCl

$$\rho_{\text{PCM}} = 1429.2 \text{ [kg/m}^3\text{]} \tag{A.16}$$

$$\Delta h_{\text{fus}}(930 \text{ K}) = 338 \text{ [kJ/kg]} \tag{A.17}$$

$$c_{\text{PCM}} = \begin{cases} 950 & \text{if } \text{T}_{\text{PCM}} < 930 \text{ K} \\ 1218 & \text{if } \text{T}_{\text{PCM}} > 930 \text{ K} \end{cases} \tag{A.18}$$

$$k_{\text{PCM}} = \begin{cases} 0.9 & \text{if } \text{T}_{\text{PCM}} < 930 \text{ K} \\ 0.5 & \text{if } \text{T}_{\text{PCM}} > 930 \text{ K} \end{cases} \tag{A.19}$$

Equations were derived from the data provided in the sources: Janz et al. (1975), Smirnov et al. (1987), Goswami (2011) , Sergeev et al. (2015), and Gheribi et al. (2015).

A.3.3 KNO_3-$NaNO_3$

$$\rho_{\mathrm{PCM}} = 1756 \text{ [kg/m}^3\text{]} \tag{A.20}$$

$$\Delta h_{\mathrm{pt}}(378 \text{ K}) = 27.3 \text{ [kJ/kg]} \tag{A.21}$$

$$\Delta h_{\mathrm{fus}}(495 \text{ K}) = 94 \text{ [kJ/kg]} \tag{A.22}$$

$$c_{\mathrm{PCM}} = 720.9 + 0.556 T_{\mathrm{PCM}} \tag{A.23}$$

$$k_{\mathrm{PCM}} = \begin{cases} 259 - 0.0578 T_{\mathrm{PCM}} & \text{if } \mathrm{T_{PCM}} < 933 \text{ K} \\ 60.3 + 0.0327 T_{\mathrm{PCM}} & \text{if } \mathrm{T_{PCM}} > 933 \text{ K} \end{cases} \tag{A.24}$$

Equations were derived from the data provided in the sources: Barin et al. (1977) and Akiyama et al. (1992).

A.3.4 Aluminium

$$\rho_{\mathrm{PCM}} = 2180 \text{ [kg/m}^3\text{]} \tag{A.25}$$

$$\Delta h_{\mathrm{fus}}(933 \text{ K}) = 397 \text{ [kJ/kg]} \tag{A.26}$$

$$c_{\mathrm{PCM}} = 720.9 + 0.556 T_{\mathrm{PCM}} \tag{A.27}$$

$$k_{\mathrm{PCM}} = \begin{cases} 259 - 0.0578 T_{\mathrm{PCM}} & \text{if } \mathrm{T_{PCM}} < 933 \text{ K} \\ 60.3 + 0.0327 T_{\mathrm{PCM}} & \text{if } \mathrm{T_{PCM}} > 933 \text{ K} \end{cases} \tag{A.28}$$

Equations were derived from the data provided in the sources:Barin et al. (1977) and Akiyama et al. (1992).

A.3.5 NaCl

$$\rho_{\mathrm{PCM}} = 1128 \text{ [kg/m}^3\text{]} \tag{A.29}$$

$$\Delta h_{\mathrm{fus}}(1073 \text{ K}) = 397 \text{ [kJ/kg]} \tag{A.30}$$

$$c_{\mathrm{PCM}} = 743.7 + 0.3593 T_{\mathrm{PCM}} \tag{A.31}$$

$$k_{\mathrm{PCM}} = \begin{cases} 9.285\text{x}10^{-6} T_{\mathrm{PCM}}^2 - 1.682\text{x}10^{-2} T_{\mathrm{PCM}} + 9.53 & \text{if } \mathrm{T_{PCM}} < 1073 \text{ K} \\ 9.07\text{x}10^{-4} T_{\mathrm{PCM}} - 0.269 & \text{if } \mathrm{T_{PCM}} > 1073 \text{ K} \end{cases} \tag{A.32}$$

Equations were derived from the data provided in the sources: Barin et al. (1977), Smirnov et al. (1987), and Akiyama et al. (1992) and Gheribi et al. (2015).

The units of the of the PCM properties provided in this section are: c_{PCM} [J/kg], k_{PCM} [W/mK] and T_{PCM} [K]. The apparent density ρ_{PCM} takes into account the liquid density of the salt at melting point and a void to allow for the salt expansion upon melting.

Appendix B

Spatial discretisation of governing equations using OCFE

B.1 C-S model

B.1.1 Interior collocation procedure

The backward difference temporal discretisation of the governing energy equations for the fluid, solid and wall yields:

$$A_f T_f^{n+1} + B_f \frac{\partial T_f}{\partial z}^{n+1} + C_f \frac{\partial^2 T_f}{\partial z^2}^{n+1} + D_f \frac{\partial^2 T_f}{\partial r^2}^{n+1} + E_f \frac{\partial T_f}{\partial r}^{n+1} + F_f T_s^{n+1} = T_f^n \quad \text{(B.1)}$$

$$A_s T_s^{n+1} + B_s \frac{\partial T_s}{\partial z}^{n+1} + C_s \frac{\partial^2 T_s}{\partial z^2}^{n+1} + D_s \frac{\partial^2 T_s}{\partial r^2}^{n+1} + E_s \frac{\partial T_s}{\partial r}^{n+1} + F_s T_f^{n+1} = T_s^n \quad \text{(B.2)}$$

$$A_w T_w^{n+1} + B_w \frac{\partial T_w}{\partial z}^{n+1} + C_w \frac{\partial^2 T_w}{\partial z^2}^{n+1} + D_w \frac{\partial^2 T_w}{\partial r^2}^{n+1} + E_w \frac{\partial T_w}{\partial r}^{n+1} = T_w^n \quad \text{(B.3)}$$

The two-dimensional collocation procedure is carried out at the four interior nodes of each finite element. For an element located in the packed bed region, the element number is given by the superscript 'kl', where $0 \leq k \leq N_r$ and $0 \leq l \leq N_z$.

The spatial discretisation yields:

$$A_f \sum_{i=1}^{4}\sum_{j=1}^{4} a_{ij}^{kl}\phi_i\phi_j + \frac{B_f}{\Delta z^l}\sum_{i=1}^{4}\sum_{j=1}^{4} a_{ij}^{kl}\phi_j\frac{\mathrm{d}\phi_j}{\mathrm{d}w} + \frac{C_f}{\left(\Delta z^l\right)^2}\sum_{i=1}^{4}\sum_{j=1}^{4} a_{ij}^{kl}\phi_i\frac{\mathrm{d}^2\phi_j}{\mathrm{d}w^2} + \frac{D_f}{\left(\Delta r^k\right)^2}\sum_{i=1}^{4}\sum_{j=1}^{4} a_{ij}^{kl}\frac{\mathrm{d}^2\phi_i}{\mathrm{d}v^2}\phi_j + \frac{E_f}{\Delta r^k}\sum_{i=1}^{4}\sum_{j=1}^{4} a_{ij}^{kl}\frac{\mathrm{d}\phi_i}{\mathrm{d}v}\phi_j + F_f T_s^{n+1} = T_f^n \tag{B.4}$$

$$A_s \sum_{i=1}^{4}\sum_{j=1}^{4} b_{ij}^{kl}\phi_i\phi_j + \frac{B_s}{\Delta z^l}\sum_{i=1}^{4}\sum_{j=1}^{4} b_{ij}^{kl}\phi_i\frac{\mathrm{d}\phi_j}{\mathrm{d}w} + \frac{C_s}{\left(\Delta z^l\right)^2}\sum_{i=1}^{4}\sum_{j=1}^{4} b_{ij}^{kl}\phi_i\frac{\mathrm{d}^2\phi_j}{\mathrm{d}w^2} + \frac{D_s}{\left(\Delta r^k\right)^2}\sum_{i=1}^{4}\sum_{j=1}^{4} b_{ij}^{kl}\frac{\mathrm{d}^2\phi_i}{\mathrm{d}v^2}\phi_j + \frac{E_s}{\Delta r^k}\sum_{i=1}^{4}\sum_{j=1}^{4} b_{ij}^{kl}\frac{\mathrm{d}\phi_i}{\mathrm{d}v}\phi_j + F_s T_f^{n+1} = T_s^n \tag{B.5}$$

For an element located in the wall region, where $N_r + 1 \leq k \leq N_w + 1$ and $0 \leq l \leq N_z$ the spatial discretisation yields:

$$A_w \sum_{i=1}^{4}\sum_{j=1}^{4} e_{ij}^{kl}\phi_i\phi_j + \frac{B_w}{\Delta z^l}\sum_{i=1}^{4}\sum_{j=1}^{4} e_{ij}^{kl}\phi_i\frac{\mathrm{d}\phi_j}{\mathrm{d}w} + \frac{C_w}{\left(\Delta z^l\right)^2}\sum_{i=1}^{4}\sum_{j=1}^{4} e_{ij}^{kl}\phi_i\frac{\mathrm{d}^2\phi_j}{\mathrm{d}w^2} + \frac{D_w}{\left(\Delta r^k\right)^2}\sum_{i=1}^{4}\sum_{j=1}^{4} e_{ij}^{kl}\frac{\mathrm{d}^2\phi_i}{\mathrm{d}v^2}\phi_j + \frac{E_w}{\Delta r^k}\sum_{i=1}^{4}\sum_{j=1}^{4} e_{ij}^{kl}\frac{\mathrm{d}\phi_i}{\mathrm{d}v}\phi_j = T_w^n \tag{B.6}$$

The coefficients in Eqs.(B.4) and (B.5) are:

$$A_f = 1 + \frac{h_p^{n+1} a_p \Delta t}{\varepsilon \rho_f^{n+1} c_f^{n+1}} \tag{B.7}$$

$$B_f = \frac{\Delta t}{\varepsilon \rho_f^{n+1} c_f^{n+1}}\left(c_f^{n+1} G_z^{n+1} - \frac{\partial k_{\mathrm{eff,fz}}^{n+1}}{\partial z}\right) \tag{B.8}$$

$$C_f = -\frac{k_{\mathrm{eff,fz}}^{n+1}\Delta t}{\varepsilon \rho_f^{n+1} c_f^{n+1}} \tag{B.9}$$

$$D_f = -\frac{k_{\mathrm{eff,fr}}^{n+1}\Delta t}{\varepsilon \rho_f^{n+1} c_f^{n+1}} \tag{B.10}$$

$$E_f = -\frac{\Delta t}{\varepsilon \rho_f^{n+1} c_f^{n+1}}\left(\frac{k_{\mathrm{eff,fr}}^{n+1}}{r} + \frac{\partial k_{\mathrm{eff,fr}}^{n+1}}{\partial r}\right) \tag{B.11}$$

$$F_f = -\frac{h_p^{n+1} a_p \Delta t}{\varepsilon \rho_f^{n+1} c_f^{n+1}} \tag{B.12}$$

$$A_s = 1 + \frac{h_p^{n+1} a_p \Delta t}{(1-\varepsilon)\rho_s c_s^{n+1}} \tag{B.13}$$

$$B_s = -\frac{\Delta t}{(1-\varepsilon)\rho_s c_s^{n+1}} \left(\frac{\partial k_{\text{eff,s}}^{n+1}}{\partial z} \right) \tag{B.14}$$

$$C_s = -\frac{k_{\text{eff,s}}^{n+1} \Delta t}{(1-\varepsilon)\rho_s c_s^{n+1}} \tag{B.15}$$

$$D_s = -\frac{k_{\text{eff,s}}^{n+1} \Delta t}{(1-\varepsilon)\rho_s c_s^{n+1}} \tag{B.16}$$

$$E_s = -\frac{\Delta t}{(1-\varepsilon)\rho_s c_s^{n+1}} \left(\frac{k_{\text{eff,s}}^{n+1}}{r} + \frac{\partial k_{\text{eff,s}}^{n+1}}{\partial r} \right) \tag{B.17}$$

$$F_s = -\frac{h_p^{n+1} a_p \Delta t}{(1-\varepsilon)\rho_s c_s^{n+1}} \tag{B.18}$$

Assuming constant thermophysical properties for the wall, the coefficients in Eq.(B.6) are:

$$A_w = 1 \tag{B.19}$$

$$B_w = -\frac{k_w \Delta t}{\rho_w c_w} \tag{B.20}$$

$$C_w = -\frac{k_w \Delta t}{\rho_w c_w} \tag{B.21}$$

$$D_w = -\frac{k_w \Delta t}{\rho_w c_w} \tag{B.22}$$

$$E_w = -\frac{k_w \Delta t}{r \rho_w c_w} \tag{B.23}$$

B.1.2 Boundary collocation procedure:

The numerical solution requires the collocation of the points on the boundary conditions. The collocation of the boundary nodes is presented for the fluid, solid and wall phases.

Packed bed inlet ($0 \leq r \leq R$ **and** $z = 0$)**:**

Fluid:

$$\sum_{i=1}^{4} \sum_{j=1}^{4} a_{ij}^{kl} \phi_i \phi_j = T_{\text{in}} \tag{B.24}$$

Solid:

$$\sum_{i=1}^{4}\sum_{j=1}^{4} b_{ij}^{kl}\phi_i\frac{\mathrm{d}\phi_j}{\mathrm{d}w} = 0 \tag{B.25}$$

Packed bed exit ($0 \leq r \leq R$ and $z = L_z$):

Fluid:

$$\sum_{i=1}^{4}\sum_{j=1}^{4} a_{ij}^{kl}\phi_i\frac{\mathrm{d}\phi_j}{\mathrm{d}w} = 0 \tag{B.26}$$

Solid:

$$\sum_{i=1}^{4}\sum_{j=1}^{4} b_{ij}^{kl}\phi_i\frac{\mathrm{d}\phi_j}{\mathrm{d}w} = 0 \tag{B.27}$$

Packed bed centreline ($r = 0$ and $0 \leq z \leq L_z$):

Fluid:

$$\sum_{i=1}^{4}\sum_{j=1}^{4} a_{ij}^{kl}\frac{\mathrm{d}\phi_i}{\mathrm{d}v}\phi_j = 0 \tag{B.28}$$

Solid:

$$\sum_{i=1}^{4}\sum_{j=1}^{4} b_{ij}^{kl}\frac{\mathrm{d}\phi_i}{\mathrm{d}v}\phi_j = 0 \tag{B.29}$$

Packed bed inner wall ($r = R$ and $0 \leq z \leq L_z$):

Fluid:

$$\sum_{i=1}^{4}\sum_{j=1}^{4} a_{ij}^{kl}\phi_i\phi_j = T_w^{n+1} \tag{B.30}$$

Solid:

$$\frac{-k_{\text{eff,s}}}{\Delta r^k}\sum_{i=1}^{4}\sum_{j=1}^{4} b_{ij}^{kl}\frac{\mathrm{d}\phi_i}{\mathrm{d}v}\phi_j = \overline{h}_r\left(T_{sb}^{n+1} - T_w^{n+1}\right) \tag{B.31}$$

Wall:

$$\frac{-k_w}{\Delta r^k}\sum_{i=1}^{4}\sum_{j=1}^{4} e_{ij}^{kl}\frac{\mathrm{d}\phi_i}{\mathrm{d}v}\phi_j = \dot{q}_f + \dot{q}_s \tag{B.32}$$

As described by Visser (2007), the solid temperature at half a particle diameter from the wall can be calculated using linear interpolation from the solid temperature at the bed wall:

$$T_{sb} = -\frac{d_p}{2}\left.\frac{\partial T_s}{\partial r}\right|_{r=R} + T_s|_{r=R} \tag{B.33}$$

The linearised radiation coefficient is given by:

$$\overline{h}_r = 4h_r\left(\frac{T_{sb}+T_w}{2}\right)^3 \tag{B.34}$$

Packed bed wall at inlet ($R \leq r \leq= R_o$ and $z = 0$):

$$\sum_{i=1}^{4}\sum_{j=1}^{4} e_{ij}^{kl}\phi_i\frac{\mathrm{d}\phi_j}{\mathrm{d}w} = 0 \tag{B.35}$$

Packed bed wall at exit ($R \leq r \leq= R_o$ and $z = L_z$):

$$\sum_{i=1}^{4}\sum_{j=1}^{4} e_{ij}^{kl}\phi_i\frac{\mathrm{d}\phi_j}{\mathrm{d}w} = 0 \tag{B.36}$$

Outer Packed bed wall ($r = R_o$ and $0 \leq z \leq L_z$):

$$\frac{k_w}{\Delta r^k}\sum_{i=1}^{4}\sum_{j=1}^{4} e_{ij}^{kl}\frac{\mathrm{d}\phi_i}{\partial v}\phi_j + h_c\sum_{i=1}^{4}\sum_{j=1}^{4} e_{ij}^{kl}\phi_i\phi_j = h_c T_a \tag{B.37}$$

B.2 D-C model

B.2.1 Interior collocation procedure

The D-C model is an extension to the C-S model that includes an extra energy equation to account for one-dimensional heat transfer within the spherical particles. The governing energy equations for the fluid and wall in D-C model are unchanged from the C-S model. The interior collocation of the fluid and wall is presented above in Eqs.(B.4) and (B.6) respectively. The backward difference temporal discretisation of the governing energy equations for the solid phase in the D-C model yields:

$$A_s T_s^{n+1} + B_s \frac{\partial T_s}{\partial z}^{n+1} + C_s \frac{\partial^2 T_s}{\partial z^2}^{n+1} + D_s \frac{\partial^2 T_s}{\partial r^2}^{n+1} + E_s \frac{\partial T_s}{\partial r}^{n+1} + F_s T_f^{n+1} + \dot{q}_p^{n+1} = 0 \tag{B.38}$$

$$A_p T_p^{n+1} + D_p \frac{\partial^2 T_p}{\partial r^2}^{n+1} + E_p \frac{\partial T_p}{\partial r}^{n+1} = T_p^n \tag{B.39}$$

For the D-C model T_s refers to the two-dimensional surface temperature field of the particles, while T_p is the internal particle temperature. The two-dimensional collocation procedure is carried out at the four interior nodes of each finite element for T_s. For an element located in the packed bed region, the element number is given by the superscript 'kl', where $0 \leq k \leq N_r$ and $0 \leq l \leq N_z$.

The spatial discretisation yields:

$$\begin{aligned} &A_s \sum_{i=1}^{4}\sum_{j=1}^{4} b_{ij}^{kl}\phi_i\phi_j + \frac{B_s}{\Delta z^l}\sum_{i=1}^{4}\sum_{j=1}^{4} b_{ij}^{kl}\phi_i\frac{\mathrm{d}\phi_j}{\mathrm{d}w} + \frac{C_s}{\left(\Delta z^l\right)^2}\sum_{i=1}^{4}\sum_{j=1}^{4} b_{ij}^{kl}\phi_i\frac{\mathrm{d}^2\phi_j}{\mathrm{d}w^2} \\ &+ \frac{D_s}{\left(\Delta r^k\right)^2}\sum_{i=1}^{4}\sum_{j=1}^{4} b_{ij}^{kl}\frac{\mathrm{d}^2\phi_i}{\mathrm{d}v^2}\phi_j + \frac{E_s}{\Delta r^k}\sum_{i=1}^{4}\sum_{j=1}^{4} b_{ij}^{kl}\frac{\mathrm{d}\phi_i}{\mathrm{d}v}\phi_j + F_s T_f^{n+1} + \dot{q}_p{}^{n+1} = 0 \end{aligned} \tag{B.40}$$

The term $\dot{q}_p$ represents the heat flux at the surface ($\zeta = d_p/2$) of each particle and is calculated by:

$$\dot{q}_p{}^{n+1} = -k_p \frac{\partial T_p}{\partial \zeta}^{n+1} \tag{B.41}$$

Within each representative particle a one-dimensional collocation procedure is applied. The element number is given by the superscript 'm', where $0 \leq m \leq N_p$. The spatial discretisation yields:

$$A_p \sum_{i=1}^{4} g_i^m \phi_i + \frac{D_p}{(\Delta\zeta^m)^2} \sum_{i=1}^{4} g_i^m \frac{\mathrm{d}^2\phi_i}{\mathrm{d}v^2} + \frac{E_p}{\Delta\zeta^m} \sum_{i=1}^{4} g_i^m \frac{\mathrm{d}\phi_i}{\mathrm{d}v} = T_p^n \tag{B.42}$$

The coefficients in Eqs.(B.40) and (B.42) are:

$$A_s = h_p^{n+1} a_p \tag{B.43}$$

$$B_s = -\frac{\partial k_{\mathrm{eff,s}}^{n+1}}{\partial z} \tag{B.44}$$

$$C_s = -k_{\mathrm{eff,s}}^{n+1} \tag{B.45}$$

$$D_s = -k_{\mathrm{eff,s}}^{n+1} \tag{B.46}$$

$$E_s = -\left(\frac{k_{\mathrm{eff,s}}^{n+1}}{r} + \frac{\partial k_{\mathrm{eff,s}}^{n+1}}{\partial r} \right) \tag{B.47}$$

$$F_s = -h_p^{n+1} a_p \tag{B.48}$$

$$A_p = 1 \tag{B.49}$$

$$D_p = -\frac{k_p^{n+1}\Delta t}{\rho_p c_p^{n+1}} \tag{B.50}$$

$$E_p = -\frac{\Delta t}{\rho_p c_p^{n+1}} \left(\frac{2k_p^{n+1}}{\zeta} + \frac{\partial k_p^{n+1}}{\partial \zeta} \right) \tag{B.51}$$

B.2.2 Boundary collocation procedure

The boundary conditions for the fluid, solid (surface) and wall are the same for the D-C model as the C-S model. The collocation procedure for these boundary conditions is outlined above in Eqs.(B.24)-(B.37). For the representative spherical particles a further two boundary conditions are required for each particle.

Particle centre ($\zeta = 0$):

$$\sum_{i=1}^{4} g_i^m \frac{\mathrm{d}\phi_i}{\mathrm{d}v} = 0 \tag{B.52}$$

Particle surface ($\zeta = d_p/2$):

$$\sum_{i=1}^{4} g_i^m \phi_i = T_s^{n+1} \tag{B.53}$$

Appendix C

Mesh dependency

Mesh dependency studies were conducted for the solutions of the C-S and D-C heat transfer models for each simulation. Table C.1 presents the meshes that were utilised in this work. Figure C.1 demonstrates the mesh refinement approach that was conducted for the C-S model for sensible heat storage. Figure C.2 demonstrates the mesh refinement approach that was conducted for the D-C model for latent heat storage.

Table C.1: Mesh Parameters

Section	Model	Particle Type	N_x	N_r^*	N_w	N_p	dt[s]
5.3-5.4	C-S	Denstone	50	40	17	N/A	10
6.3	D-C	EPCM	N/A	N/A	N/A	20	1
6.4	D-C	EPCM	30	40	17	N/A	10
7.3	C-S	Alumina	60	50	17	N/A	100**
7.5	D-C	Alumina	50	40	17	20	10
7.5	D-C	EPCM	50	40	17	20	10

*non-uniform radial spacing utilised

**second order backward difference time stepping utilised

Energy stored in the packed bed was chosen as the parameter for the mesh refinement process. This parameter gives a good overall indication of the convergence of the fluid and solid temperature profiles, for different mesh sizes. For each chosen mesh, the energy stored in the fluid and solid phases was calculated at each time step. The transient profiles of energy stored for the current mesh were then compared to the finest resolution mesh utilised. The RMS deviations of the energy profiles was then calculated between the current mesh and

the finest resolution mesh. These values then normalised by the maximum value of energy stored in the packed bed for the finest resolution mesh.

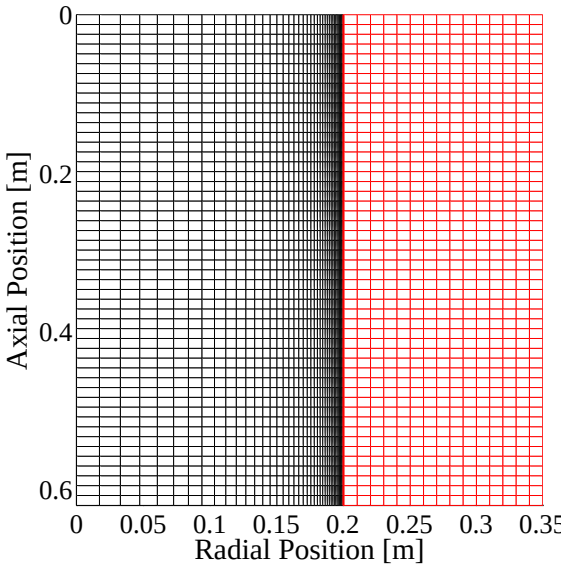

(a) Chosen mesh bed(black), red (wall)

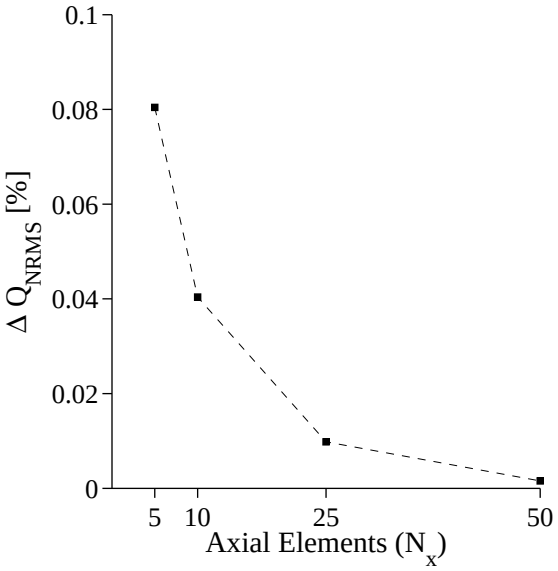

(b) Axial mesh compared to $N_x = 75$

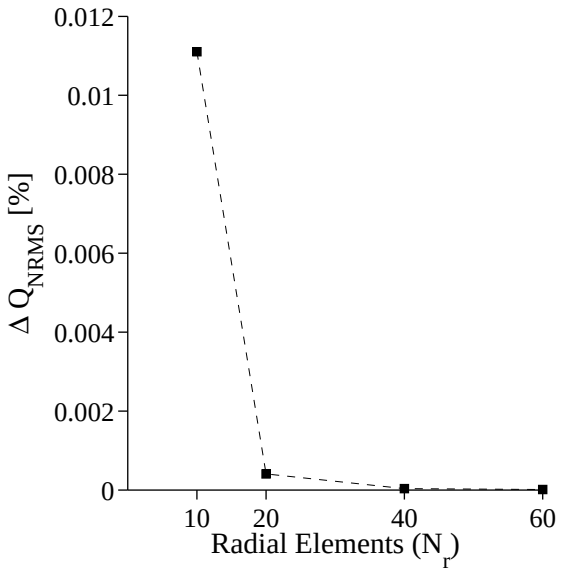

(c) Radial mesh compared to $N_r = 75$

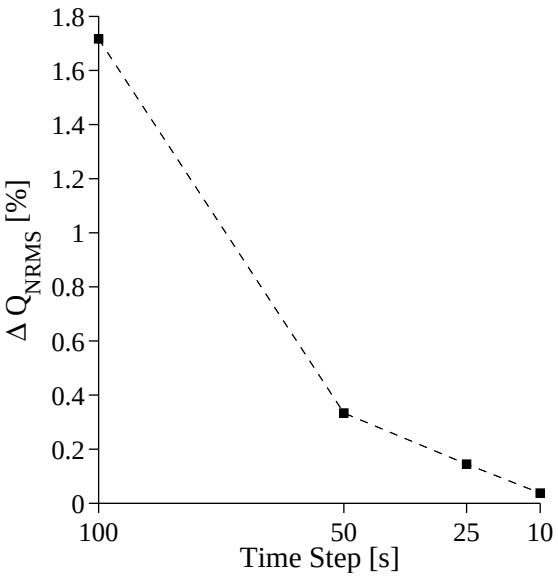

(d) Time step compared to $dt = 5$s

Figure C.1: Mesh refinement study for C-S model of packed bed test facility, Denstone experimental validation

The meshes used in this work are relatively fine and provide highly accurate solutions in reasonable simulation times. However, the results show that the numerical method is highly efficient. Very course spatial meshes (for example $N_z = 10$) could be implemented without significantly reducing the accuracy of the solution. This is due to the forth order accuracy

of the Hermite spline basis functions. Thus the OCFE approach could be used on course meshes for very fast solutions as first order estimates or for real time control systems for a working storage unit.

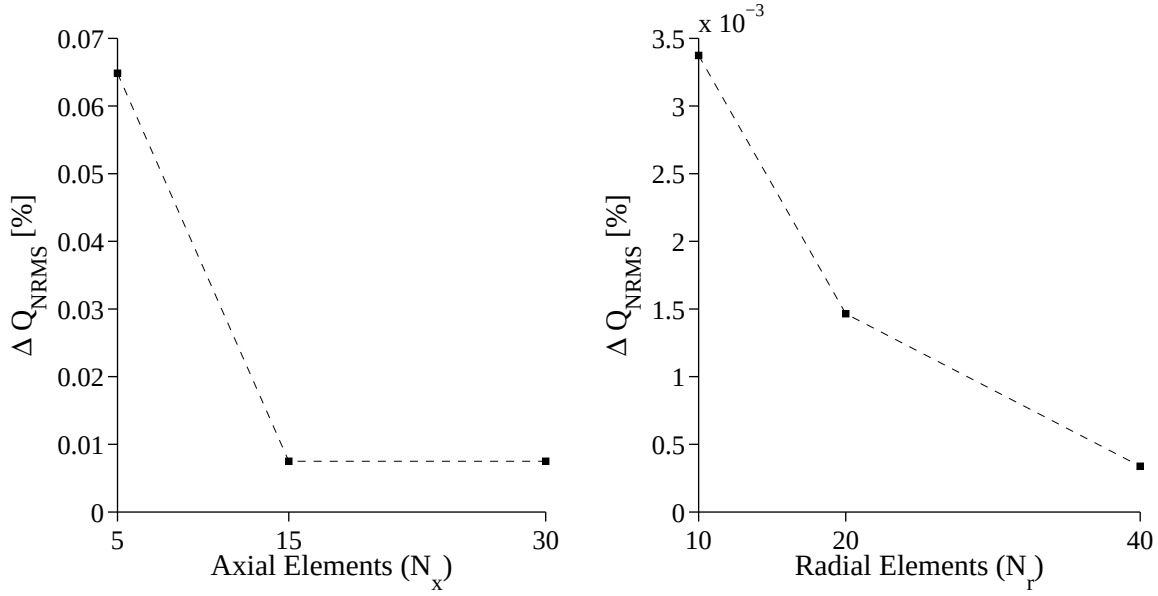

(a) Axial mesh compared to $N_z = 40$

(b) Radial mesh compared to $N_r = 50$

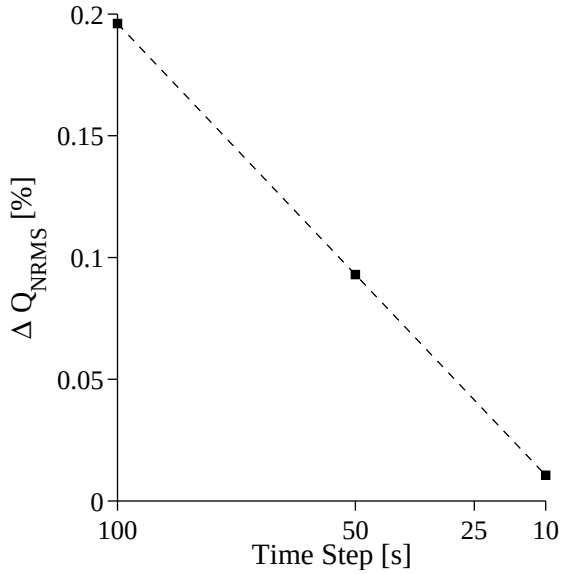

(c) Time step compared to $dt = 5$s

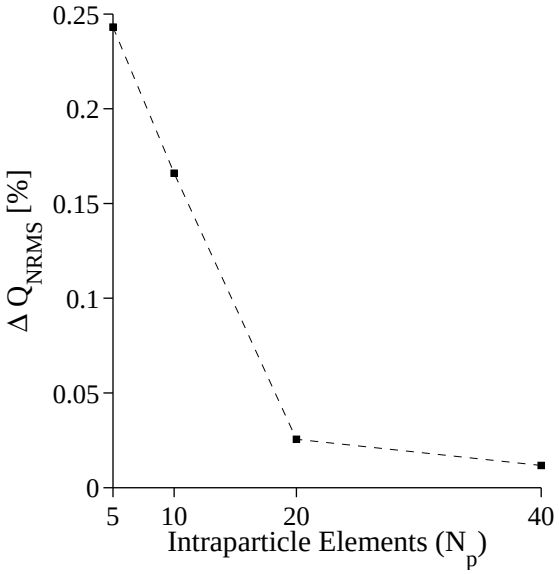

(d) Particle mesh compared to $N_p = 50$

Figure C.2: Mesh refinement study for D-C model of packed bed test facility, Na_2SO_4 experimental validation

Appendix D

Analytical heat transfer models

D.1 Schumann problem analytical solution

The Schumann model is a simplified form of the C-S model to which various analytical solutions exist (Schumann, 1929). Subject to the assumptions of (1) plug flow, (2), constant void fraction (3) no radial heat transfer (4) no heat losses, (5) constant thermophysical properties and (6) no dispersion in the fluid or solid phases. The C-S model reduces to:

$$\varepsilon\rho_f c_f \frac{\partial T_f}{\partial t} + G_z c_f \frac{\partial T_f}{\partial z} = h_p a_p \left(T_s - T_f\right) \tag{D.1}$$

$$(1-\varepsilon)\rho_s c_s \frac{\partial T_s}{\partial t} = h_p a_p \left(T_f - T_s\right) \tag{D.2}$$

The analytical solution proposed by Schumann (1929) involves the treatment of an infinite series of terms, which are themselves constructed from an infinite series. Klinkenberg (1948) provided an alternative analytical solution, which is accurate to within 0.6% of the exact Schumann solution, with an error that decreases as the model progresses in time. This analytical solution is presented in non-dimensionalised form for a step change in the inlet fluid temperature:

$$\Theta_f = \frac{1}{2}\left(\sqrt{Z_K} + \frac{1}{8\sqrt{Z_K}} - \sqrt{Y_K} + \frac{1}{8\sqrt{Y_K}}\right) \tag{D.3}$$

$$\Theta_s = \frac{1}{2}\left(\sqrt{Z_K} - \frac{1}{8\sqrt{Z_K}} - \sqrt{Y_K} - \frac{1}{8\sqrt{Y_K}}\right) \tag{D.4}$$

where:

$$\Theta_f = \frac{T_f - T_i}{T_c - T_i} \tag{D.5}$$

$$\Theta_s = \frac{T_s - T_i}{T_c - T_i} \tag{D.6}$$

$$Y_K = \frac{h a_p z}{G c_f} \tag{D.7}$$

$$Z_K = \frac{h a_p z}{\rho_s c_s (1-\varepsilon)} \left(t - \frac{\varepsilon \rho_f z}{G_z} \right) \tag{D.8}$$

D.2 Stefan problem analytical solution

This section details the Neumann solution to the Stefan problem. The melting and solidification solutions are presented.

D.2.1 Melting of semi-infinite slab

The slab of material is initially at a uniform temperature of $T_{\text{PCM}}(z,0) < T_m$. The PCM at the wall undergoes a step change in temperature to $T_{\text{PCM}}(0,t) > T_m$. This initiates a phase change front that propagates through the material over time. The thermophysical properties in each region are constant but different, being $\rho_{l,\text{PCM}}, c_{l,\text{PCM}}, k_{l,\text{PCM}}$ in the liquid layer and $\rho_{s,\text{PCM}}, c_{s,\text{PCM}}, k_{s,\text{PCM}}$ in the solid layer. The thermal diffusivity in the liquid and solid is:

$$\alpha_{s,\text{PCM}} = \frac{k_{s,\text{PCM}}}{\rho_{s,\text{PCM}} c_{s,\text{PCM}}} \tag{D.9}$$

$$\alpha_{l,\text{PCM}} = \frac{k_{l,\text{PCM}}}{\rho_{l,\text{PCM}} c_{l,\text{PCM}}} \tag{D.10}$$

Details of the analytical solution are presented by Hu and Argyropoulos (1996). The position of phase change front is:

$$\delta_{\text{PCM}}(t) = 2\lambda \sqrt{\alpha_{l,\text{PCM}} t} \tag{D.11}$$

The solution of the PCM temperature is based on the interface position to determine if the PCM is liquid or solid.

Liquid region for $0 \leq z \leq \delta_{\mathbf{PCM}}$:

$$T_{\mathrm{PCM}}(z,t) = T_{\mathrm{PCM}}(0,t) + \frac{T_m - T_{\mathrm{PCM}}(0,t)}{\operatorname{erf}\lambda} \operatorname{erf}\left(\frac{z}{2\sqrt{\alpha_l t}}\right) \tag{D.12}$$

Solid region for $\delta_{\mathbf{PCM}} \leq z$:

$$T_{\mathrm{PCM}}(z,t) = T_{\mathrm{PCM}}(z,0) + \frac{T_m - T_{\mathrm{PCM}}(z,0)}{\operatorname{erfc}\left(\lambda\sqrt{\alpha_{l,\mathrm{PCM}}/\alpha_{s,\mathrm{PCM}}}\right)} \operatorname{erfc}\left(\frac{z}{2\sqrt{\alpha_{s,\mathrm{PCM}} t}}\right) \tag{D.13}$$

The parameter λ is solved using the transcendental align:

$$\begin{aligned}\lambda\sqrt{\pi} =& \frac{\mathrm{St}_l}{\exp(\lambda^2)\operatorname{erf}(\lambda)} \\ &- \frac{\mathrm{St}_s\sqrt{\alpha_{s,\mathrm{PCM}}}}{\sqrt{\alpha_{l,\mathrm{PCM}}}\exp(\alpha_{l,\mathrm{PCM}}\lambda^2/\alpha_{s,\mathrm{PCM}})\operatorname{erfc}\left(\lambda\sqrt{\alpha_{l,\mathrm{PCM}}/\alpha_{s,\mathrm{PCM}}}\right)}\end{aligned} \tag{D.14}$$

where the Stefan number for the liquid and solid phases are:

$$\mathrm{St}_l = \frac{c_l\left(T_{\mathrm{PCM}}(0,t) - T_m\right)}{\Delta h_{\mathrm{fus}}} \tag{D.15}$$

$$\mathrm{St}_s = \frac{c_s\left(T_m - T_{\mathrm{PCM}}(z,0)\right)}{\Delta h_{\mathrm{fus}}} \tag{D.16}$$

D.2.2 Solidification of semi-infinite slab

For the solidification case, the slab of material is initially at a uniform temperature of $T_{\mathrm{PCM}}(z,t) > T_m$. The PCM at the wall undergoes a step change in temperature to $T_{\mathrm{PCM}}(0,t) < T_m$. The temperature within PCM is then calculated according to three regions, based on temperature:

Solid region for $0 \leq z \leq \delta_{\mathbf{PCM}}$:

$$T_{\mathrm{PCM}}(z,t) = T_{\mathrm{PCM}}(0,t) + \frac{T_m - T_{\mathrm{PCM}}(0,t)}{\operatorname{erf}\lambda} \operatorname{erf}\left(\frac{z}{2\sqrt{\alpha_{s,\mathrm{PCM}} t}}\right) \tag{D.17}$$

Liquid region for $\delta_{\text{PCM}} \leq z$:

$$T_{\text{PCM}}(z,t) = T_{\text{PCM}}(z,0) + \frac{T_m - T_{\text{PCM}}(z,0)}{\operatorname{erfc}\left(\lambda \sqrt{\alpha_{s,\text{PCM}}/\alpha_{l,\text{PCM}}}\right)} \operatorname{erfc}\left(\frac{z}{2\sqrt{\alpha_{l,\text{PCM}} t}}\right) \tag{D.18}$$

The parameter λ is solved using the following transcendental align:

$$\begin{aligned} \lambda \sqrt{\pi} = & \frac{\text{St}_s}{\exp(\lambda^2)\operatorname{erf}(\lambda)} \\ & - \frac{\text{St}_l \sqrt{\alpha_{l,\text{PCM}}}}{\sqrt{\alpha_{s,\text{PCM}}}\exp(\alpha_{s,\text{PCM}}\lambda^2/\alpha_{l,\text{PCM}})\operatorname{erfc}\left(\lambda \sqrt{\alpha_{s,\text{PCM}}/\alpha_{l,\text{PCM}}}\right)} \end{aligned} \tag{D.19}$$

where the Stefan number for the liquid and solid phases are:

$$\text{St}_l = \frac{c_l (T_{\text{PCM}}(z,0) - T_m)}{\Delta h_{\text{fus}}} \tag{D.20}$$

$$\text{St}_s = \frac{c_s (T_m - T_{\text{PCM}}(0,t))}{\Delta h_{\text{fus}}} \tag{D.21}$$

Appendix E

Uncertainty analysis

E.1 Mass flow

The mass flow rate through the conical inlet flow meter is calculated by:

$$\dot{m}_f = C_d \pi \frac{d_c^2}{4} \sqrt{2\Delta P_c \frac{P_a}{RT_f}} \tag{E.1}$$

and for the orifice plate:

$$\dot{m}_f = \frac{C_d}{\sqrt{1-\beta_o^4}} Y \pi \frac{d_o^2}{4} \sqrt{2\Delta P_o \frac{P_a}{RT_f}} \tag{E.2}$$

where:

$$\beta_o = d_o / D_o \tag{E.3}$$

According to BS EN ISO 5801:2008 (BSI, 2008), the compound discharge coefficient for a conical inlet flow meter is calculated by:

$$C_d = 0.01 \log_{10}(\mathrm{Re}_c) + 0.887 \tag{E.4}$$

The uncertainty in mass flow measurement through the conical inlet is calculated using the root mean square theory, as described by Kumar (1998):

$$\frac{\delta \dot{m}_f}{\dot{m}_f} = \left[\left(\frac{\delta C_d}{C_d} \right)^2 + \left(2\frac{\delta d_c}{d_c} \right)^2 + \left(\frac{1}{2}\frac{\delta \Delta P_c}{\Delta P_c} \right)^2 + \left(\frac{1}{2}\frac{\delta P_f}{P_f} \right)^2 + \left(\frac{1}{2}\frac{\delta T_f}{T_f} \right)^2 \right]^{\frac{1}{2}} \tag{E.5}$$

The uncertainty in the compound discharge coefficient C_d for a conical inlet is Reynolds number dependent and is calculated according to BS EN ISO 5801:2008, where:

$$\frac{\delta C_d}{C_d} = \pm \left(1.5 + \left(\frac{20000}{\mathrm{Re}_c} - \frac{1}{15} \right) \right) \% \tag{E.6}$$

For the orifice plate the discharge coefficient and expansibility factor are calculated using BS EN ISO 5801:2008, where:

$$\begin{aligned} C_d = 0.5959 + 0.0312\beta_o^{2.1} - 0.184\beta_o^8 + 0.0029\beta_o^{2.5} \left(\frac{10^6}{\mathrm{Re}_{D_o}} \right)^{0.75} \\ + 0.039\beta_o^4 \left(1 - \beta_o^4 \right)^{-1} - 0.0158\beta_o^3 \end{aligned} \tag{E.7}$$

and

$$Y = 1 - \left(0.41 + 0.35\beta_o^4 \right) \frac{\Delta P_o}{\kappa P_u} \tag{E.8}$$

As stated in BS 1042 (BSI, 1981), the uncertainty in mass flow rate for an orifice plate is calculated by:

$$\begin{aligned} \frac{\delta \dot{m}_f}{\dot{m}_f} = \Bigg[& \left(\frac{\delta C_d}{C_d} \right)^2 + \left(\frac{\delta Y}{Y} \right)^2 + \left(\frac{\beta_o^4}{C_d} \right) \left(2\frac{\delta D_o}{D_o} \right)^2 \\ & + \left(1 + \frac{\beta_o^4}{C_d} \right) \left(2\frac{\delta d_o}{d_o} \right)^2 + \left(\frac{1}{2}\frac{\delta \Delta P_o}{\Delta P_o} \right)^2 + \left(\frac{1}{2}\frac{\delta P_f}{P_f} \right)^2 + \left(\frac{1}{2}\frac{\delta T_f}{T_f} \right)^2 \Bigg] \end{aligned} \tag{E.9}$$

According to BS EN ISO 5801:2008 the uncertainty in C_d for an orifice plate is 0.6% for $\mathrm{Re}_{D_o} > 1260\beta_o^2 D_o$, where D_o is in millimetres and $\beta_o < 0.6$. The uncertainty in the expansibility factor is calculated by:

$$\frac{\delta Y}{Y} = 4 \left(\frac{\Delta P_o}{P_u} \right) \% \tag{E.10}$$

Table E.1 presents the maximum uncertainties calculated for the sensible heat and latent heat storage experiments that was conducted. The maximum uncertainty is determined based on the minimum mass flow rate for each experiment.

Table E.1: Uncertainty in mass flow measurements

Flow meter type	Experiment details	Relevant Figure	min m_f [kg/s]	$\delta m_f/m_f$ [%]
	Alumino-silicate particles			
Conical inlet	Heating 20-160 °C	5.1; 5.2; 5.4	0.0293	2.5
	Cooling 350 °C -ambient	5.1; 5.2; 5.4	0.0293	2.5
	Heating ambient-350 °C	5.5(a)	0.0262	2.5
	Heating 350-900 °C	5.6(a); 5.12(a)	0.0226	2.5
	Cooling 900-350 °C	5.7(a); 5.12(b)	0.0235	2.5
Orifice plate	Heating ambient-600 °C	5.5(b)	0.0283	1.5
	Heating 600-900 °C	5.6(b); 5.13(a)	0.0273	1.5
	Cooling 900-600 °C	6.16(b); 5.13(b)	0.0341	1.5
	Encapsulated Na_2SO_4 particles			
Conical inlet	Heating ambient-230 °C	6.10; 6.11	0.023	2.5
	Cooling 230 °C -ambient	6.10; 6.11	0.0235	2.5
	Preheating cycle	6.14; 6.18(a)	0.0182	2.6
	Melting cycle	6.15; 6.18(a)	0.0172	2.6
	Solidifying cycle	6.16; 6.17; 6.18(b)	0.0175	2.6

It is important to determine what effect the uncertainty in flow rate has on the predicted temperature profiles in the packed bed. The flow rate essentially governs the speed that the thermocline moves along the axial length of the packed bed. Thus the uncertainty in flow rate measurements predominantly affects the accuracy of the axial temperature profile predictions. To quantify this effect, a series of simulations were conducted for the 350-900 °C sensible heating test. The mass flow rate was increased by $\pm 2.5\%$ about the measured value from the experiment. A comparison of the axial thermocline profiles is shown in Figure E.1. At the inlet of the packed bed the flow rate uncertainty does not influence the predictions. As the thermocline moves deeper into the bed the deviations increase. As shown in Figure E.2 the highest differences are at the packed bed exit. The 2.5% uncertainty in mass flow rate causes a maximum 17.4 °C change at the bed exit, which when normalised by the temperature range is 2.9%.

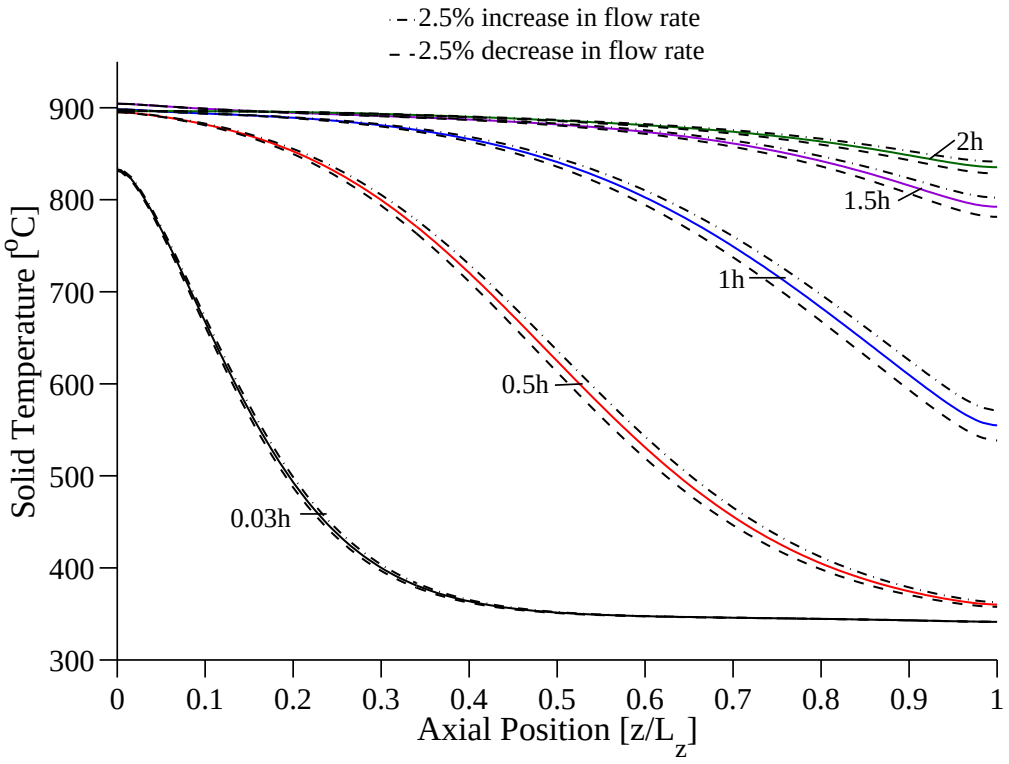

Figure E.1: Effect of mass flow rate uncertainty on thermocline predictions

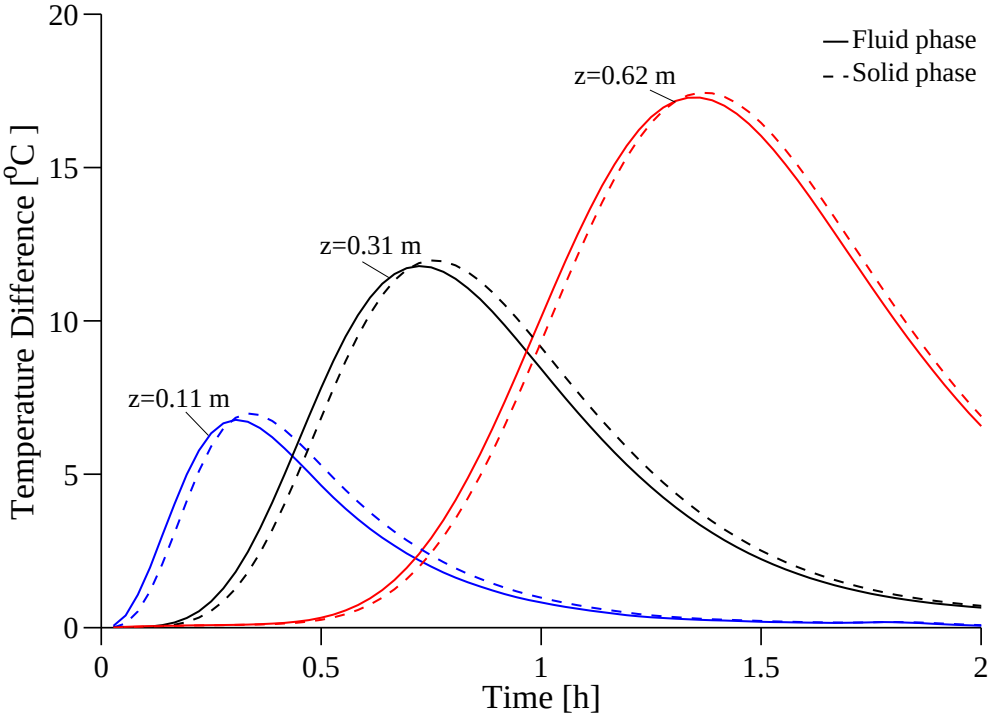

Figure E.2: Effect of mass flow rate uncertainty on axial temperature profiles for a 550°C temperature range

E.2 Radiation effects on fluid temperature measurements

For the sensible heat testing presented in Chapter 5, the solid temperature was measured inside the packed bed. For the latent heat testing the fluid temperature was measured within the packed bed. Attempts were made to measure the PCM temperature within a series of Na_2SO_4 particles. However, the high test temperature, combined with the corrosive molten salt lead to failures of these thermocouples. Therefore only the fluid temperature profiles could be utilised. Inside the packed bed the fluid thermocouples exchange thermal energy with the adjacent solid particles via radiation. Therefore at very high temperature, the thermocouple can under-read the actual fluid temperature during the heating cycle, and over-read the temperature during the cooling cycle. An analysis was conducted to determine the effect of radiation between the solid particles and the fluid temperature measurements. An energy balance on the cylindrical thermocouple yields:

$$V_{\mathrm{tc}}\rho_{\mathrm{tc}}c_{\mathrm{tc}}\frac{\partial T_{\mathrm{tc}}}{\partial t} = h_{\mathrm{tc}}A_{\mathrm{tc}}\left(T_f - T_{\mathrm{tc}}\right) + \frac{\sigma A_{\mathrm{tc}}}{1/\gamma_{\mathrm{t/c}} + 1/\gamma_p - 1}\left(T_p^4\big|_{\zeta=d_p/2} - T_{\mathrm{t/c}}^4\right) \tag{E.11}$$

where h_{tc} is calculated using the interstitial flow velocity, assuming convective flow over a cylinder (Hilpert correlation from Incropera and Dewitt (2002)). As the thermocouple time constant is much lower than the heating/cooling rate (36s compared to 4°C/min), a quasi steady state analysis can be used:

$$h_{\mathrm{tc}}\left(T_f - T_{\mathrm{tc}}\right) = \frac{\sigma}{1/\gamma_{\mathrm{tc}} + 1/\gamma_s - 1}\left(T_{\mathrm{tc}}^4 - \left(T_f - \Delta T_{fs}\right)^4\right) \tag{E.12}$$

The solution of Eq.(E.12) requires the surface temperature of the particle to be known, which was not possible to measure in the packed bed. Therefore the following approximation was applied:

$$T_p\big|_{\zeta=d_p/2} = T_f - \Delta T_{fs} \tag{E.13}$$

where ΔT_{fs} is the difference between the fluid and particle surface temperature predicted by the numerical model. Equation (E.12) can then be used to solve for T_f using a Newton Raphson method. The validity of the quasi steady state assumption was tested by comparing the results from Eq.(E.11) and (E.12), where $\partial T_{\mathrm{tc}}/\partial t$ was calculated using the measured temperature profiles. There was no notable difference in the results. This approach was not possible on all the thermocouples due to the influence of noise on the calculated temporal gradients.

Using this approach the effects of radiation on the fluid temperature measurements were estimated. These results are presented in Figure E.3. As the difference between the particle surface and fluid in the packed bed is of the order of 50 °C there are not significant changes in the temperature profiles. The trends are not changed and are still in good agreement with the predicted temperature profiles.

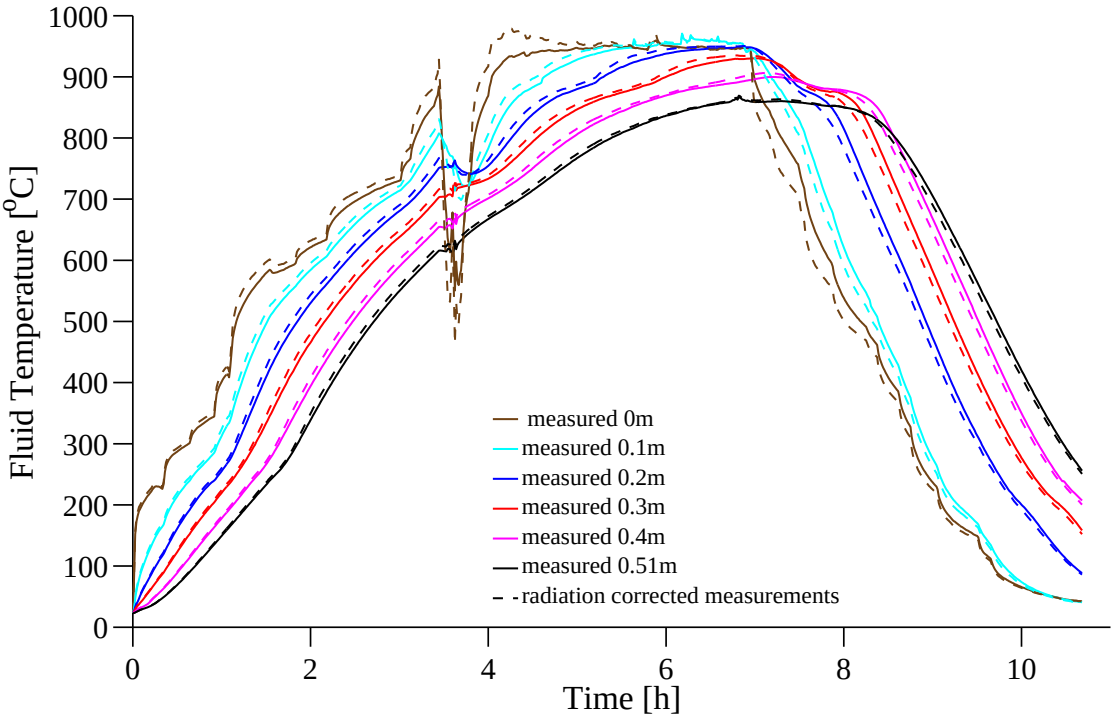

Figure E.3: Radiation corrected centreline fluid temperature profiles for 45 mm macro-encapsulated Na_2SO_4 particles for high temperature test.

Appendix F

Single EPCM particle heat transfer

This section outlines the solution of the temperature profiles within a single EPCM particle for validation against the experimental data presented by Akiyama et al. (1992) and Yagi and Akiyama (1995). The temperature profiles are predicted using the one-dimensional heat transfer equation from the D-C model, given by Eq.(2.23). There are two regions of heat transfer within the particle, namely the shell and PCM. The governing energy equation for the shell is given by:

$$\rho_{\mathrm{sh}} c_{\mathrm{sh}} \frac{\partial T_{\mathrm{sh}}}{\partial t} = \frac{1}{\zeta^2} \frac{\partial}{\partial \zeta} \left(\zeta^2 k_{\mathrm{sh}} \frac{\partial T_{\mathrm{sh}}}{\partial \zeta} \right) \tag{F.1}$$

and for the PCM is:

$$\rho_{\mathrm{PCM}} c_{\mathrm{PCM}} \frac{\partial T_{\mathrm{PCM}}}{\partial t} = \frac{1}{\zeta^2} \frac{\partial}{\partial \eta} \left(\zeta^2 k_{\mathrm{PCM}} \frac{\partial T_{\mathrm{PCM}}}{\partial \zeta} \right) \tag{F.2}$$

At the particle centre ($\zeta = 0$) a symmetry conditions is applied:

$$\frac{\partial T_{\mathrm{PCM}}}{\partial r} = 0 \tag{F.3}$$

At the interface between the PCM and the shell ($\zeta = d_p/2 - w_{\mathrm{sh}}$), the continuity of heat flux is applied where:

$$T_{\mathrm{PCM}} = T_{\mathrm{sh}} \tag{F.4}$$

$$k_{\mathrm{PCM}} \frac{\partial T_{\mathrm{PCM}}}{\partial r} = k_{\mathrm{sh}} \frac{\partial T_{\mathrm{sh}}}{\partial r} \tag{F.5}$$

while at the outer surface of the particle ($\zeta = d_p/2$), the particle exchanges energy with the fluid by convection and with the shield wall by radiation, where:

$$k_{\text{sh}} \frac{\partial T_{\text{sh}}}{\partial r} = h_p \left(T_f - T_{\text{sh}}\right) + \gamma_{\text{sh}} \sigma \left(T_{\text{rs}}^4 - T_{\text{sh}}^4\right) \tag{F.6}$$

As the intra-particle heat transfer equation is one-dimensional it is not possible to apply a locally varying heat transfer coefficient to the system. For this reason an average heat transfer coefficient across the surface of the sphere must be used. In order to calculate the average heat transfer coefficient, the Akiyama et al. model utilises the Ranz-Marshall correlation (Ranz and Marshall, 1952), for $0 < \text{Re}_p < 200$, where:

$$\text{Nu}_p = 2 + 0.6\text{Re}_p^{1/2} Pr^{1/3} \tag{F.7}$$

Akiyama et al. (1992) and Yagi and Akiyama (1995) only provide the nitrogen gas flow rate, and do not give the calculated heat transfer coefficients that were utilised. The details given regarding the test apparatus do not indicate the thickness of the radiation shield or how the blockage ratio of the sphere influences the heat transfer coefficient. Thus it is not possible to utilise Eq.(F.7) directly to calculate the heat transfer coefficient. In order to compare the predictions of the current model to those of the Akiyama et al. model, the heat transfer coefficient that was applied to the Akiyama et al. model needs to be calculated.

As the Akiyama et al. model is based on one dimensional heat transfer, it is possible to use the predicted surface temperature profiles from this model to calculate the average heat transfer coefficient that was originally applied. This approach involves conducting an overall energy balance for the test. This method is outlined below, for the melting cycle of the PCM.

The first step is to conduct an energy balance on the PCM sphere across the entire test. The energy stored by the sphere is equal to the total energy transferred to the sphere by convection and radiation:

$$Q_{\text{stored}} = Q_{\text{conv}} + Q_{\text{rad}} \tag{F.8}$$

As the initial and final temperatures of the sphere are uniform, the energy stored during the heating test can be calculated according to Eq.(F.9), where T_m, T_i and T_c represent the melting, initial and final temperatures of the EPCM respectively, while T_f and T_{rs} represent

the temperature of the nitrogen gas flow and the radiation shield.

$$Q_{\mathrm{st}} = m_{\mathrm{sh}} \int_{T_i}^{T_c} c_{\mathrm{sh}}\,\mathrm{d}T + m_{\mathrm{PCM}} \left(\int_{T_i}^{T_m} c_{s,\mathrm{PCM}}\,\mathrm{d}T + \Delta h_{\mathrm{fus}} + \int_{T_m}^{T_c} c_{l,\mathrm{PCM}}\,\mathrm{d}T \right) \tag{F.9}$$

The energy transferred to the sphere by convection and radiation heat transfer is given by:

$$Q_{\mathrm{conv}} = \int_0^{t_{\max}} A_p h_p \left(T_f - T_{\mathrm{sh}}\right)\,\mathrm{d}t \tag{F.10}$$

and

$$Q_{\mathrm{rad}} = \int_0^{t_{\max}} A_p \sigma \gamma_{\mathrm{rs}} \left(T_{\mathrm{rs}}^4 - T_{\mathrm{sh}}^4\right)\,\mathrm{d}t \tag{F.11}$$

By assuming an average convection heat transfer coefficient across the test, it can be removed from the integral in Eq.(F.10) and solved:

$$h_p = \frac{Q_{\mathrm{st}} - Q_{\mathrm{rad}}}{A_p \int_{t_0}^{t_{\max}} \left(T_f - T_{\mathrm{sh}}\right)\,\mathrm{d}t} \tag{F.12}$$

The values of T_f and T_{rs} that were applied to the Akiyama et al. model are known from the experimental data. Therefore by using the predicted surface temperature profile from the Akiyama et al. model, the value of h_p that was applied can be calculated. Across all the tests that were analysed, this method provided good agreement between the predictions from the current model and those from the Akiyama et al. model when natural convection effects were ignored.

Appendix G

Analysis of core geometries for sensible heat storage

This section presents the one-dimensional heat transfer modelling that was utilised to analyse the different core geometries for sensible heat storage. The results from this analysis are presented in Section 7.4.

G.1 Heat transfer

In order to compare the thermal performance of the different inventory types a simplified modelling approach was adopted. The C-S model was utilised in one-dimension, assuming: (1) plug fluid flow; (2) no heat losses to ambient; (3) no radial temperature variations. The aim of this design study was to compare the different inventory geometries. Thus the simplified modelling approach is justified, as it allows a large number of parametric simulations to be run at a low computational cost. In one-dimensional form the C-S model is given by:

$$\varepsilon \rho_f c_f \frac{\partial T_f}{\partial t} + c_f G_z \frac{\partial T_f}{\partial z} = h_p a_p (T_s - T_f) + \frac{\partial}{\partial x}\left(k_{\text{eff,f}} \frac{\partial T_f}{\partial x} \right) \tag{G.1}$$

$$(1-\varepsilon)\, \rho_s c_s \frac{\partial T_s}{\partial t} = h_p a_p (T_f - T_s) + \frac{\partial}{\partial x}\left(k_{\text{eff,s}} \frac{\partial T_s}{\partial x} \right) \tag{G.2}$$

The parameters of $h_p a_p$, ε, $k_{\text{eff,f}}$ and $k_{\text{eff,s}}$ were varied according to each inventory type and size.

For the randomly packed bed the inter-phase heat transfer coefficient h_p was calculated using the correlation of Yoshida et al. (1962), given by Eq.(2.50). As shown in Figure 2.3, this correlation predicts values of h_p that are lower than the correlations of Gunn (1978), Wakao et al. (1979) and KTA (1983). However, the Yoshida et al. correlation was chosen as it allows the direct comparison of different packing materials via the shape factor ψ_p. Table 2.2 provides a list of the particle shape factors.

For the checker bricks and honeycomb monoliths the inter-phase heat transfer is calculated using assuming laminar flow in a duct:

$$\mathrm{Nu}_d = \mathrm{Nu}_d \left(1 + 0.095 \mathrm{Re}_d Pr \frac{d_d}{L}\right)^{0.45} \tag{G.3}$$

where $\mathrm{Nu}_d = 3.66$ for a circular duct and $\mathrm{Nu}_d = 2.98$ for a square duct (Mills, 1992).

The effective solid conductivity of the packed bed is calculated using the modified Zehner-Bauer-Schlnder correlation given by Eqs.(2.38)-(2.45). The fluid thermal dispersion in the packed bed is calculated according to Eq.2.46. For the honeycomb and checker bricks the effective conductivities are:

$$k_{\mathrm{eff,s}} = (1-\varepsilon) k_s \tag{G.4}$$

$$k_{\mathrm{eff,s}} = \varepsilon k_f \tag{G.5}$$

G.2 Pressure drop

Gas turbine cycle efficiencies are sensitive to pressure drop which must be minimised. In this analysis the pressure drop through the storage media was limited to a maximum of 1% of the compressor delivery pressure. As described by Borbely and Kreider (2001), the pressure loss on the pressurised side of a recuperator is typically 2%. The limit for the storage inventory was set to 1% as there will be additional pressure loss associated with the piping and inlet diffuser.

The pressure drop in the randomly packed bed was calculated using the Ergun pressure drop equation (Ergun, 1952), given by Eq.(2.71). For the Berl saddles the effective particle diameter is used, as defined by:

$$d_p = \frac{6(1-\varepsilon)}{a_p} \tag{G.6}$$

The pressure drop through the honeycomb and checker brick channels is calculated using the pressure drop equation for laminar flow in a pipe (Mills, 1992):

$$\frac{\Delta P}{L_z} = 2\rho_f \frac{f_p}{d_p} \left(\frac{U_z}{\varepsilon}\right)^2 \tag{G.7}$$

where friction factors for the different duct geometries are given by:

$$f_p = \frac{14.25}{Re_d} \tag{G.8}$$

and for a circular duct:

$$f_p = \frac{16}{Re_d} \tag{G.9}$$

This simplified approach does not take into account the pressure drop effects at the inlet and exit to the regenerator.

G.3 Methodology

Table G.1 presents the parameters of the storage systems that were analysed. The charge and discharge temperatures were set to 1000 °C and 600 °C respectively for both storage cycles to allow a comparison of the results. Currently the highest achieved temperature of a pressurised solar air receiver is 1000 °C. The mass flow rate and storage pressure for Storage A and Storage B are based on gas turbines that have been used in operational SGT plants.

Table G.1: Parameters of storage systems investigated

Details	Storage A	Storage B
CSP plant type	Microturbine	Pilot
Discharging mass flow rate [kg/s]	0.8	17.9
Storage pressure [bar]	4.5	9.9
Maximum pressure drop across storage [kPa]	4.5	9.9
Charging inlet temperature [°C]	1000	1000
Discharging inlet temperature [°C]	600	600
Maximum decrease in outlet discharge temperature [°C]	50	50
Maximum discharge power [MW_{th}]	0.37	8.2
Discharge time [hrs]	6	6
Storage mass [tonnes]	18	410

A series of simulations were conducted based on each regenerator inventory type for Storage A and B concepts. The storage mass and discharging mass flow rates were fixed by the design conditions in Table G.1. In order to determine the relationship between utilisation factor and pressure drop, for each inventory type, the storage mass flux was varied over the range 0.1-1 kg/m^{2}s. For a specified mass flux the associated regenerator length was calculated according to:

$$L_z = \frac{m_s}{(1-\varepsilon)\rho_s}\frac{G_z}{\dot{m}_f} \tag{G.10}$$

Figure G.1(a) shows the effect of varying the mass flux in Storage A and B for a packed bed of spherical particles. As the specified mass flux increases the inter-phase heat transfer coefficient also increases. In order to increase the mass flux the container diameter decreases and the bed length increases (fixed volume). These factors increase the rate of heat transfer in the storage, resulting in a steeper axial temperature profile and higher utilisation factors. However, the pressure drop increases exponentially with mass flux and can exceed the pressure drop limits under certain conditions. The smaller particles have the highest specific surface area and therefore the best utilisation factors, but decreasing the particle diameter also increases the pressure drop.

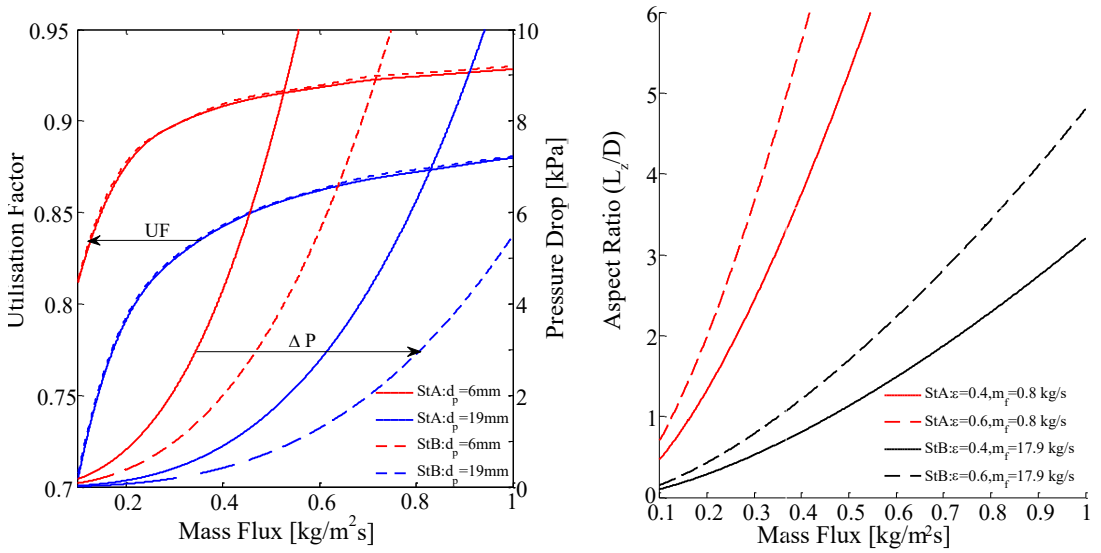

(a) Utilisation factor and pressure drop

(b) Aspect ratio

Figure G.1: Effect of mass flux variation in a packed bed of spheres

Figure G.1(a) shows that the utilisation factor as a function of mass flux is equivalent for Storage A and Storage B. This is due to the design conditions being linearly scaled i.e. $\left(m_s/\dot{m}_f\right)_{\text{StA}} \approx \left(m_s/\dot{m}_f\right)_{\text{StB}}$. The pressure drop characteristics differ due to the different storage pressures. Increasing the storage pressure reduces the volumetric air flow rate, thus reducing the pressure drop.

The geometry of the regenerator was constrained by the design conditions and the specified mass flux. Figure G.1(b) presents the aspect ratio of the regenerator as a function of the chosen mass flux. This graph indicates that high aspect ratios are required to achieve mass fluxes greater than 0.4 kg/m^{2}s in Storage A. This is due to the low mass flow rate of 0.8 kg/s. High aspect ratios are undesirable for thermal storage systems as they increase the surface area to volume ratio of the unit, resulting in higher heat losses to ambient. There are also practical problems associated with manufacturing and installing high aspect ratio beds into a receiver tower. Therefore an aspect ratio limit of five was applied in this analysis. This limits the applicable mass flux range for Storage A but not for Storage B.